Insights into Catalysts from Metal Adsorption and Adhesion Energies: How Metal Chemical Potential Depends on Nanoparticle Size and Support Material and How Solvents Affect Stability of Adsorbates

John R. Rumptz

A dissertation
submitted in partial fulfillment of the
requirements for the degree of

Doctor of Philosophy

University of Washington
2022

Reading Committee:
Charles T. Campbell, Chair
Eric M. Stuve
David G. Castner

Program Authorized to Offer Degree:
Chemical Engineering

University of Washington

Abstract

Insights into Catalysts from Metal Adsorption and Adhesion Energies: How Metal Chemical Potential Depends on Nanoparticle Size and Support Material and How Solvents Affect Stability of Adsorbates

John R. Rumptz

Chair of the Supervisory Committee:
Charles T. Campbell
Chemistry

Heterogeneous catalysts consisting of transition metal nanoparticles anchored to oxide and carbon support materials are ubiquitous in chemical production and pollution control. Despite their importance, the fundamental principles which control the performance and stability of these materials are still poorly understood. This dissertation provides insights into these fundamental principles through an investigation of the energetics of adsorption and adhesion of metals onto the surfaces of oxide and carbon supports, as well as studies on how the solvent environment can affect the final catalyst performance.

Understanding the bonding energetics of transition metal atoms and nanoparticles to well-defined support surfaces helps to elucidate the effect of the support material on catalyst

performance by providing important properties that correlate with performance, including the chemical potential of the metal versus particle size and metal monomer’s adsorption energy. The most suitable method for measuring these energies is metal vapor single-crystal adsorption calorimetry. Using these techniques, we studied a variety of metals and support surfaces.

The first of these experiments investigated the structure, energetics, and charge transfer of Ni supported on $CeO_{2-x}(111)$ using a combination of experimental methods and theoretical calculations. This study showed that Ni preferentially binds to the oxygen atoms in the CeO_{2-x} support and thus can be stabilized at edge-site defects on the surface. Furthermore, this binding to oxygen atoms is associated with oxidation of the deposited Ni atoms.

The adsorption and adhesion of Ag to rutile TiO_2 was studied using the same experimental techniques. This study began with an investigation of the TiO_2 surface structure using low-energy electron diffraction which allowed us to determine that our TiO_2 growth procedures resulted in $TiO_2(100)$ films on Mo(110). Measurements of the heats of adsorption and particle size showed that at 300 K, particles bind to defect sites on the surface while particles deposited at 100 K are not able to diffuse to these more energetically favorable sites. This study concluded with the determination of the $Ag/TiO_2(100)$ adhesion energy which qualitatively confirmed a trend of decreasing adhesion energies with the enthalpy of oxide reduction.

The use of carbon materials as a support for metal nanoparticles has become increasingly common, especially for use in electrocatalysis. Despite their importance, metals on these carbon supports are much less studied than on oxide supports. The first calorimetrically measured heats of adsorption of metal atoms onto graphene are reported here. The chemical potential of silver atoms in Ag nanoparticles on graphene follows the same equation as developed for metal chemical potential versus size as on oxide supports, which depends on metal / support adhesion energy. A large adhesion energy and weak monomer bonding for silver onto graphene was found, suggesting that carbon-based supports can provide excellent catalyst thermal stability. The adsorption and adhesion of nickel atoms and nanoparticles on this same support material was also studied. It was found that these particles grow with a unique growth morphology. These studies will form the basis of future research on trends of the adsorption and adhesion of metals onto carbon-based materials.

The adhesion energies of liquid solvents onto well-defined single crystal materials were also measured here. Catalysis in liquid solvents has become more important with the development of powerful electrocatalysts and fuel cells, however it is not well known how the solvent affects the binding of small molecules to the surface. It has been shown that these solvent adhesion energies can be used with a simple bond-additivity model to predict the adsorption energies of small molecules onto single crystalline surfaces in a solvent. These adhesion energies provide researchers with a way to determine how the choice of solvent affects the stability of small, adsorbed molecules and thus the reactivity of catalysts in different solvents.

Table of Contents

List of Figures

List of Tables

Acknowledgements

Funding for this work was provided by the Department of Energy, Office of Basic Energy Sciences, Chemical Sciences Division Grant Number #DEFG02-96ER14630 and the National Science Foundation under Grant Number #CHE-1665077.

While the short section for acknowledgements allowed to me in this dissertation is certainly not enough to extend my gratitude to all the wonderful people who have helped me, encouraged me, and been there for me in the last years of my life while I have been pursuing a PhD, I will try my best to extend my gratitude to some specific people. If I have forgotten to mention anyone important, please accept my sincere apologies here as it was not due to malice, but due to the lack of space provided.

First and foremost, I would like to thank my family and friends who have supported me throughout this lengthy and often strenuous process. My parents, Eric and Caroline, have encouraged me and provided all types of much needed support throughout my studies. My brothers, Ben and Kyle, have always been there for me as well. While there are too many to name individually, my friends have helped to bring me joy throughout this process and get me through the most difficult periods of my doctoral studies.

Next, I would like to sincerely thank my advisor, Professor Charles T. Campbell. It is safe to say that without Professor Campbell’s support and guidance, my academic journey would not have been nearly as successful. As an advisor, Professor Campbell was the ideal blend of challenging when I needed a push forward and hands-off to allow me to time to recharge and think critically through scientific problems on my own. Professor Campbell’s unbelievable depth of knowledge was a constant inspiration and helped me to find solutions to problems that I initially believed to be dead ends. I am incredibly thankful to have had the pleasure of working so closely with you Charlie.

I would also like to sincerely thank each member of the Campbell group past and present for their hard work in setting up such a successful research program. I’d like to extend my utmost gratitude to Dr. Zhongtian Mao for being such an incredibly intelligent and patient mentor while he taught me more details about my instrument that I ever thought possible. To Griffin Ruehl and Elizabeth Harman; thank you for all the fantastic conversations and for making my time in the lab so great. Thank you to Dr. Kun Zhao and Nida Janulaitis for their incredibly hard work in the lab, coaxing useful data out of our often-difficult instrument. I am certain that they will continue the great work of Cal3 after my departure and wish them both the absolute best with their future endeavors. Thank you to my undergraduate research assistants, especially Jackson Mayo, Ziareena Almualem, and Sharon Lin for helping me with taking data on Cal3 and for their patience as I sometimes struggled to teach them difficult concepts.

I would finally like to specifically thank the many members of the Chemistry and Chemical Engineering departments who made my time in graduate school such a great experience. In particular, I’d like to thank the personnel of the UW Chemistry Electronics Shop, especially Bill Beaty, for helping to fix the seemingly constant instrumental issues that appeared during my doctoral studies. Cal3 surely would not have been nearly as productive without Bill’s dedicated help.

Chapter Contributions

The experimental methods described in Chapter 2 are the culmination of work from major developments in single crystal adsorption calorimetry by Professor Charles Campbell as well as the work of many previous students in the Campbell group. While I did my best to describe our experimental methods in my own words, my descriptions are likely very similar to those given in past Cal3 papers, especially *Review of Scientific Instruments, 84*(12), 123901 (2013). I'd like to thank Professor Campbell and all those previous students for developing such a sophisticated instrument to give me a platform to perform the research described in the rest of this dissertation.

Chapter 3 was my first major experimental project on Cal3 and was supervised by my friend and mentor on Cal3, Dr. Zhongtian Mao. Along with Professor Campbell, Dr. Mao designed the experiments described in that work while my main role in that work was assisting in all experiments and data workup and having many conversations to make sure Dr. Mao's ideas were sound (they almost always were).

Chapter 4 was my second major experimental project on Cal3 and in that work I started to play a much more major role in the data collection and analysis. While Dr. Mao was still the supervisory lead for that project, at this stage we were able to split the workload evenly between our schedules (I worked mornings and he worked nights) to keep Cal3 as productive as possible. In addition, I created some of the published figures and wrote some sections of the published paper.

Chapter 5 was the first experimental project on Cal3 in which I was the project leader. While I had major help with developing graphene / Ni(111) growth procedures from Professor

Campbell and Dr. Mao, most of the experiments described in that chapter as well as most of the writing in that chapter represent my work alone.

Chapter 6 was another major experimental project in which I was the project leader. However, this work would not have been possible without the tireless help of Cal3's postdoctoral student, Dr. Kun Zhao. Many experiments described in that chapter as well as many parts of the writing represent the collaborative work between Dr. Zhao and myself.

Chapters 7 and 8 represent a collaborative effort of Professor Campbell and me. The central idea to study the adhesion energies of solvents to model the adsorption of solvents came from work by Professor Nirala Singh and Professor Campbell (*ACS Catalysis*, *9*(9), 8116-8127.). The work described in Chapter 7 extended that idea to all the solvent systems studied by Cal2. After Professor Campbell shared the idea with me, I went through all the previous data, calculated adhesion energies, and together we wrote that paper. The work described in Chapter 8 was much more independent, however it would not have been at all possible without many important conversations and corrections made by Professor Campbell.

Chapter 1. Introduction

Chemical catalysis is vital to humanity. Life as we know it could not exist without catalysts like enzymes inside cells that facilitate biological chemistry. Despite their importance, catalysts were relatively unknown until the 18th and 19th centuries, and it was many more years until chemists began to understand their function. Tremendous progress in catalysis was made in the 20th century and many Nobel prizes were awarded to chemists for the discovery of new catalysts and for elucidating their mechanisms. Today, the vast majority of industrial chemistry requires the use of man-made catalysts in chemical reactors.[1–5] It would be impossible to feed the world or to enjoy the luxuries of modern life without these man-made catalysts. In addition to their role in the production of chemicals, man-made catalysts are also crucial for their role in reducing pollution. For instance, urban air pollution was so bad in Los Angeles until the invention of the catalytic converter that wearing gas masks was not uncommon.[6] Undoubtably, catalysts are central to the function of modern society.

The most common type of man-made catalyst is the heterogeneous catalyst.[1,2] These catalysts typically consist of small metal nanoparticles supported on a high surface area oxide or carbon material. By adsorbing molecules from a fluid phase onto the solid surface, a chemical reaction can take a different pathway which can dramatically improve reaction rates and selectivity to the desired products. It is well-known that the catalyst performance can be significantly altered by using different materials for the metal nanoparticles and the support and by using differently sized nanoparticles.[1,7–12] These can be tuned to achieve solid catalysts with high activity and selectivity that are able to continuously cycle through the new reaction. Eventually, the catalyst material begins to deactivate through carbon (coke) formation or some other poison blocking the active material, or by sintering of the particles which decreases the active surface area of the catalyst.[12–16]

In addition to their importance as heterogeneous catalysts, late transition metal nanoparticles and films on oxide and carbon materials form the basis of many other modern technologies including microelectronics,[17–20] advanced sensors,[21–25] and fuel cells.[26–29] In all these technologies, the morphology of the metal and the interaction of the metal with the support material's surface play a critical role in the device performance. Despite the importance of these properties, there is a lack of fundamental understanding of the physiochemical interactions between the metal and the support material. As such, there is a tremendous motivation to study the binding strength of metal atoms, nanoparticles, and films to oxide and carbon materials.

Traditional methods for measuring the bonding strength of adsorbed atoms and molecules to solid surfaces include temperature-programmed desorption (TPD) and the analysis of equilibrium adsorption isotherms. However, analysis of the results of both these methods requires the adsorption / desorption process to be reversible.[30] In order to desorb a metal anchored to a support, very high temperatures are needed which can cause restructuring of the metal phase, sintering of the metal nanoparticles (i.e., forming fewer, larger particles), and diffusion of the metal into the bulk support material.[30] These are all non-reversible processes occurring before desorption, so measurements by TPD or adsorption isotherms lose valuable bonding information about the original metal structure of interest. As such, these two methods are only suitable for measuring metal – support bonding in very rare cases.

A method to circumvent the limitations inherent to TPD and adsorption isotherm measurements is to directly measure the heats of adsorption calorimetrically. The first instruments capable of measuring calorimetric heats of adsorption to a single crystal surface were developed in Cambridge, England by the group of Sir David King.[31] Their method involved dosing small amounts of the adsorbate from a molecular beam onto a single crystal sample and measuring the miniscule temperature rise caused by adsorption using an infrared pyrometer. This first single crystal adsorption calorimeter (SCAC) represented tremendous progress in measuring irreversible heats of adsorption, however the technique was still limited by the use of an optical pyrometer heat detector which required incredibly thin single crystal samples (~0.2 μm).[30,31] A dramatic improvement to the technique was developed by the Campbell group which replaced the pyrometer with a pyroelectric ribbon heat detector instead.[30,32] This new heat detector maintains sensitivity with samples thicker than 1 μm which allowed for a wider variety of samples, higher temperature annealing for a range of sample preparations, as well as sensitivity at very low temperatures.[30,33] Further improvements were made to this design which allowed for the direct measurement of heats of adsorption of metal nanoparticles supported on single crystal oxide and carbon materials.[34] This newest design is described in detail in Chapter 2 of this dissertation and the measurements taken with this instrument represent the focus of this dissertation, as described in detail in later chapters.

The calorimetrically measured heats of adsorption of metal vapor as it adds to nanoparticles on a support can be used to extract other important thermodynamic quantities including the chemical potential of atoms in the particles as well as the adhesion energy of the particles to the support.[35–38] The chemical potential of metal atoms in supported nanoparticles was recently shown to be a good descriptor of both the activity and stability of catalyst materials.[35–38] Small metal nanoparticles with a high chemical potential bind small molecules more strongly but are more susceptible to deactivation via sintering. A stronger binding of the particle to the support (or high adhesion energy) stabilizes the particles and reduces their chemical potential. Thus, changing the support material and particle size can be used to tailor the activity and stability of these supported particles.

Chapter 3 of this thesis describes a series of experiments studying the adsorption and adhesion of nickel vapor onto cerium oxide (CeO_2 or ceria). Nickel supported on ceria is an important catalyst material with a wide range of current and potential applications.[39–45] In addition, previous work from our group has shown that the adhesion energies of metals on oxides follow a predictable trend, with more oxophilic metals adhering more strongly to the oxide.[35–37] Since $CeO_2(111)$ is one of the best-studied oxide surfaces by our group, we wanted to investigate whether the trends in adhesion energies extend to more oxophilic metals such as nickel.

While the work studying the adsorption and adhesion of nickel proved that these predictive trends extend to more oxophilic metals,[36,46,47] there were still open questions regarding how the adhesion energies of a given metal vary as a function of the oxide support material. Previous work from our group hinted at the fact that the adhesion energy of a given metal may decrease with the enthalpy of oxide reduction,[35–37] however there were not enough oxides with carefully measured adhesion energies to construct a predictive trend. The work described in Chapter 4 studying the adsorption and adhesion of silver on titanium oxide (TiO_2 or titania) attempted to provide more insight into this problem. In addition, Ag nanoparticles supported on TiO_2 films and powders are promising materials for novel catalysts and photocatalysts.[48–52] Reported here are measurements of the heats of adsorption of Ag vapor onto the clean $TiO_2(100)$ surface. To the best of our knowledge, these are the first direct measurements of the heats of adsorption of any metal onto any single crystalline surface of TiO_2.

While the work described in Chapters 3 and 4 add to the growing body of knowledge of the adsorption and adhesion of metal particles to single crystal oxide supports, very little is known about the strength of metal adsorption onto carbon supports. Carbon supports are commonly used in catalysts due to their low cost, many possible carbon structures, as well as the conductivity of carbon materials.[53–58] This latter property makes carbon supports especially promising as a support in electrocatalysis which show tremendous promise in clean energy applications.[53–56,58] Motivated by these facts, we performed a study of the heats of adsorption of metals on graphene supported on Ni(111). Chapters 5 and 6 of this dissertation describe a series of experiments on the adsorption, adhesion, and morphology of silver and nickel nanoparticles on this technologically important material. We expect that these measurements will provide experimental comparisons for theoretical calculations of bond strengths for silver and nickel on graphene and graphite. In addition, we hope our measurements provide a starting point for identifying new trends in adsorption and adhesion energies of late transition metals on carbon surfaces like those developed by our group for oxide surfaces.

In gas-phase catalysis, the properties of the metal atoms as well as the support material play a vital role in the catalyst performance as described above. In liquid-phase catalysis and electrocatalysis, the effect of the solvent has an equally powerful effect on the catalyst performance.[59–63] It is well known from experiments and theory that solvent effects can dramatically influence the adsorption energies of small molecules dissolved in the solvent.[64–67] Many excellent studies have been done on solvent effects using density functional theory (DFT) calculations to model implicit dielectric solvents or explicitly including solvent molecules in the calculations.[65–67] However it is still not clear exactly how the solvent changes the adsorption energies from the more studied gas-phase adsorption energies.

A recent experimental study on the adsorption of phenol in water by Campbell and Singh proposed that a simple bond-additivity model could be used to estimate the heats of adsorption of small molecules in a liquid solvent.[64] This model used a thermodynamic cycle that showed the adsorption energy of a molecule onto a catalyst surface in a solvent could be related to the adsorption energy of that molecule in the gas-phase modified by the surface energy of the solvent, the solvation energy of the molecule in that solvent, and the adhesion energy of the solvent to the catalyst surface. The surface energies and solvation energies are straightforward to obtain through experimental measurements,[64,68–71] while the adhesion energy of solvents to well-defined surfaces is much less studied. Motivated by this fact and equipped with methods our group has developed for measuring adhesion energies of metals to supports, we set about to determine the adhesion energies of many solvents to well-defined surfaces. Chapters 7 and 8 of this dissertation describe work done in determining the adhesion energies of 23 different solvent / surface adhesion energies using previously published heat of adsorption versus coverage data from SCAC and TPD. We hope that these important measurements help to elucidate the role the solvent plays in modifying the adsorption energies of small molecules dissolved in those solvents.

While the topics described in this dissertation may at first glance seem somewhat disparate and disconnected, they all represent work done with the larger goal of describing how catalyst performance depends on the catalyst structure and reactive environment. A better understanding of how these factors influence the catalyst operation will lead to more logical design of novel catalysts. These improved catalysts will help to synthesize chemicals with a smaller energy cost and a smaller toll on the environment which has become increasingly important in the 21st century.

Chapter 2. Experimental Methods

All experimental measurements reported here were carried out in a custom-built ultrahigh vacuum (UHV) chamber colloquially known as Cal3. This instrument and the corresponding experimental methods have been described in detail previously.[34,72,73] This chapter will serve as a brief introduction to the UHV chamber instrumentation as well as provide details on the sample growth and characterization procedures of importance to the subsequent chapters in this dissertation.

2.1 Instrumentation

The sample preparation, characterization, and experiments described in this work were all carried out in a sophisticated UHV instrument with a base pressure of ~2×10^{-10} torr. This apparatus consists of three connected UHV chambers separated by gate valves to isolate the sensitive analysis instrumentation from the sample preparation conditions and metal evaporation source. The sample can be moved between the UHV chambers using a manipulator which can be cooled with liquid nitrogen and can monitor the sample temperature using a thermocouple. The preparation chamber is designed to clean and prepare the experimental samples and is equipped with a sample heater, pyrometer, ion gun, quadrupole mass spectrometer (QMS), and multiple gas dosers. The analysis chamber is designed to perform sensitive experiments on the prepared samples and is equipped with the single crystal adsorption calorimetry (SCAC) apparatus and low-energy electron diffraction (LEED) as well as spectroscopic methods including Auger spectroscopy (AES), x-ray photoelectron spectroscopy (XPS), and low-energy ion scattering spectroscopy (LEIS) which all use a PHI 10-360 precision hemispherical energy analyzer. The metal evaporation chamber consists of an electron beam evaporator along with a quartz crystal microbalance (QCM) for measuring the metal atom flux.

2.2 Sample Preparation and Characterization

The systems investigated in this work consist of ultrathin oxide and carbon films grown directly on thin 1-2 μm single crystal metal samples. The ultrathin film growth and characterization procedures for each thin film studied (CeO_{2-x}(111), TiO_2(100), and C(0001)) will be described below as well as briefly in the corresponding chapters of this dissertation. The single crystal metal samples were provided by the Thin Film Laboratory at Aarhus University in Denmark. The new single crystal samples were cleaned using a combination of 1 kV Ar^+ ion sputtering and annealing in UHV or O_2 to remove residual salts, carbon, and oxygen from the samples. The samples were cleaned using the aforementioned methods until a clean spectrum was observed in XPS and the single crystal gave a sharp LEED pattern. More detailed cleaning procedures for each metal can be found reported in the literature.[74]

CeO_{2-x}(111) thin films were grown on Pt(111) single crystals using growth procedures described previously in the literature.[73] The Pt(111) sample was held at 873 K for 20 minutes while exposed to a flux of cerium atoms in an environment of 1×10^{-6} torr O_2. After exposure to cerium, the sample was further annealed for 5 minutes at the same temperature and in the same O_2 environment to ensure an ordered thin film with minimal oxygen vacancies. XPS and LEED observations after growth show that this growth procedure resulted in ~4 nm films of $CeO_{1.95}$(111) which are sufficiently thick to give bulk-like behavior for metal adsorption experiments.[73] In order to obtain reduced CeO_{2-x}(111) thin films, the sample was grown using a similar procedure as above, however the O_2 pressure was reduced to 1×10^{-7} torr and the post-growth annealing procedure was changed to heat the sample for ~1 minute in UHV. This modified procedure gave thin films of the same thickness as the oxidized ceria but with a stoichiometry of $CeO_{1.8}$(111) based on fitting the Ce 3d peak line shape in the XPS spectra.[75]

TiO_2(100) thin films were grown on Mo(110) single crystal samples using a procedure described in the literature.[76,77] This method involved exposing the Mo(110) sample heated to ~625 K to a flux of titanium atoms while in a background of ~2×10^{-7} torr O_2 for 20 minutes. The sample was then post-annealed at 800 K for an additional 10 minutes in the same oxygen environment but without additional exposure to the titanium flux. This procedure resulted in TiO_2 thin films with a thickness between 2-3 nm measured by the attenuation of the Mo $3d_{5/2}$ peak in the XPS spectrum. The Ti $2p_{3/2}$ peak indicated that the thin films were nearly fully oxidized with only minimal oxygen vacancies created using these growth procedures. The TiO_2 thin films were further characterized using LEED and were determined to be rutile TiO_2(100) thin films with three distinct domains rotated at ~120˚ with respect to each other. Further details on this LEED structural characterization can be found in section 4.3.1 and the references therein.

The graphene (C(0001)) films were grown on Ni(111) single crystals using a direct growth method described in detail in the literature.[78–80] In this method, the clean Ni(111) was first annealed at 873 K in vacuum for 5 minutes before the sample was exposed to 1×10^{-6} torr ethylene (C_2H_4) for 30 minutes while the sample was held at 873 K. No post-growth annealing was performed for graphene on Ni(111) since high temperatures after growth can lead to the dissolution of the graphene into the Ni(111) sample.[79,81] After growth, the presence of graphene was determined by the C-KVV peak in AES which has distinctive line shapes for graphitic and carbidic carbons. The graphene films were further characterized using 1 kV He^+ LEIS which showed >95% attenuation of the nickel LEIS peak compared to the clean Ni(111) sample after growth of a complete film of graphene. No carbon LEIS peak was observed in the He^+ LEIS spectra due to a previously reported nearly complete ion-neutralization for low energy He^+ ions interacting with graphitic carbon.[82–84]

2.3 Metal Adsorption Calorimetry

While a complete description of the metal adsorption calorimetry setup can be found in the literature,[34] a brief description of the experiments will be provided here as well. After growth and characterization of the studied oxide or carbon film, the sample was transferred to the calorimetry position where the sample sits on a thermal reservoir with the single crystal surface normal pointed directly at the metal source. The geometry of the calorimetry setup can be seen more clearly in Figure 2.1. The thermal reservoir can be cooled using N_2 gas precooled with liquid nitrogen to control the sample temperature down to a minimum of ~100 K. The metal evaporator can generate a stable flux of gaseous metal atoms monitored by a QCM and collimated through a series of apertures until the flux reaches the sample. Based on the geometry of the aperture system, the resulting metal atom beam reaching the sample has a circular umbra of 4.00 mm and a penumbra of 4.52 mm resulting in an effective beam diameter of 4.26 mm. The metal beam is chopped using into pulses with a 100 ms duration and a 2 second period using a stepper motor immediately before the aperture system.

The heat released in each pulse is measured directly using a polyvinylidene fluoride (PVDF) ribbon placed in gentle thermal and mechanical contact with the back of the sample. The signal response of the PVDF heat detector is initially calibrated using pulses of a HeNe laser with a known wavelength (633 nm) and power and with spot dimensions and pulse durations identical to the metal beam spot used during calorimetry. Since the flux of metal atoms originates from a high temperature metal evaporator, it is necessary to measure and subtract out the contribution from optical radiation from the total measured heat signal. The signal due to radiation is measured by placing a transparent barium fluoride (BaF_2) window directly in the path of the metal beam which allows a known fraction of optical radiation (~90%) to pass through, but blocks metal atoms from reaching the sample surface. The transmittance of the BaF_2 window is measured before and after each calorimetry run by measuring the signal of the HeNe laser pulses through the window and comparing the signal to the pulses without the window in the path. The fraction of the measured signal with and without the window in the path gives the transmission coefficient assuming the transmission is the same for the HeNe laser and the infrared radiation from the hot metal source. Finally, the heat associated with pulses of metal atoms is measured by firing pulses of metal atoms at the sample and measuring the signal response of the PVDF heat detector. After subtracting the contribution due to radiation, we correct the measured heat for the difference in the internal energy between a flux of high temperature metal atoms (~2000 K) and a Boltzmann distribution at the sample temperature (100 K or 300 K) so that the reported heats of adsorption are equal to the negative of the standard enthalpy of adsorption at the sample temperature.

To obtain the desired heat of adsorption per mole of metal adsorbed on the surface, it is also necessary to measure the metal atom flux and the sticking probability of the metal onto the studied surface. The metal atom flux is measured before and after calorimetry at the sample position using an on-axis quartz crystal microbalance (QCM) that can be translated into the same position as the sample surface. During the on-axis flux measurements and during calorimetry, the flux is also measured continuously using an off-axis QCM in the metal evaporator. The fluxes measured on-axis before and after calorimetry are then used to scale the flux of the off-axis QCM so that we can accurately estimate the flux at the sample position continuously during the calorimetry measurement. This scaling procedure assumes that the ratio of the on-axis and off-axis fluxes varies linearly with time as has been demonstrated previously and can be seen clearly in Figure 2.2.

The sticking probability during the calorimetry experiments is measured simultaneously with the heats of adsorption using a modified version of the King and Wells method described in the literature.[85,86] A quadrupole mass spectrometer (QMS) is situated near the calorimetry position at the magic angle of 35˚ to minimize the deviations in the signal due to changes in the angular distribution of the atoms leaving the sample surface. During calorimetry, the QMS then measures a fraction of the metal atoms that do not stick to the sample surface and thus do not contribute to the measured heat of adsorption. A zero-sticking reference is measured after each calorimetry experiment by translating a heated tungsten or tantalum flag to the sample position and measuring the QMS signal associated with pulses in which no metal atoms stick. The ratio of the non-sticking measurement and the zero-sticking measurement (scaled by the respective fluxes) then determines the fraction of atoms that do not stick to the surface during calorimetry which can easily be converted to the fraction of atoms that do stick during the experiment (since the fraction of atoms that stick plus the fraction of atoms that do not stick equals 100%). Combining the measured heats of adsorption, the measured flux during calorimetry, and the measured sticking probability we can finally determine the heat of adsorption as a function of the cumulative metal coverage. The absolute metal coverage is defined differently for each surface investigated and these definitions can be found in the respective chapters of this dissertation.

2.4 Low Energy Ion Scattering Growth Morphology

The growth morphologies of the deposited metals were determined using He^+ low-energy ion scattering (LEIS) measurements with a scattering angle of 135˚ and an incident ion energy of 1 keV. In these growth mode experiments, the metal was dosed onto the thin film surface in discrete amounts while the flux in each dose was measured with a QCM. After depositing a known amount of metal in each dose, a He^+ LEIS spectrum was taken of both the deposited metal and the thin film substrate. After taking LEIS spectra up to a high coverage (>3 ML), a large amount of metal was deposited on the substrate (>10 nm) and a LEIS spectrum was taken of this thick overlayer to serve as a reference of complete coverage of the metal. The deposited metal LEIS signal was normalized by the thick layer and the substrate LEIS signal was normalized by the clean substrate before any metal was deposited. These normalized LEIS signals then directly give the fraction of the substrate surface covered by metal particles. We then determined the average thickness of the metal particles by dividing the average metal film thickness from QCM measurements by the fraction of the surface covered with particles from LEIS measurements. This average particle thickness as a function of coverage was then fit with an appropriate model (usually a hemispherical cap model) to determine the particle density as well as the average particle diameter as a function of coverage.

2.5 Figures

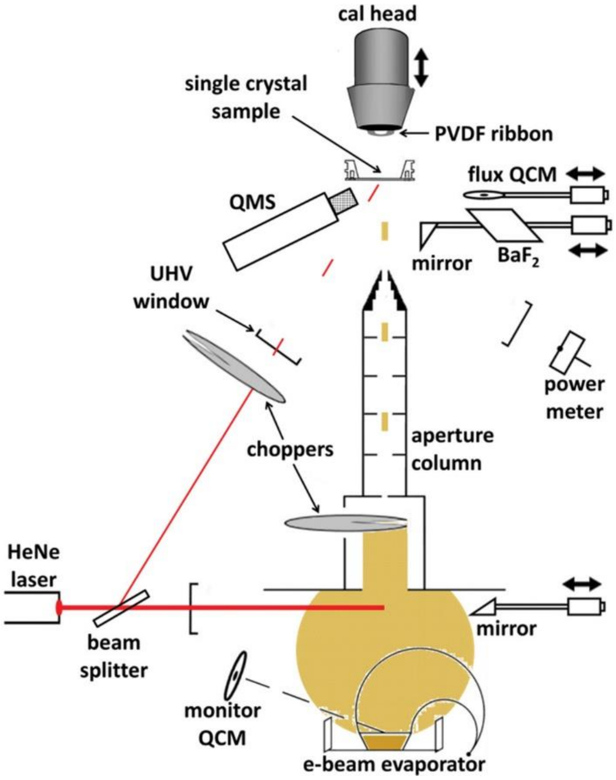

Figure 2.1. A schematic of the calorimeter, which uses an e-beam evaporator and a chopper to create a pulsed atomic beam of gaseous metal atoms (copper colored in the figure) which impinges upon the surface of a single crystalline sample. The transient heat input due to the adsorption of each gas pulse is detected by a flexible pyroelectric PVDF ribbon that is gently pressed against the back of the single crystal. As shown, this ribbon is mounted in the shape of an arch on the “cal head,” which can be translated to bring the ribbon into contact with the single crystal, or removed for crystal cleaning and surface analysis. The single crystal is mounted to a platen, which sits on a fork on a thermal reservoir during calorimetry but is moved for surface analysis. Also illustrated are the components for the real-time flux and relative reflectivity measurements. Not to scale.

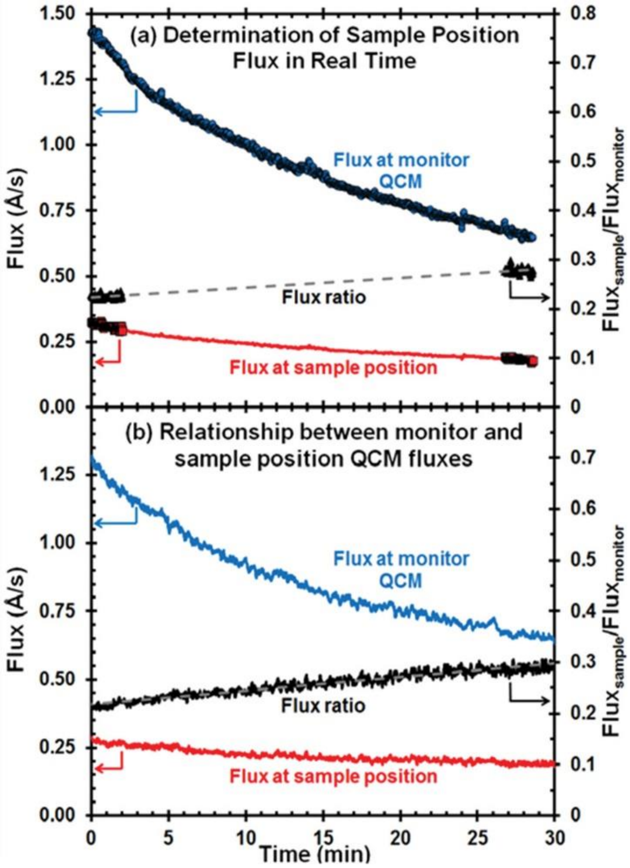

Figure 2.2. (a) Plot of the flux (in angstroms per second) from the electron beam evaporator running at constant emission current vs. time at both the sample position QCM and the off-axis monitor QCM. Measured flux data are plotted as points, while the calculated flux at the sample position is plotted as a continuous red line. Also plotted is the ratio between the two fluxes, which is fit to the linear dashed line as a function of time. The flux ratio is used to calculate the flux at the sample position based on the flux at the monitor QCM. (b) Similar data for a control run where the flux was collected with a QCM located at the sample position throughout the entire experiment. This shows that the changing flux ratio is well approximated as changing linearly with time. The dashed line showing the best linear fit to the flux ratio is essentially hidden within the scatter of the data.

Chapter 3. Ni Nanoparticles on $CeO_2(111)$: Energetics, Electron Transfer, and Structure by Ni Adsorption Calorimetry, Spectroscopies, and Density Functional Theory

This chapter has been published as:

Mao, Z., Lustemberg, P. G., Rumptz, J. R., Ganduglia-Pirovano, M. V., & Campbell, C. T. (2020). *ACS Catalysis*, 10(9), 5101-5114.

Chapter Abstract

The morphology, interfacial bonding energetics, and charge transfer of Ni clusters and nanoparticles on slightly reduced $CeO_{2-x}(111)$ surfaces at 100−300 K have been studied using single-crystal adsorption calorimetry (SCAC), low-energy ion scattering spectroscopy (LEIS), X-ray photoelectron spectroscopy (XPS), low-energy electron diffraction (LEED), and density functional theory (DFT). The initial heat of adsorption of Ni vapor decreased with the extent of pre-reduction (x) of $CeO_{2-x}(111)$, showing that stoichiometric ceria adsorbs Ni more strongly than oxygen vacancies. On $CeO_{1.95}(111)$ at 300 K, the heat dropped quickly with coverage in the first 0.1 ML, attributed to nucleation of Ni clusters on stoichiometric steps, followed by the Ni particles spreading onto less favorable terrace sites. At 100 K, the clusters nucleate on terraces due to slower diffusion. Adsorbed Ni monomers are in the +2 oxidation state, and they bind more strongly by ∼45 kJ/mol to step sites than terraces. The measured heat of adsorption versus average particle size on terraces agrees well with DFT calculations. The Ce 3d XPS line shape showed an increase in Ce^{3+}/Ce^{4+} ratio with Ni coverage, providing the number of electrons donated to ceria per Ni atom. The charge transferred per Ni is initially large but strongly

decreases with increasing cluster size for both experiments and DFT, and it shows large differences between clusters at steps versus terraces. This charge is localized on the interfacial Ni and Ce atoms in their atomic layers closest to the interface. This knowledge is crucial to understanding the nature of the active sites on the surface of Ni/CeO_2 catalysts, for which metal−oxide interactions play a very important role in the activation of O−H and C−H bonds. The changes in these interactions with Ni particle size (metal loading) and the extent of reduction of ceria help to explain how previously reported catalytic activity and selectivity change with these same structural details.

3.1 Introduction

Nickel supported on CeO_2 is an important catalyst material with promise in a wide variety of applications,[39,40,90–95,41–45,87–89] perhaps most importantly in the direct conversion of methane to methanol.[45] Ceria is a widely used support material for late-transition-metal catalysts[96–98] and is well known to enhance the stability of supported metals to resist deactivation by sintering.[96,97,99–102] The (111) face of CeO_2 is the most studied and well understood among the low-index faces of ceria in terms of the structure and reactivity. Thus, the interaction of Ni with the CeO_2(111) surface is of fundamental interest in catalysis. Recent works have shown that Ni−ceria interactions are crucial to achieving high catalytic performance.[43–45,89,92] In particular, it has been found that oxidized Ni species (Ni^{2+}) at the Ni−ceria interface that result from the transfer of two 4s electrons from Ni to the empty 4f band of ceria, generating two Ce^{3+} ions, activate O−H and C−H bonds at room temperature. Moreover, the metal loading has a drastic effect on the catalytic properties. For example, as the coverage of Ni increases and 3D nanoparticles form, the dissociation of O−H bonds is hindered on the Ni atoms that are not in direct contact with the ceria support,[89] and the ability of the system to dissociate methane is also hindered due to the formation of NiC_x on the surface.[44] Because the strong electronic perturbations in chemisorbed Ni species on ceria, which produce dramatic changes in their chemical properties, are extremely sensitive to the coverage of Ni on the ceria substrate, it is crucial to understand how the structure, heat of adsorption, and amount of Ni → ceria charge transfer changes with Ni coverage.

Here, we study the morphology and interfacial energetics of vapor-deposited Ni on slightly reduced $CeO_2(111)$ surfaces using metal vapor adsorption calorimetry, surface analysis techniques, and density functional theory. The results reveal that Ni grows as 3D particles and clarify electronic details of the Ni−CeO_2 interactions. The results show that the heat of Ni adsorption and the number of electrons donated to ceria per Ni atom change strongly as the size of the Ni clusters grows and with the extent of reduction of the ceria support and that the Ni clusters bind more weakly to the (111) terrace sites than to step edges.

These results help explain the unique properties of ceria as a support for Ni nanoparticle catalysts.

3.2 Methods

3.2.1 Experimental Methods

A description of the single crystal adsorption calorimetry apparatus and experimental procedures are presented in detail in Chapter 2. They are described briefly again here to allow the reader to understand this chapter without the need to reference back to Chapter 2.

The apparatus and methods for SCAC, XPS, LEIS and LEED were described in detail previously.[34,75,103,104] The $CeO_{2-x}(111)$ thin films ($x = 0.05$ and 0.2) were grown on a clean Pt(111) single-crystal surface up to a thickness of 4 nm using the same methods as described previously, which had shown to produce ordered (111) terraces with ∼5% step sites.[73] They are thick enough to give a bulk-like behavior based on the adsorption energy of Ag vapor. [73] A sharp ($\sqrt{2} \times \sqrt{2}$) LEED pattern was observed for the as-grown $CeO_{2-x}(111)$ films, indicating that the surface was well ordered and the epitaxial relationship with the underlying Pt was in agreement with prior reports.[105] The Ce oxidation states were characterized with XPS based on line shape fitting of the Ce 3d peaks as described previously.[75]

Metal vapor adsorption calorimetry was performed as described previously.[34] In brief, a pyroelectric polyvinylidene fluoride (PVDF) ribbon is pressed against the backside of a 1 μm-thick Pt(111) single-crystal sample as the heat detector. During SCAC, a well-defined 4.26 mm-diameter beam of Ni atoms is generated from an e-beam evaporator, collimated through a series of apertures, chopped into 100 ms pulses with a period of 2 s, and finally dosed onto the sample. The heat release during the adsorption of Ni atoms is detected using the PVDF ribbon. For each calorimetry run, the heat detector response is calibrated by pulses from a HeNe laser with known energy. To subtract the signal from thermal radiation, the sample is blocked by a BaF_2 window that only allows a known fraction of radiation to penetrate. The signal associated with the radiation is corrected with the BaF_2 transmission and subtracted from the total heat signal to leave only the part that is due to Ni vapor adsorption. As we always do in SCAC,[33] this heat is corrected for the difference in the metal vapor's internal energy (2RT in a directed beam) between the metal vapor source temperature (~2000 K) and the surface temperature (100 or 300 K) so that the heats reported below are equal to the negative of the standard enthalpy of Ni adsorption at the surface temperature.

The flux of Ni atoms is measured with an on-axis quartz crystal microbalance (QCM) and an off-axis QCM. The off- axis QCM facing directly to the e-beam evaporator monitors the flux throughout the whole experiment. The on-axis QCM is placed at the sample position only before and after adsorption calorimetry. The beginning and ending fluxes measured by the on-axis QCM are used to scale the off-axis QCM fluxes so that it provides the Ni flux at the sample position for all times during the calorimetry.[34] The sticking probability of each pulse is measured simultaneously with its heat using a modified King and Well's method.[34] Combining the flux and the sticking probability, we calculate the amount of Ni atoms that sticks to the sample in each pulse. The differential heat of adsorption versus the cumulative coverage of Ni is thus available. The Ni coverages are reported here in monolayers (ML), where 1 ML is defined as 7.89×10^{14} atoms per cm^2, which is the areal density of coordinatively unsaturated O atoms on the ideal bulk-terminated $CeO_2(111)$ surface.

The growth morphology of adsorbed Ni on $CeO_{2-x}(111)$ was determined using He^+ low-energy ion scattering (LEIS) with an incident angle of 45° from normal and a scattering angle of 135°. The normalized LEIS signals give the fraction of surface area that is covered by Ni nanoparticles.[72]

3.2.2 Computational Methods

All electronic structure calculations were carried out using the spin-polarized DFT approach as implemented in the Vienna ab initio simulation package (VASP) {vasp site, http://www.vasp.at; version vasp.5.3.5}.[106,107] Ce (4f, 5s, 5p, 5d, 6s), O (2s, 2p), and Ni (3p, 3d, 4s) electrons were explicitly treated as valence states within the projector augmented wave (PAW) method[108] with a plane-wave cutoff energy of 415 eV, whereas the remaining electrons were considered as part of the atomic core. Total energies and forces were calculated with a precision of 10^{-6} eV and 10^{-2} eV/Å for electronic and force convergence, respectively, within the DFT+U approach by Dudarev et al.[109] ($U_{eff} = U - J = 4.5$ eV for the Ce 4f electrons) with the generalized gradient approximation (GGA) proposed by Perdew, Burke, and Ernzerhof (PBE).[110]

We note that questions regarding the best value for the U parameter are still under debate.[111–113] Nonetheless, most DFT+U studies of reduced ceria-based systems agree that U values in the range of 4.5−6.0 eV with GGA are suitable for the description of the localization of charge driving the $Ce^{4+} \rightarrow Ce^{3+}$ reduction. However, one should bear in mind that there is in general no unique U that gives a reasonable account of all systems' properties.[114–116] Long-range dispersion corrections were also considered, employing the so-called DFT-D3 approach.[117,118]

3.3 Results

3.3.1 Ni Sticking Probability on $CeO_{2-x}(111)$

The sticking probability was measured using the signal for non-sticking Ni gas atoms in each pulse detected with the transient QMS signal for Ni gas and normalized to the signal for the reference zero-sticking pulse from a hot W flag, where no permanent sticking occurs. For all three systems we studied ($CeO_{1.95}(111)$ at 300 K, $CeO_{1.8}(111)$ at 300 K, $CeO_{1.95}(111)$ at 100 K), the sticking probability started at ∼97% and increased to unity within the first 0.5 ML.

3.3.2 Ni Growth Morphology on $CeO_{2-x}(111)$

Gaseous Ni was deposited onto $CeO_{2-x}(111)$ films at 300 and 100 K in discrete amounts. The Ni and Ce signals in He^+ LEIS were monitored after each such Ni dose. The integrated Ni signals were normalized to the signal from a thick Ni overlayer (>10 nm average thickness). The Ce signals were normalized to those for a clean $CeO_{2-x}(111)$ surface taken at the beginning of each experiment. The normalized Ni LEIS signal gives the fraction of surface covered and shadowed by Ni nanoparticles, and the normalized Ce signals give the fraction of the surface that is not masked by Ni. The normalized Ni and Ce LEIS signal data are plotted versus Ni coverage in Figure 3.1 and compared with two typical growth models. The straight dashed lines correspond to the normalized LEIS signal that would be expected if Ni grew in a layer-by-layer mode. They do not fit well with the measured LEIS data. The solid curved lines correspond to the three-dimensional (3D) growth mode assuming that Ni grows as 3D particles with the shape of flat disks with a constant aspect ratio (height/diameter) of 0.25 on $CeO_{1.95}(111)$ and 0.20 on $CeO_{1.8}(111)$, as suggested by STM studies.[119] In the flat-disk model, we assume that the Ni particles all have this same shape at all coverages and the same size at any given coverage and the particle number density *n* does not change with metal coverage (i.e., the saturation number density of nuclei is reached by the first dose, as is generally the case for such systems[120]). This model is applied only up to the coverage where ∼35% of the surface is covered by particles since particles overlap with each other at a higher area fraction. A previous work showed that, if the particles grow as hemispherical caps, the total surface area masked by particles in the LEIS signals for the incident and detection angles used here is 1.207 times the metal/support interfacial area due to a shadowing effect.[72] This ratio, calculated in the same way, is changed to 1.318 for $CeO_{1.95}(111)$ and 1.255 for $CeO_{1.8}(111)$ based on their flat-disk aspect ratios (height/diameter = 0.25 and 0.20, respectively). With these assumptions, the particle number density n is the only fitting parameter in the equation, and it is determined from the best fitting line in Figure 3.1. Following this approach, the flat-disk model gives a good fit to the LEIS data, as shown in Figure 3.1, and the best-fit particle number densities on $CeO_{2-x}(111)$ at 300 and 100 K are shown. The extent of reduction of ceria has only a minor effect on the Ni particle density. At 300 K, it was 3.6×10^{12} particles/cm^2 on $CeO_{1.95}(111)$ and 4.5×10^{12} particles/cm^2 on $CeO_{1.8}(111)$. A similar small increase in the particle density with extent of reduction was reported based on STM images.[119] Comparing the growth of Ni on $CeO_{1.95}(111)$ at 300 and 100 K, a huge temperature effect was observed. The Ni particle density on $CeO_{1.95}(111)$ was 1.3×10^{13} particles/cm^2 at 100 K, about 4-fold higher than that at 300 K.

3.3.3 Heat of Adsorption of Ni on $CeO_{2-x}(111)$

The heats of adsorption of Ni gas atoms on $CeO_{2-x}(111)$ for x = 0.05 and 0.2 at 300 K and for x = 0.05 at 100 K are plotted in Figure 3.2 as a function of Ni coverage. At 300 K on $CeO_{1.95}(111)$, Ni has an initial heat of adsorption of 345 kJ/ mol, and it decreases rapidly to 323 kJ/mol by 0.2 ML. The heat then increases, slowly approaching the sublimation heat of bulk Ni at 430 kJ/mol by 9 ML. This type of reverse in slope with coverage has been seen before and attributed to the adsorption of metal adatoms to stronger-binding defects (step edges) at the lowest coverage that become saturated as coverage increases.[75] Thus, an initial heat of 345 kJ/mol on $CeO_{1.95}(111)$ is attributed to Ni adsorption at step edges. The minimum heat occurs at 0.1−0.2 ML Ni, which is consistent with a step-site density of ∼5% of the total sites, given that some Ni atoms will bind to other Ni atoms in clusters rather than directly at step sites as the step sites approach saturation by Ni atoms. On $CeO_{1.8}(111)$, where the degree of reduction is larger and there are many more O vacancies, the initial heat at 300 K is 65 kJ/mol lower than that on $CeO_{1.95}(111)$ (280 vs 345 kJ/mol), and the heat remains lower up to ∼0.2 ML. This clearly shows that Ni atoms do not prefer oxygen vacancies on $CeO_2(111)$, the opposite as we observed for Ag and Au adsorption[73,104] but the same as that for Cu.[75] This is consistent with the fact that Cu and Ni are much more oxophilic than Ag and Au, so they prefer to bind to the surface O atoms. The stronger binding of Au and Ag atoms to oxygen vacancies than to stoichiometric terrace sites was also predicted by DFT calculations[121–126] and confirmed experimentally[127–130] in previous literature, though the decoration of oxygen vacancies by Au atoms has been challenged by recent STM experiments.[126] On $CeO_{1.8}(111)$, there is no minimum in the heat of Ni adsorption versus coverage of the type seen on $CeO_{1.95}(111)$ here. We attribute this to the preferential loss of the step-edge oxygen atoms (by far, the least stable type of lattice O[131]) upon reduction so that the step edges on $CeO_{1.8}(111)$ no longer have enough O atoms to make more stable sites for Ni than stoichiometric terrace sites.

At 100 K, the heat of Ni adsorption on $CeO_{1.95}(111)$ is initially 45 kJ/mol lower than that at 300 K and remains lower until 2 ML. There is also no minimum in heat versus coverage of the type seen at 300 K. We attribute this to the lack of mobility of the metal adatoms at 100 K so that they cannot diffuse to the stronger-binding step sites as they do at 300 K and thus remain on terrace sites and nucleate particles there instead.

Dividing the Ni particle number density from the flat-disk model fit in Figure 3.1 (particles/cm^2) by the Ni coverage (atoms/cm^2) gives the average number of Ni atoms per particle at each coverage. Assuming that these particles have the same density as bulk Ni(s) gives the volume per particle. Combining this volume with the disk shape (aspect ratio stated above) also gives the average Ni particle (flat disk) diameter at each coverage. Using this approach, the heat-versus-coverage data in Figure 3.2 have been replotted as Ni heat of adsorption versus the average Ni particle (flat-disk) diameter, as shown in Figure 3.3a.

Figure 3.3a shows the heat of Ni adsorption versus particle diameter on $CeO_{1.95}(111)$ at 300 and 100 K and $CeO_{1.8}(111)$ at 300 K. At 300 K, the heat of Ni adsorption on Ni nanoparticles smaller than 1.5 nm in diameter supported on $CeO_{1.95}(111)$ is higher than that on Ni nanoparticles supported on $CeO_{1.8}(111)$, indicating that Ni does not bind more strongly to oxygen vacancies on this surface. Above 1.5 nm diameter, the extent of reduction of CeO_{2-x} does not show a significant influence on the heat of Ni adsorption onto Ni nanoparticles. The plot for $CeO_{1.95}(111)$ at 100 K stops at 1.5 nm diameter because the fractional surface area masked by Ni nanoparticles reaches ~35% here, and the flat-disk model used to fit the LEIS data is no longer appropriate at higher coverages. The heat of Ni adsorption on $CeO_{1.95}(111)$ at 100 K for a given particle diameter below 1.3 nm is lower than the value for $CeO_{1.95}(111)$ at 300 K. At 0.6 nm diameter, the difference is ∼40 kJ/mol. We attribute this difference to the nucleation of Ni particles at step edges, where they bind more strongly than on $CeO_2(111)$ terraces (by ∼40 kJ per mole of Ni atoms at the smallest sizes measured). Due to the much slower diffusion of Ni atoms at 100 K, they are not able to nucleate particles at step edges, but at 300 K, they can. When the particle diameter exceeds ∼1.3−1.5 nm, the heats of Ni adsorption under all three conditions (i.e., $CeO_{1.95}(111)$ at 300 K, $CeO_{1.8}(111)$ at 300 K, $CeO_{1.95}(111)$ at 100 K) only show small differences between each other. Apparently, the new Ni atoms, which add to particles larger than ∼1.4 nm, predominantly bind to sites that are far enough from step edges and that they feel little effect of the step sites. Because of the much larger particle number density at 100 K than at 300 K, this particle size (>1.4 nm) is not reached until a 4-fold higher coverage at 100 K. This size difference explains why the heats of adsorption in Figure 3.2 at 100 K remain below those at 300 K until very high coverage.

As reported previously,[38] we can convert the differential heats of Ni adsorption measured here to the chemical potential of Ni atoms by assuming that the entropic contribution to the free energy is negligible compared to the huge enthalpic differences measured here. The difference between the chemical potential of Ni atoms in nanoparticles with a given diameter *D* and the chemical potential of Ni atoms in bulk Ni metal (set as the zero reference of chemical potential) is equal to the sublimation heat of bulk Ni minus the heat of Ni adsorption onto Ni nanoparticles with diameter *D*.[38] The data in Figure 3.3a have been replotted in Figure 3.3b as the chemical potential of Ni atoms in Ni nanoparticles versus the average particle diameter. As seen, the chemical potential generally decreases with increasing particle size, as has been reported for many related systems, and is largely related to the increasing number of metal−metal bonds per atom with increasing size.[38,75,103,104] The chemical potential initially increases with increasing particle size for $CeO_{1.95}(111)$ at 300 K due to the initial population of more stable sites at step edges, which saturate quickly as coverage increases.

It appears from Figure 3.3 that Ni particles do not nucleate at step edges on the $CeO_{1.8}(111)$ surface even at 300 K or that step edges do not bind Ni significantly more strongly than terraces on this heavily reduced ceria surface, especially since O vacancies prefer to form at step edges, as noted above.

3.3.4 Charge Transfer from Ni to $CeO_{2-x}(111)$ during Deposition

The change of the Ce oxidation state in the $CeO_{2-x}(111)$ surface during Ni deposition was monitored by the change in the Ce 3d XPS peak line shape. The percentage of Ce^{3+} in the Ce 3d XPS probe depth (~1 nm) was determined from line shape fitting of the XPS Ce 3d peak as described previously.[34,132] The Ce^{3+} percentage is plotted with respect to Ni coverage in Figure 3.4. The Ce^{3+} percentage increases rapidly with the Ni coverage up to 2 ML for $CeO_{1.95}(111)$ at 300 and 100 K. Above 2 ML, the Ce^{3+} percentage does not change much with the Ni coverage, remaining very near the high-coverage (10 ML) limits of 22% at 300 K and 19% at 100 K. For $CeO_{1.8}(111)$, the Ce^{3+} percentage also increases in the first 2 ML but only from 41 to 46% and again stays fairly constant with coverage above 2 ML.

To quantify the extent of charge transfer per Ni atom to the film, we assume that the Ce atoms in the $CeO_{2-x}(111)$ film are reduced by the electrons donated from the Ni atoms by the percentage plotted in Figure 3.4 but only down to the XPS probe depth of 1.0 nm, with no reduction below that. (Using the TPP-2M equation[133] to calculate, the electron inelastic mean free path in CeO_2 for Ce 3d XPS peak is 1.24 nm. Since the XPS data was taken with the energy analyzer at 45° to the normal angle of the sample, 70% of the XPS signal of the Ce 3d peak comes from the first 1.0 nm-thick layer of ceria in the sample.) Using the number of Ce atoms per unit area in this probe depth (2.5×10^{15} Ce atoms per cm^2), the data point in Figure 3.4 at each Ni coverage can then be converted to the average number of electrons donated per Ni atom, as done previously for Cu on this same surface.[75] If we further assume that Ni can only be in the form of neutral Ni or Ni^{2+}, this average number of electrons donated per Ni atom can be converted to the fraction of total Ni that is oxidized to Ni^{2+}. Figure 3.5a shows the resulting number of electrons donated per Ni atom and the fraction of Ni^{2+}, calculated based on the data in Figure 3.4, plotted versus Ni coverage. These both decrease rapidly with coverage and are much smaller values on more reduced ceria.

We observed that the Ni $2p_{3/2}$ XPS peak's binding energy (BE) at low Ni coverages had large contributions in the region expected for Ni^{2+}. This was studied in more detail by Carrasco et al.,[89] as shown in Figure 3.5b, where their Ni $2p_{3/2}$ BE values for Ni on $CeO_2(111)$ at 300 K are plotted as a function of Ni coverage. For a coverage of 0.15 ML of Ni, they reported a shift of ~2 eV with respect to the reported value for metallic Ni, which indicates the formation of Ni^{2+}.[134] Zhou and Zhou[135] also observed with XPS that when ~0.5 ML Ni (which is ~1.2 ML in the definition of this paper) is deposited onto the fully oxidized $CeO_2(111)$ at 300 K, about 25% of the total Ni is oxidized to Ni^{2+}.

For the convenience of comparison to DFT calculations, the number of electrons donated per Ni atom and the fraction of Ni^{2+} are also replotted as a function of the average number of Ni atoms per Ni nanoparticle in Figure 3.6. Here, one clearly sees that the fraction of Ni^{2+} is larger for a given particle size when grown at 300 K (where they nucleate at steps and have a higher heat of adsorption) than at 100 K where they nucleate at terraces and are less stable. Thus, step edges seem to be important in making the Ni^{2+} species stable. Alternatively, the temperature could have a direct effect in which the process to make Ni^{2+} might have some activation barrier that is not reached at 100 K.

3.3.5 DFT Models

The $Ni_n/CeO_2(111)$ (n =1−7, 9, 13, 19, 24, 26, 29, and 32) surfaces were modeled with DFT by supercells with (3 × 3) surface periodicity (see Figure 3.7) with the calculated ceria bulk equilibrium lattice constant (CeO_2: 5.485 Å, DFT+U). A CeO_2 slab of six atomics layers, i.e., two O−Ce−O trilayers, separated by at least a 13 Å-thick vacuum layer, was used as model of the ceria support. Monkhorst− Pack[136] grids with (2 × 2 × 1) k-point sampling were used. All atoms in the three bottom atomic layers were fixed at their optimized bulk-truncated positions during geometry optimization, whereas the rest of the atoms were allowed to fully relax. The structures of the ceria-supported Ni_1, Ni_2, Ni_4.flat, and Ni_4.pyr aggregates (Figure 3.7) correspond to the ones previously reported,[44,45,87,94] for which the locations of the Ce^{3+} ions resulting from the metal−support interaction were optimized. For the other Ni aggregates considered, some different adsorption sites were explored, but different Ce^{3+} configurations were not. Note that for Ni_n (n > 19), the (3 × 3) surface unit cell is not large enough to isolate the Ni_n aggregates, and the models correspond to continuous rows of supported Ni atoms, i.e., infinitely long 1D islands (i.e., stripes or wires) of Ni that are several Ni atoms wide. Selected calculations were performed for some $Ni_n/CeO_2(111)$ systems with (4 × 4), (2 × 2), and (1 × 1) surface periodicity and (1 × 1 × 1), (3 × 3 × 1), and (6 × 6 × 1) k-point sampling, respectively, in order to evaluate possible variations in the number of electrons transferred from the Ni_n aggregates to the ceria support as a function of Ni loading.

Reduced extended $CeO_{2-x}(111)$ surfaces were modeled with different concentrations of oxygen vacancies (Θ_{Ovac} = 1/4, 1/2, and 3/4; Θ_{Ovac} = Nv/N, where Nv and N are the number of surface plus subsurface vacancies in the reduced overlayer and the total number of oxygen atoms in a single non-reduced oxygen atomic layer of the same cell, respectively) using a slab of nine atomic layers with (2 × 2) periodicity, as employed in a previous work.[44] Furthermore, one and two layers of Ce_2O_3 on $CeO_2(111)$ and the fully reduced (A-type) $Ce_2O_3(0001)$ surface (Ce_2O_3: $a_0/c_0 = 3.92/6.18$ Å and internal parameters $u_{Ce}/u_O = 0.2471/0.6448$, ferromagnetic state, and DFT+U) were also modeled; only the interaction of Ni_1 species on the reduced supports was considered, and this was done without accounting for long-range dispersion corrections.

The oxidation state of a given Ce ion (Ce^{4+} or Ce^{3+}) was determined by considering its local magnetic moment (the difference between up and down spins on the ion), which can be estimated by integrating the site- and angular momentum- projected spin-resolved density of states over spheres with radii chosen as the Wigner−Seitz radii of the PAW potentials. The magnetic moments of the Ce^{4+} ($4f^0$) and Ce^{3+} ($4f^1$) ions are 0 and ∼1 μ_B, respectively, because the occupations of the Ce f states are 0 and ∼1, respectively. As for the oxidation state of the Ni atoms in the supported clusters, using the Bader analysis method,[137] we obtained that only those Ni atoms in direct bonds to the ceria support are partially oxidized, and thus, the average oxidation state of these atoms is calculated as the total number of electrons transferred to the ceria support divided by the number of Ni atoms with direct bonds to the support (Figure 3.7).

The integral heat of adsorption of Ni gas atoms forming Ni_n clusters on the $CeO_2(111)$ support was calculated at 0 K as $E_{ads} = -1/n\ [E(Ni_n/CeO_2) - E(CeO_2) - n \times E(Ni_{atom})]$, where $E(Ni_n/CeO_2)$ and $E(CeO_2)$ are the total energies of the $Ni_n/CeO_2(111)$ and $CeO_2(111)$ surfaces and $E(Ni_{atom})$ is that of a gas-phase Ni^0 atom in the d^9s^1 configuration, calculated with a (12 × 11 × 16) Å^3 periodic cell and the Γ-point. The lattice parameter of bulk fcc Ni was optimized (Ni_{bulk}: 3.48 Å, DFT+D3) using a Monkhorst−Pack grid with (15 × 15 × 15) k-point sampling of the

Brillouin zone, and the heat (enthalpy) of sublimation of bulk Ni (bulk cohesive energy) was calculated to be $\Delta H_{sub,Ni}^{calc}$ = 518 kJ/mol. These are in good agreement with prior results.[138,139]

We modeled stoichiometric <110>-type steps by adding a continuous stripe (or wire) of CeO_2 that was three atomic layers thick and covered three-fifths of the surface on top of a six layer-thick (5 × 3) $CeO_2(111)$ slab (like described above) and (1 × 2 × 1) k-point sampling. This is similar to the methods that have been used previously to model steps of $CeO_2(111)$ using DFT.[131,140] Reduced <110>-type steps with varying fractions of missing step-edge oxygen atoms ($\Theta_{Ovac,step}$ = 1/3, 2/3, and 1) were also modeled. This added "CeO_2 wire" had stoichiometric Ce_9O_{18} per (5 × 3) unit cell when not reduced, decreasing to Ce_9O_{15} for the most fully reduced step edge. The adsorption of Ni_1 species on these stoichiometric and reduced step edges was studied. The locations of the Ce^{3+} ions, resulting from the removal of the step-edge oxygen atoms and from the Ni-ceria interactions, were not optimized in detail when modeling step sites.

3.3.6 Ni Monomers at $CeO_2(111)$ and $CeO_{2-x}(111)$ Terraces : DFT Results

On $CeO_2(111)$, an isolated Ni_1 species was found to adsorb on a hollow site coordinated to three surface oxygen atoms with E_{ads} = 374 kJ/mol, in line with previous studies (Figure 3.7).[44,87] As a result of strong metal−support interactions between Ni_1 and CeO_2, two electrons from Ni are transferred to the support, generating two Ce^{3+} ions, and the Ni atom becomes oxidized to Ni^{2+} (d^8). This is qualitatively consistent with the experimental observations in Figure 3.5, although the extent of charge transfer is not as large experimentally. This is probably related to the fact that the experimental surface is not stoichiometric CeO_2 but instead is already partially reduced to $CeO_{1.95}$, and the extent of charge transfer decreases with the degree of reduction (see above). For Cu adsorption on $CeO_{2-x}(111)$, we also found that such small amounts of pre-reduction (2.5%) greatly decreased the extent of charge transfer at the lowest Cu coverages compared to stoichiometric CeO_2.[75]

Figure 3.8a shows the calculated heat of adsorption of a nickel atom on reduced CeO_{2-x}(111) surfaces. The two excess electrons resulting from the creation of a (neutral) oxygen vacancy have been reported to be localized at cation sites in the outermost plane of cations but not adjacent to the vacancies, driving the $Ce^{4+} \rightarrow Ce^{3+}$ reduction; the energetically most stable near-surface oxygen vacancy structures for a broad range of vacancy concentrations all have their vacancies at subsurface oxygen sites.[141–144] As the degree of near-surface reduction increases, the adsorption energy of the Ni atom decreases, and at the same time, Ni adatoms recover their metallic character ($Ni^{2+} \rightarrow Ni_1^{+} \rightarrow Ni^0$). In other words, as the concentration of Ce^{3+} ions increases, it gradually becomes more and more difficult for Ni to transfer electrons to the already reduced support, as observed experimentally (Figure 3.6). The results in Figure 3.8 also help explain the experimental observations that the binding of Ni at low coverage is stronger on a ceria surface, which is less reduced (cf. Figure 3.2and Figure 3.3a). This suggests that the ability of ceria to stabilize oxidized nickel species (Ni^{2+}) on the CeO_2 surface by re-localizing electrons on localized f-states (Ce^{3+}) is a key factor in determining the Ni heat of adsorption.

3.3.7 Ni Monomers at CeO_2(111) and CeO_{2-x}(111) Step Sites: DFT Results

Comparison of the heats of adsorption of Ni monomers on the flat stoichiometric CeO_2(111) terraces (374 kJ/mol, Figure 3.7) and at stoichiometric <110> step edges (Figure 3.8c) shows that the step edge binds Ni_1 more strongly by 95 kJ/mol (Figure 3.8d). In both sites, Ni binds as Ni_1^{2+}. These calculations thus predict that decoration of the stoichiometric step with Ni species will occur before adsorption on the terraces. The heat of adsorption of three Ni_1 species (Figure 3.8e), which corresponds to the maximum possible coverage of monodispersed

Ni_1 species at the step edge, is almost the same as single Ni_1, still also more strongly bound by ~90 kJ/mol per Ni atom to the step edge than isolated Ni_1 species on the flat terrace. (While the structure shown has two Ni^{1+} atoms and one Ni^{2+}, a similar structure with all three of these Ni atoms as Ni^{2+} has the same energy, within error bars.) This is consistent with the observed minimum in the heat of Ni adsorption versus coverage on the $CeO_{1.95}(111)$ surface at 300 K (Figure 3.2), which we attributed to the existence of stronger-binding defect (step-edge) sites that are occupied first, i.e., at low Ni coverage.

However, on the more reduced $CeO_{1.8}(111)$ surface, no minimum in the calorimetric heat of Ni adsorption versus coverage has been observed, and the measured heat is always lower than that on the nearly stoichiometric surface (Figure 3.3a). This is consistent with the calculated heat of adsorption of Ni at the step as a function of the step-edge oxygen vacancy fraction ($\Theta_{Ovac,step}$, Figure 3.8b), which shows that as the number of available step-edge oxygen atoms decreases, step sites eventually become less stable than terrace sites when all the step-edge oxygen atoms are removed.

We also calculated the average step-edge oxygen vacancy formation energy as a function of the step-edge O vacancy fraction ($\Theta_{Ovac,step}$) and found that oxygen atoms at the step are always easier to remove than those at the terrace. The average defect formation energies were 169, 207, and 219 kJ/mol for $\Theta_{Ovac,step} = 1/3$, 2/3, and 1, respectively, and 265 kJ/mol at a terrace site, calculated using the model in Figure 3.8c without optimizing the location of the excess charge. This validates our claim above (based on prior literature) that the O vacancies are mainly at the step edges, which also suggests that on the more reduced $CeO_{1.8}(111)$ surface studied experimentally here, there may be no O atoms on the step edges.

3.3.8 Ni Clusters on Stoichiometric $CeO_2(111)$ Terraces: Heat of Adsorption and Charge Transfer by DFT

The formation of Ni_2 dimeric structures was considered, as studied in a previous work.[94] In the case of two Ni atoms at neighboring hollow sites separated by 3.56 Å (Figure 3.7), each Ni atom transfers two electrons to the ceria support, generating four Ce^{3+} ions and two Ni^{2+} species. The adsorption energy of such a Ni pair is E_{ads} = 355 kJ/mol (per Ni atom, relative to Ni gas). Therefore, bringing two Ni^{2+} species closer but without forming a Ni−Ni bond destabilizes the system by 38 kJ/mol [$2 \times E_{ads}(Ni_2) - 2 \times Eads(Ni_1)$], which implies a repulsive interaction of 38 kJ/mol between the positively charged Ni^{2+} atoms at this separation. We addressed whether a Ni_2 dimeric structure forming a Ni−Ni bond (Ni_2.b) is energetically preferred over two well-separated Ni_1^{2+} species by adsorbing such a Ni_2.b species which have an optimized Ni−Ni bond length of 2.20 Å (cf. Figure 3.7). This results in one Ce^{3+} ion and thus two partially oxidized $Ni^{0.5+}$ atoms. The adsorption energy of the Ni_2.b dimer is only E_{ads} = 329 kJ/mol, i.e., the system is 90 kJ/mol less stable than two isolated Ni_1^{2+} species. Even though the Ni atoms in the Ni_2.b dimer have a low charge, it is still too high to allow intrinsic Ni−Ni bonding that exceeds the $Ni^{0.5+}$–$Ni^{0.5+}$ charge repulsion. This repulsive interaction of the two ceria-supported $Ni^{0.5+}$ species of 90 kJ/mol for the Ni_2.b/$CeO_2(111)$ system (cf. Figure 3.7) is 68 kJ/mol lower than the simple Coulomb repulsion of two +0.5 point charges at the same separation (2.20 Å) in vacuum (158 kJ/mol). The difference reflects some type of attractive bonding between the two Ni cations that partially overcomes the Coulomb repulsion.

In the case of a Ni_3 cluster, the Ni atoms form a flat triangle with three nearly equal Ni−Ni bonds of length 2.31−2.32 Å (Figure 3.7), two Ce^{3+} ions are formed, and therefore each of the three Ni atoms has a charge of +0.67. The adsorption energy of the Ni_3 trimer is E_{ads} = 382 kJ/mol; hence, compared to three isolated Ni_1^{2+} species, the Ni_3 cluster is 24 kJ/mol more stable (or 8 kJ/mol per Ni atom).

As for Ni_4, both three-dimensional clusters with a pyramidal shape (Ni_4.3D) and bi-dimensional flat rhombohedral-shaped (Ni_4.2D) clusters were considered, as studied previously.[87] The stability of these clusters is comparable, namely, E_{ads} = 389 and 386 kJ/mol for Ni_4.3D and Ni_4.2D, respectively (Figure 3.7). These Ni_4 species also reduce the ceria support upon adsorption with the formation of two Ce3+ ions. In the Ni_4.3D case, these two electrons are transferred from the three Ni atoms, forming the pyramid base, which are partially oxidized (3 × $Ni^{0.66+}$); whereas, the top Ni atom remains as Ni^0. In Ni_4.flat, all four Ni atoms in direct contact with the support are oxidized (4 × $Ni^{0.5+}$). As with the Ni atoms in the Ni_3 cluster, those in the Ni_4 clusters do not repel each other. For instance, the Ni_4.2D structure (4 × $Ni^{0.5+}$) is more stable by 228 kJ/mol [4 × E_{ads}(Ni_4.2D) − 4 × E_{ads}(Ni_2.b)] than two isolated Ni_2.b dimers (2 × $Ni^{0.5+}$ each). Even if the Ni atoms in the Ni_4.2D and Ni_2.b structures have a similar charge (+0.5), the larger number of Ni−Ni bonds in the Ni_4.flat cluster, with one bond length of 2.26 Å and four average bond lengths of 2.31 Å, is what optimally stabilizes the structure.

As the number of Ni atoms in the nanoparticles increases beyond three, the formation of 3D structures is preferred over flat ones (cf. Figure 3.7), in agreement with the experimental observation that Ni grows as 3D particles. For instance, the energy gained by adding one Ni atom to the flat Ni_4.2D cluster [5 × E_{ads}(Ni_5) − 4 × E_{ads}(Ni_4.2D)] is larger by 10 kJ/mol if a Ni_5.3D structure is formed (436 kJ/mol) (Figure 3.7) as compared to a 2D Ni_5 aggregate (426 kJ/mol). The configuration of the Ni_5, Ni_6, and Ni_7 nanoparticles corresponds to 3D structures with four, five, and six Ni atoms, respectively, in contact with the ceria support, with 2 × Ce^{3+} ions for the Ni_5 and Ni_6 structures and 3 × Ce^{3+} ions for the Ni_7 one. As for the case of Ni_4, electrons are transferred only from the Ni atoms in direct contact with atoms of the ceria support, and these are partially oxidized (4 × $Ni^{0.5+}$, 5 × $Ni^{0.4+}$, and 6 × $Ni^{0.5+}$ for the Ni_5, Ni_6, and Ni_7 nanoparticles, respectively); whereas, the Ni atoms on the top (not in direct contact to the ceria) remain as Ni^0. Also, for the Ni_9 (3 × Ce^{3+}), Ni_{13} (5 × Ce^{3+}), and Ni_{19} (5 × Ce^{3+}) aggregates, only the six, nine, and fifteen Ni atoms, respectively, in direct contact with the oxide support are partially oxidized (6 × $Ni^{0.50+}$, 9 × $Ni^{0.56+}$, and 5 × $Ni^{0.34+}$, respectively); whereas, the Ni atoms on the top of oxidized nickel retain their metallic character (Ni^0). Finally, the continuous stripes of Ni that we considered (i.e., Ni_{24}, Ni_{26}, Ni_{29}, and Ni_{32}) donate four electrons for Ni_{24} and Ni_{32} and five electrons for Ni_{26} and Ni_{29} to the support (5 × Ce^{3+}). In the Ni_{24}, Ni_{26}, Ni_{29}, and Ni_{32} stripes, also only the atoms in direct contact with the ceria support are partially oxidized (cf. Figure 3.7).

In summary, the DFT results produce firm computational evidence that for low Ni loadings on the $CeO_2(111)$ surface, for which a large dispersion of small Ni nanoparticles is observed,[39,135] the ceria support induces strong electronic perturbations in chemisorbed Ni species that are directly at the Ni−ceria interface, whereas there is a rapid weakening of the Ni−ceria interactions with increasing Ni loading, for which 3D nanoparticles form.[39,135]

3.4 Discussion

Figure 3.9 compares the calculated integral heat of adsorption for the thermodynamically stable $Ni_n/CeO_2(111)$ systems with those obtained experimentally (cf. Figure 3.2), where the calculated points have been shifted by −88 kJ/mol [$\Delta H_{sub,Ni}^{calc}\left(518\,\frac{kJ}{mol}\right) - \Delta H_{sub,Ni}^{exp}\left(430\,\frac{kJ}{mol}\right)$]. This correction corresponds to the 88 kJ/mol difference between the calculated bulk cohesive energy (sublimation energy) of bulk Ni(solid) with the PBE exchange−correlation functional with long-range dispersion corrections (DFT-D3), as compared to the experimental value.

The experimentally determined heats of adsorption are larger than the DFT ones for one and three atom clusters by 15 and 10 kJ/mol, respectively, after this 88 kJ/mol correction in Figure 3.9. This may be due to the fact that the cluster sizes could have been underestimated in the first two pulses in the heat measurements of Figure 3.2, Figure 3.3, and Figure 3.9. Although the LEIS measurements of Figure 3.1 are consistent with a constant number density of Ni clusters independent of coverage, those measurements did not extend down to such low coverages as the heat measurements, so it is possible that in the first two heat points, the Ni clusters had not yet reached their saturation density, as we assumed here in estimating cluster sizes. For a higher Ni loading, the DFT heats plotted in Figure 3.9 are larger than the experimental ones. This is actually to be expected based on the wire-like nature of the Ni aggregates modeled by DFT, which have more Ni−Ni bonds per Ni atom than in the corresponding isolated clusters studied experimentally.

The comparison and the discussion above reveal that, due to the strong Ni−ceria support interaction and its large charge transfer, at least three Ni atoms are required to make Ni clusters stable. Only then can the intrinsic Ni−Ni bond energies help win out over repulsive interactions between partially charged Ni atoms at the Ni−ceria interface.

Figure 3.10b shows the number of electrons transferred per Ni atom versus cluster size as calculated by DFT. The extent of charge transfer per Ni atom clearly decreases rapidly with cluster size, but for a given size, we found it to be generally independent of the size of the unit cell, as discussed below. Figure 3.10b compares this number of electrons transferred per Ni atom versus particle size as calculated with the experimental results reported in Figure 3.5a and Figure 3.6.

As seen in Figure 3.10b, the charge transferred per Ni atom decreases strongly with particle size in all three curves. However, it decreases much more rapidly in the DFT calculations than in the closest corresponding experiment (i.e., $CeO_{1.95}(111)$ at 100 K, where the particles are at terrace sites like in the DFT). The transferred charge in the experiments also decreases with size much more rapidly at 100 K than at 300 K so that the charge transferred per Ni atom on $CeO_{1.95}(111)$ is 3- to 4-fold larger for the same particle size at 300 K than at 100 K. This may be related to the fact that the clusters are at step edges at 300 K but on terraces at 100 K, although this is surprising since the 2.5% O vacancies in this $CeO_{1.95}(111)$ surface concentrate at step edges and O vacancies clearly decrease the extent of charge transfer (see above). However, step edges may have other electronic or structural characteristics that enhance charge transfer in spite of these extra O vacancies. For example, charge-transfer-induced lattice strain is probably relieved more easily near the steps. (Earlier DFT calculations have shown that such a charge transferred to $CeO_2(111)$ and the corresponding conversion of Ce^{4+} to Ce^{3+} lead to lattice expansion parallel to the surface.[145]) Given that the DFT calculations are at 0 K, the three curves in Figure 3.10b separate by temperature, with greater charge transfer at higher temperature. Temperature seems unlikely to be the intrinsic reason for this since the only reasonable explanation would be some activation energy associated with charge transfer of a type that we have never seen reported.

For the same particle size in Figure 3.10b, the total Ni coverages are quite different for the three curves for $CeO_2(111)$ and $CeO_{1.95}(111)$ since the Ni clusters are much closer together in the DFT models than in the experiments at 100 K and they are closer together in the experiments at 100 K than at 300 K. It is possible that there are strong dipole‒dipole repulsions between clusters since the clusters carry so much charge and have their counter charge in the outermost ceria plane at the metal−ceria interface according to the DFT results. These repulsions get stronger as the distance between parallel dipoles decreases and are therefore well known to lead to depolarization of adsorbate−substrate bonds as their coverage increases.[146] Therefore, these different coverages would affect charge transfer in the way seen here: higher coverages lead to less charge transfer for the same cluster size. The data for these curves in Figure 3.10b are replotted versus coverage in Figure 3.11. When plotted in this way, all three data sets converge into a single curve, which lends support to the proposal that the differences in Figure 3.10b are largely associated with this effect of coverage (cluster separation) on dipole−dipole repulsions between clusters. We tested this effect directly with DFT by changing the unit cell size for the same cluster size and shape. For one Ni atom with (4 × 4), (3 × 3), and (2 × 2) periodicity, DFT shows that two electrons are transferred to the ceria support (Ni^{2+}); whereas, for the (1 × 1) unit cell, only two-thirds of the electron is transferred ($Ni^{0.66+}$). However, for both the Ni_3 and Ni_4.3D clusters with (3 × 3) and (2 × 2) periodicity, two electrons are transferred independent of the size of the unit cell (3 × $Ni^{0.67+}$). This can be seen as the pairs of DFT points in Figure 3.11 with nearly the same charge transfer but quite different coverages (cf. Ni_5.3D and Ni_{13} with about 0.4 electrons donated per Ni atom but corresponding to 0.56 and 1.45 ML, respectively). This gives rise to the greatest deviations from the single curve fit through these data in Figure 3.11. Since these DFT calculations do not show a direct effect of coverage on charge transfer, we cannot be sure that the nice correlation with coverage in Figure 3.11 that seems to bring all three data sets into pretty close agreement is really due to the direct effect of coverage (i.e., cluster separation). It may be that the largest unit cell size in the DFT calculations is still not large enough to see this effect since the cluster density used in the DFT models is much higher than that in the experiments. An alternative explanation is that the charge transfer in the 300 K experiments is greater for the same cluster size than that in the 100 K experiments due to the fact that the clusters are at step edges at 300 K but on terraces at 100 K (see above).

The experimental charge transfer at 300 K in Figure 3.11 is quite large. For example, for particles with 278 atoms, approximately one-third electron is transferred per Ni atom so that the particle has a charge of +93. Since the aspect ratio of the particle is 0.25, about one-third of the Ni atoms are on the interface. Therefore, the measured total charge transfer will be realized if each Ni atom at the Ni−CeO_2 interface transfers one electron to ceria. Apparently, there is not too much Coulombic repulsion because of attractions to the negative charge on ceria (i.e., Ce^{3+} ions) at the interface, as indicated by the DFT calculations. The high strength of this interfacial bonding decreases the chemical potential of the Ni atoms in a way that can be directly related to the superior sinter resistance of these materials via well-known rate equations.[12,13]

The results above clearly show that the electronic character of the Ni atoms changes with Ni particle thickness and size, with the location of the Ni atoms within the 3D particles (i.e., whether in the interfacial layer or in layers further away from the CeO_2 support), and with the extent of reduction of the CeO_2 support. We next show how these changes can be related to some of the unique catalytic properties of Ni/CeO_2 materials that have been reported and how these vary with the structural properties of these materials at the atomic scale.

First, let us consider highly dispersed Ni on CeO_2 with few oxygen vacancies, where all the Ni atoms are either isolated monomers or small 2D clusters. We show above that these Ni atoms are highly cationic. It has been recently shown[43,44,89,92] that well-dispersed, small Ni nanoparticles on a non-reduced ceria support, with all the Ni atoms being interfacial, promote the activation of both O−H and C−H bonds at room temperature with lower activation barriers than for extended metallic Ni surfaces. Most importantly, this type of material can perform direct catalytic conversion of methane to methanol at a low temperature (450 K), using a mixture of oxygen and water as the oxidant, with ∼30% selectivity.[45] This we attribute to the highly cationic character of the surface Ni atoms. These same types of structural features were also reported to be most active for catalyzing the water-gas shift (WGS) reaction ($CO + H_2O \rightarrow CO_2 + H_2$), where higher Ni loadings (larger Ni particles) had shown to be less active.[39,89]

For larger Ni nanoparticles, we find that neutral Ni atoms are above the oxidized interfacial Ni atoms and thus are exposed to gas-phase reactants. The calculated O−H bond cleavage activation energy at these neutral Ni atoms is higher than that at the Ni monomers and few-atom Ni clusters discussed above and not very different from that on Ni(111).[89] Hence, the Ni atoms at the rim of these larger nanoparticles are the only effective sites for O−H bond cleavage. These larger particles with both neutral Ni atoms and cationic Ni at the particle perimeters appear to be the most active for converting $CO + H_2O$ into methane.[39] In fact, the selectivity of $Ni/CeO_2(111)$ model catalysts was reported to depend strongly on Ni loading. Specifically, low-loaded systems catalyze the production of $CO_2 + H_2$, whereas high-loaded systems catalyze the production of CH_4. The Ni loading also has a strong effect on the rate at which the system exposed to CH_4 deactivates: during dry reforming of methane on high-loaded systems, coke forms and deactivates the catalyst.[44]

The nature of the ceria support is also important. As discussed above, the binding of Ni nanoparticles on CeO_2 surfaces becomes increasingly weak as the degree of reduction of the ceria surface increases; the amount of charge transferred from Ni to CeO_2 for the same small Ni particle size also decreases strongly with the extent of reduction. Therefore, if operating conditions are changed for low-loaded Ni/CeO_2 catalysts in such a way that CeO_2 gets more reduced, this will markedly reduce the charge on the Ni atoms. This is the case during methane dry reforming with CO_2 over low-loaded Ni/CeO_2 catalysts at 650 K.[43,44,92] The C−H cleavage barrier remains low even though, as we show above, the charge transfer from Ni to ceria is decreased due to ceria reduction, but now the C−O bond cleavage barrier in CO_2 also becomes low[43] due to the presence of surface oxygen vacancies.

3.5 Conclusions

Ni atoms adsorb on slightly reduced ceria $CeO_{2-x}(111)$ and form three-dimensional nanoparticles at 300 and 100 K, which increase in size with increasing Ni loading. The extent of reduction of ceria has a minor effect on the Ni particle number density at 300 K, while decreasing the temperature from 300 to 100 K results in 4-fold higher Ni particle number density on $CeO_{1.95}(111)$. The heat of Ni adsorption onto $CeO_{1.95}(111)$ at 300 K starts from 345 kJ/mol (attributed to step edges), decreases within the first 0.2 ML to 323 kJ/mol (as step edge sites saturate), and increases afterward (due to growing particle size) until the bulk heat of Ni sublimation is reached by 9 ML. On $CeO_{1.8}(111)$ at 300 K, this initial drop in heat of adsorption was not observed, attributed to weaker Ni binding to step edges when full of O vacancies. The heat of adsorption is generally lower on the more reduced ceria surface (by up to 65 kJ/mol initially at 300 K), again suggesting that the oxophilic Ni atoms do not prefer O vacancies. DFT calculations support this. On $CeO_{1.95}(111)$ at 100 K, Ni atoms adsorb mainly on terraces due to slow Ni adatom diffusion with an initial heat of adsorption that is 45 kJ/mol lower than that at 300 K, where Ni atoms mainly adsorb on step edges. This highlights Ni's strong preference for step edges over terraces. Upon adsorption, Ni atoms donate electrons to the support to generate Ce^{3+}. DFT calculations show that this charge is localized on the interfacial Ni and Ce atoms in their atomic layers closest to the interface. As the coverage and particle size grow, the average number of electrons donated per Ni atom decreases in both experiments and DFT calculations.

For the same size, Ni particles exhibit less charge transfer to $CeO_{1.95}(111)$ at 100 K (when on terraces) than at 300 K (when at step edges). The charge transfer from Ni particles is much less on $CeO_{1.8}(111)$ compared to $CeO_{1.95}(111)$ at both temperatures.

Ni/CeO_2 interactions that produce strong electronic perturbations in the Ni nanoparticles result in important changes in their chemical and catalytic properties, as discussed for the examples of both O−H and C−H bond cleavage. Manipulating these interactions by, for example, controlling the degree of reduction of the support, as well as particle size and metal loading, can lead to improved catalytic activity and/ or selectivity. Our findings help explain some of the outstanding catalytic properties of Ni/CeO_2 materials and how they depend upon their atomic-level structural details. This may aid in the rational design of catalysts that involve O− H and C−H bond dissociation.

3.6 Figures

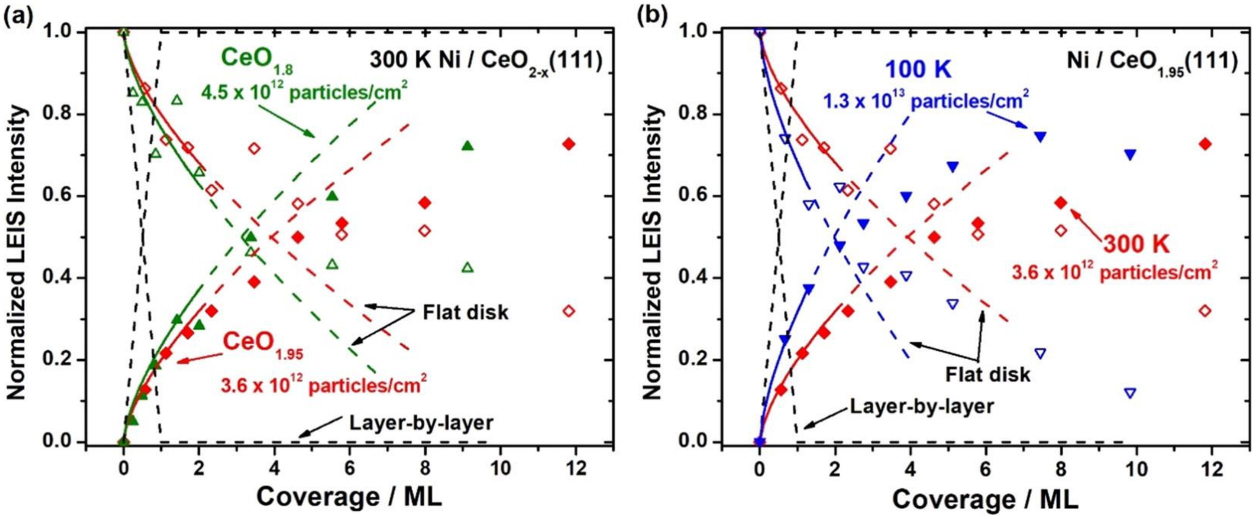

Figure 3.1. Integrated Ni (closed symbols) and Ce (open symbols) LEIS signal intensities (normalized to thick multilayer Ni and clean $CeO_{2-x}(111)$, respectively) as a function of Ni coverage after deposition onto (a) $CeO_{1.95}(111)$ (red diamonds) and $CeO_{1.8}(111)$ (green triangles) at 300 K and (b) $CeO_{1.95}(111)$ at 300 K (red diamonds) and 100 K (blue triangles). The black dashed lines correspond to the normalized LEIS signal that would be observed if Ni grew in a layer-by-layer fashion, while the colored solid lines correspond to Ni growing as flat disks with a fixed aspect ratio (0.25 on $CeO_{1.95}$ and 0.20 on $CeO_{1.8}$) and fixed particle densities of 3.6×10^{12} particles/cm^2 (red), 4.5×10^{12} particles/cm^2 (green), and 1.3×10^{13} particles/cm^2 (blue). This model is only reasonable when less than ~35% of the surface is covered since particles will soon start to overlap with each other at higher coverage. The colored dashed lines after that are only a guide to the eye.

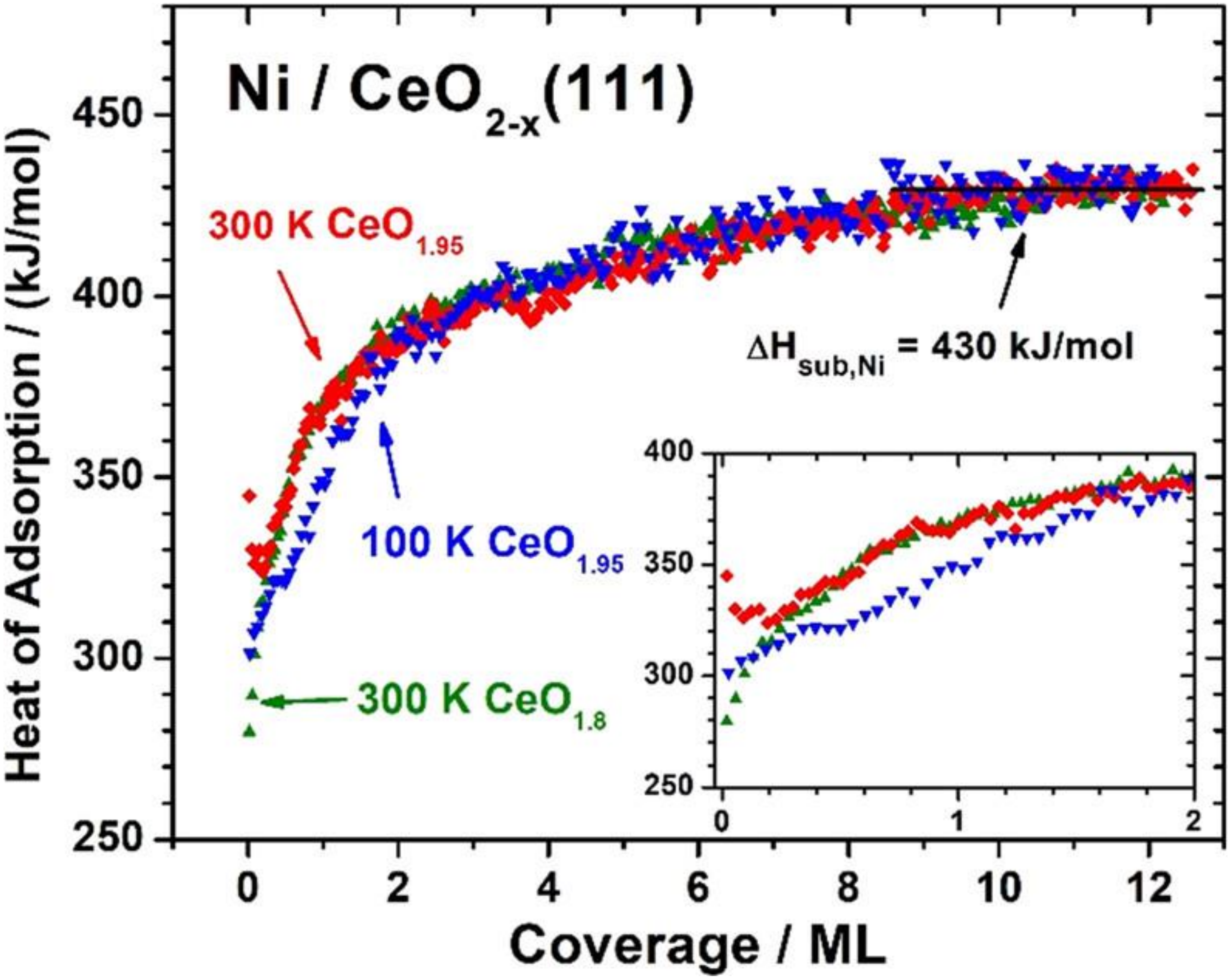

Figure 3.2. Differential heat of Ni atom adsorption on $CeO_{1.95}$(111) at 300 K (red diamonds), $CeO_{1.8}$(111) at 300 K (green triangles), and $CeO_{1.95}$(111) at 100 K (blue triangles) as a function of Ni coverage. 1 ML is defined as $7.89 \times 10^{18}/m^2$, which is the areal density of coordinatively unsaturated O atoms on the ideal bulk-terminated CeO_2(111) surface.

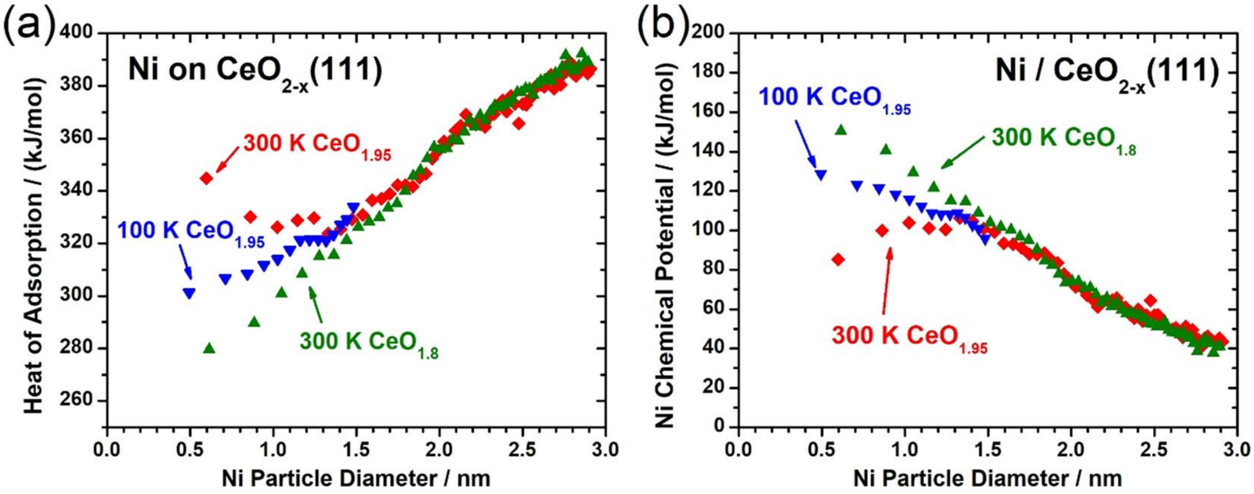

Figure 3.3. (a) Differential heat of Ni adsorption on $CeO_{2-x}(111)$ at 300 and 100 K as a function of Ni average particle (flat-disk) diameter to which Ni atoms add. (b) Chemical potential of Ni atoms in Ni particles versus the average Ni particle diameter on $CeO_{2-x}(111)$ at 300 and 100 K. Red diamonds, green triangles, and blue triangles correspond to $CeO_{1.95}$ at 300 K, $CeO_{1.8}$ at 300 K, and $CeO_{1.95}$ at 100 K, respectively.

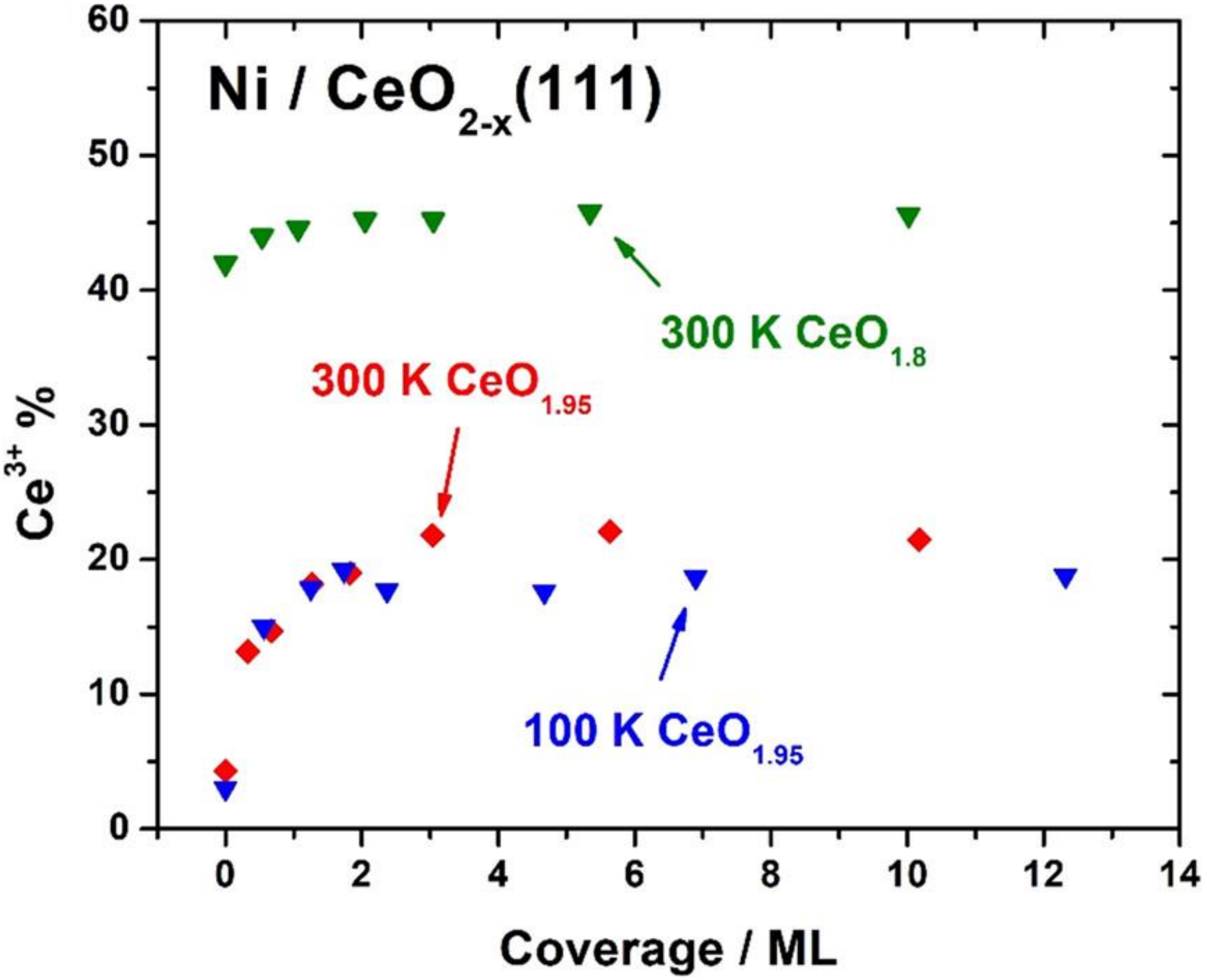

Figure 3.4. Percentage of Ce3+ (with the rest, as Ce4+) in the XPS probe depth versus Ni coverage based on line shape fitting of the XPS Ce 3d peak measured during Ni deposition on CeO1.95(111) at 300 K (red), CeO1.8(111) at 300 K (green), and CeO1.95(111) at 100 K (blue).

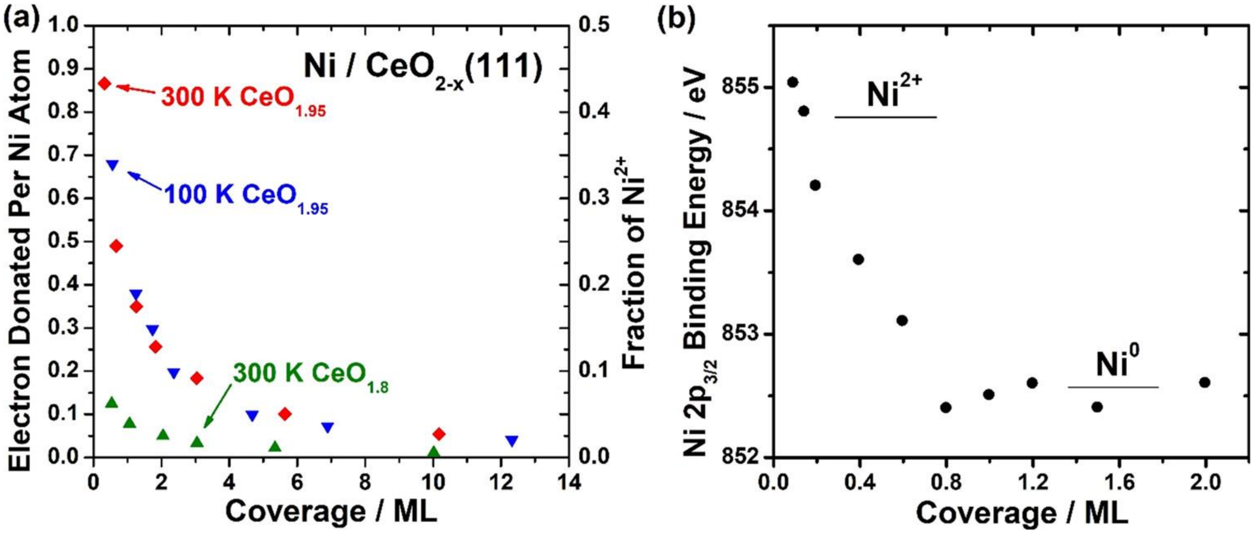

Figure 3.5(a) Average number of electrons donated to ceria per Ni atom and the corresponding fraction of total Ni that is oxidized (assuming it is Ni^{2+}) plotted as a function of Ni coverage. (b) Variation of the Ni 2p$_{3/2}$ XPS binding energy as a function of Ni coverage on CeO$_2$(111) at 300 K, as reported in the Supporting Information of ref [89].

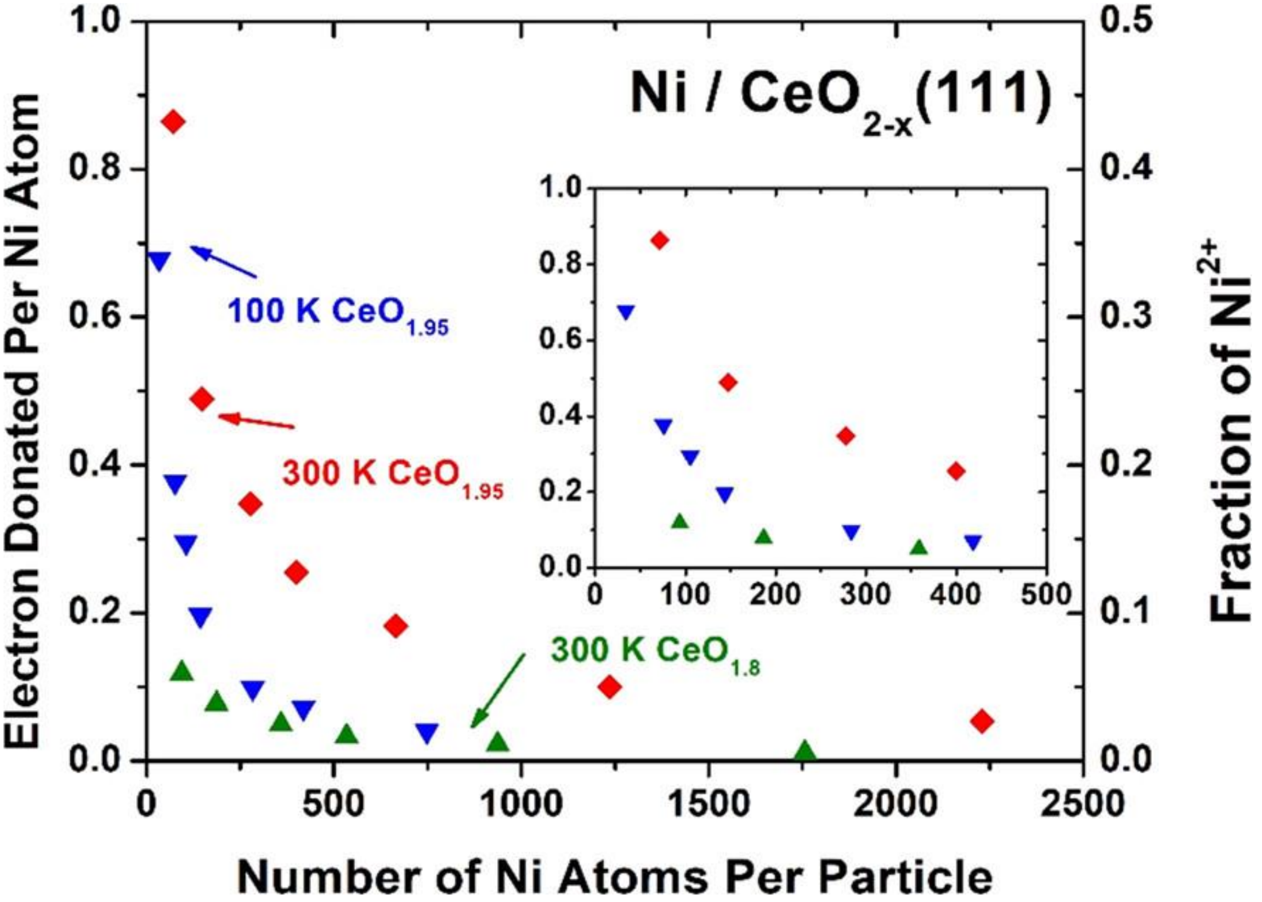

Figure 3.6 Average number of electrons donated to ceria per Ni atom and the corresponding fraction of total Ni that is oxidized (assuming it is Ni^{2+}) from Figure 3.5a replotted as a function of number of Ni atoms per particle.

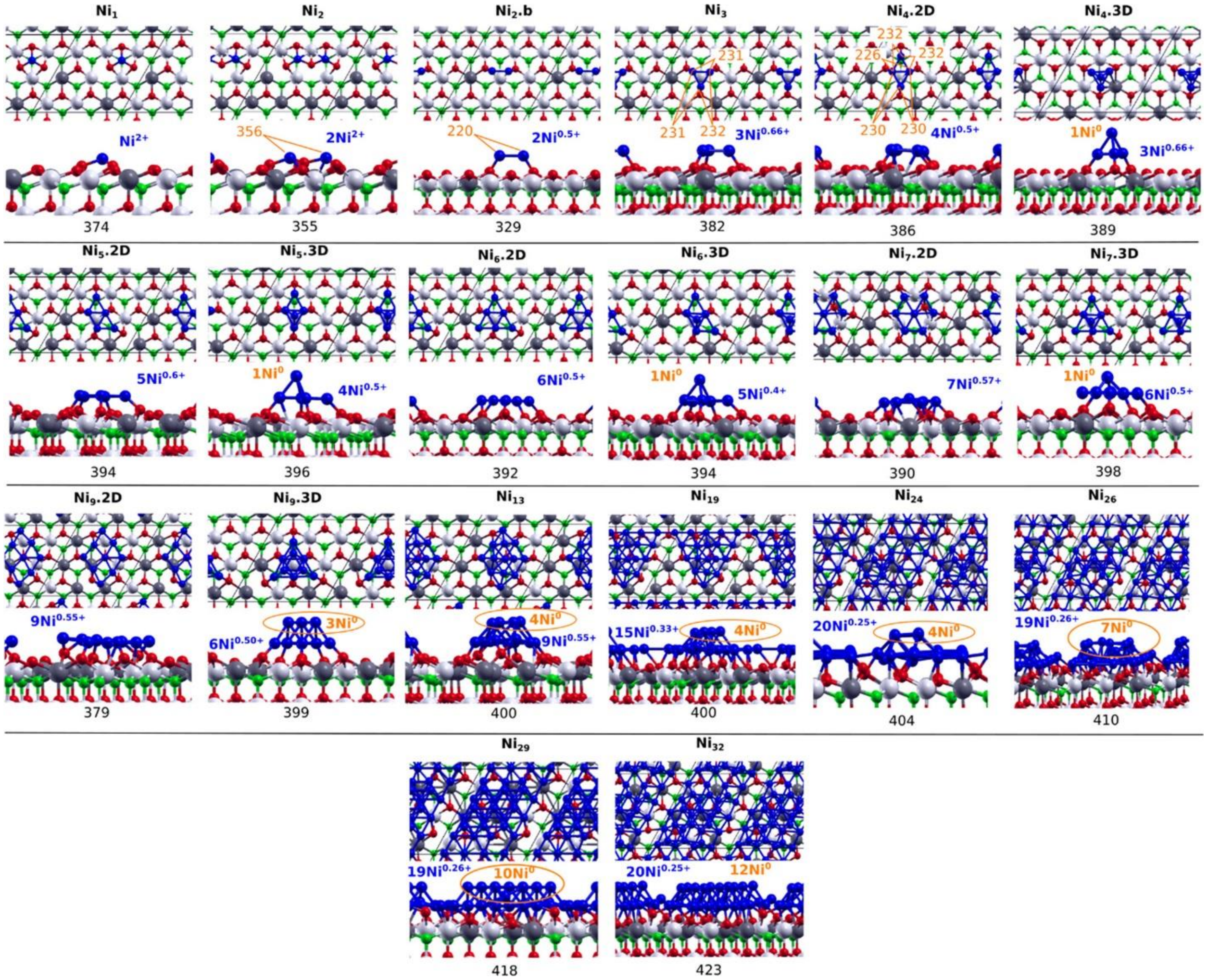

Figure 3.7. Models of $Ni_n/CeO_2(111)$ (n =1−7, 9, 13, 19, 24, 26, 29, and 32). Surface/subsurface oxygen atoms in the outermost O−Ce−O trilayer are depicted in red/green, Ce^{4+} in white, and Ce^{3+} in gray. Values of the integral heat of adsorption of Ni_n species are listed below each structure in kJ/mol per Ni atom (relative to Ni gas). Optimized Ni−Ni bond lengths in pm for Ni_2, Ni_3, and Ni_4.2D are indicated in orange.

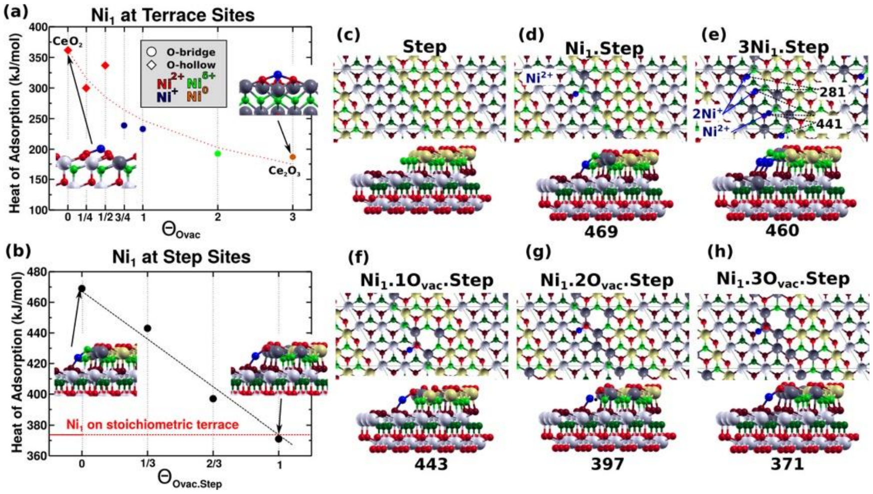

Figure 3.8. (a) Calculated heat of adsorption of a single Ni atom on the $CeO_2(111)$ surface and $CeO_{2-x}(111)$ with different concentrations of subsurface oxygen vacancies (Θ_{Ovac} = 1/4, 1/2, and 3/4; see text). Also shown are the results for one and two layers of Ce_2O_3 on $CeO_2(111)$ and a slab of pure $Ce_2O_3(0001)$ plotted at $\Theta_{Ovac,\ step}$ = 1, 2, and 3, respectively. The Ni oxidation state is color coded as shown ($0 < \delta < 1$), and the adsorption site corresponds to the most stable one. Note that the slab model and method used in these calculations slightly differ from those used to obtain the values reported in Figure 3.7 (see text), explaining the difference of 11 kJ/mol in the heat of adsorption of a single Ni atom on the $CeO_2(111)$ surface. (b) Calculated heat of adsorption of Ni monomer at a < 110>-type step as a function of the step-edge O vacancy fraction ($\Theta_{Ovac,step}$ = 0, 1/3, 2/3, and 1). The red dotted line corresponds to the heat of adsorption of one Ni atom on the stoichiometric terrace (374 kJ/ mol, Figure 3.7). Atomic structures of the (c) stoichiometric <110>-type steps with (d) one and (e) three Ni atoms and of the (f−h) reduced steps with one Ni atom. Values of the heat of adsorption of Ni species are listed below each structure in kJ/mol per Ni atom (relative to Ni_1 gas).

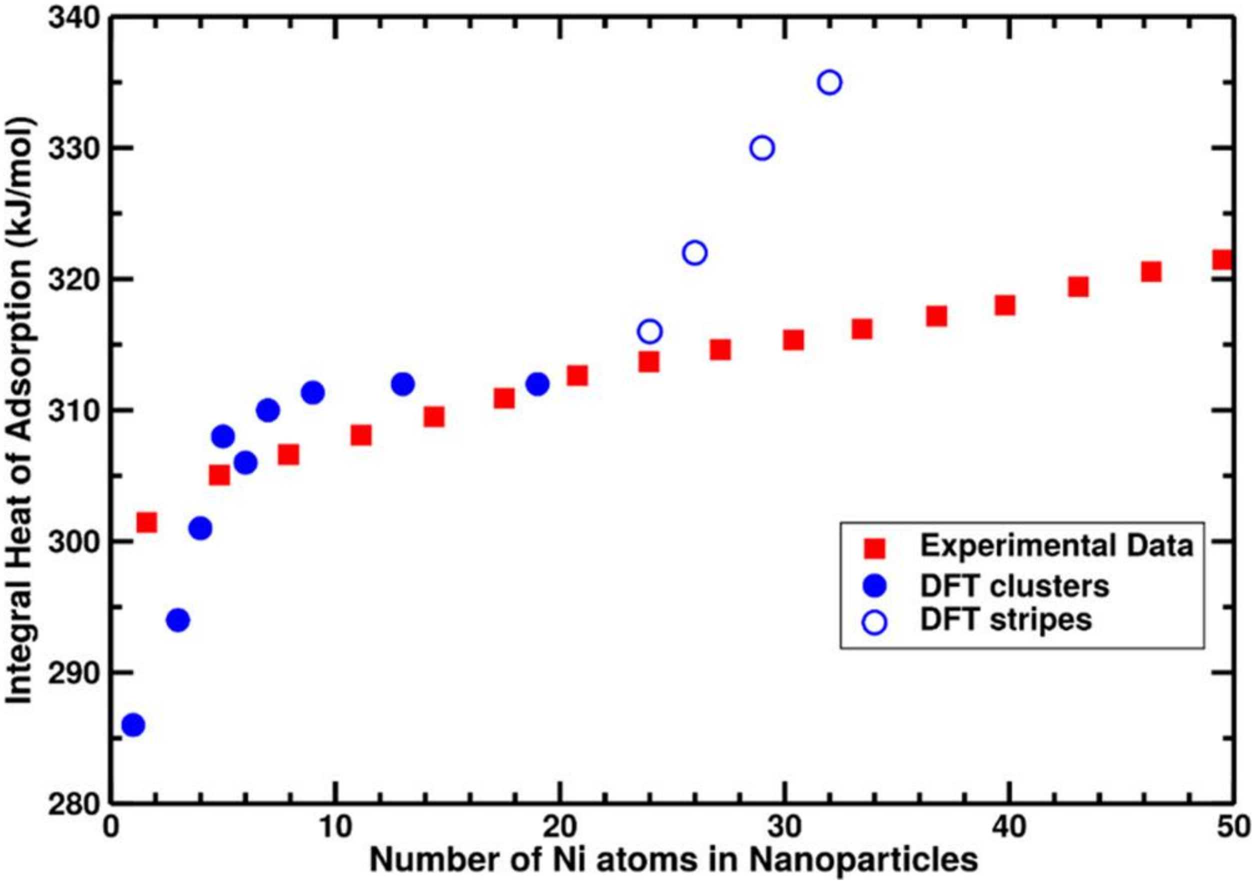

Figure 3.9. Integral heat of adsorption as a function of the number of Ni atoms in the Ni_n aggregates. Experimental data for adsorption at 100 K (where terrace sites are predominantly populated) (red squares) and calculated DFT data (blue filled and empty circles). For $n > 19$, the Ni_n aggregates in DFT correspond to continuous Ni stripes or wires (blue empty circles). The DFT points were shifted by 88 kJ/mol to smaller values (see text).

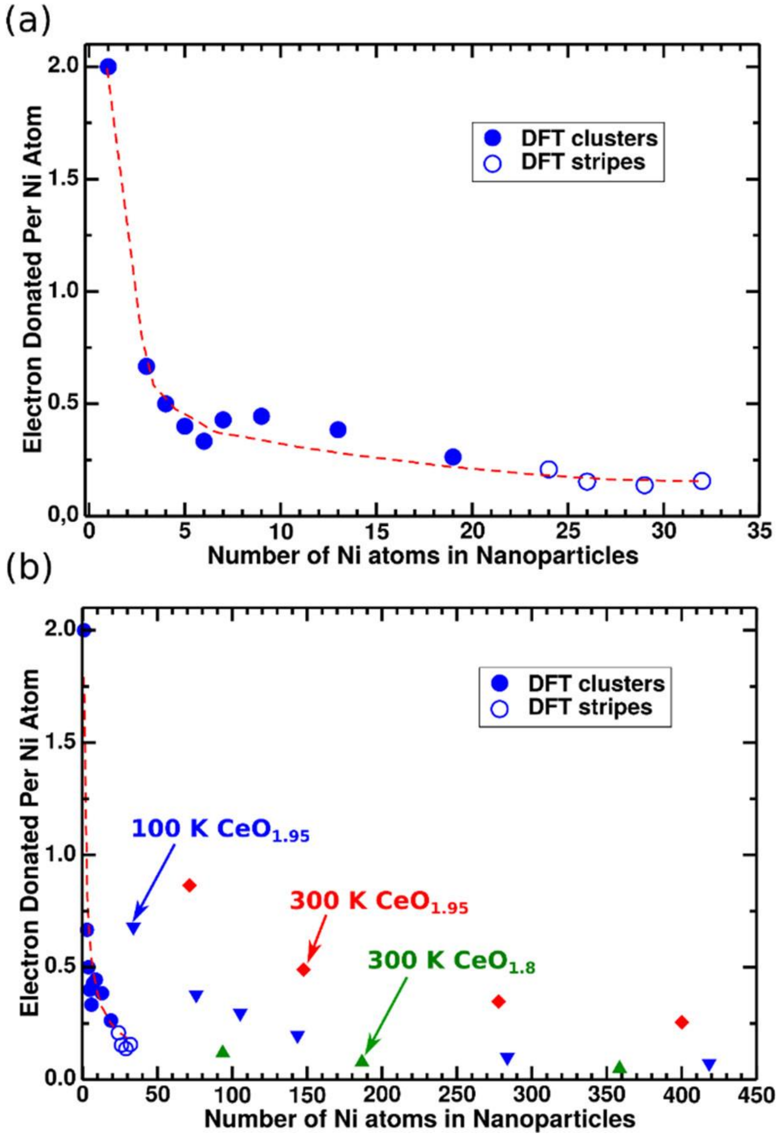

Figure 3.10. (a) Calculated number of electrons donated per Ni atom as a function of the number of Ni atoms in the nanoparticle. (b) DFT data from part (a) replotted over a larger range for comparison with the experimental data from Figure 3.6.

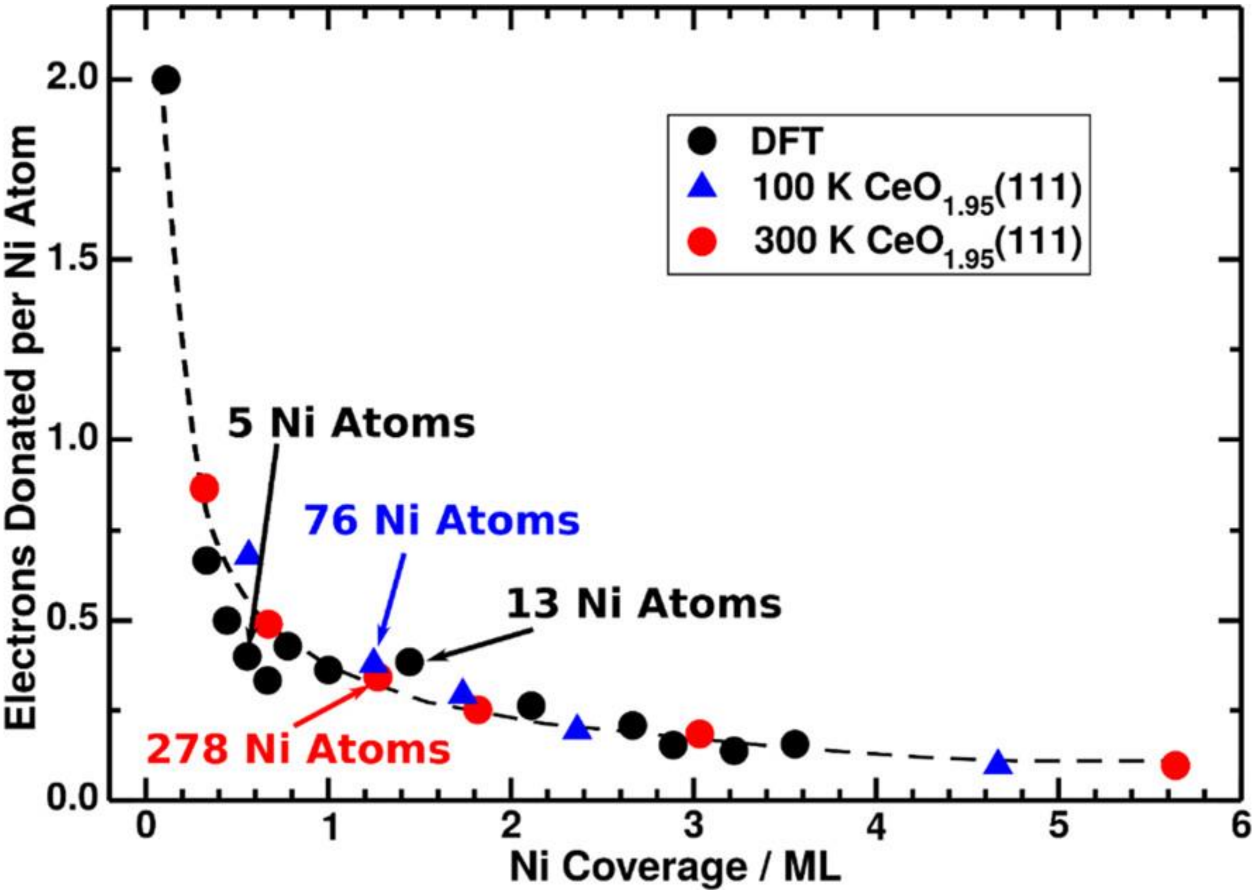

Figure 3.11. Number of electrons donated per Ni atom versus total Ni coverage as calculated by DFT for $CeO_2(111)$ and as measured for $CeO_{1.95}(111)$ at 100 and 300 K. The numbers of atoms in the nanoparticles are also indicated for the points closest to 1.3 ML. The curve fit is just to guide the eye.

Chapter 4. Energetics of Ag Adsorption on and Adhesion to Rutile TiO_2(100) Studied by Microcalorimetry

This chapter has been published as:

Mao, Z., Rumptz, J. R., & Campbell, C. T. (2021). *The Journal of Physical Chemistry C*, 125(5), 3036-3046.

Chapter Abstract

The adsorption and adhesion energies of vapor-deposited Ag on rutile TiO_2(100) films have been measured using single-crystal adsorption calorimetry and He^+ low-energy ion scattering spectroscopy. Ag grows as three-dimensional nanoparticles at 300 and 100 K. The saturation particle density is 8×10^{16} particles/m^2 at 300 K and 2.5×10^{17} particles/m^2 at 100 K. The differential heat of adsorption starts low, increases with Ag coverage, and finally approaches the sublimation enthalpy of Ag at both 300 and 100 K. At 300 K, the differential heat of adsorption starts from 208 kJ/mol and rises rapidly to 265 kJ/mol by 1 ML. At 100 K, Ag grows nanoparticles with smaller particle size on the terraces, while at 300 K, the Ag nanoparticles have bigger particle size and grow on step edges with stronger binding strength to the nanoparticles. Thus, the heat of Ag adsorption at 100 K starts at 141 kJ/mol (near the monomer size limit on terrace sites) and remains lower than that at 300 K until 1.5 ML. The adhesion energy of Ag(solid) to rutile TiO_2(100) is found to be large (∼2.44 J/m^2), supporting a trend of decreasing adhesion energy with the enthalpy of oxide reduction.

4.1 Introduction

Late transition metal nanoparticles supported on materials with high surface areas are widely used as heterogeneous catalysts and electrocatalysts in energy, chemical, and environmental technologies. In a catalyzed reaction, the binding energies of the intermediates and the activation energies of the elementary steps vary with the properties of the metal nanoparticles on which the reaction takes place, which can significantly alter the activity and/or selectivity.[11,147] The properties of the metal nanoparticles depend not only on the metal element but also on the support material to which the nanoparticles are attached. For such materials, the thermodynamic stability of the metal atoms in the metal nanoparticles (i.e., their energy or chemical potential) has been shown to be a descriptor that relates to their catalytic performance (activity and thermal stability).[9,35,148] For a given particle size below 6 nm, the greater the bond strength (adhesion energy) between the metal nanoparticle and the support, the lower the metal chemical potential.[35] Changing the strength of the metal− support interactions allows tuning the metal chemical potential and the electronic and structural properties of the supported metal nanoparticles, providing ample opportunities to improve catalysts.[43,92,99,149,150] Although the supported metal nanoparticles can be highly active for catalyzing reactions, they often deactivate via sintering.[12–16] Strong interfacial bonding between the metal nanoparticles (or isolated metal adatoms) and the support surface can stabilize the metal nanoparticles (i.e., lower the metal atoms' chemical potential), providing sinter resistance and improved long-term stability in catalytic activity.[38,99,151–153] Thus, the interaction strengths between the metal atoms or metal nanoparticles and the support materials play a key role in the performance of the catalysts. Understanding the nature and the strength of the interfacial bonding (adhesion energy) is crucial in catalyst design from both basic and applied point of view. Here, we report the Ag chemical potential versus size and the adhesion energy of Ag nanoparticles on the rutile TiO_2(100) surface as measured by Ag vapor adsorption calorimetry.

In our previous studies, the bonding strengths (adhesion energies, in J/m^2) between metal nanoparticles and different support materials were measured for numerous systems consisting of late transition metals on clean, single-crystalline oxide surfaces.[35,37,38,154] Based on results on MgO(100) and $CeO_{1.95}$(111) surfaces, a trend was discovered whereby for a given oxide surface, the adhesion energies of different metals correlate linearly with the metal's oxophilicity.[37] This trend has shown its predictive power for Ni onto MgO(100).[46] However, it remains unclear how the adhesion energy correlates with the properties of the different oxide surfaces. Thus, the adhesion energies of metals on additional oxide surfaces are needed to unravel the correlation between adhesion energies and oxide surface properties. Here, we report the adhesion energy of Ag to rutile TiO_2(100) and compare it to that of other oxides. Because of the quantitative correlation of adhesion energy with metal oxophilicity,[37] this result for Ag allows one to estimate adhesion energies of other late transition metals to rutile TiO_2(100).

Titania is an important support material in catalysis research and applications.[155–162] Rutile TiO_2 surfaces are some of the most thoroughly studied of all oxide single-crystalline surfaces with respect to the structure and gas adsorption properties[155,163–169] and with respect to metal vapor adsorption and nanoparticle nucleation/growth.[7,170–173] However, to the best of our knowledge, the adhesion energy has only been measured for one such metal-on-TiO_2 system: Au on rutile TiO_2(110).[174,175] These measurements were done using the nanoparticle shape. No one has measured the heat of adsorption of Ag (or any other transition metal) on any ordered single-crystal surface of TiO_2, although the heat of Ag adsorption was recently measured versus coverage on 5 nm- diameter anatase TiO_2 powder.[176] Thus, we have chosen rutile TiO_2(100) for this study. To the best of our knowledge, this (100) face is the only one that has been prepared in the thin film-on-metal form required for metal vapor adsorption calorimetry.

In this paper, we investigate the bonding energetics of Ag atoms and Ag nanoparticles onto rutile $TiO_2(100)$ thin films by depositing gaseous Ag atoms to the $TiO_2(100)$ film in discrete amounts. Using single-crystal adsorption calorimetry (SCAC), the heat released upon Ag adsorption on $TiO_2(100)$ is measured directly, which reflects the binding strength between the Ag nanoparticles and the $TiO_2(100)$ film. The growth morphology of the Ag nanoparticles on $TiO_2(100)$ is determined with He^+ low-energy ion scattering (LEIS). Combining the heat data from SCAC and the morphology information from LEIS, the adhesion energy of Ag onto $TiO_2(100)$ is calculated with two methods.

Nanoparticles of Ag supported on TiO_2 are a promising material for photocatalysis and heterogeneous catalysis.[48–52] TiO_2 is most widely used as photocatalysts for water splitting, pollutant degradation, and antibacterial applications.[48,51,177–181] However, practical application is hindered by low quantum yields.[50,51,177] Decorating TiO_2 with noble metal nanoparticles such as Ag facilitates separation of electron−hole pairs and promotes photocatalytic activity.[49,50,182,183] Supported Ag nanoparticles are also investigated extensively because of their use as heterogeneous catalysts for important industrial reactions such as ethylene oxidation to epoxide.[184–186] The catalytic activity and selectivity of supported Ag nanoparticles depend strongly on the size, the shape, and the support of the Ag nanoparticles.[185,187] Therefore, the growth of Ag nanoparticles supported on oxide surfaces and the interaction between Ag and the oxide are of interest both from a fundamental point of view and with regard to applications.

The growth of small Ag clusters and nanoparticles on TiO_2 has been studied previously with both experimental and theoretical approaches. Among all the facets of the three common phases of TiO_2 (rutile, anatase, and brookite), rutile $TiO_2(110)$ has attracted the most attention. Theoretical study using density functional theory (DFT) gives that Ag single atoms bind the bridging oxygen sites of rutile $TiO_2(110)$ strongly with an adsorption energy of 2.07 eV, while the adsorption energy is 1.74 eV on the less-favored oxygen-top sites.[188] DFT calculations also report the adsorption energy of small Ag clusters on rutile $TiO_2(110)$ and Ag single atoms on other facets of TiO_2.[189–191] Measurements in ultra-high vacuum (UHV) systems suggest that Ag particles grow in a three- dimensional (3D) fashion with the shape close to hemispherical caps on rutile $TiO_2(110)$.[192,193] At low coverage, the Ag particles preferentially nucleate along the step edge of rutile $TiO_2(110)$, and the majority of the nucleation occurs in the first 0.05 ML of metal deposition.[194]

4.2 Experimental Methods

A description of the single crystal adsorption calorimetry apparatus and experimental procedures are presented in detail in Chapter 2. They are described briefly again here to allow the reader to understand this chapter without the need to reference back to Chapter 2.

The TiO_2 thin films were grown on a 1 μm-thick Mo(110) single crystal using a recipe first presented by Guo et al.[76] This method involves exposing the Mo(110) sample held at 625 K to a flux of titanium generated by the resistive heating of a titanium-coated filament in a background of 2×10^{-7} torr of oxygen gas and post-annealing to 800 K in the same O_2 background. The TiO_2 thin films prepared for all experiments were estimated to have a thickness greater than 2 nm (but <3 nm) from the attenuation of the Mo $3d_{5/2}$ peak in XPS and the inelastic mean free path of electrons originating from this level. In addition, the Ti $2p_{3/2}$ XPS peak shape indicated an oxidized TiO_2 film with a small fraction of O vacancies for all samples used in experiments.

The SCAC experiments were performed as described previously.[34] The Ag metal beam is generated by evaporating Ag pellets in an e-beam evaporator. The Ag vapor is then collimated through a series of 4.26 mm-diameter apertures and dosed onto the TiO_2 film in 100 ms pulses with a period of 2 s. The flux of the Ag beam is measured with two quartz crystal microbalances (QCMs). An off-axis QCM facing directly the e- beam evaporator monitors the flux throughout the experiment. Before and after each calorimetry run, an on-axis QCM is placed at the sample position to measure the initial and final fluxes. The initial and final fluxes measured at the sample position are used to scale the fluxes measured by the off-axis QCM so that it provides Ag fluxes for all times at the sample position. Upon Ag adsorption, the heat released is detected using a pyroelectric polyvinylidene fluoride (PVDF) ribbon that is pushed against the backside of the 1 μm-thick Mo(110) single crystal. The response of the PVDF ribbon as a heat detector is calibrated with a HeNe laser with known energy for each experiment. The heat detected using the PVDF ribbon is a combination of the heat of adsorption and the radiation from the hot metal evaporator. To subtract the signal from the thermal radiation, a BaF_2 window is placed in front of the sample to block the Ag atoms but only allow a known fraction (~95%) of thermal radiation to go through. The signal associated with the thermal radiation is measured with the BaF_2 window and subtracted from the total heat signal. The heat is then further corrected for the difference of the internal energy between a pulse of gaseous metal atoms coming from a high-temperature evaporator (~1400 K) and a collection of the same number of gaseous metal atoms in a Boltzmann distribution at the sample temperature (300 or 100 K).[33] The corrected heat equals the negative of the standard enthalpy of Ag adsorption at the sample temperature. The sticking probability for each pulse is measured simultaneously with its heat using modified King and Well's method.[86] The number of Ag atoms that stick to the sample surface in each pulse is calculated with the flux times the sticking probability, and the differential heat of adsorption per mole adsorbed can thus be calculated from the measured heat.

The growth morphology of adsorbed Ag on the TiO_2 film was determined with He^+ LEIS with an incident angle of 45° from normal and a scattering angle of 135°. The normalized LEIS signals of Ag and Ti give the fraction of surface area that is covered by Ag nanoparticles at a given coverage, as described previously.[72]

4.3 Results and Discussion

4.3.1 Structural Characterization of TiO_2 Thin Films

The structure of the prepared TiO_2 film is characterized using low-energy electron diffraction (LEED). The starting clean Mo(110) surface showed the expected LEED pattern. The LEED pattern of a clean Pt(111) surface, used as a LEED reference, is given in Figure 4.1 at a beam energy of 90 eV. It shows the characteristic (1 × 1) hexagonal pattern expected. Because we have extensive experience with LEED on Pt(111) in this same LEED apparatus, we use the LEED pattern of Pt(111) and its lattice parameter as reference to determine the exposed facet of the prepared TiO_2 film from its LEED pattern. For Pt(111), we name the basis vectors of the unit cell as $\mathbf{a_1}$ and $\mathbf{b_1}$. The lengths of the basis vectors [i.e., the lattice parameters of Pt(111)] are $a_1 = b_1 = 2.77$ Å. The angle between $\mathbf{a_1}$ and $\mathbf{b_1}$ is $\gamma_1 = 60°$. The basis vectors of the reciprocal lattice are named as $\mathbf{a_1^*}$ and $\mathbf{b_1^*}$. The lengths of $\mathbf{a_1^*}$ and $\mathbf{b_1}$* are named as a_1* and b_1*, measured from the LEED pattern. For an unknown surface, we measure the lengths of the basis vectors of its reciprocal lattice, a_2* and b_2*. If the LEED patterns are taken at different beam energies, a_2* and b_2* are corrected by multiplying a factor, $\sqrt{E_2/E_1}$, where E_1 and E_2 are the beam energies at which the LEED patterns are taken. The angle between $\mathbf{a_2^*}$ and $\mathbf{b_2^*}$ (γ_2*) can be used to obtain the angle γ_2 between the basis vectors of the real lattice since $\gamma_2^* + \gamma_2 = 180°$. The lattice parameters of the unknown surface can then be calculated using the equation $a_1 a_1^* \sin \gamma_1 = a_2 a_2^* \sin \gamma_2$ and $b_1 b_1^* \sin \gamma_1 = b_2 b_2^* \sin \gamma_2$.[195]

The method described above was first tested on clean Mo(110). The LEED spots observed for the clean Mo(110) taken at a beam energy of 70 eV are shown as the red spots in Figure 4.1 (adjusted outward to account for the small beam energy difference to 65 eV). Based on the observed Mo(110) LEED pattern, the Mo(110) lattice parameters were found to be a = b = 0.282 nm, which is in good agreement with the theoretical lattice parameters of 0.272 nm. The 4% difference is probably associated with this UHV calorimetry system's geometric constraints, which prevents locating the surface exactly at the center of radius of the LEED screen.

The LEED pattern of the prepared TiO_2 film taken at a beam energy of 65 eV is shown in Figure 4.1. The observed TiO_2 LEED pattern does not correspond to a simple (1 × 1) structure of any of the low-index TiO_2 surfaces. Following the same growth procedure as we used here, Goodman and coworkers prepared TiO_2 films by depositing Ti in an O_2 atmosphere onto a Mo(110) single crystal.[76,77] To characterize the film structure, they used LEED in one study and only STM but not LEED in the second. Unfortunately, the authors concluded different structures in these two papers but did not mention this difference in the second paper or discuss it. They used different post-annealing temperatures in these papers: rutile TiO_2(100) was observed by LEED when the film was post-annealed to 800 K[76] and rutile TiO_2(110) was observed by STM when the film was post-annealed to 900−1200 K, with three different orientations, each rotated by ~120° with respect to the others.[77]

Although the three rotated orientations might explain the hexagonal pattern we observed, the rutile TiO_2(110) structure with three orientations would look very different from our observed LEED pattern due to very different lattice parameters for this facet. However, we found that rutile $TiO_2(100)$ with three orientations rotated by 120° would look very similar to it. Specifically, by overlaying simulated TiO_2 LEED patterns with three orientations on the observed LEED spots, we find a good match to the observed LEED spots using simulated lattice parameters of a = 0.475 nm and b = 0.304 nm, as shown in Figure 4.2. These are in good agreement with the theoretical rutile $TiO_2(100)$ lattice parameters of a = 0.465 nm and b = 0.297 nm (just ∼2% larger). Thus, we propose that the film we prepared is rutile $TiO_2(100)$ with three orientations, each rotated by ∼120° with respect to the others. The three orientations may arise from the quasi-hexagonal nature of the Mo(110) packing and alignment of TiO_2 unit cell edges along its step edges. To the best of our knowledge, no one has reported growth of $TiO_2(100)$ thin films with three rotational domains. As noted above, a similar simulation of the rutile- $TiO_2(110)$ structure with three orientations looked very different from our observed LEED pattern, so we rejected this previously proposed structure and concluded that the titania film we study here instead exposes the rutile $TiO_2(100)$ surface in domains with three rotated orientations. The LEED spots are very broad (∼10% of the spot-to-spot separation), indicating that these domains are small (∼10 lattice parameters wide). Also, it would be difficult to know from the LEED patterns if a large fraction of the surface was disordered, although using a clean single-crystal surface for thin-film growth usually results in a larger extent of surface homogeneity (i.e., no large regions with different structures).

4.3.2 Oxidation State of TiO_2 Thin Films

The XPS Ti $2p_{3/2}$ peak for these TiO_2 thin films showed a small shoulder on the main Ti^{4+} $2p_{3/2}$ peak (at the known binding energy for stoichiometric TiO_2), with a binding energy 2.1 eV lower than that of the main peak, which is consistent with the XPS binding energy of Ti^{3+}.[196] The intensity of this shoulder was about 7% of the total Ti $2p_{3/2}$ peak area. The photoelectrons have a kinetic energy of ~1000 eV, so that the inelastic mean free path for such electrons in TiO_2 is ~1.6 nm.[197] Since the XPS data were taken with the energy analyzer at 45° off the sample normal, 70% of the XPS signal of the Ti $2p_{3/2}$ peak comes from the first 1.1 nm-thick layer of the TiO_2 film. Thus, ~7% of the Ti is Ti^{3+}, and there are ~4% oxygen vacancies in this probe depth.

4.3.3 Growth Morphology of Ag Particles on TiO_2(100)

The growth morphology of Ag on this rutile TiO_2(100) film was determined using He^+ LEIS. Gaseous Ag was deposited onto the TiO_2(100) films at 300 K and 100 K in discrete amounts. After each dose, the Ag and Ti LEIS signals were measured. The integrated Ag LEIS signals were normalized to the signal from a thick Ag overlayer (>10 nm average thickness), and the Ti LEIS signals were normalized to the signal from the clean TiO_2(100) film. The normalized Ag and Ti LEIS signals directly measure the fraction of the surface area that is covered by the Ag particles including a shadowing effect.[72] The evolution of the normalized Ag and Ti LEIS signals is plotted versus Ag coverage in Figure 4.3 and compared with two typical growth models. The Ag coverages reported in this paper are given in monolayer (ML), where 1 ML is defined as 7.36×10^{18} atoms/m^2, which is the areal number density of coordinatively unsaturated O atoms on the ideal bulk-terminated TiO_2(100) surface. The straight dashed lines in Figure 4.3 simulate the normalized LEIS signals that would be expected if Ag followed a layer-by-layer growth mode. They are clearly not in agreement with the measured LEIS data. The solid curved lines correspond to the best fit of these data to a 3D growth model called the hemispherical cap model.[72] It assumes that Ag grows as 3D particles with the shape of hemispherical caps and that the Ag particle number density (*n*) is saturated by the first dose after which the Ag particles only grow in size and that the Ag particles all have the same shape and same size at any given coverage. Although no study of Ag nanoparticles on TiO_2(100) has been reported before, STM studies of Ag nanoparticles grown on rutile $TiO_2(110)$ show that the majority of the islands have nucleated by 0.05 ML (i.e., the saturation density of islands is nearly reached already by ∼0.05 ML)[194] as is generally the case for such systems consisting of late transition metal nanoparticles supported on oxide surfaces.[120] This model is applied up to the coverage where ∼35% of the surface area is covered by particles since the particles may begin to overlap with each other beyond this coverage. This model predicts that the normalized Ag LEIS intensity [I(θ)/I(∞)] increases with the Ag coverage (θ) and Ag particle number density (*n*) as follows[72]

$$\frac{I(\theta)}{I(\infty)} = f_{shadow} \times \pi \times \left(\frac{3 \times \theta \times n_{ML} \times M_{Ag}}{2\pi \times N_A \times \rho_{Ag}}\right)^{2/3} n^{1/3} \qquad (4.1)$$

where n_{ML} is the defined monolayer density (7.36×10^{18} atoms/m^2), M_{Ag} is the Ag molar mass, N_A is the Avogadro constant, and ρ_{Ag} is the bulk Ag density. f_{shadow} is the shadowing factor and equals 1.207 when the nanoparticles have the shape of hemispherical caps and the LEIS is taken with an incident angle of 45° from normal and a scattering angle of 135° as used here.[72] The particle number density *n* is the only unknown parameter that can be obtained by fitting the LEIS data. The normalized Ag LEIS signal gives the fraction of the surface area that is covered and shadowed by Ag nanoparticles, and the normalized Ti LEIS signal gives the fraction of the surface area where TiO_2 is still exposed. Thus, the normalized Ti LEIS signal is just 1 − [*I(θ)/I(∞)*]. Because the Ti signal has more relative noise than the Ag signal, the Ag signal is used to get the best fit to this model, which also fits the Ti signal within its noise.

The best fits in Figure 4.3 give particle number densities of 8.0×10^{16} particles/m^2 at 300 K and 2.5×10^{17} particles/m^2 at 100 K. Since the surface O atom density on $TiO_2(100)$ is 7.36×10^{18} atoms/m^2, the particle number density is equivalent to one Ag particle per 92 surface O atoms at 300 K and per 29 surface O atoms at 100 K. The particle number density at 100 K is about 3.1-fold higher than that at 300 K. The higher particle number density at 100 K is most likely the result of the smaller diffusion constant of Ag adatoms at lower temperature.[120] Venable's homogeneous nucleation model predicts that the saturation particle number density (for the same flux) varies as the inverse cube root of the Ag monomer diffusion constant across the surface (k_{diff}),[120] implying that k_{diff} is 3.13 = 30 times larger at 300 K than 100 K. This 30-fold difference implies an activation energy for diffusion (E_{diff}) equal to $E_{diff} = R \times \ln(30)/[(1/100\text{ K}) - (1/300\text{ K})] = (510\text{ K})R = 4.2$ kJ/ mol. However, a previous STM study showed that Ag atoms nucleate preferentially on step edges of rutile $TiO_2(110)$ at room temperature.[198] If the Ag atoms also favor the step edges on rutile $TiO_2(100)$ and the diffusion length of Ag atoms at 300 K is long enough for them to diffuse to the step edges (probably present at domain boundaries) after landing on the surface, the nucleation of Ag atoms should also take place mostly on the step edges. At 100 K, due to the higher density of Ag clusters, the Ag adatoms may not be able to reach the step edges before adding to another diffusing Ag adatom or existing Ag cluster. Indeed, the heats of Ag adsorption at 100 and 300 K below indicate that the clusters nucleate at step edges at 300 K but not at 100 K. This suggests that the Ag atoms at 100 K follow a homogeneous nucleation model, whereas the Ag particle number density at 300 K may be limited instead by the density of step edges on the $TiO_2(100)$ film. In this case, the estimate given above of E_{diff} (4.2 kJ/mol) is only a lower limit and the true value could be larger.

4.3.4 Differential Heat of Adsorption

The heats of Ag atom adsorption on this rutile $TiO_2(100)$ film at 300 and 100 K are plotted as a function of cumulative Ag coverage in Figure 4.4. All heats of adsorption reported here have been corrected for the difference of the internal energy between a pulse of gaseous metal atoms coming from a high-temperature evaporator and a collection of the same number of gaseous metal atoms in a Boltzmann distribution at the surface temperature, as described before.[33] At 300 K, the heat of Ag adsorption starts at 208 kJ/mol and rises to 265 kJ/mol by 1 ML. It then increases slowly until ∼5ML where the sublimation enthalpy of bulk Ag (285 kJ/mol[199]) is reached. At 100 K, the heat of adsorption starts at 141 kJ/mol and remains lower than that at 300 K until 1.5 ML. Since the particle number density is threefold higher at 100 K than at 300 K, the particles are threefold smaller at 100 K than at 300 K for any given coverage and thus have a higher fraction of low-coordinated Ag atoms. This results in the lower heat of Ag adsorption at 100 K.

To eliminate the effect of different particle densities, we replot the heats of Ag adsorption as a function of the average effective Ag particle diameter in Figure 4.5. The particle diameter at a given coverage is calculated based on the particle number density measured with the hemispherical cap model fit to the LEIS data. We divide the best-fit particle number density (in particles/m^2) by the Ag coverage (in atoms/m^2) to get the average size of Ag particles (in atoms) and then calculate the effective particle diameter assuming that it has the shape of a hemispherical cap, as we did previously.[46,47,75,103,104]

For both 300 and 100 K, the heat of adsorption increases with increasing particle size. This is due to the higher number of metal−metal bonds that an Ag atom can form upon addition to a bigger particle.[7,46] For a given particle size smaller than 1 nm in diameter, the heat of Ag adsorption on $TiO_2(100)$ at 100 K is still lower than that at 300 K. At 300 K, most Ag particles nucleate at step edges, which bind the Ag atoms strongly and lead to a higher heat of adsorption. At 100 K, the Ag atoms are not able to nucleate at step edges due to the slower diffusion. Instead, they form particles mostly at terrace sites and the heat of Ag adsorption for these particles is lower. As the Ag coverage increases, the particles grow bigger and the Ag atoms that add to the particles in each pulse feel less binding strength from the site of nucleation, and the difference between the heat of adsorption at 300 and 100 K becomes smaller. For particles with a diameter of 1.0−1.2 nm, there is no significant difference between the heat of Ag adsorption at 300 and 100 K. The plot of 100 K stops at 1.23 nm since the fraction of the surface area masked by the Ag particles reaches ∼35%, and the fitting of the LEIS data is no longer valid at higher coverage due to particle overlapping. The heat of adsorption for particles bigger than 1.2 nm in diameter at 100 K is slightly higher than that at 300 K, which indicates that the particle overlapping may start earlier than we expected with the higher particle density at 100 K, leading to some larger particles than predicted by the LEIS fit.

Note that the smallest particle in Figure 4.5 (created with the first Ag vapor pulse on the surface at 100 K) has an effective hemispherical diameter of only 0.41 nm. The volume of such a hemisphere (0.018 nm^3) corresponds to an average cluster size of only 1.1 Ag atoms [again using the density of bulk Ag(solid)]. It has a chemical potential of 144 kJ/mol relative to bulk Ag (Figure 4.5) and a heat of adsorption of only 141 kJ/ mol relative to gaseous Ag monomers. This compares to DFT estimates of the Ag monomer adsorption energy on rutile TiO_2(110) of 2.07 eV (199 kJ/mol)[188] and on anatase TiO_2(101) of 1.04 eV (100 kJ/mol).[189]

The initial heat of adsorption at 300 K (208 kJ/mol) is 67 kJ/mol higher than that of this (near) monomer formed at 100 K due to the larger initial size (3.7 atoms vs 1.1 atom) but also partially due to the effect of step edges (which is about 40 kJ/ mol, as estimated from the difference in heats between 300 and 100 K at this size in Figure 4.5). This initial heat at 300 K of 208 kJ/mol is very similar to the value of 195 kJ/mol measured for Ag on 5 nm-diameter anatase powder at 300 K.[176]

4.3.5 Adhesion Energy of Ag Particles onto TiO_2(100)

The adhesion energy, E_{adh}, of metal nanoparticles onto a flat surface can be calculated using the measured heat of adsorption with two different methods. The first method is using an equation derived from a thermodynamic cycle,[200] which is shown for this special case of hemispherical particles in Figure 4.6.

As shown in Figure 4.6, the adsorption of metal atoms on the oxide surface (step 3, which heat we measure with SCAC) can be divided into two hypothetical steps. In the first step, the gaseous metal atoms form free metal nanoparticles with the shape of a hemispherical cap in vacuum. The energy change in this step can be calculated with the sublimation enthalpy ΔH_{sub} (285 kJ/mol for Ag) and the surface energy $\gamma_{v/m}$ (1.22 J/m^2 for Ag[19]) of the bulk metal. The total surface area of the free metal nanoparticles is required for the energy calculation in the first step. It is calculated as $(1 + f) \times A$, where A is the total interfacial area between the metal nanoparticles and the oxide surface and f is a roughness factor of its top surface ($f = 2$ for hemispherical caps). In the second step, the free metal nanoparticles formed in the first step are attached to the oxide surface, and the energy change equals (by definition) the product of the adhesion energy and the total interfacial area between the metal nanoparticles and the oxide surface. The overall energy change of these two steps equals the formation energy of the supported metal nanoparticles on the oxide surface from gaseous metal atoms, which equals the negative (the enthalpy change of adsorption is negative, but the heats of adsorption are reported as positive numbers) integrated heat of adsorption $\sum n\, \Delta H_{ads}$ measured in the SCAC experiments. From this thermodynamic cycle, the adhesion energy equals[200]

$$\sum_{n} \Delta H_{ads} = -n\,\Delta H_{sub} + A\,[\,(1+f)\gamma_{v/m} - E_{adh}] \qquad (4.2)$$

(4.2) assumes that the metal nanoparticles reach the large-size limit, so that the surface energy and the adhesion energy of the metal nanoparticles are the same as those for the bulk metal. To approach as closely as possible to the large-size limit but keep the surface area covered by Ag nanoparticles no more than 35%, the heat of Ag adsorption at 300 K can be integrated up to 2 ML, corresponding to a particle diameter of 2.28 nm. For 100 K, the heat of Ag adsorption can be integrated only up to 1 ML, corresponding to a particle diameter of 1.25 nm. These particle sizes are too small to have reached the large-size limit for either $\gamma_{v/m}$ or E_{adh}, as proven in our previous work.[35] There, we introduced an empirical correction factor $(1 + D_0/D)$ to model the increasing surface energy and adhesion energy of metal nanoparticles with decreasing particle size, where D is the diameter of the hemispherical metal nanoparticles and $D_0 = 1.5$ nm. Notice that the diameter of 2.28 and 1.25 nm is still comparable with $D_0 = 1.5$ nm, and the empirical correction factor $(1 + D_0/D)$ is 1.66 and 2.20, respectively. This shows that at the coverage up to which the heat of Ag adsorption is integrated, the Ag particles are still too small to reach the large-size limit and require this correction factor. Thus, the surface energy and the adhesion energy onto $TiO_2(100)$ for such small particles are higher than those for bulk Ag and (4.2) does not work here.

To address the size dependency of the surface energy and the adhesion energy, Figure 4.6 and (4.2) are corrected by including this empirical correction factor $(1 + D_0/D)$. The surface energy in Figure 4.6 should be replaced with $(1 + D_0/D)\,\gamma_{v/m}$, and the adhesion energy should be replaced with $(1 + D_0/D)E_{adh}$, where $\gamma_{v/m}$ or E_{adh} represents their large-size limits. (4.2) is thus modified following the same method, so it now reads instead as

$$\sum_n \Delta H_{ads} = -n\,\Delta H_{sub} + A\,[\,(1+f)\gamma_{v/m} - E_{adh}](1 + D_0/D) \qquad (4.3)$$

The new calculation is carried out by plugging the integrated heat of Ag adsorption and the Ag particle diameter into (4.3). The calculated adhesion energy of Ag particles (in the large-size limit) onto $TiO_2(100)$ is 2.46 J/m^2 for 300 K and 2.41 J/ m^2 for 100 K. Although the heats of Ag adsorption are integrated up to different coverages for 300 and 100 K and the Ag particles have different sizes at the cutoff coverages, E_{adh} is already corrected for its size dependency with the factor $(1 + D_0/D)$. Thus, E_{adh} calculated with (4.3) is the adhesion energy of bulk (large-size) Ag onto $TiO_2(100)$, no matter what coverage the heat of adsorption is integrated up to in the calculation. The adhesion energy at 300 K is 2% higher than that at 100 K, which we attribute to the higher binding strength of the step edge to the Ag particles and the larger contribution of step edges to the measurement at 300 K.

The second method to estimate E_{adh} is through fitting a plot of measured Ag chemical potential versus particle diameter. The differential heat of Ag adsorption measured in Figure 4.5 can be converted to the chemical potential of Ag atoms by assuming that the entropic contribution to the free energy is negligible compared to this measured enthalpic difference.[38] For Ag nanoparticles with a given diameter D, the chemical potential of Ag atoms in the nanoparticles relative to that of bulk Ag equals the sublimation enthalpy of bulk Ag minus the heat of Ag adsorption onto the Ag nanoparticles with diameter D. Following this procedure, Figure 4.5 can be replotted as the chemical potential of Ag atoms versus the effective particle diameter, as shown in Figure 4.7. Then, (4.4) (taken from ref [35]) can be used to fit this plot of chemical potential versus effective particle diameter

$$\mu(D) = (3\gamma_{v/m} - E_{adh})(1 + D_0/D)(2V_M/D) \tag{4.4}$$

here $\mu(D)$ is the chemical potential of Ag atoms in nanoparticles of diameter D and V_m is the molar volume of bulk Ag. The factor $(1 + D_0/D)$ is the empirical correction that models the increasing surface energy and adhesion energy with decreasing particle size, as introduced in (4.3). It has been shown that (4.4) gives good fit for five systems consisting of metal nanoparticles supported on metal oxide surfaces with E_{adh} calculated using (4.2) and $D_0 = 1.5$ nm. If one keeps $D_0 = 1.5$ nm, E_{adh} becomes the only variable in (4.4) and E_{adh} can be obtained by fitting the plot of chemical potential versus particle diameter.[46] The calculation of E_{adh} is further tested by fitting the plot of chemical potential in Figure 4.7. The best fit of (4.4) to the data in Figure 4.6 gives $E_{adh} = 2.56$ J/m^2, within a difference of only 6% compared to the result of (4.3) given above (2.41−2.46 J/m^2). The curve fits the plot in Figure 4.7 well except for the first few data points at 300 K (where step edges dominate and stabilize the Ag relative to terrace sites on the oxide, so we do not expect agreement) and a few data points at 100 K where the particles have diameter below 0.6 nm. Below 0.6 nm, the Ag particles might be too small to form a shape of hemispherical caps as we assumed or the factor of $(1 + D_0/D)$ is not accurate enough for describing Ag particles smaller than 0.6 nm. It is also possible that at 100 K and these lowest coverages, the Ag clusters have not yet reached their saturation number density, and are slightly larger than estimated here.

To summarize, fitting our calorimetry results to (4.3) and (4.4) shows that the adhesion energy of large-size Ag particles to rutile $TiO_2(100)$ terraces is 2.43 to 2.56 J/m^2. This is much larger than the measured adhesion energies of Ag to MgO(100) (0.3 J/m^2)[200] and slightly larger than those for Ag on $CeO_{1.9}(111)$ (2.3 J/m^2).[99] Since the metal/oxide interaction mainly depends on the bonding at the interface to the surface oxygen (i.e., the coordinatively unsaturated O atoms), we try to correlate the adhesion energies with the standard-state enthalpies of reduction of the oxide per mole of oxygen atoms ($\Delta H_{red,\mathrm{OxSup}}$) and the areal density of surface oxygen atoms (N_O), as we did before.[35] For $CeO_{1.9}(111)$ and $TiO_2(100)$, $\Delta H_{\mathrm{red,OxSup}}$ is the enthalpy to reduce the oxide support to a stable oxide with the next lower oxidation state (i.e., Ce_2O_3 and Ti_2O_3), giving values of 382 kJ/mol for CeO_2 and 367 kJ/ mol for TiO_2, which are quite similar. For MgO, $\Delta H_{\mathrm{red,OxSup}}$ (to Mg) is 602 kJ/mol, which is much larger. To be comparable to these values, the measured adhesion energy per unit area is first divided by N_O and multiplied by the Avogadro constant to get the adhesion energy per mole of surface oxygen atoms, giving values of 16, 175, and 209 kJ per mole of surface O atoms for MgO(100), $CeO_{1.9}$(111), and TiO_2(100), respectively. These results are qualitatively consistent with our previous study, where we reported a rough trend that the stronger the surface oxygen atoms are bonded to the oxide lattice, the weaker are their bonds across a metal/oxide interface in metal adhesion. [35] The surface O atoms are bonded similarly weakly to CeO_2 and TiO_2, giving similarly high E_{adh} to Ag. In contrast, surface O atoms bond very strongly to MgO, giving the lowest E_{adh} to Ag.

Our earlier comparison of the adhesion energies of gold to MgO(100), $CeO_{1.9}$(111), and rutile-TiO_2(110) (0.31−0.67, 2.53, and 0.54−0.71 J/m^2 or 17−36, 193, and 62−82 kJ per mole of surface O atoms, respectively[37]) does not fit the expected behavior nearly so well, with the adhesion of Au to TiO_2(110) being much weaker than that expected based on its easy reducibility. We currently do not know how to explain the weak adhesion of Au to TiO_2(110), given the strong adhesion of Ag to TiO_2(100) measured here. This may be related to some intrinsic difference in the way Ag bonds to these two facets of rutile or to the higher surface defect density on the thin film required for our calorimetric measurement. The measurements of Au on TiO_2(110)[174,175] appear to us to be of very high quality and on crystal surfaces with far fewer defects.

We note that none of the abovementioned values of adhesion energies which are in units of J/m^2 depend upon our assignment of the surface structure here to rutile-TiO_2(100) (based on the LEED pattern seen). However, the conversion of these into units of kJ per mole of surface O atoms does depend on that assumption. For example, since this face has 41% more O atoms per unit area than rutile-$TiO_2(110)$, those values would be 41% too low if the surface instead has an O- atom packing density like the (110) face.

In previous studies, it was found that Ag atoms bind more strongly to oxygen vacancies than to stoichiometric terraces on $CeO_{2-x}(111)$.[73,201] In SCAC experiments, the initial heat of Ag adsorption is 200 kJ/mol on $CeO_{1.9}(111)$ and 220 kJ/mol on $CeO_{1.8}(111)$, and the adhesion energy of Ag to $CeO_{1.9}(111)$ is slightly lower than that of $CeO_{1.8}(111)$ by 0.2 J/m^2.[99] For the interface between Ag(111) and rutile $TiO_{2-x}(100)$, DFT calculation gives an adhesion energy of 25.0 meV/Å^2 (0.4 J/ m^2) for stoichiometric $TiO_2(100)$, and the adhesion energy increases to 62.3 meV/Å^2 (1.0 J/m^2) when the first layer of O on $TiO_2(100)$ is removed completely.[202] For anatase $TiO_2(101)$, DFT calculations also found that Ag single atoms bind much more strongly at surface oxygen vacancies and slighter more strongly near subsurface oxygen vacancies than on the fully oxidized anatase (101) facet.[189] As shown by XPS, the first 1.1 nm-thick layer of the prepared rutile $TiO_2(100)$ contains ~4% oxygen vacancies. Thus, the heat of Ag adsorption and the adhesion energy of Ag(solid) to rutile $TiO_2(100)$ measured here are probably higher than for a stoichiometric TiO_2 film. However, considering the low fraction of oxygen vacancies, this is not expected to be a major effect unless the vacancies are segregated to the surface.

4.3.6 XPS Investigation of Ag/$TiO_2(100)$

The Ag $3d_{5/2}$ XPS peak was monitored during Ag deposition. Figure 4.8 shows the Ag $3d_{5/2}$ peak binding energy (BE) as a function of Ag coverage. At 300 K, the Ag $3d_{5/2}$ BE at 0.13 ML of Ag deposition is 368.96 eV, which is 0.86 eV higher than the bulk value measured on a 10 nm-thick Ag film (368.1 eV). The Ag $3d_{5/2}$ peaks shift to lower BE as the Ag coverage increases. At 100 K, the Ag $3d_{5/2}$ BE at 0.31 ML is 369.02 eV. The Ag $3d_{5/2}$ BE also decreases with increasing Ag coverage, but the BE shifts are more gradual in the first 2 ML than at 300 K. The Ti 2p XPS peaks were also taken simultaneously with Ag $3d_{5/2}$. The intensity of the Ti 2p peak decreases as the Ag coverage increases. The Ti^{3+} shoulder does not grow relative to the Ti^{4+} main peak, and the BE of Ti^{4+} stays constant at ∼458.8 eV, which suggests that the Ag atoms are not oxidized upon deposition. The higher Ag $3d_{5/2}$ BEs at low Ag coverage can be attributed to a final state effect, whereby the XPS core-hole final state is less stabilized by electron screening in smaller metal particles, so that the BE increases with decreasing particle size.[7] The higher Ag $3d_{5/2}$ BE at 100 K than at 300 K at all coverages is due to the fact that Ag forms smaller particles at 100 K than at 300 K, differing by a factor of 3.1 at any coverage according to the particle number densities determined by fitting the LEIS data. Goodman et al. reported the growth of Ag on rutile $TiO_2(110)$ studied with XPS, LEIS, and STM, and the Ag $3d_{5/2}$ BE shifts are very similar to what we observed here on $TiO_2(100)$[198] The Ag $3d_{5/2}$ shifts to higher BE at low Ag coverages at 300 and 100 K. The Ag $3d_{5/2}$ BE shift is ∼1.0 eV over the entire coverage range at 100 K, while it is approximately 0.7 eV at 300 K.

4.4 Conclusions

The TiO_2 film was prepared by reactive evaporation of Ti onto the Mo(110) single crystal at 625 K in 2×10^{-7} torr of oxygen gas and post-annealing to 800 K in the same O_2 background. Using LEED, the surface structure of the TiO_2 film was determined to be rutile $TiO_2(100)$ with three orientations, each rotated by ∼120° with respect to the others. The LEIS experiments showed that Ag grows as 3D nanoparticles at 300 and 100 K. The number density of Ag nanoparticles was 8×10^{16} particles/m^2 at 300 K and 2.5×10^{17} particles/m^2 at 100 K. The heat of Ag adsorption on rutile $TiO_2(100)$ at 300 K was initially 208 kJ/mol and increased slowly with coverage until the sublimation enthalpy of Ag was achieved at 5 ML. At 100 K, the initial heat of Ag adsorption was 141 kJ/mol (forming a cluster of average-size 1.1 Ag atoms), which is 67 kJ/mol lower than at 300 K. The heat of adsorption at 100 K remained lower than at 300 K until 1.5 ML. The higher heat of adsorption at 300 K is a result of the bigger particle size observed for any given coverage at 300 K and also attributed partially to the preferential nucleation of Ag nanoparticles at more stable step edges at 300 K but mainly at terraces at 100 K. When the heat of adsorption was plotted versus the particle diameter, the heat of adsorption at 300 K was only higher than that at 100 K for particles with diameter <1 nm due to the stronger binding strength at step edges. The adhesion energy of Ag onto rutile TiO2(100) was determined by calculating the energy change of a thermodynamic cycle and by fitting the Ag chemical potential versus the Ag particle diameter. The adhesion energy calculated with the thermodynamic cycle was 2.46 J/m^2 at 300 K and 2.41 J/m^2 at 100 K. The adhesion energy of 2.56 J/m^2 was obtained by fitting the chemical potential versus particle size to our theoretical model, which agrees within 5% of the average value from the thermodynamic cycle method.

4.5 Figures

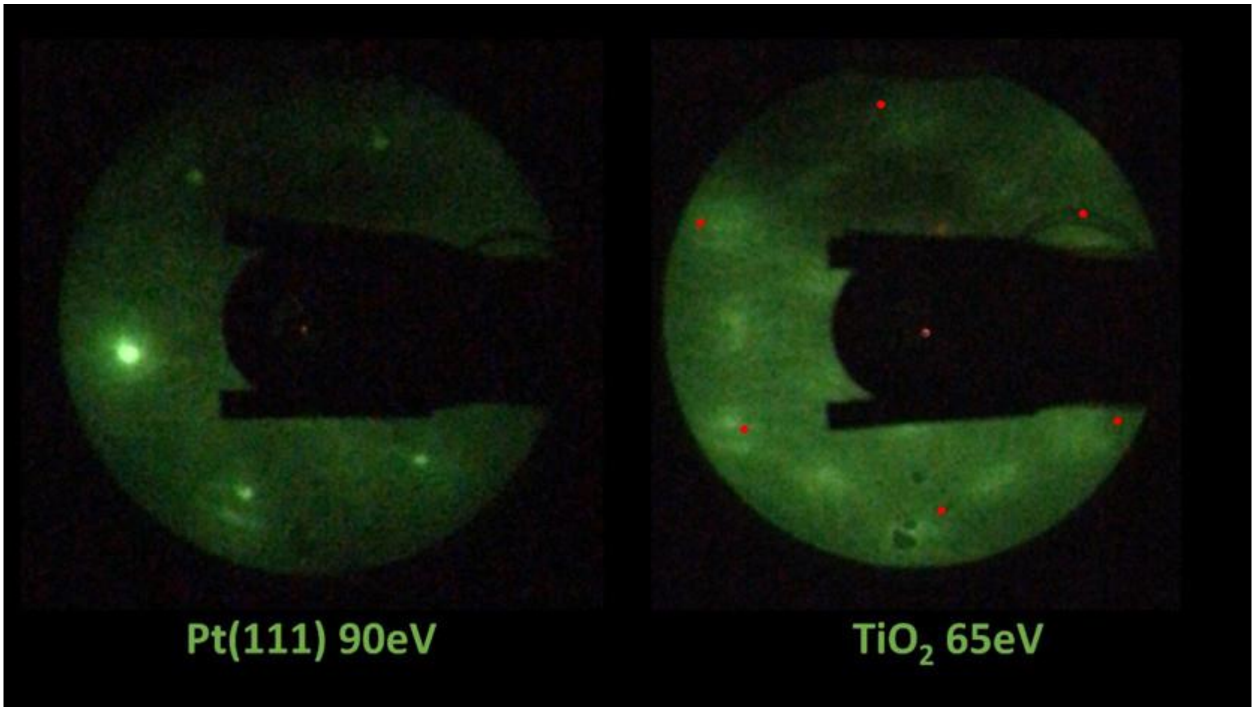

Figure 4.1. LEED patterns for the reference Pt(111) surface and the TiO_2 film grown on Mo(110), at 90 eV and 65 eV, respectively. The (0,0) spot in the middle of the screen is hidden by the sample holder in all cases. The first-order LEED spot locations of the starting Mo(110) surface are shown as red dots on the film's patterns. (These were measured at 70 eV and adjusted outward by a factor of 70/65 to correct to an energy of 65 eV.)

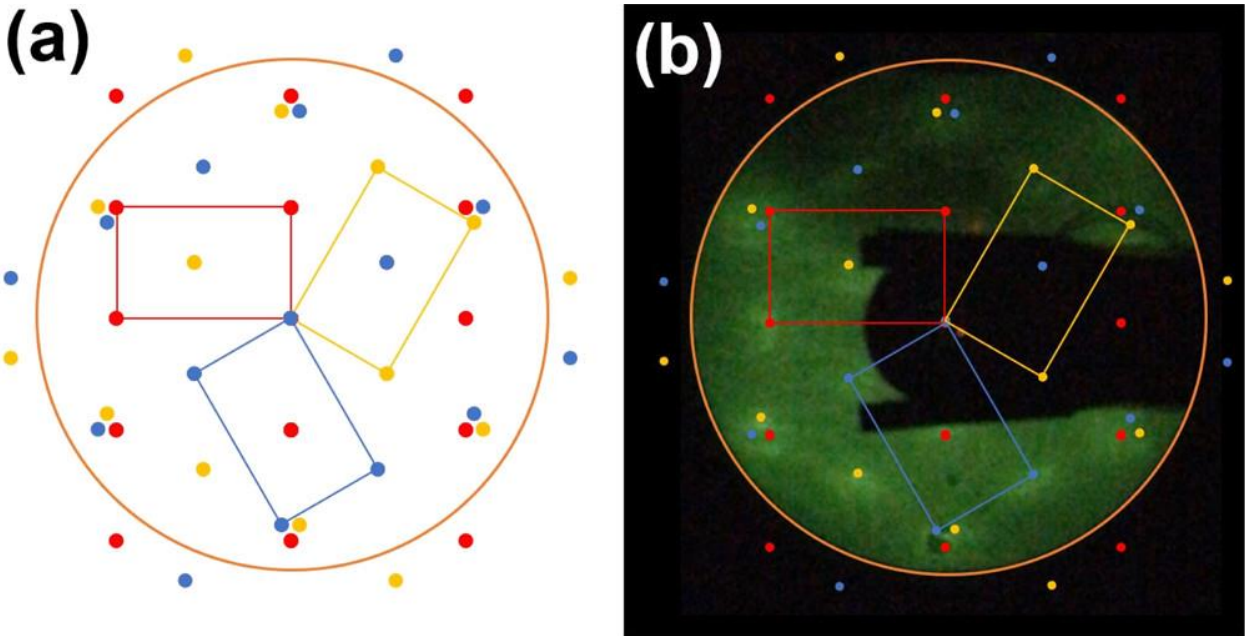

Figure 4.2. (a) Simulated rutile $TiO_2(100)$ LEED with three rotational orientations and lattice parameters of a = 0.475 nm and b = 0.304 nm. The three orientations are distinguished with three different colors (red, yellow, and blue). (b) Simulated rutile $TiO_2(100)$ LEED overlaid onto the TiO_2 LEED pattern observed at 65 eV.

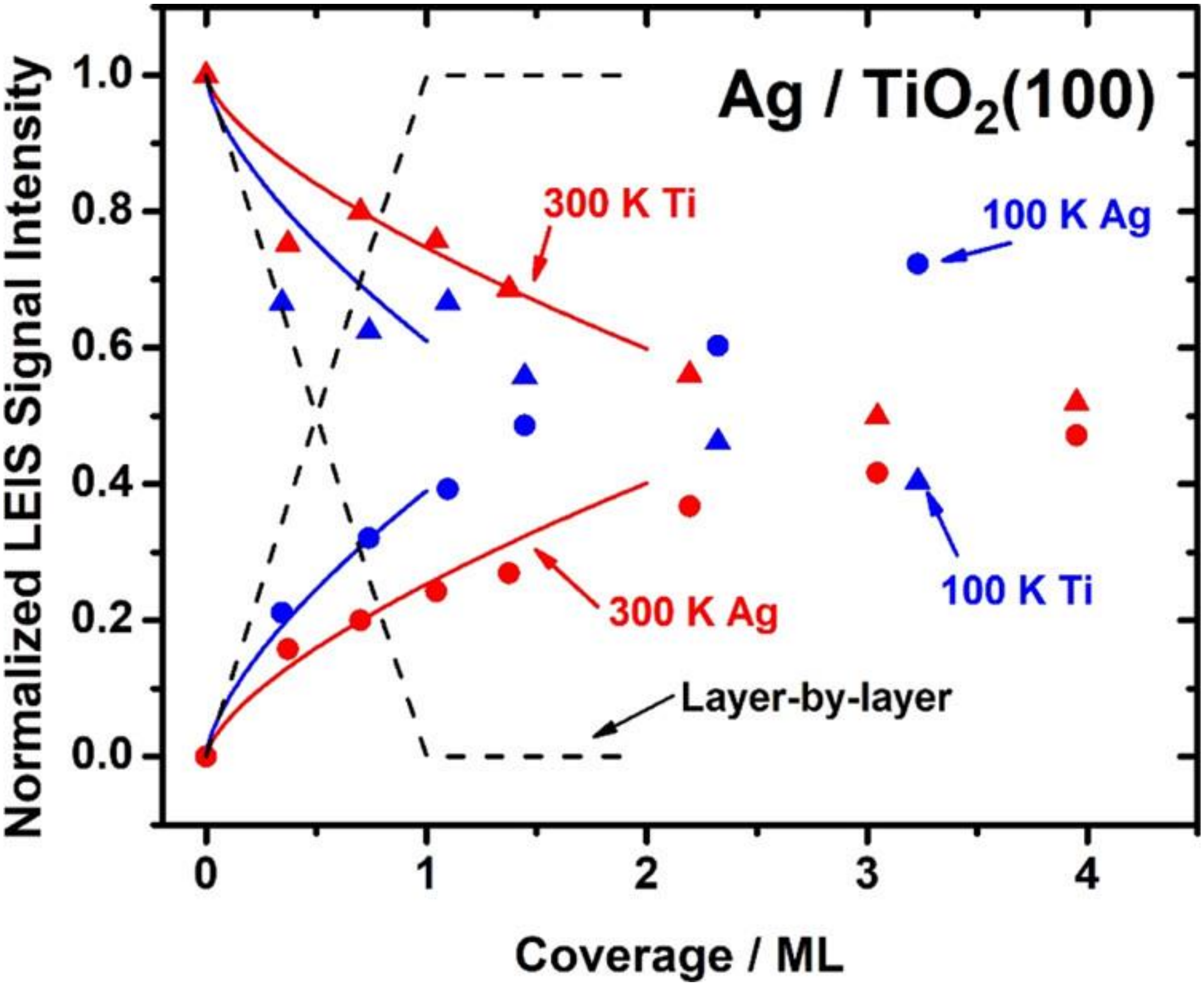

Figure 4.3. Integrated Ag (circles) and Ti (triangles) LEIS signal intensities (normalized to thick multilayer Ag and clean TiO_2, respectively) as a function of Ag coverage after deposition of Ag onto $TiO_2(100)$ at 300 K (red symbols) and 100 K (blue symbols). The black dashed lines correspond to the normalized LEIS signal that would be observed if Ag grew in a layer-by-layer mode. The colored solid lines correspond to Ag growing as 3D hemispherical caps with a fixed particle density of 8.0×10^{16} particles/m^2 (red) and 2.5×10^{17} particles/m^2 (blue).

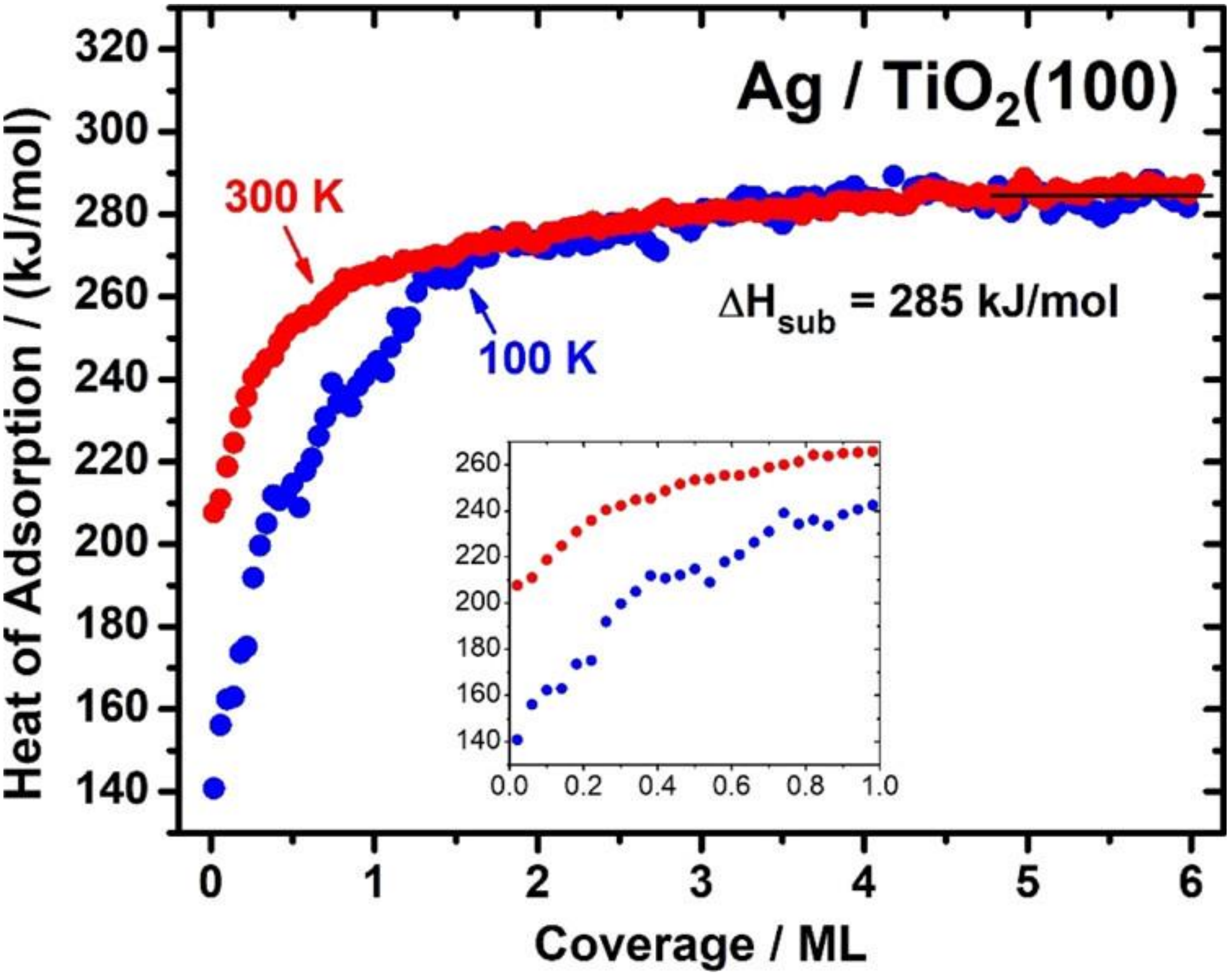

Figure 4.4. Differential heat of Ag atom adsorption on $TiO_2(100)$ at 300 K (red circles) and 100 K (blue circles) as a function of Ag coverage. The inset shows more details at the low-coverage region (0−1.0 ML).

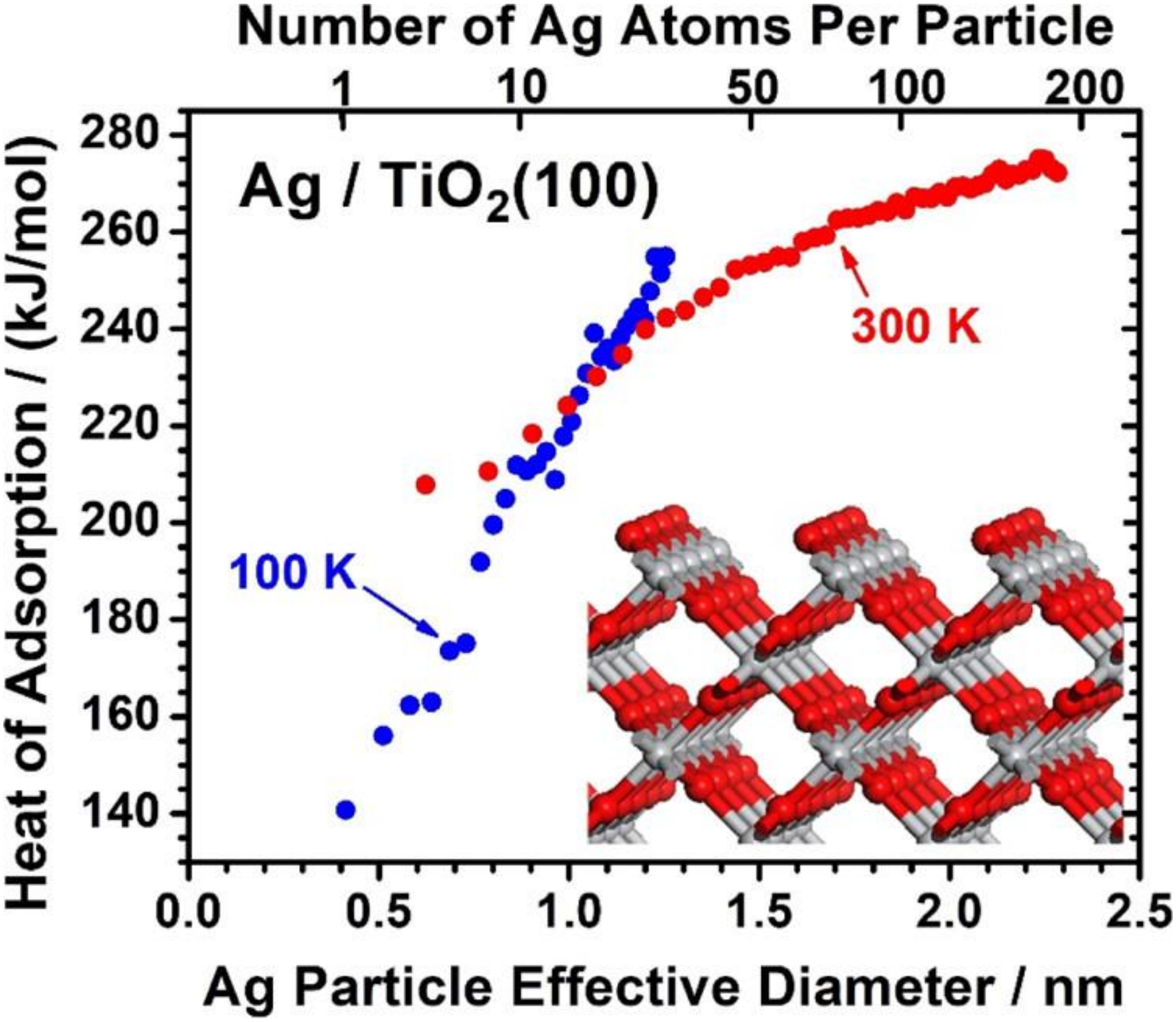

Figure 4.5. Differential heat of Ag adsorption on TiO_2(100) at 300 and 100 K as a function of the average effective Ag particle diameter to which the Ag atoms add upon adsorption. The inset shows the geometry of the un-reconstructed TiO_2(100) surface. Red: O; gray: Ti.

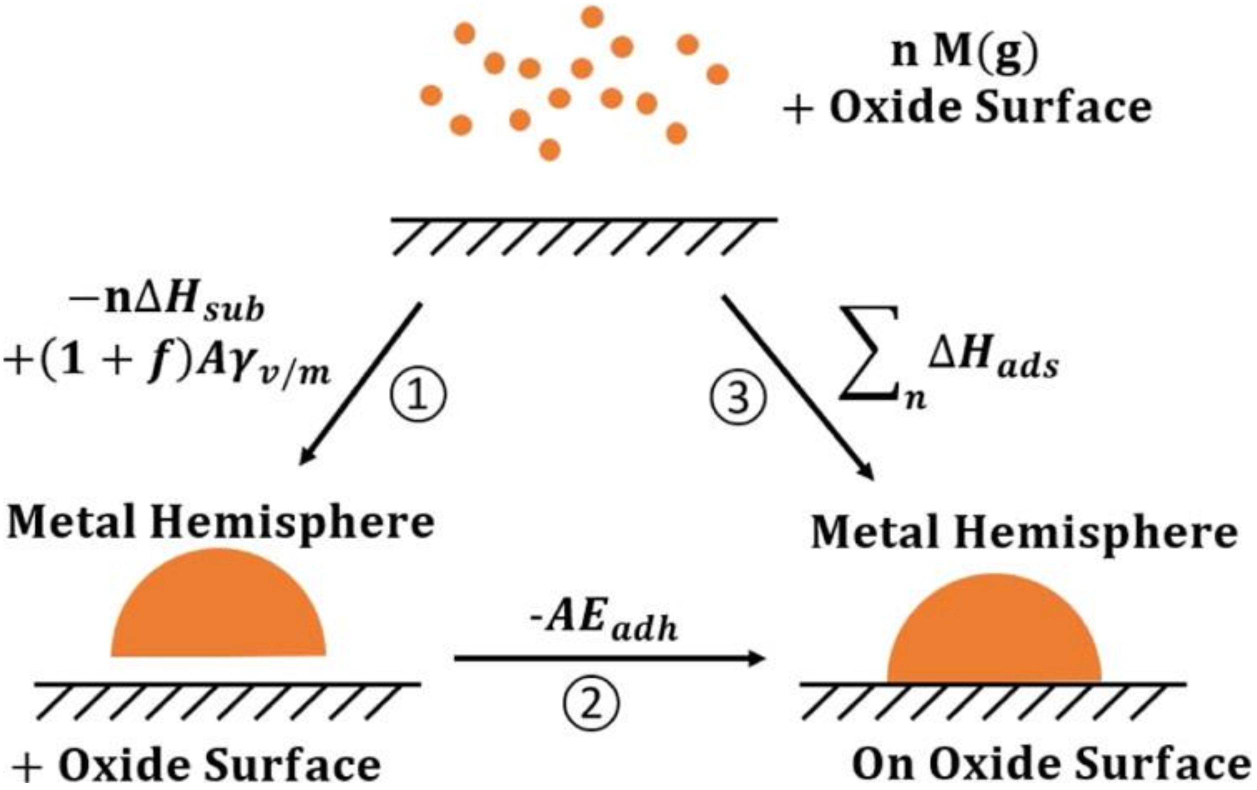

Figure 4.6. Thermodynamic cycle that connects adsorption and adhesion energies for metal adsorption on an oxide surface. It includes three steps: (1) The gaseous metal atoms form hemispherical nanoparticles in vacuum. (2) The hemispherical nanoparticles are attached onto the oxide surface. (3) The gaseous metal atoms adsorb on the oxide surface and form hemispherical metal nanoparticles, which equals the sum of steps 1 and 2.

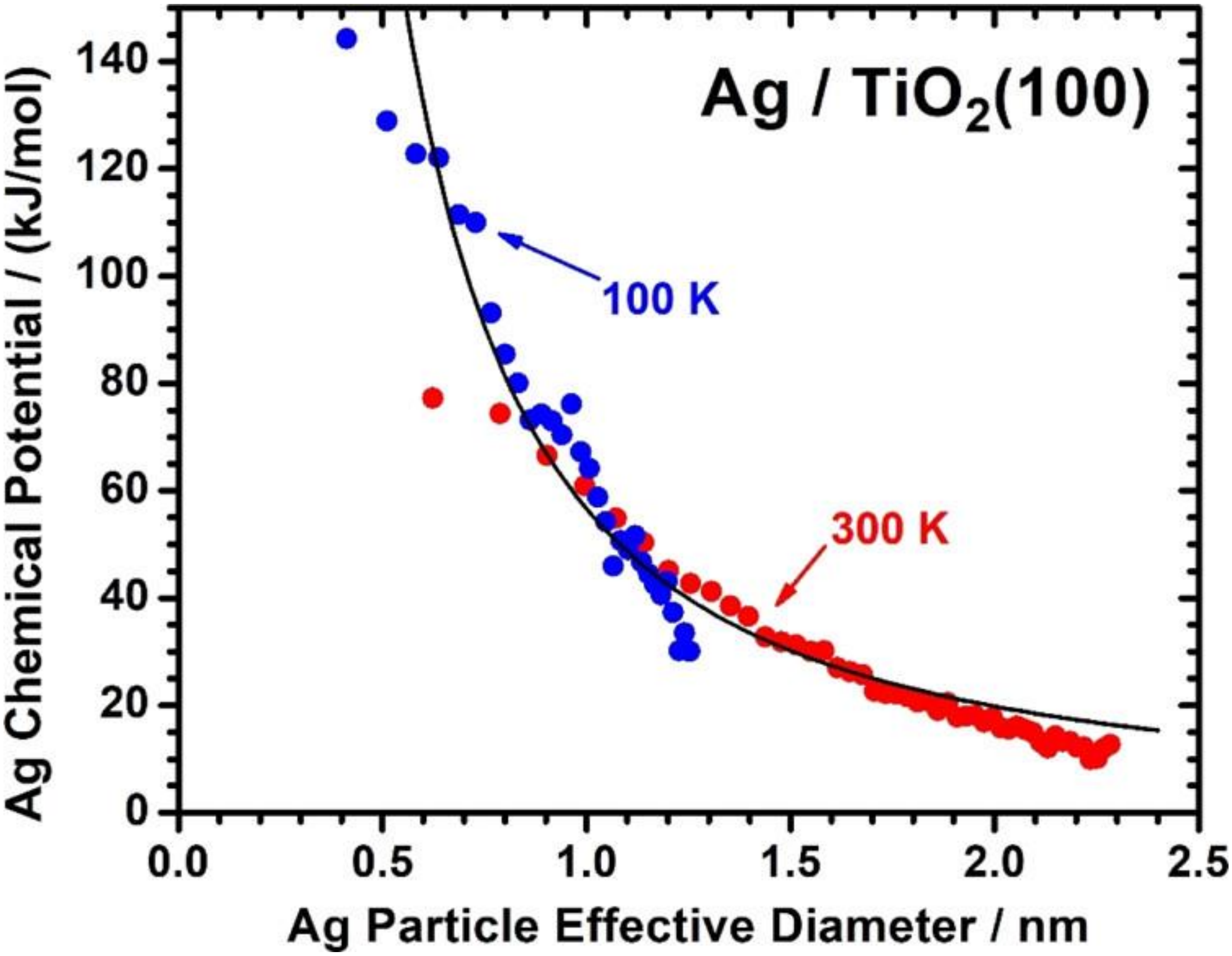

Figure 4.7. Chemical potential of Ag atoms in nanoparticles vs the effective particle diameter on $TiO_2(100)$ at 300 K and 100 K. The black solid curve is the fitting line of (4.4) with $E_{adh} = 2.56$ J/m^2 and $D_0 = 1.5$ nm.

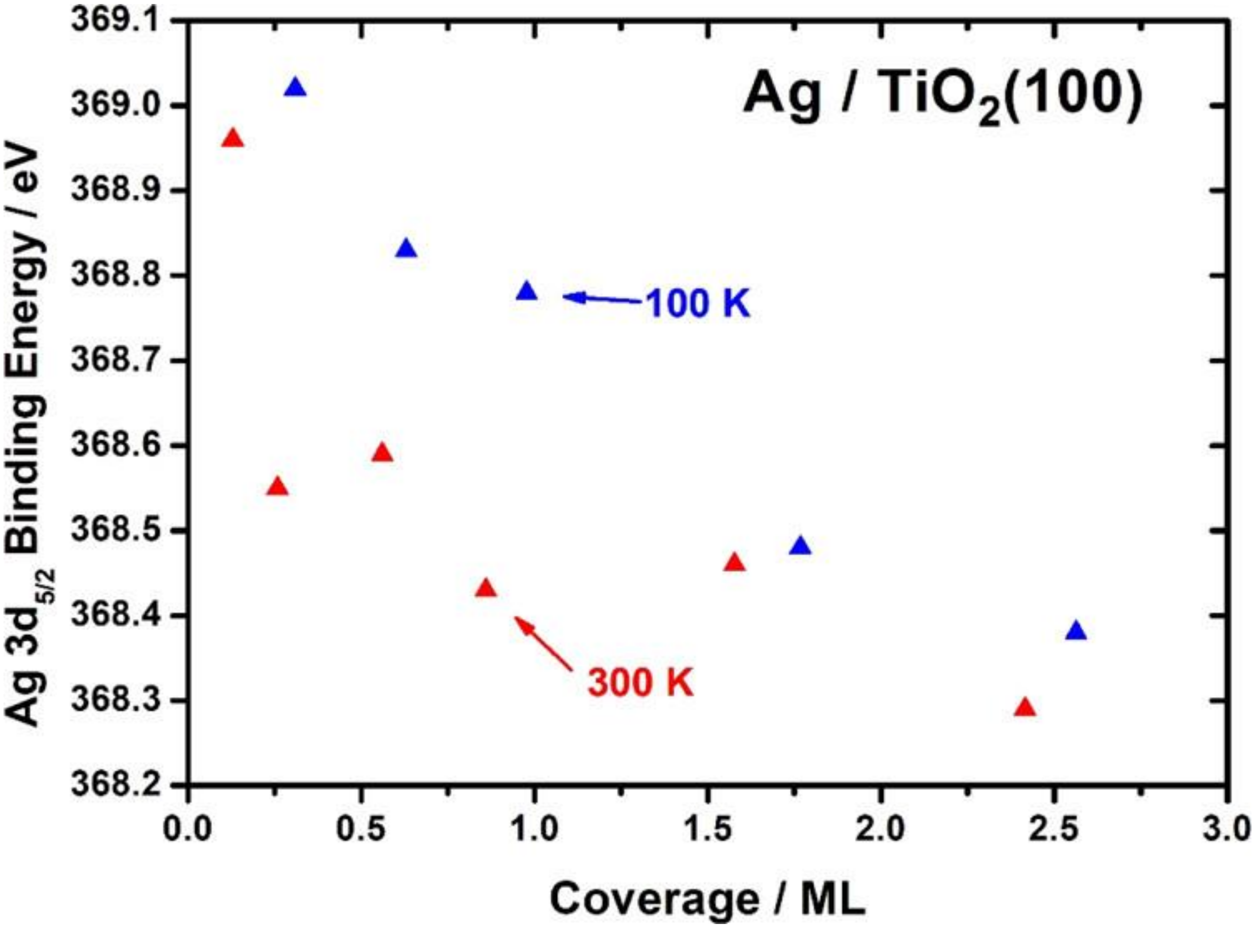

Figure 4.8. Variation in the Ag $3d_{5/2}$ XPS binding energies as a function of Ag coverage on rutile TiO_2(100) at 300 (red) and 100 K (blue).

Chapter 5. Size-Dependent Adsorption and Adhesion Energetics of Ag Nanoparticles on Graphene Films on Ni(111) by Calorimetry

This chapter has been published as:

Rumptz, J. R., Mao, Z., & Campbell, C. T. (2022). *ACS Catalysis,* 12 (5), 2888-2897.

Chapter Abstract

Interest in the use of carbon supports for late transition metal nanoparticle catalysts has expanded rapidly due to the increasing importance of electrocatalysts for clean energy and environmental technologies and the use and storage of renewable electricity. Compared to oxide supports, almost nothing is known about the effect of metal nanoparticle size on the energies of the metal atoms within carbon-supported nanoparticles, yet these energies are crucial for understanding their surface reactivity and sintering kinetics. Here, the growth morphology and adsorption energetics of vapor-deposited Ag onto clean graphene/Ni(111) surfaces have been studied using a combination of single crystal adsorption calorimetry (SCAC) and He^+ low-energy ion scattering (LEIS). The differential heat of Ag adsorption is 207 kJ/mol for making ∼30 atom Ag particles on graphene terraces at 100 K and 16 kJ/mol higher for making ∼9 atom Ag clusters at defect sites at the same temperature. The heat of adsorption increases rapidly with Ag coverage as 3D Ag nanoparticles nucleate and grow in size, asymptotically reaching within 5 kJ/mol of the bulk Ag sublimation enthalpy (285 kJ/mol) by 2 ML. The heats of adsorption and Ag nanoparticle densities from LEIS ($\sim 10^{16}/m^2$) were combined to provide the Ag/graphene adhesion energy ($E_{adh} = 1.8$ J/m^2 in the large-particle limit) and the Ag chemical potential (μ) versus effective particle diameter (D). The Ag chemical potential was well-fitted by $\mu(D) = (3\gamma_{v/M} - E_{adh})(1 + (1.5\ \text{nm})/D)(2V_m/D)$, where $\gamma_{v/M}$ is the surface energy of bulk Ag and V_m is its molar volume. The same equation is known to fit similar data for late transition metals on clean

surfaces of metal oxide single crystals. The adhesion energy of Ag measured here on graphene falls within the wide range measured for Ag on those oxide surfaces and is almost as large as on the oxide that binds Ag particles most strongly, namely $CeO_2(111)$, which is well-known to be very effective at resisting catalyst deactivation by metal sintering. These results imply that carbon supports will be effective at resisting sintering and that Ag particles smaller than 6 nm on graphene will bind small adsorbed reaction intermediates more weakly than supports with weaker adhesion to Ag, like MgO(100).

5.1 Introduction

Late transition metal nanoparticles supported on high-surface-area support materials are important heterogeneous catalysts and electrocatalysts for energy, environmental, and chemical technologies. It is well-known that the performance of these metal nanoparticle catalysts is influenced strongly by the choices of metal and support material and by the metal nanoparticle size and structure.[7–9,11,157,203–205] These performance-based properties include the catalytic activity, selectivity, and long-term thermal stability of the metal/support system. As such, a better fundamental understanding of these structure–performance relationships will help to design new catalyst materials with more desirable properties for technological purposes. Our group has shown that the chemical potential of metal atoms in supported nanoparticles provides a convenient descriptor of their performance as heterogeneous catalysts that captures many of the effects of particle size, support, and even alloying.[35,36,38]

Using microcalorimetric measurements of the differential heats of adsorption of metal vapor as it adds to predeposited metal nanoparticles on the surfaces of single-crystalline oxide supports, our group has determined this metal-atom chemical potential as a function of particle diameter for monometallic nanoparticles on different oxide supports.[35,36] It was found from these measurements that this chemical potential has a predictable dependence upon the particle size and the adhesion energy at the particle/support interface.[35,36] Furthermore, this adhesion energy was measured for many combinations of late transition metals and oxide supports and found to follow some predictable trends.[36] However, all those results are for oxide support materials (like $CeO_2(111)$, MgO(100), etc.). Essentially nothing is known about the chemical potential versus nanoparticle size for metal on carbon-based supports. Here, we report the first experimental measurements of the metal chemical potential versus particle size for nanoparticles of any metal element on any carbon support material, specifically for Ag nanoparticles supported on single-layer graphene(0001) on Ni(111). We also report the metal/support adhesion energy for that Ag/graphene interface. The only other experimental metal/graphene adhesion energy of which we are aware is for Ni on graphene/Ni(111), based on particle shape measurements with scanning tunneling microscopy (STM).[78] Both the Ag chemical potential and Ag/graphene adhesion energy are determined here from heats of Ag vapor adsorption versus Ag coverage on clean graphene as Ag nanoparticles nucleate and grow in size on the surface, measured using single-crystal adsorption calorimetry (SCAC). To the best of our knowledge, this is also the first SCAC measurement of the adsorption energetics of any metal vapor on any carbon-based support system and the first measurements of chemical potential versus size for nanoparticles of any metal on any carbon support. The results show that such a carbon support binds Ag nanoparticles nearly as strongly as the previously measured oxide that binds Ag nanoparticles most strongly, $CeO_2(111)$, and that the Ag chemical potential for a given nanoparticle size below 6 nm is only slightly higher for Ag on this carbon support than for Ag on $CeO_2(111)$ but much lower than for Ag on a weak-binding support like MgO. Given reported correlations between metal chemical potential and catalyst performance (i.e., sinter resistance and bonding strength to small adsorbates),[13,35,36,38,99,102,206] this further suggests that such carbon supports will be almost as effective for resisting catalyst deactivation by sintering as $CeO_2(111)$ and that small adsorbed reaction intermediates will bind to Ag nanoparticles rather weakly.

The use of carbon as a support material has become increasingly common,[53–58] in part because carbon is conductive and can serve as an electrode material for electrocatalysis and the increasing importance of electrocatalysis for clean-energy storage. Whether it is in the form of activated carbon, carbon black, modified graphite, carbon nanofibers, or carbon nanotubes, the dominant building block in a carbon support's structure is the graphite unit cell.[57] There are extensive modifications that can be made to C(0001) to change its surface properties including creating sputter-induced defects,[79,207,208] partial oxidation of the surface,[57] and chemical doping.[209,210] The many applications of the C(0001) surface as well as its extensive modifications make it an attractive material surface for research.

Silver nanoparticles supported on carbon form the basis for one of the best electrocatalysts for CO_2 reduction to CO,[54] a very important reaction for clean energy. Silver nanoparticles on oxide supports are also commonly employed as selective oxidation catalysts, for example, in methanol partial oxidation and ethylene epoxidation.[211–215] It is thus unsurprising that many groups are beginning to investigate silver on carbon-based supports for electrocatalytic oxidation reactions as well.[216–218] In addition, due to unique optoelectronic properties, silver nanoparticles have been shown to have increased reactivity due to surface plasmon resonance and find applications in surface enhanced Raman spectroscopy (SERS).[219–222]

There have been many previous studies of the adsorption of gaseous Ag monomers and small clusters on graphite and graphene surfaces using both experimental methods[208,221–229] and theoretical methods[208,229–235] (typically density functional theory). While the exact results of these studies can vary tremendously with the methods used, there is some consensus that a weak interaction between Ag metal and the graphite support leads to the clustering of Ag monomers to form 3D particles.[208,223,224,230–234] Microscopy images show that these particles grow preferentially at the step edges when grown on graphite at room temperature and above.[223,224]

In this paper, we study the bonding energetics of Ag atoms in Ag nanoparticles grown by Ag vapor deposition on a single layer of graphene supported on Ni(111) using SCAC. The single-layer graphene films studied here were grown on clean Ni(111) using a method described in the literature.[78,80,236] This produces a single atomic layer of C(0001) with an in-plane lattice constant within 1.5% of that in bulk graphite(0001), in registry with the underlying Ni(111) surface, with two carbon atoms per Ni atom.[79,80,236,237] Due to the strong in-plane bonding and weak bonding between (0001) layers in graphite, the surface binding of Ag to this single layer of graphene(0001) is expected to approximate that for thicker graphite(0001) surfaces, although the interaction with the underlying Ni(111) is likely to have some effect. The particle density and growing Ag nanoparticle size are measured using low-energy ion scattering (LEIS). Using the coverage-dependent heats of adsorption of Ag vapor along with the particle size from LEIS, we determine the Ag chemical potential versus particle size and the Ag(solid)/C(0001) adhesion energy. The results presented here help to explain the morphology and chemical bonding of metal nanoparticles supported on carbon-based materials.

5.2 Experimental Methods

A description of the single crystal adsorption calorimetry apparatus and experimental procedures are presented in detail in Chapter 2. They are described briefly again here to allow the reader to understand this chapter without the need to reference back to Chapter 2.

A full description of the single-crystal adsorption calorimetry (SCAC) apparatus and detailed experimental procedures is presented elsewhere.[34] Briefly, the calorimetry experiments were done in an ultrahigh-vacuum (UHV) chamber with a base pressure $<2 \times 10^{-10}$ Torr. This chamber is also equipped with X-ray photoelectron spectroscopy (XPS), Auger electron spectroscopy (AES), He^+ low-energy ion scattering (LEIS), low-energy electron diffraction (LEED), quadrupole mass spectrometry (QMS), and two quartz crystal microbalances (QCMs). Surface spectroscopy measurements were obtained with a PHI 10−360 precision energy analyzer with a PHI 72− 250 position sensitive detector.

The Ag metal beam is generated by evaporating Ag pellets in an e-beam evaporator. The Ag vapor is collimated through a series of apertures to give an average beam diameter of 4.26 mm. The beam is then pulsed with a chopper with a pulse duration of 100 ms and a period of 2 s. The Ag flux is monitored with two QCMs: one on-axis QCM to measure the flux at the sample position (possible only just before and just after calorimetry) and another off-axis QCM to continuously monitor the flux during the experiment. The flux varies with time (typically dropping by ∼15% during a run), so the continuously measured off-axis flux was scaled at all times in a method described previously to provide the flux at all times at the sample position.[34]

The heat released is measured using a pyroelectric polyvinylidene fluoride (PVDF) ribbon in physical and thermal contact with the 1 μm thick Ni(111) single-crystal sample. The PVDF ribbon is calibrated for each experiment using a HeNe laser with known energy. The total heat detected with the PVDF ribbon is a combination of the heat of adsorption as well as the thermal radiation from the hot metal source. The signal from thermal radiation was measured by placing a barium fluoride (BaF_2) window in front of the sample to block Ag atoms from reaching the sample but allowing a known fraction of thermal radiation to transmit through the window

(>90%, measured with and without the window in the path). The resulting signal from thermal radiation was then subtracted from the total heat signal. The measured heat was further corrected to account for the difference in internal (translational) energy between the directed flux of gas-phase Ag atoms coming from the high-temperature electron beam evaporator (∼1380 K)[73] and a collection of the same gas atoms in a Boltzmann distribution at the surface temperature (300 or 100 K). The resulting heat is thereby equal to the negative of the standard enthalpy of Ag adsorption at the sample temperature.

The sticking probability of each pulse is measured simultaneously with the adsorption heats using a modified King and Well's method described previously.[34,238] The number of Ag atoms that stick to the sample surface in each pulse is then equal to the flux times the pulse duration and the sticking probability. The differential heat of adsorption per mole of adsorbed Ag as a function of the cumulative Ag coverage can then be calculated from the measured heats, fluxes, and sticking probabilities. The Ag coverages reported here are given in units of ML, with 1 ML defined as 1.87×10^{19} atoms/m^2 , which is the areal density of Ni atoms on the Ni(111) surface as well as exactly 1/2 the areal density of C atoms on the graphene surface, which grows in registry with the Ni(111) substrate.[79,237]

5.3 Results and Discussion

5.3.1 Graphene Growth and Characterization

Graphene films were grown on a clean 1 μm thick Ni(111) single crystal using a direct growth method described in the literature.[78,80,236] Before growth, the Ni(111) sample was cleaned by cycles of flashing the sample at 800 °C followed by 1.0 kV Ar^+ ion sputtering until the presence of the C 1s carbon peak could not be detected by XPS. The clean Ni(111) sample was then annealed in vacuum at 600−650 °C for 5 min before the sample was exposed to 10^{-6} Torr of ethylene for 30 min while the sample was held at 600−650 °C. After growth, the presence of graphene was confirmed by AES. Previous work has shown that the C−KVV AES line has a distinctive shape for graphitic and carbidic carbon, which allowed an easy determination of the surface phase.[78,239,240] In line with previous work, we found that samples grown at temperatures below 500 °C showed the presence of nickel carbide, while samples grown between 600 and 650 °C consistently showed the line-shape characteristic of graphene.[78] The quality of the graphene films was further confirmed by He^+ LEIS. For a complete graphene film, the nickel LEIS signal attenuates >95% (relative to clean Ni), while the nickel LEIS signal is still apparent for an incomplete film.

5.3.2 Ag Sticking Probability on Graphene/Ni(111)

The sticking probability of Ag atoms to graphene/Ni(111) was monitored during calorimetry experiments by measuring the transient QMS signal of Ag atoms during each deposited pulse. This signal was then normalized to a zero-sticking signal of Ag atoms pulsed onto a hot W flag where no permanent sticking occurs, as described by our group previously.[33] The fraction of atoms that sticks times the Ag vapor flux was then used to scale the absorbed heat per pulse and the accumulated Ag coverage during all experiments. The sticking probabilities versus coverage at 300 and 100 K are shown in Figure 5.1. The Ag coverages reported here are given in units of ML, with 1 ML defined as 1.87×10^{19} atoms/m^2 , which is the areal density of Ni atoms on the Ni(111) surface as well as exactly 1/2 the areal density of C atoms on the graphene surface, which grows in registry with the Ni(111) substrate.[79,237] At 300 K, the sticking probability starts low at 75% and increases slowly to a value of 86% by 4 ML. At 100 K, the sticking probability starts much higher at an initial value of 87% and gradually rises to a value slightly greater than 98% at the highest coverages measured. The decrease in sticking probabilities with increasing surface temperature is commonly reported for metal adsorption, where it has been attributed primarily to the increased desorption rate of diffusing metal adatoms as the temperature is raised.[46,241] Since the ratio of the desorption rate to diffusion rate is much greater at 300 K in comparison to 100 K, diffusing Ag adatoms are much more likely to desorb at this higher temperature before they find other Ag adatoms or Ag clusters, to which they can bond.

5.3.3 Ag Growth Morphology on Graphene/Ni(111)

The Ag growth morphology on graphene/Ni(111) at 300 and 100 K was determined using He^+ LEIS measurements. Gaseous Ag was deposited onto the graphene/Ni(111) substrate in discrete amounts, and the Ag LEIS signal was measured after each dose. In contrast to previous systems studied by our group with LEIS, the substrate's LEIS signal (for the element C in this present study) could not be measured due to near unity ion neutralization probability for He^+ ions scattering off of graphitic carbon species.[82–84] The integrated Ag LEIS signal was normalized to the signal from a thick Ag overlayer (>10 nm), which served as the Ag reference signal of complete coverage of the surface by Ag. This normalized Ag LEIS signal then gives the fraction of the surface covered and shadowed by Ag particles.

The resulting integrated Ag LEIS signal versus Ag coverage is shown in Figure 5.2 and is compared with two growth models. The layer-by-layer growth model (shown as a straight black dashed line) corresponds to the signal that would be observed if Ag grew in a layer-by-layer fashion. As can be seen in Figure 5.2, this model does not fit the data well. The solid lines correspond to a hemispherical cap growth model first described by Diebold et al., in which all particles are assumed to have the same hemispherical shape and same particle size at a given coverage and temperature.[72,242] Furthermore, the particles are assumed to have a constant number density at all coverages in agreement with classical nucleation theory, in which a saturation number density is reached after a very small initial nucleation stage on the order of a few percent of a ML.[7,120] This hemispherical cap model is applied only up to coverages at which <33% of the surface is covered by particles, because at higher coverages, the particles will begin to overlap and the model assumptions break down. As described previously,[72] the hemispherical cap model predicts the normalized Ag LEIS intensity increases with the particle density and coverage as expressed in the following equation

$$\frac{I(\theta)}{I(\theta=\infty)} = \pi f_{shadowing}\left(\frac{3\theta n_{ML} M_{Ag}}{2\pi N_a \rho_{Ag}}\right)^{2/3} n^{1/3} \tag{5.1}$$

where θ is the coverage, $[I(\theta)/I(\theta=\infty)]$ is the normalized Ag LEIS signal, n_{ML} is the monolayer definition (1.87×10^{19} atoms/m^2), M_{Ag} is the Ag molar mass, N_A is Avogadro's number, ρ_{Ag} is the bulk Ag density, and n is the Ag particle number density. The factor $f_{shadowing}$ is a shadowing factor that represents the additional interfacial area masked by the three-dimensional shape of the hemispherical particles at the incident and detection angles used.[72] For the analysis geometry used in these experiments (incident ions normal to the surface and detected ions measured at 45° from the surface normal), the shadowing factor is calculated to equal 1.207.[72] Since both θ and $[I(\theta)/I(\theta=\infty)]$ are measured, the only unknown variable in the above is the particle density n, which we determine by the best fit of (5.1) to the experimental data.

As shown in Figure 5.2, the best fits of this model to a series of multiple experiments at each temperature give particle densities of 4.4×10^{15} particles/m^2 at 300 K and 1.1×10^{16} particles/m^2 at 100 K. The particle density at 100 K is roughly 2.5 times larger than the particle density at 300 K. This is most likely due to the smaller diffusion constant of Ag adatoms across the surface at lower temperatures. Venable's theory of vapor-deposited crystal growth predicts that the saturation particle density varies as the cube root of adatom diffusion constant (k_{diff}) for the same flux.[120] Applying that model to this data, we find that $k_{diff}(300\ K)/k_{diff}(100\ K) \approx 2.5^3 \approx 16$, which implies an activation barrier for diffusion of $E_{diff} = R\ \ln(16)/\ [(1/100) - (1/300)] = 3.5$ kJ/mol. Density functional theory (DFT) calculations of the diffusion barrier for Ag/C(0001) from the literature report a diffusion barrier between 0.3 and 7.6 kJ/mol.[208,233,243] The value for E_{diff} reported here falls within this range.

Most experimental studies of evaporated films of Ag (either from Ag monomers or from small, mass-selected Ag cluster ions) on graphite(0001) or graphene surfaces found that the Ag agglomerates into 3D clusters at room temperature, as we find here.[208,221–223,229] One early STM study reports “flat” Ag clusters referred to as 2D clusters on graphite, but that study was performed at very low coverages (~0.001 ML),[228] much lower than here.

5.3.4 Differential Heat of Adsorption of Ag on Graphene/Ni(111)

The differential heats of adsorption as a function of coverage of Ag onto graphene/Ni(111) at 300 and 100 K are shown in Figure 5.3. Each point corresponds to a pulse of Ag vapor from the molecular beam (with ~0.012 ML per pulse) but averages several runs. The heats of adsorption here are corrected to account for the difference in internal energy between a flux of gas-phase Ag atoms coming from a high-temperature electron beam evaporator (~1380 K)[73] and a collection of the same gas atoms in a Boltzmann distribution at the surface temperature (300 or 100 K), as described in previous work.[33] In this way, the heat of adsorption equals the negative of the standard enthalpy of adsorption at each temperature. At 300 K, the heat of adsorption initially starts at 230 kJ/mol and rapidly increases to 270 kJ/mol within the first 0.1 ML of deposition. The heats of adsorption then slowly increase until reaching a plateau of 280 kJ/mol by 2 ML, which is within 1.8% of the reported enthalpy of sublimation of bulk Ag (ΔH_{sub} = 285 kJ/mol).[199]

Due to errors (~10%) known to be present in calibrating the calorimeter's absolute heat sensitivity factor for these graphene/Ni(111) surfaces, we adjusted this factor to ensure that the heat of adsorption and corresponding Ag chemical potential for the largest particle sizes measured (6−8 nm at 300 K and 3−5 nm at 100 K) agreed with the model described below for chemical potential versus particle size (taken from references [35] and [36]). This resulted in heats of adsorption at the highest coverages measured (3.5 to 4 ML) agreeing with the reported heat of sublimation of bulk Ag (ΔH_{sub} = 285 kJ/mol) within 1.8% at 300 K and within 0.5% at 100 K.

At 100 K, the heat of adsorption of Ag onto graphene/ Ni(111) is initially 223 kJ/mol and drops down to 207 kJ/mol by the second pulse of Ag gas. This initial decrease in the heat of adsorption, which was seen in every run at 100 K, might be due to the population of stronger-binding defect sites in the first gas pulse that get saturated by the second pulse. This effect might be washed out at 300 K by the more rapid growth in particle size at 300 K, where 2.5 times as many Ag atoms add to each cluster between the first and second pulses compared to 100 K (since there are 2.5 times fewer Ag clusters at 100 K). As shown below, the heat increases rapidly with particle size due to the formation of more Ag−Ag bonds to the newly arrived Ag atom when attaching to a larger Ag cluster. (For example, a Ag atom adding to a Ag_3 cluster can make three new Ag−Ag bonds at most, whereas it makes six Ag−Ag bonds (on average) when adding to Ag particles in the large-size limit.) After the initial decrease, the heat of adsorption at 100 K quickly rises to reach ~275 kJ/mol by 0.5 ML and further increases slowly until the enthalpy of sublimation for bulk Ag is reached by 2.5 ML. The slower increase in the heats of adsorption with Ag coverage at 100 than 300 K can again be explained by the fact that the particles are 2.5 times smaller at 100 K at any given coverage, so fewer Ag−Ag bonds are made when a new Ag atom is adsorbed at 100 K.

To better compare heats of adsorption with the same nanoparticle size between 300 and 100 K, we show the heats of adsorption of Ag onto graphene/Ni(111) as a function of the effective particle diameter in Figure 5.4. The average effective particle diameter at any coverage is calculated from the total Ag coverage (in atoms per unit area) divided by the Ag particle areal density, which equals the average particle size in atom number. By assuming all particles have the mass density of bulk Ag(solid), this also gives the particle volume, which for the assumed hemispherical shape also provides the effective diameter. Besides the very small-particle regime ($D_{eff} < 2$ nm), we observe a remarkable agreement in the heats as a function of particle size regardless of temperature. Except for this very small-size regime, the heat of adsorption at both temperatures gradually increases with effective particle diameter. This is caused by the higher number of Ag−Ag bonds that can be formed by addition of a gas-phase Ag atom to a larger particle. As the particles reach a bulk-like size (around 5 nm), the addition of another gas-phase Ag atom comes very close to the bulk enthalpy of sublimation.

The heats of adsorption in Figure 5.4 can be compared to DFT calculations of Ag monomers and clusters on graphite(0001) and graphene surfaces. Calculations of Ag monomer adsorption on C(0001) show a very weak interaction (between about 0 and 76 kJ/mol) between Ag and C(0001),[208,230,231,233–235] which could explain the very low sticking probability we observe, and is consistent with the low heats we observe for the smallest clusters (see below). One of these studies also included calculations of Ag monomer adsorption on a stepped graphite surface and showed a 15−30 kJ/mol preference for adsorption energy near the step-edge defect.[231] This is consistent with the 16 kJ/mol difference we measured between the first and second pulses of Ag deposition at 100 K, which we attributed to defect sites.

We can make a more direct comparison of our results with calculations that provide the energy change of gas-phase Ag to form larger Ag clusters supported on C(0001).[232–234] These calculations all show that as the particles grow in size, the adsorption energy rapidly grows in magnitude as the Ag cohesive energy starts to dominate the monomer adsorption energy. One such study reports an energy change of −159 to −164 kJ per mole of Ag atoms for 13 × Ag(gas) → Ag_{13}(adsorbed) for 3D Ag clusters on free-standing graphene.[234] Another study found an energy change of −224 to −229 kJ per mole of Ag atoms for n × Ag(gas) → Ag_n(adsorbed) with n = 7−9 for pseudoepitaxial growth of 2D Ag on graphene/SiC(0001) (up from only −35 and −111 kJ/mol at n = 1 and 2, respectively).[233] These can be compared with the measured heats of adsorption in the first pulses of our experiments where the first pulse at 300 K forms clusters of ∼26 atoms (on average) and an average heat of adsorption of 230 kJ/mol, and the first two pulses at 100 K form clusters of ∼9 and ∼30 atoms, respectively, with heats of adsorption of 223 and 207 kJ/mol, respectively. The differences between our experimental results and those calculations could be attributed to any of the following reasons: (1) the larger cohesive energy for the larger particles we studied, (2) stabilization of particles in our experiments by defect sites in the first pulse at 100 K, (3) stabilization of particles in our experiments due to long-range attractive interactions with the underlying Ni(111) substrate, or (4) intrinsic errors in their DFT calculations or our experiments. While the exact details of these differences are unknown, it is promising that there is only a relatively small difference between those calculations and our experimental results despite the complicated system studied and slightly different substrates.

A recent study reported the heat of Ag vapor adsorption versus coverage on graphite measured using equilibrium adsorption isosteres at very high temperatures,[244] but that approach seems unreasonable given the strong thermodynamic driving force for Ag on graphene to agglomerate into large particles as shown in Figure 5.4 and Figure 5.5. Indeed, the Ag particles in that study were found to have diameters of a few hundred nanometers, and the sample had a lot of alumina particulate impurity.

5.3.5 Chemical Potential and Adhesion Energy of Ag Particles on Graphene/Ni(111)

If we neglect entropic contributions to the free energy (which are much smaller than enthalpic effects for supported metal nanoparticles), we can calculate the chemical potential of Ag atoms in supported metal nanoparticles. The chemical potential of metal atoms in supported nanoparticles relative to the bulk metal (set as a reference with zero chemical potential) is equal to the metal bulk heat of sublimation minus the differential heat of adsorption.[38] The resulting chemical potential of Ag nanoparticles supported on graphene/Ni(111) as a function of the effective diameter is shown in Figure 5.5.

As seen in Figure 5.5, the Ag chemical potential rapidly decreases as the particle size increases, as has been shown for many metals supported on single-crystal oxides.[35] Previous work from our group has shown that the chemical potential of late transition metals supported on oxides as a function of diameter (*D*) is very well-approximated by[35]

$$\mu(D) = \left(3\gamma_{v/m} - E_{adh}\right)(1 + D_0/D)(2V_m/D) \tag{5.2}$$

where $\gamma_{v/m}$ is the surface free energy of the bulk metal (1.22 J/m^2 for Ag),[245] E_{adh} is the adhesion energy of the metal/support interface (here, the adhesion energy between bulk Ag and graphene/Ni(111)), V_m is the molar volume of the bulk metal (10.3 cm^3/mol for Ag), and (1 + D_0/D), with D_0 = 1.5 nm, is an empirical factor that has been shown to account for the increase in $\gamma_{v/m}$ and E_{adh} (relative to their bulk values) as the supported particles decrease in size. [35] If we keep D_0 = 1.5 nm as the empirical factor here, the only unknown remaining in (5.2) is E_{adh}.

As discussed in previous work,[36,246] the adhesion energy can be extracted from our calorimetric heat measurements in two main ways. The first method (described in detail in previous work from our group)[7,30] is to use a conceptual three-step thermodynamic cycle that connects the heat of adsorption with the adhesion energy of a supported hemisphere (for the largest size measured). In the first step, the gaseous metal atoms form a free-standing hemispherical particle in vacuum. The energy change of this step is the negative sublimation enthalpy times the number of metal atoms ($-n\Delta H_{sub}$) plus the energy cost to form the hemispherical metal surface in vacuum ($+A[(1 + f)\gamma_{v/M}]$). Here, A is the interfacial area between the metal particle and the support, and $(1 + f)$ is a factor that accounts for the additional top surface area of the particle ($f = 2$ for hemispherical caps). In the second step, the metal hemisphere in vacuum is attached to the support surface with a downhill energy change of the interfacial area times the adhesion energy ($-AE_{adh}$). The overall energy change of these two steps is equal to the formation energy of the supported metal particles (from gas atoms), which can alternatively be expressed as the negative differential enthalpy of adsorption (or negative differential heat of adsorption measured calorimetrically), integrated from zero coverage up to the coverage that gives the largest effective particle diameter measured ($\sum \Delta H_{ads}$). Combining all steps of this cycle, the following equation results[7,30]

$$\sum_{n} \Delta H_{ads} = -n\Delta H_{sub} + A[(1+f)\gamma_{v/m} - E_{adh}] \tag{5.3}$$

This equation assumes that the particles' diameter (D) has reached the large-size limit for both $\gamma_{v/m}$ and E_{adh}, which is not the case here. We extend that integral here only up to $D = 8$ nm at 300 K and $D = 5$ nm at 100 K, due to possible particle overlap at larger particle sizes. The empirical correction factor of $(1 + D_0/D)$ was used in (5.2) to correct $\gamma_{v/m}$ and E_{adh} for small particles (relative to their bulk values). When applied to the largest particles considered here, it shows that $\gamma_{v/m}$ and E_{adh} are still 19−30% larger than the true large-size limit and thus require the use of this correction factor to accurately calculate the adhesion energy. To account for the size dependence of surface energy and adhesion energies, we therefore introduce the same empirical correction factor of $(1 + D_0/D)$ used in (5.2) to slightly correct (5.3) as well, as was done previously.[36,246] The resulting corrected equation is

$$\sum_n \Delta H_{ads} = -n\Delta H_{sub} + A[(1+f)\gamma_{v/m} - E_{adh}]\left(1+\frac{D_0}{D}\right) \tag{5.4}$$

where D is the largest effective diameter reached in the integrated heat term. The only parameter in (5.4) not provided in the literature or measured in our experiments is then the adhesion energy. Substituting the known values into (5.4) and solving, we calculate an adhesion energy of 1.72 J/m^2 using the heat data from 300 K or 1.67 J/m^2 using the heat data from 100 K, with an average of 1.70 J/m^2 . The chemical potential fit of (5.2) using E_{adh} = 1.70 J/m^2 overlaid on the measured chemical potential is shown in Figure 5.5 as a dotted black curve slightly above the solid black curve.

As mentioned above, the only unknown variable remaining in (5.2) is the adhesion energy. It follows that an alternative method to extract the adhesion energy from our calorimetric heat measurements is to fit (5.2) to the measured Ag chemical potential. Since the lowest diameter chemical potential at 100 K is significantly stabilized by defects, we omit that point in the fitting process. Using all 300 and 100 K chemical potential data except that lowest diameter point at 100 K, we find the best fit to (5.2) is with an adhesion energy of 1.90 J/m^2 . The fit of (5.2) with E_{adh} = 1.90 J/m^2 is shown in Figure 5.5 as a dotted black curve slightly below the solid black curve. Without a clear reason to expect that one of these methods is more accurate than the other, we assume the adhesion energy of Ag to graphene/Ni(111) is given by the average of these two values with an uncertainty of ~0.1 J/m^2 . Thus, the adhesion energy of Ag particles supported on graphene/Ni(111) measured in these experiments is E_{adh} = 1.80 ± 0.10 J/m^2.

5.3.6 Comparison to Ag on Oxide Support Materials

This adhesion energy for Ag to graphene of ~1.8 J/m^2 can be compared to those reported for Ag to MgO(100), CeO_2(111), and TiO_2(100) of 0.30, 2.3, and 2.44 J/m^2, respectively,[99,200,246] showing that graphene on Ni binds Ag nanoparticles within the range measured on these oxides. It binds Ag almost as strongly as the most strongly bonding of these oxide supports (CeO_2(111)) and much more strongly than the weakest (MgO(100)). As seen from (5.2), this means that for a given Ag nanoparticle size (below 6 nm) on these different supports, the Ag chemical potential will be considerably lower for Ag on this model carbon support compared to Ag on MgO(100) and slightly higher compared to Ag on CeO_2(111). This has two important implications with respect to catalyst performance. Given the quantitative kinetic relationship that shows that sintering rates for a given particle size increase with increasing chemical potential,[13,35,99,206,247] this means that such a carbon support will be almost as effective as CeO_2 at reducing sintering rates and enhancing long-term catalyst sinter resistance to prevent deactivation, compared to weak-binding supports like MgO. Given the qualitative correlations, which show that metal nanoparticles that possess a lower metal chemical potential bind small adsorbed catalytic reaction intermediates (like O, OH, CH_3, and CO) more weakly,[35,36,38,102] for a given Ag nanoparticle size, the Ag nanoparticles will bind such small adsorbates more weakly when supported on such a carbon support than when supported on a weak-binding support like MgO but slightly more strongly than when the support is CeO_2.

Recent theoretical estimates of adhesion energies for other oxides based on DFT[248,249] may be useful in comparing these experimental adhesion energies of Ag to graphene and a few oxides (and their implications with respect to Ag chemical potential) to those from a broader range of oxides. The sticking probability for Ag on graphene/Ni(111) (Figure 5.1) is lower than was measured for Ag on any of these oxide surfaces.[73,99,200,246] The value of 0.75 at 300 K is much lower than the smallest of those, 0.943 for Ag on MgO(100),[200] meaning that a Ag gas atom that strikes graphene is 4.4 times more likely to desorb again into the gas phase than when it hits MgO(100). Lower sticking probabilities are thought to correlate with weaker bonding of the metal monomer to the surface.[154] This weaker bonding also correlates with a lower saturation number density of metal clusters, due to the kinetics of nucleation.[154] Indeed, this density seen here at 300 K ($4.4 \times 10^{15}/m^2$, Figure 5.2) is ~6- fold lower than for Ag on MgO(100).[154] It is clear that Ag monomers bond significantly more weakly to graphene support than to any of the oxide supports that have been studied. This also has an important implication with respect to catalyst performance, specifically sinter resistance. The weaker the monomer bonds to the support surface, the slower is the rate of metal nanoparticle sintering (at the same temperature) for nanoparticles on different supports with the same metal chemical potential and number density.[13,99,247]

5.4 Conclusions

The He^+ LEIS growth mode experiments showed that Ag supported on graphene/Ni(111) grows with a particle number density of 4.4×10^{15} particles/m^2 at 300 K and 1.1×10^{16} particles/m^2 at 100 K. This difference is attributed to the higher mobility of Ag adatoms at 300 K with an estimated activation barrier for diffusion of ~3.5 kJ/mol. QMS measurements showed an initial sticking probability of 75% at 300 K and 85% at 100 K. This is consistent with expectation, since the ratio of the desorption rate to the diffusion rate is much lower at 100 K than 300 K (since the activation energy for desorption is larger than for diffusion). The heat of

Ag adsorption at 300 K is 230 kJ/mol initially but quickly rises to 270 kJ/mol in the first 0.1 ML of coverage and further increases to within 5 kJ/mol of the bulk Ag sublimation enthalpy (285 kJ/mol) by 2 ML. The increase in heat with coverage is due to the larger Ag nanoparticles at higher coverage, which bind Ag atoms more strongly. At 100 K, the heat of adsorption is 223 kJ/mol in the first metal pulse but drops to 207 kJ/mol in the next pulse. The higher heats in the first Ag pulse at 100 K are attributed to the very small Ag clusters binding initially to stronger-binding defect sites on the graphene/Ni(111) surface, which saturate before the second pulse. Thereafter, the heat rises with coverage to nearly the bulk Ag sublimation enthalpy by 2 ML, again due to increasing Ag particle size as at 100 K. The Ag chemical potential determined from these heats of adsorption decreases as a function of nanoparticle size, shows a remarkable agreement between the two temperatures studied, and is well-approximated by (5.2). This is the same relationship developed by our group that describes the chemical potential of metals supported on oxide supports. The adhesion energy of Ag to graphene/Ni(111) determined from these heat measurements is 1.70 J/m^2 when calculated from the integral heat of adsorption at high coverage and is 1.90 J/m^2 when calculated by fitting the measured chemical potential to (5.2), giving an average of 1.80 ± 0.10 J/m^2 . This adhesion energy, when compared to that for Ag on various oxide supports and combined with (5.2) for then comparing the Ag chemical potential for nanoparticles of the same size on different supports, has important implications with respect to the performance of Ag catalysts on such carbon supports including low chemical potential and high sinter resistance.

5.5 Figures

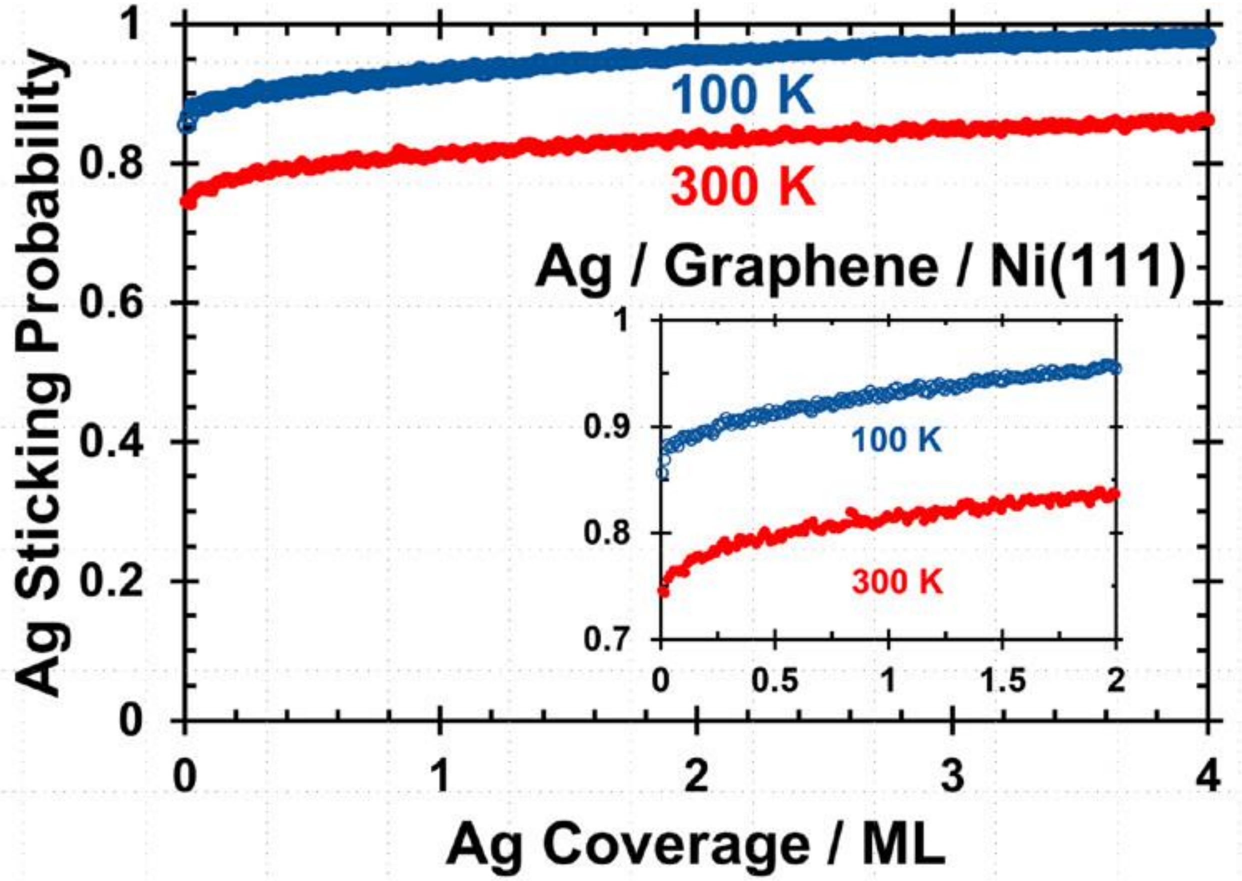

Figure 5.1. Sticking probability of Ag gas atoms onto graphene/Ni(111) as a function of Ag coverage at 300 K (red, filled points) and 100 K (blue, open points). The absolute coverage of 1 ML here is defined as 1.87×10^{19} atoms/m^2.

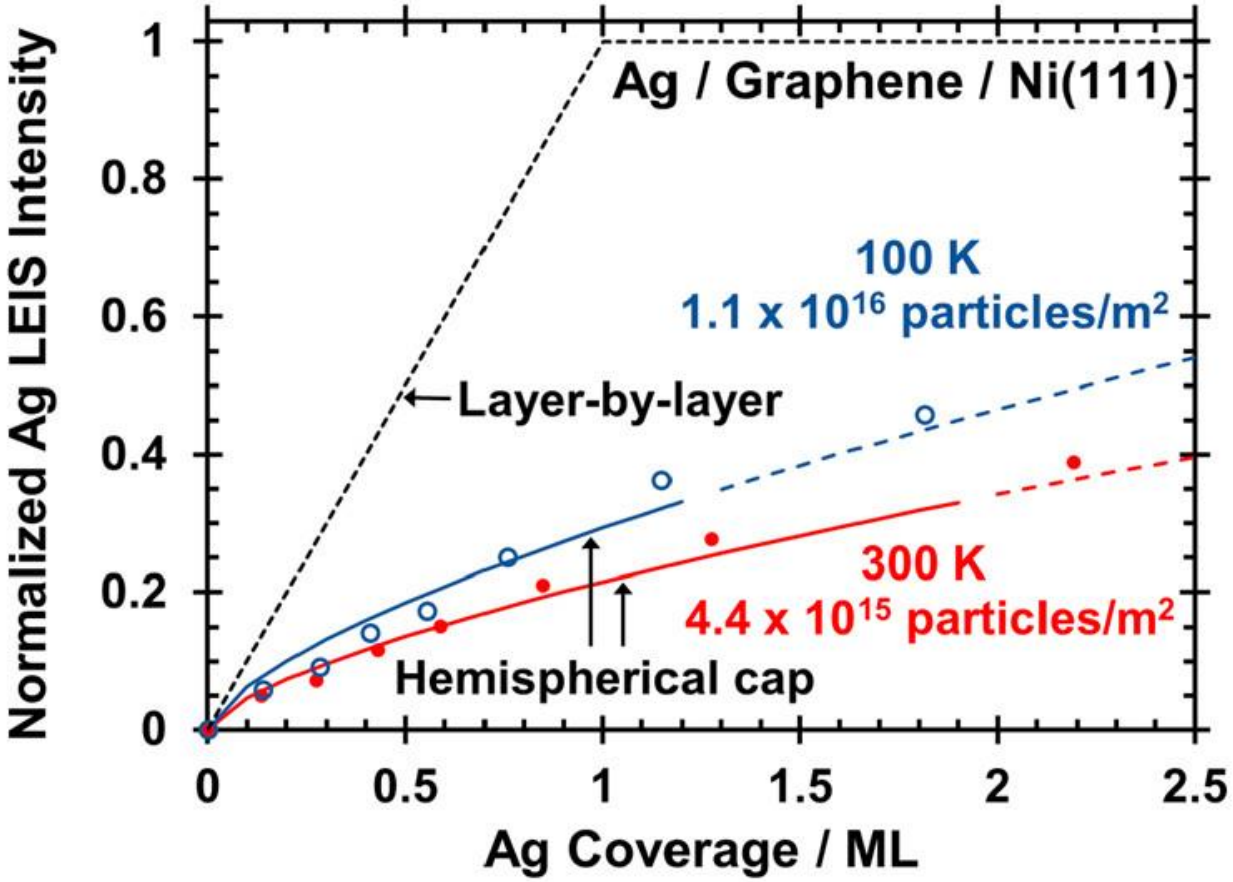

Figure 5.2. Integrated Ag LEIS signal normalized to a thick multilayer Ag film as a function of the Ag coverage after deposition onto graphene/Ni(111) at 300 K (red, filled points) and 100 K (blue, open points). The black dashed line corresponds to the LEIS signal that would be observed for a layer-by-layer growth mode for Ag atoms packing with the same areal density as Ni(111). The solid lines correspond to the Ag growing as hemispherical particles with a particle density of 4.4×10^{15} particles/m^2 at 300 K (red) and 1.1×10^{16} particles/m^2 at 100 K (blue). The dotted lines above the Ag coverages that give a normalized Ag LEIS signal of 0.33 are only a guide to the eye, since the model should not be applied at those higher coverages.

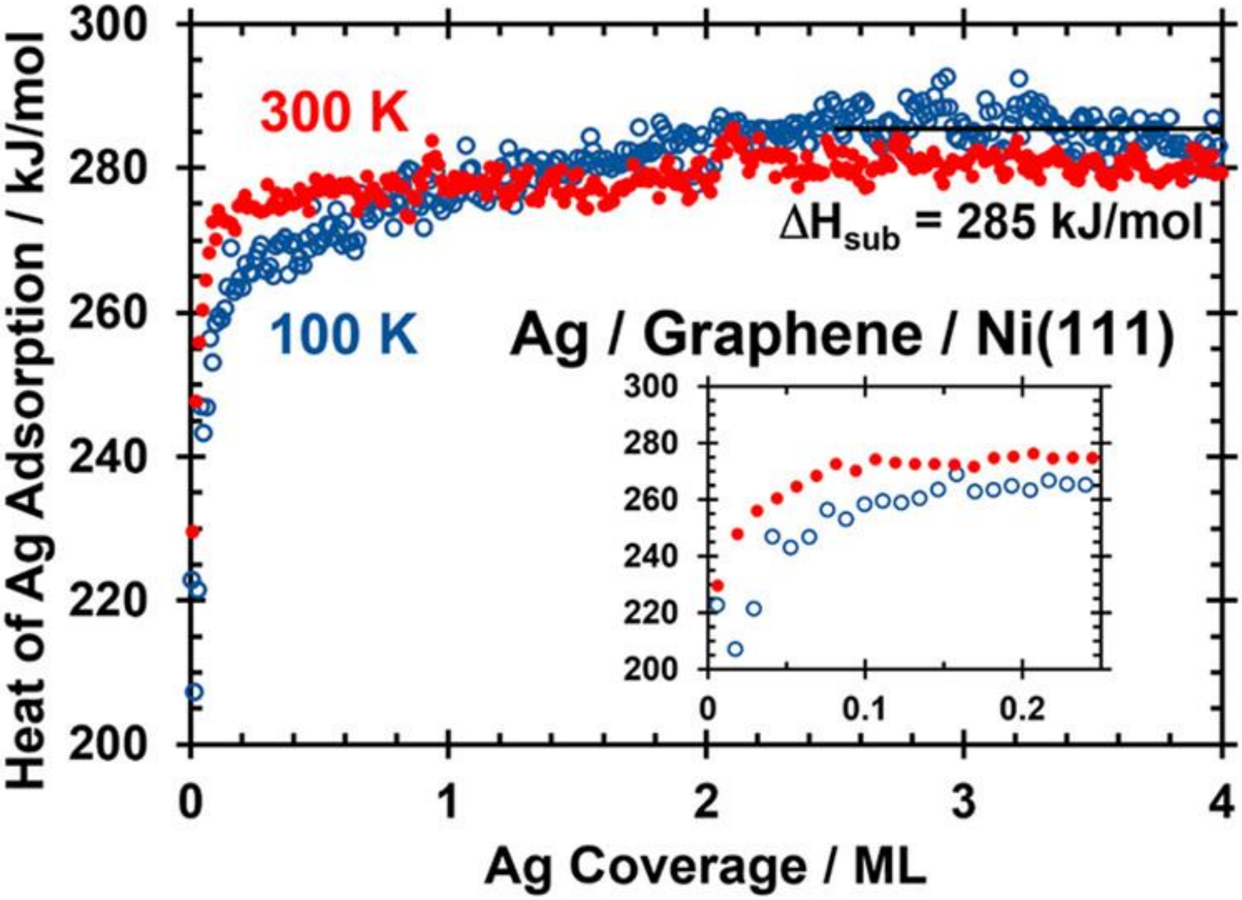

Figure 5.3. Differential heat of adsorption of Ag atoms onto graphene/Ni(111) as a function of Ag coverage at 300 K (red, filled points) and 100 K (blue, open points). The inset shows the low-coverage regime (until 0.25 ML) on an expanded scale.

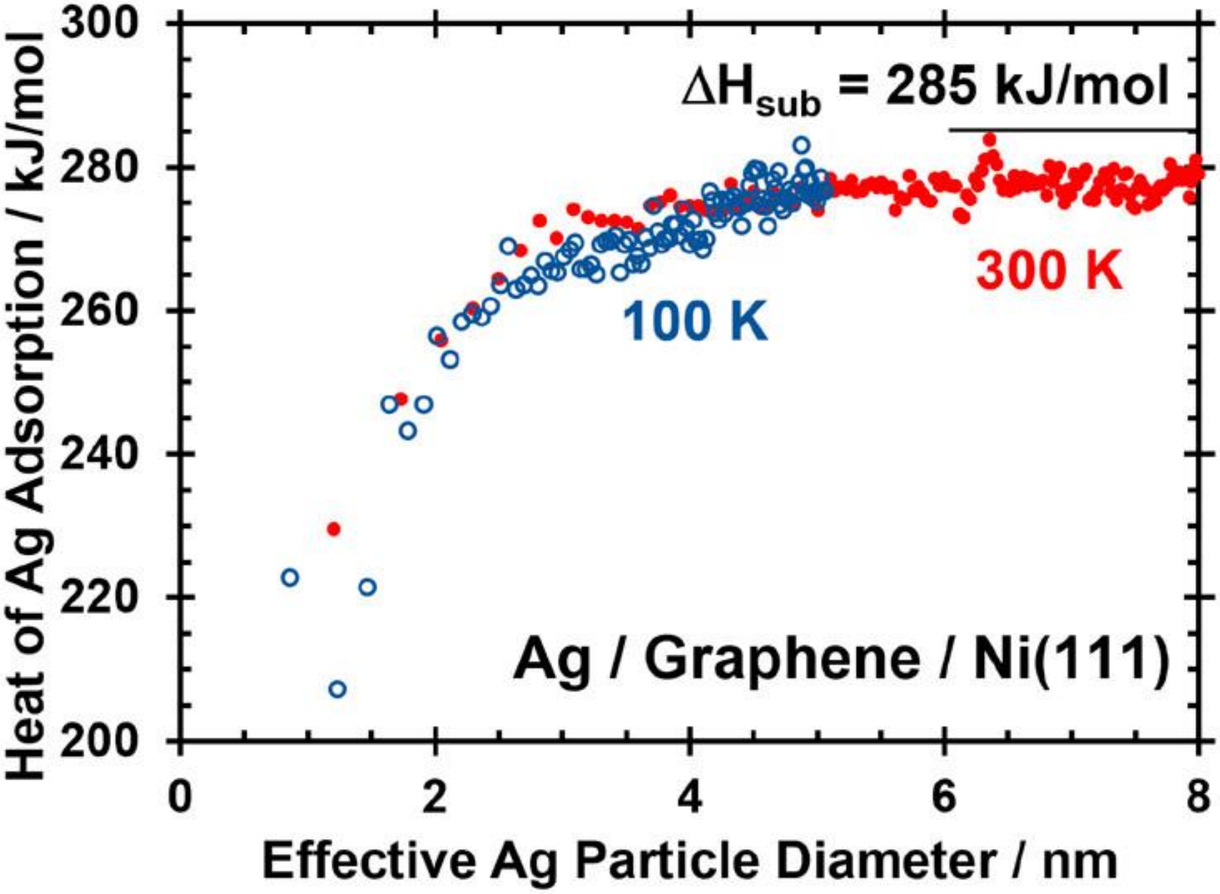

Figure 5.4. Differential heat of Ag adsorption on graphene/Ni(111) at 300 K (red, filled points) and 100 K (blue, open points) as a function of the effective Ag particle diameter, to which Ag atoms add during particle growth.

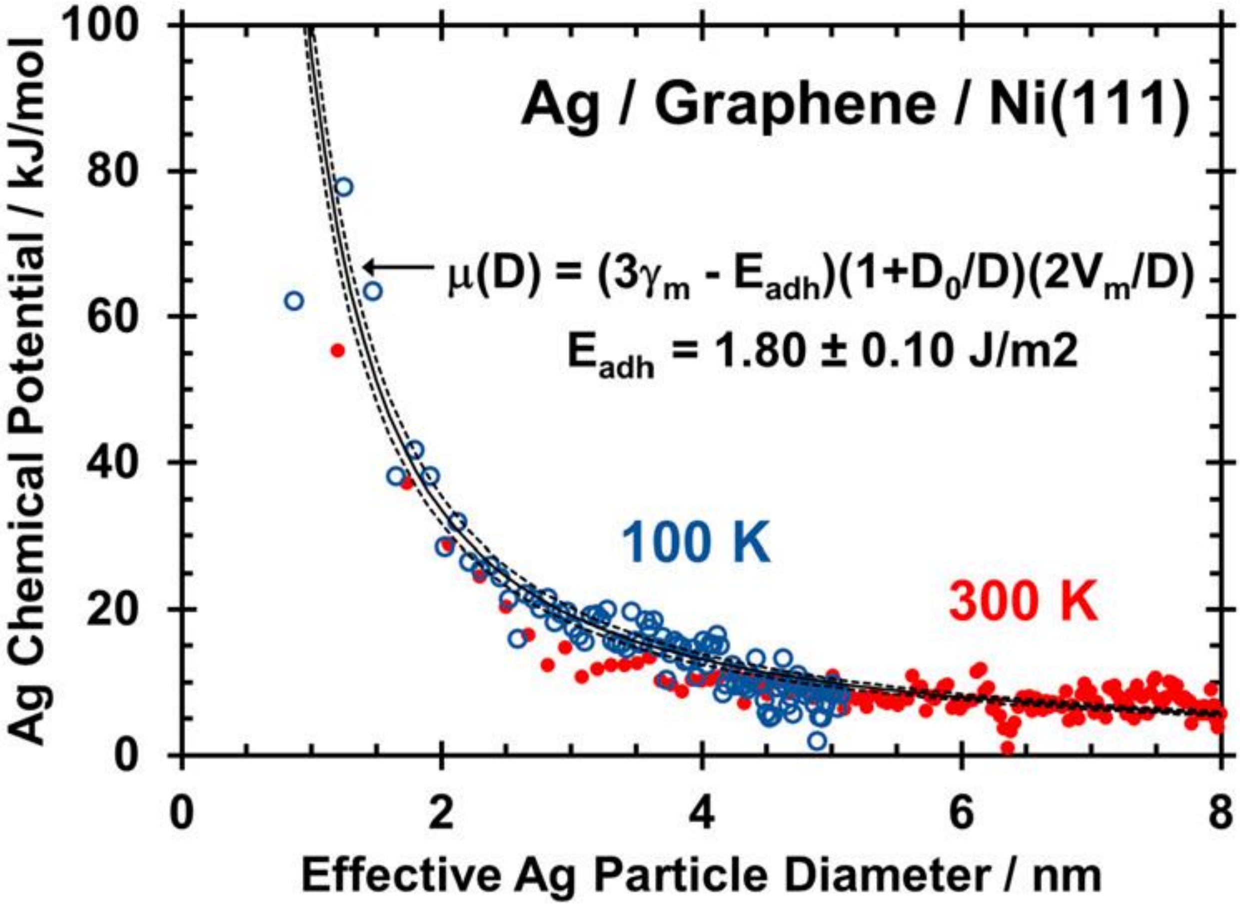

Figure 5.5. Chemical potential of Ag atoms in nanoparticles on graphene/Ni(111) vs the effective particle diameter at 300 K (red, filled points) and 100 K (blue, open points). The black solid line shows the hemispherical cap approximation ((5.2)) with E_{adh} = 1.80 J/m^2. The dotted black curve slightly above the solid black curve shows the same model ((5.2)) but with the value for E_{adh} determined by the integral-heat method (E_{adh} = 1.70 J/m^2). The dotted black curve slightly below the solid black curve shows the best fit of that same hemispherical cap model ((5.2)) to the measured chemical potential versus size (combining both the 100 and 300 K data but omitting the first point at 100 K, which is attributed to defect sites). This fitting method gave the best fit with the adjustable parameter E_{adh} = 1.90 J/m^2.

Chapter 6. Size-Dependent Energy of Ni Nanoparticles on Graphene Films on Ni(111) and Adhesion Energetics by Adsorption Calorimetry

This chapter contains unpublished results

Chapter Abstract

The use of carbon supports for late transition metal nanoparticle catalysts has grown substantially in recent years due to efforts to develop electrocatalysts for clean energy applications and catalysts for new aqueous-phase biomass-related conversions, and due to the evolution of new carbon materials with unique properties (e.g., graphene, carbon nanotubes, etc.). However, much less is known about the bonding energetics of catalytic metal nanoparticles on carbon supports in comparison with oxide supports, which are more common for thermal catalysis. Here we report the growth morphology and heats of adsorption of Ni vapor deposited onto graphene/Ni(111) at 300 K and 100 K determined from He^+ low-energy ion scattering (LEIS) and single crystal adsorption calorimetry (SCAC). These results suggest that Ni grows as flat-topped FCC islands with a thickness of ~1.5 nm when deposited at 300 K. At 100 K, Ni grows as smaller nanoparticles, well modeled as hemispherical HCP nanoparticles with a density of 2.23×10^{16} particles/m^2. The heat of Ni adsorption at 300 K is initially 336 kJ/mol and rapidly increases with coverage before reaching the bulk heat of Ni sublimation (430 kJ/mol) by 2 ML. The heat of Ni adsorption at 100 K begins at 230 kJ/mol and reaches the bulk heat of Ni sublimation by 3.5 ML. The Ni chemical potential as a function of average particle diameter in the 0.5 to 4 nm range at 100 K was determined from the LEIS and SCAC measurements. By fitting the measured chemical potential as a function of diameter, we determined an adhesion energy of 3.60 J/m^2 for large Ni particles on graphene/Ni(111). This adhesion energy is in good agreement with STM and DFT investigations of Ni/graphene/Ni(111).

6.1 Introduction

Late transition metal nanoparticles anchored to high-surface-area support materials are widely used as heterogeneous catalysts and electrocatalysts for energy, environmental, and chemical applications. The adsorption energies of small molecules and reaction intermediates onto the metal nanoparticles greatly affect the activity and selectivity of these catalysts. It is well-known that these adsorption energies and the catalyst thermal stability are strongly influenced by the size of the metal nanoparticles as well as the support material to which the nanoparticles bind.[7,9,35,203,205,250,251] Thus, a fundamental understanding of these nanoparticle size and support effects is important to designing improved catalysts.

Previous work by our group has shown that the chemical potential of metal atoms in supported nanoparticles contains important information about both these particle size and support effects in catalysis.[35,36,38] That work demonstrated that the metal chemical potential can be modelled as a function of the nanoparticle size and the adhesion energy of the metal to the support material.[35,36] A higher chemical potential leads to stronger adsorption of small molecules and intermediates as well as a larger driving force for catalyst deactivation via sintering.[35,37,38]

Carbon supports are important and widely used for heterogeneous catalysts, electrocatalysts, and photocatalysts due to carbon's resistance to chemical degradation, high-temperature stability, simple fabrication methods, low cost, and high electrical conductivity.[252–255] While there is a wide variety of carbon-based support materials (e.g. activated carbon, carbon black, graphite), many of these materials share the same graphitic building block.[254] The interesting chemical properties and applications of graphitic carbon in heterogeneous catalysis make it an appealing template for research. Recently, our group studied the energetics of Ag atoms and nanoparticles on graphene supported on Ni(111).[256] The Ag monomer was found to bind more weakly to graphene than it does to the surfaces of metal oxide supports. It was also found that Ag nanoparticles have a lower adhesion energy (in the large-size limit) to graphene/Ni(111) than onto reducible metal oxides such as $CeO_2(111)$ and $TiO_2(100)$, but higher adhesion energy than on irreducible metal oxides such as MgO(100). The bonding of Ag to the graphene support is somewhat unique in combining weak monomer bonding with moderately strong nanoparticle adhesion, which has advantages as a catalyst support.[256] This motivates the investigation of other later transition metals on graphene.

Nickel based heterogeneous catalysts are incredibly important for a wide variety of chemical reactions.[39,40,257–260] It is also well-known that the selectivity of these Ni catalysts is strongly affected by size and support material.[46,47,261,262] For example, in CO_2 hydrogenation on Ni catalysts, small molecule such as CO and CH_4 dominate on small nanoparticles, while carbon-carbon chain formation require larger particles with available neighboring sites for C-C coupling.[261,262] For this same reaction, different metal oxide supports vary the hydrogenation products via binding different intermediates.[261,262]

Nickel nanoparticles supported on graphitic materials are used as an alternative to expensive platinum-based electrocatalysts for oxidation reactions.[263–266] It has been shown that the nature of the interaction of the Ni nanoparticles with the carbon support can have a large influence on the reactivity of these catalysts.[56,265,266] In addition, it is well-known that the particle size can have a major effect on the catalyst kinetics for Pt-group metals.[261,267–271]

There are many excellent theoretical (mostly DFT) calculations of the bonding strength between Ni and graphitic materials[78,208,272–275] and experimental measurements of the particle morphology of Ni on graphitic supports.[78,276–278] While the exact details of these studies can vary tremendously, there is some consensus that Ni forms strong bonds with C(0001) and clustering of Ni monomers leads to the formation of 3D Ni particles on graphite and graphene.[78,272–277] Despite all the previous work done investigating the surface science of Ni on C(0001), to our knowledge there is only one experimental measurement of the bonding strength between Ni and a graphitic support, whereby an adhesion energy of 3.5 J/m^2 at the Ni/graphene interface was estimated from the shape of graphene-supported Ni nanoparticles.[78]

In this paper, we report the bonding energetics of Ni atoms in Ni nanoparticles grown by Ni vapor deposition onto a graphene-covered Ni(111) support using single crystal adsorption calorimetry (SCAC). These measurements determined the heat of adsorption of Ni vapor atoms as they adsorb onto the graphene substrate and bond to previous formed Ni nanoparticles of controlled size. The growth morphology of this vapor deposited Ni was measured using low-energy ion scattering (LEIS). From the coverage dependent heats of adsorption and particle size from LEIS, we determined the chemical potential as a function of the average Ni particle diameter and the adhesion energy of Ni to graphene/Ni(111). The results presented here indicate the formation of an HCP phase for very small Ni nanoparticles and provide important details of the chemical bonding energetics of Ni to carbon-based support materials.

6.2 Experimental Methods

A full description of the single-crystal adsorption calorimetry (SCAC) apparatus and detailed experimental procedures is presented elsewhere.[34] Briefly, the calorimetry experiments were done in an ultrahigh-vacuum (UHV) chamber with a base pressure <2 × 10^{-10} Torr. This chamber is also equipped with X-ray photoelectron spectroscopy (XPS), Auger electron spectroscopy (AES), He$^+$ low-energy ion scattering (LEIS), low-energy electron diffraction (LEED), quadrupole mass spectrometry (QMS), and two quartz crystal microbalances (QCMs).

Surface spectroscopy measurements were obtained with a PHI 10−360 precision energy analyzer with a PHI 72−250 position sensitive detector.

The Ni metal beam is generated by evaporating Ni pellets in an e-beam evaporator. The Ni vapor is collimated through a series of apertures to give an average beam diameter of 4.26 mm. The beam is then pulsed with a chopper with a pulse duration of 100 ms and a period of 2 s. The Ni flux is monitored with two QCMs: one on-axis QCM to measure the flux at the sample position (possible only just before and just after calorimetry) and another off-axis QCM to continuously monitor the flux during the experiment. The flux varies with time (typically dropping by ∼10% during a run), so the continuously measured off-axis flux was scaled at all times in a method described previously to provide the flux at all times at the sample position.[34]

The heat released is measured using a pyroelectric polyvinylidene fluoride (PVDF) ribbon in thermal and mechanical contact with the 1 μm thick Ni(111) single-crystal sample. The PVDF ribbon is calibrated for each experiment using a HeNe laser with known energy. The total heat detected with the PVDF ribbon is a combination of the heat of adsorption as well as the thermal radiation from the hot metal source. The signal from thermal radiation was measured by placing a barium fluoride (BaF_2) window in front of the sample to block Ni atoms from reaching the sample but allowing a known fraction of thermal radiation to transmit through the window (>90%, measured with and without the window in the path). The resulting signal from thermal radiation was then subtracted from the total heat signal. The measured heat was further corrected to account for the difference in internal (translational) energy between the directed flux of gas-phase Ni atoms coming from the high-temperature electron beam evaporator (∼2000 K)[47] and a collection of the same gas atoms in a Boltzmann distribution at the surface temperature (300 or

100 K).[33] The resulting heat is thereby equal to the negative of the standard enthalpy of Ni adsorption at the sample temperature.

The sticking probability of each pulse is measured simultaneously with the adsorption heats using a modified King and Well's method described previously.[34,238] The number of Ni atoms that stick to the sample surface in each pulse is then equal to the flux times the pulse duration and the sticking probability. The differential heat of adsorption per mole of adsorbed Ni as a function of the cumulative Ni coverage can then be calculated from the measured heats, fluxes, and sticking probabilities. The Ni coverages reported here are given in units of monolayers (ML), with 1 ML defined as 1.87×10^{19} atoms/m^2, which is the areal density of Ni atoms on the Ni(111) surface as well as exactly ½ the areal density of C atoms on the graphene surface, which grows in registry with the Ni(111) substrate.[79,237]

6.3 Results

6.3.1 Graphene Growth and Characterization

Graphene films were grown on a clean 1 μm thick Ni(111) single crystal sample using a direct growth method from ethene gas previously described in the literature.[78,80,236,256] Before growth, the Ni(111) sample was cleaned by cycles of flashing the sample at 800 ^{o}C followed by 1.0 kV Ar$^+$ ion sputtering until the presence of the C 1s carbon peak could no longer be detected by XPS. The clean Ni(111) sample was then annealed in vacuum at 600-650 ^{o}C for 5 min before the sample was exposed to 10^{-6} Torr of ethylene for 30 min while the sample was continually held at 600-650 ^{o}C. After growth the presence of graphene was confirmed by AES. Previous work has shown that the C-KVV AES line has distinctive shapes for graphitic or carbidic carbon which provided an easy method to determine the surface carbon phase.[78,239,240] In line with previous work, we found that samples grown at temperatures below 500 ^{o}C showed the presence of nickel carbide while samples grown between 600 and 650 °C consistently showed the line-shape characteristic of graphene.[78] The quality of all graphene films was further confirmed with He^+ LEIS in this study, which was quantified by the ratio of the nickel LEIS signal from the sample after graphene growth to that from the clean Ni(111). This ratio showed that the graphene films covered >95% of the Ni(111) surface for all samples investigated here.

6.3.2 Ni Sticking Probability on Graphene/Ni(111)

The sticking probability of Ni gas atoms to graphene/Ni(111) was monitored during calorimetry experiments by measuring the transient QMS signal for Ni atoms during each deposited pulse of the atomic beam. This signal was then normalized to a zero-sticking signal for Ni atoms, measured by pulsing the Ni atomic beam onto a hot W foil, where no permanent sticking occurs, as described previously by our group.[33] The fraction of atoms that stick times the Ni vapor flux and pulse duration was then used to determine the number of Ni atoms per unit area that adsorbed in each pulse. This was used to scale the adsorbed heat per pulse (to get the heat per mole adsorbed) and to calculate the accumulated Ni coverage for all calorimetry and growth mode experiments.

The sticking probability of Ni on graphene/Ni(111) as a function of Ni coverage at 300 and 100 K is shown in Figure 6.1. The Ni coverages reported here are given in units of ML, with 1 ML defined as 1.87×10^{19} atoms/m^2, which is exactly ½ the areal density of C atoms on the graphene surface, which grows in registry with the Ni(111) substrate, with 2 C atoms per surface Ni atom.[80,236,237] The results in Figure 6.1 show that the sticking probability at 300 K starts at 94% and increases slowly with Ni coverage, rising to a value of 97% by 4 ML. At 100 K, the sticking probability starts higher at 96% and gradually rises until reaching slightly higher than 99% by 4 ML.

The higher sticking probability seen here at lower sample temperatures is commonly reported for metal adsorption, where it has been attributed primarily to the decreased desorption rate of diffusing metal adatoms as the temperature is decreased.[46,241] Since the ratio of the desorption rate to the diffusion rate of Ni is much smaller at 100 K when compared with 300 K, the diffusing Ni adatoms are more likely to desorb at the higher temperature before they find other Ni adatoms of Ni clusters to which they can bind.

The sticking probabilities reported here for Ni atoms deposited onto graphene/Ni(111) are up to 20% larger than those previously reported for Ag deposition on the same surface.[256] This can be attributed to a stronger binding of Ni monomers onto the graphene substrate compared with Ag monomers. This hypothesis is corroborated by previously reported DFT calculations of the adsorption energy of Ni and Ag monomers onto a graphene support, which consistently show a much higher adsorption energy for Ni monomers when compared with Ag monomers.[243,279,280] The sticking probabilities measured here for Ni atoms on graphene/Ni(111) are also larger than those measured previously by our group for Ni atoms on MgO(100) at the same temperatures.[46] This also implies a stronger binding of Ni monomers to graphene than to MgO(100).

6.3.3 Ni Growth Morphology on Graphene/Ni(111)

The growth morphology of Ni on graphene/Ni(111) at 300 and 100 K was determined using He^+ LEIS measurements. Ni was vapor deposited onto the graphene/Ni(111) substrate in discrete amounts and the Ni LEIS signal was measured after each dose. The substrate's LEIS signal (graphitic carbon) could not be measured due to a near unity ion neutralization probability for He^+ ions scattered from graphitic carbon, as was the case for Ag deposition on graphene/Ni(111).[82–84,256] The integrated Ni LEIS signal was normalized to the signal from a thick Ni layer (>10 nm) which served as the Ni reference signal for complete coverage of the graphene surface by Ni. This normalized Ni LEIS signal then gives the fraction of the surface covered (and shadowed) by Ni particles.

The normalized Ni LEIS signals versus Ni coverage are shown in Figure 6.2a, along with fits of these data to different growth models for the Ni particle growth morphologies. Data shown are the averages from several repeated LEIS signal versus coverage measurements. The growth models analyzed in this study include layer-by-layer, constant height and hemispherical cap models. A layer-by-layer growth model (shown as a straight black dashed line) shows the signal that would be observed if Ni grew in a layer-by-layer fashion. As can be seen in Figure 6.2a, this model does not fit the data well. Instead, we found models where the Ni grows as 3D nanoparticles fit the data well. Specifically, a constant particle height model fits the 300 K data well, and a hemispherical cap model fit the 100 K data very well. These two models will be discussed in the remainder of this section. The constant height model assumes that the Ni nanoparticles have the same height at all coverages (above some tiny coverage) and have flat tops. The hemispherical cap model assumes the Ni nanoparticles have a hemispherical shape and the same average particle diameter at a given coverage, and that the number of particles per unit area is a constant, independent of coverage (above some tiny coverage).

Using the data in Figure 6.2a, the average Ni nanoparticle thickness can easily be calculated by converting the number of Ni atoms per m^2 to the total volume of Ni per m^2 (assuming the deposited Ni particles have the same density as bulk Ni) and dividing by the fractional area covered by Ni particles, as measured with LEIS. The average thickness is then $t = \theta \times n_{ML} \times M_{Ni} / (N_A \times \rho_{Ni} \times f)$ where θ is the total Ni coverage (in ML), n_{ML} is the Ni atomic number density that defines one monolayer ($n_{ML} = 1.87 \times 10^{19}$ atoms/m^2), M_{Ni} is the molar mass of Ni (58.69 g/mol), N_A is Avogadro's number, ρ_{Ni} is the bulk density of Ni (8.9 g/cm^3), and f is the fraction of the graphene surface area covered by Ni particles, as obtained from the He$^+$ LEIS measurements. The resulting average Ni particle thickness as a function of Ni coverage is shown in Figure 6.2b. The thicknesses here at 100 K have been slightly corrected from the above equation by multiplying them by 1.207 to take into consideration the effect of shadowing of the support surface in LEIS near island edges, based on the hemispherical cap model (details below).

For the Ni growth at 300 K, the normalized Ni LEIS signal versus coverage is well-fit by a straight proportionality (red, solid line in Figure 6.2a). This line has a slope of 1/(7.33 ML). This proportionality indicates that at 300 K, flat Ni islands grow with an average thickness of 7.33 ML (1.5 nm), independent of coverage. This model is further supported by the 300 K data in Figure 6.2b (red, filled points) which shows the average Ni island thickness is nearly constant with $t = 1.54 \pm 0.18$ nm.

This growth model in which Ni grows as islands with a constant height at 300 K is further supported by STM observations on the growth morphology of Ni on graphene from the literature.[78,276] Both these STM observations at room temperature clearly showed that Ni vapor deposited onto graphene forms triangular islands with flat-topped terraces. The study by Lahiri et al. included a room temperature STM measurement of Ni on graphene/Ni(111) and showed that the islands had an apparent height of 1.58 ± 0.42 nm, with the flat tops being Ni(111) terraces, for a wide range of island widths (1-11 nm).[78] The study by Sicot et al. included a 300 K STM measurement of Ni on graphene/Rh(111) with an average apparent height of 1.8 nm and edge lengths between 5 to 18 nm at a Ni coverage of 0.9 ML.[276] Since the (111) face is the most stable (lowest surface energy) facet of FCC Ni, this shape provides energetic stability. A previous study has provided a kinetics-based explanation for why particles can grow flat and keep nearly a constant height during vapor deposition as the island diameter (or width) grows to be much larger than the height (which is unlikely based on simple thermodynamics of preferred particle shapes).[281] As shown in Figures 8 and 9 there, when small, flat, one-atom thick islands are grown in the first layer, and the energetics for a newly deposited adatom are appropriate, new atoms which land on top of an island will diffuse rapidly to the island edge and down-step to add instead to sites with stronger binding around the perimeter of the island. Essentially, if the top of the island is a flat Ni(111)-like surface, as shown by STM,[78] a new Ni monomer will not be stable there (since it can only make three Ni-Ni bonds there), whereas the sites around the island edges have locations where that Ni atom can make more Ni-Ni bonds than just three and thus are much more stable. Similarly, new Ni atoms which land on the support and diffuse to the island will prefer sites around the island perimeter, and not up-step to nucleate a new layer. This causes the islands to grow in diameter (or width for non-circular islands) without gaining height up to some critical diameter where diffusing Ni monomers on top of the island encounter each other and nucleate a cluster on top of the flat island creating a nucleation site for growth of a new layer. The rate of Ni diffusion around the island edges determines whether the islands appear circular, triangular, or some other faceted shape.[282] Importantly, the small ratio of island height to width in these STM studies means that it was a good approximation to neglect any shadowing effects near island edges in modelling the LEIS signal versus coverage curves at 300 K, as we have done in Figure 6.2.

The 100 K data is well-fit by a hemispherical cap growth model (blue line in Figure 6.2a and Figure 6.2b) first described by Diebold et al., in which all particles are assumed to have the same hemispherical shape and same average particle size at a given coverage.[72,283] These particles are assumed to have a constant areal number density at all coverages to be consistent with classical nucleation theory in which a saturation number density is reached at a very low coverage.[7,120] This model is only applied up to coverages for which $f < 33\%$, because at higher coverages the particles might begin to overlap (depending on how uniformly they are separated), so the model assumptions could break down. The regime in which the model is no longer appropriate is illustrated in Figure 6.2a and Figure 6.2b as a dashed blue line. As shown in previous work,[72] when the particles grow as hemispherical caps the total surface area masked by the particles and their shadows is 1.207 times the metal/support interfacial area if the He^+ ion beam is incident normal to the surface and the energy analyzer detects scattered ions 45^o from the surface normal, as done here. With this hemispherical cap model, the normalized Ni LEIS data can be modelled with the saturation particle density as the only fitting parameter. As shown in Figure 6.2a (blue solid line), the best fit to the 100 K LEIS data gives a particle density of 2.23×10^{16} particles/m^2.

For hemispherical particles, the average diameter equals three times the average thickness. This average particle diameter for this 100 K data, and its hemispherical-cap fit curve, (calculated as three times the average thickness) is shown as the right-hand axis in Figure 6.2b. As expected, the data for average diameter as a function of coverage also agrees well with this hemispherical cap model.

This hemispherical cap model for Ni on graphene at 100 K is somewhat different than previously reported low-temperature particle shape measurements for Ni on C(0001).[276–278] Baumer et al. studied Ni on graphite(0001) at 100 K using primarily XPS and SPA-LEED and found that the island height does not vary significantly with Ni coverage when analyzed with a flat island model.[278] However, the Ni coverages investigated in that work (<1 ML) were significantly less than those studied in the present work. Sicot et al. used STM to study 150 K Ni nanoparticles on graphene/Rh(111) and found that the particle density increased with increasing coverage while the particles remained the same size.[276] This difference from the hemispherical cap model of Figure 6.2 here (for graphene/Ni(111)) could be due to the fact that graphene/Rh(111) instead has a buckled Moiré pattern which creates a high-density periodic array of special sites, which may be more stable for particle nucleation, or due to the low fluxes used in that work (<10% of the flux in the present study). Marz et al.[277] used STM to study Ni deposited on HOPG(0001) at low temperatures and found dendritic Ni particles at high coverages. Their reported STM images at low coverages appear to show hemispherical Ni particles. The exact sample temperature for these experiments was unclear. (The sample was first cooled to 77 K, then transferred to a different chamber for Ni deposition, where the sample temperature could not be monitored. It seemed that the sample was quickly transferred back to the 77 K location for STM imaging.)

6.3.4 Heat of Adsorption of Ni on Graphene/Ni(111)

The differential heats of adsorption of Ni gas atoms onto graphene/Ni(111) as a function of Ni coverage at 300 and 100 K is shown in Figure 6.3. The data shows the measured heat of adsorption for a series of pulses (each with ~0.013 ML per pulse) as the Ni coverage on the sample increases. The curves shown for 300 and 100 K are averaged from several individual calorimetry runs to ensure replicability and to reduce the standard deviation in the measured heats of adsorption. At 300 K, the initial heat of adsorption is 336 kJ/mol which then rapidly increases to 400 kJ/mol in the first 0.1 ML. Above 0.1 ML, the heat slowly increases with coverage until reaching the bulk heat of Ni sublimation (ΔH_{sub} = 430 kJ/mol) by 2 ML. At 100 K, the heat of adsorption in the first pulse is 230 kJ/mol, increases much more slowly with coverage than at 300 K, and reaches the bulk heat of Ni sublimation by 3.5 ML.

The lower initial heat of adsorption and slower increase in the heats of adsorption at 100 K compared with 300 K is attributed primarily to Ni particle size differences between the two temperatures. At any given coverage below 2 ML, the Ni particles at 100 K are much smaller than at 300 K. For example, one STM study mentioned above showed at 0.9 ML an average flat-topped particle height of ~1.8 nm and width of ~12 nm at 300 K.[276] At this coverage for 100 K, the particle diameter in only ~3 nm (based on the hemispherical cap model fit in Figure 6.2). These tiny hemispherical caps formed at 100 K have a much larger fraction of undercoordinated atoms (i.e., atoms with fewer Ni-Ni bonds and thus which are less stable) in comparison to the larger, faceted particles formed at 300 K. Similarly, when a newly-deposited Ni adatom diffuses to and binds to a small hemispherical cap, there is a much greater chance that it attaches to a site where it is highly undercoordinated (i.e., where that new adatom forms fewer Ni-Ni bonds than at 300 K). For the larger particles at 300 K, there are sites where a new Ni adatom can make more Ni-Ni bonds, and the new Ni adatom can diffuse fast enough to find those stronger-binding sites. For example, when an adatom adds to a trimer, it can only make 3 Ni-Ni bonds, whereas when it adds to a very large particle at 300 K, it can make 6 Ni-Ni bonds at a kink site on a Ni(111) facet’s step edge. In the large particle size limit, each added Ni atom also makes 6 Ni-Ni bonds and has a differential heat of adsorption equal to the bulk heat of sublimation. (In a simple nearest neighbor bond-additivity model, the bulk sublimation energy or cohesive energy equals 6 times the Ni-Ni bond energy, since atoms in the bulk have 12 nearest neighbors and each of these 12 bonds is shared by 2 atoms: 12/2 = 6. This is twice the total Ni-Ni bond energy when Ni adds instead to a trimer.) Consequently, fewer Ni-Ni bonds on average are formed when a Ni atom attaches to a particle at 100 K when compared to 300 K at the same coverage, and the measured heats of adsorption are smaller. This continues until the hemispherical caps grow sufficiently large that they are dominated by sites where new Ni atoms can make as many Ni-Ni bonds upon adsorption as at 300 K (~3.5 ML of Ni coverage). This increase in adsorption energy with coverage as more Ni-Ni bonds are made is mitigated to some extent by the fact that more of the Ni atoms in smaller particles also bond to the underlying graphene, as quantified below via the adhesion energy at this Ni / graphene interface.

Using the average particle diameter as a function of coverage from Figure 6.2b allows us to replot the 100 K heats of adsorption versus coverage from Figure 6.3 in the form of heats of adsorption versus the effective Ni particle diameter to which the new Ni atoms add, as shown in Figure 6.4a. This procedure was not possible for the 300 K heats of adsorption since our constant height model does not allow for the determination of the Ni particle density nor their average lateral dimensions. From Figure 6.4a, we can see again that the heats of adsorption at 100 K increase rapidly with particle size due to the deposited atoms forming more Ni-Ni bonds as the particle size increases, as described above.

6.3.5 Chemical Potential and Adhesion of Ni on Graphene/Ni(111)

If we assume the size-dependent changes in the entropic contributions to the free energy are negligible compared to the very large enthalpic contributions for this system, we can calculate the chemical potential of Ni atoms in nanoparticles on graphene/Ni(111) at each size. The chemical potential relative to that of bulk Ni is simply the difference between the heat of sublimation and the measured differential heat of Ni adsorption at that size. The resulting Ni chemical potential as a function of the effective Ni particle diameter is shown in Figure 6.4b. As can be seen, the Ni chemical potential begins high (200 kJ/mol) and rapidly decreases with the particle diameter. Similar behavior has been shown for nanoparticles in this size range for many transition metals on oxides and Ag on graphene.[35]

Previous work studying metal nanoparticles supported on single crystal oxides has shown that the chemical potential for hemispherical nanoparticles is well approximated by[35,36]

$$\mu(D) = \left(3\gamma_{v/m} - E_{adh}\right)(1 + D_0/D)(2V_m/D) \qquad (6.1)$$

where $\gamma_{v/m}$ is the surface free energy of the bulk metal (2.38 J/m^2 for Ni), E_{adh} is the adhesion energy of the metal/support (Ni/graphene here) interface, V_m is the molar volume of the supported metal (6.59 m^3/mol for Ni), and $(1 + D_0/D)$ with D_0 = 1.5 nm is an empirical factor that has been shown to account for the increase in $\gamma_{v/m}$ and E_{adh} (relative to their bulk values) as the supported nanoparticles decrease in size for many different metals and oxide supports.[35,36] This equation has also been shown to fit data for Ag on graphene/Ni(111) very well.[256] Using (6.1), E_{adh} is the only unknown variable which provides a method to calculate E_{adh} by fitting the measured Ni chemical potential as a function of the diameter.

The heat of adsorption here does not reach the bulk heat of Ni sublimation at the largest particle sizes analyzed (~4 nm), in contrast to many other metal on support systems studied with SCAC and He$^+$ LEIS[75,241,246,256]. This same phenomenon has been observed for both systems involving Ni deposition studied previously by our group, namely Ni/MgO(100) and Ni/CeO$_2$(111), and was attributed to a structural phase change whereby Ni adopts hexagon close packed (HCP) structure for very small Ni particles (<5 nm) but takes on the usual face-centered cubic (FCC) structure for large particles.[36,46]

As discussed in previous work from our group,[36] (6.1) can be modified to account for this difference in crystal packing, which results in the following equation:

$$\mu(D) = \left(3\gamma_{v/m} - E_{adh}\right)(1 + D_0/D)(2V_m/D) + (\Delta H_{sub} - \Delta H^{*}_{sub}) \qquad (6.2)$$

where ΔH_{sub}^{*} is the heat of sublimation of the small-particle HCP phase (in the large-size limit) and ΔH_{sub} is the bulk FCC phase heat of sublimation (430 kJ/mol for Ni). (6.2) now has two parameters, E_{adh} and ΔH_{sub}^{*}, that are required to fit the experimental data.

Both (6.1) and (6.2) were used to fit the measured chemical potential data and these fits are shown as dotted and solid lines (respectively) in Figure 6.4b. Using (6.1) to fit the data gave a best-fit value for E_{adh} = 2.03 J/m^2 and the fit had a standard deviation of 18 kJ/mol relative to the measured values, while using (6.2) gave best-fit values of E_{adh} = 3.60 J/m^2 and ΔH_{sub}^{*} = 406 kJ/mol, and had a standard deviation of 11 kJ/mol versus measured values.

These standard deviations show that using (6.2) gives a better fit to the measured chemical potentials versus size, suggesting the formation of a different phase (HCP) for small Ni nanoparticles supported on graphene/Ni(111) than for large Ni particles (which prefer the bulk FCC phase). For Ni/MgO(100), a best-fit value of ΔH_{sub}^{*} = 405 kJ/mol was determined with the same method,[46] while Ni/CeO$_{2-x}$(111) gave a best-fit value of ΔH_{sub}^{*} = 404 kJ/mol.[36] The best-fit value of ΔH_{sub}^{*} is almost identical for all three of these systems, suggesting that very small, supported Ni nanoparticles often form the same HCP phase.

Hexagonal close packed Ni films and nanoparticles have been observed on MgO(100), Au(100), and Ru(11$\bar{2}$0), Ru(1$\bar{1}$00), and carbon nanotubes and the formation of this HCP phase has been attributed to size, lattice strain, and energetic effects.[284–288] This HCP Ni phase has also been reported for small unsupported Ni nanoparticles using a variety of different preparation methods where the HCP Ni phase can be stabilized by surface decoration by ligands.[289–291] This HCP phase will only form for metals in which the FCC structure is only very slightly more stable than the HCP structure and differential size effects can change the lattice packing. Indeed, it was found that the HCP structure for Ni nanoparticles on MgO(100) and CeO$_2$(111) had a heat of sublimation that was only 25 to 26 kJ/mol smaller than that for FCC Ni.[36,46] In addition, DFT calculations found that the HCP phase is only slightly less stable in the bulk than the normal FCC phase, but the surface energy per unit area of the HCP phase is lower than the surface energy of the FCC phase.[292] This surface energy difference could cause the HCP phase to be more stable than the FCC phase below some critical particle size. When the surface to volume ratio decreases as the nanoparticles grow, the HCP then transforms to the FCC phase, well known to be the most stable phase for very large particles.

In much of the previous work studying the HCP Ni phase, it has been argued that the HCP phase is caused by lattice strain.[36,46,284,286,287] However, in this present study, the C(0001) (graphene/Ni(111)) substrate is almost perfectly lattice matched with bulk FCC Ni(111) and lattice strain is not expected in the large size limit (although there may be lattice strain for small Ni particles, since small metal nanoparticles are well known to contract slightly in lattice constant relative to bulk metal). The Ni clusters formed on graphene here could nucleate from a HCP-like cluster structure and/or be thermodynamically stabilized due to the lower surface energy of the HCP phase mentioned above. In addition to this affect, a carbon environment also facilitates the stabilization of the Ni HCP phase. This has been found in the thermal decomposition of Ni_3C nanoparticles and PVD growth of Ni on carbon nanotubes were stabilized by a carbon shell around the Ni particles.[288,293] Here were do not observe any evidence of Ni particle encapsulation with our LEIS and SCAC experiments. However, a large fraction of the surface Ni atoms in the small nanoparticles are in contact with carbon support surface, giving rise to a similar effect.

The continued decrease in Ni chemical potential as the particles grow beyond a diameter of 3.5 nm suggests that the Ni particles may transition from the HCP phase to the thermodynamically stable FCC phase near this particle size. If we fix the value of ΔH^{*}_{sub} = 404.5 kJ/mol (the average of the values for Ni/MgO(100) and Ni/CeO$_{2-x}$(111)) and fit the chemical potential with (6.2) only up to a diameter of 3.5 nm, we instead obtain a best-fit value of E_{adh} = 3.53 J/m^2 with a standard deviation of 8.7 kJ/mol relative to measured values, in close agreement with the values calculated above.

6.4 Discussion

The adhesion energy of 3.60 J/m^2 for Ni on graphene/Ni(111) can be directly compared with the work of Lahiri et al. in which room temperature STM measurements of Ni nanoparticles on graphene/Ni(111) were used along with the Wulff construction to determine the adhesion energy for this same system.[78] Their results showed an adhesion energy of 3.5 J/m^2 in the large particle size limit (for Ni that we expect was in the FCC structure), within 3% of our value measured by calorimetry here at 100 K for HCP particles (extrapolated to the large-size limit). Despite this FCC versus HCP structural difference, this close agreement supports the conclusion that (6.2) is appropriate for analyzing the chemical potential data in Figure 6.4b. These values are also consistent with DFT calculations done in that same work,[78] which found an adhesion energy of 3.47 J/m^2 for a Ni adlayer on graphene/Ni(111). Those same DFT calculations surprisingly found an adhesion energy of only 0.81 J/m^2 at the graphene/Ni(111) interface. They attributed this large increase in interfacial bonding for Ni/graphene/Ni(111) to an increase in electronic density at the interface due to the underlying Ni(111) substrate, compared to Ni on free-standing, pristine graphene.

This adhesion energy of 3.60 J/m^2 from (6.2) can further be compared with the adhesion energy of 1.80 J/m^2 for Ag on graphene/Ni(111).[256] This stronger adhesion energy of Ni compared with Ag is consistent with DFT calculations which show a stronger binding strength of

Ni monomers to graphene.[243,279,280] In comparison to Ni on oxide supports, Ni/graphene has an intermediate adhesion energy between Ni/MgO(100) and Ni/CeO_2(111), which have adhesion energies of 3.05 J/m^2 and 4.39 J/m^2 respectively.[36,46]

This intermediate adhesion energy for Ni on graphene has important implications for the design of heterogeneous catalysts. As seen in (6.2), this intermediate adhesion energy means that for a given particle size (below ~6 nm) the Ni chemical potential on graphene will be somewhat higher than Ni on CeO_{2-x}(111) but lower than Ni on MgO(100). Given the quantitative relationship that shows that a high chemical potential leads to higher sintering rates,[12,13,38] we expect that the rate of catalyst deactivation by sintering will be lower for Ni supported on carbon compared with MgO, but higher than for Ni supported on CeO_2. In addition, many qualitative predictions have shown that metal nanoparticles with a higher chemical potential will bind small, adsorbed intermediates more strongly.[35,36,38] This suggests that nanoparticles supported on carbon will bind adsorbed intermediates more strongly than particles of the same size supported on CeO_2, but less strongly than those particles supported on MgO.

Our measured heats of adsorption can also be compared with DFT calculations in the literature. If we assume the smallest particles measured at 100 K have a hemispherical geometry and the same density as bulk Ni (8.90 g/cm^3), we can determine that these smallest particles have an average of 13 atoms with a heat of adsorption of 230 kJ/mol. This heat of Ni adsorption for making Ni_{13} on graphene/Ni(111) can be compared with DFT calculations that found a Ni gas atom adsorption energy of 2.66 – 3.02 eV/atom (262-298 kJ/mol) to form 3-dimensional Ni cluster sizes of 4 to 10 atoms bound to the surface of pristine, free-standing graphene.[272–275] While similar to our experimental measurement of 230 kJ/mol, these DFT calculations all found a 32 to 68 kJ per mol Ni stronger binding of 3D Ni clusters to free-standing graphene than we measure for 3D Ni_{13} on graphene/Ni(111).

This difference between the measured Ni_{13} binding enthalpy of 230 kJ/mol and the calculated Ni_4-Ni_{10} binding energies of 262-298 kJ/mol could be explained by the stabilization of the graphene film by the Ni(111) substrate used in our experiments. If we assume the graphene/Ni(111) adhesion energy is the same E_{adh} as measured above (3.6 J/m^2), we can convert this adhesion energy to ~116 kJ per mol surface Ni atoms using the Ni(111) surface atom density (1.87×10^{19} atoms/m^2) and Avogadro's number. This corresponds to 58 kJ per mol surface C atoms, since there are two C atoms for every Ni surface atom in this graphene film (see above). Thus, the C atoms in this graphene on Ni(111) film are stabilized by ~58 kJ/mol when bound to Ni(111) compared with free-standing graphene. This can partly explain why our measured adsorption enthalpy of making Ni_{13} on graphene/Ni(111) is significantly smaller than DFT results for making Ni_4-Ni_{10} on free-standing graphene despite the larger cohesive energy contribution expected for the larger particle size we measured.

The differences in growth modes and particle sizes between 300 K and 100 K are mainly due to the differences in the diffusion rate of Ni monomers. It is well-known that the number density of islands is typically much larger at 100 K than 300 K during metal vapor deposition.[7,38] The rapid down-stepping that enables the growth of wide, flat-topped islands at 300 K is not expected to occur at 100 K. Thus, the particles will be much smaller at 100 K than 300 K causing a much higher surface area / volume ratio. For these small Ni nanoparticles, the DFT-predicted lower surface energy of the HCP phase compared with the FCC phase[292] might dominate over the small bulk energy difference between these two phases and might cause these small nanoparticles to assume the HCP phase at 100 K, whereas at the same coverage the particles are much larger at 300 K and are more likely to assume the bulk FCC phase at 300 K. This difference in phase might also contribute to the difference in island shape between 100 K and 300 K.

6.5 Conclusions

Calorimetric adsorption energies of Ni vapor deposited onto graphene/Ni(111) are used in conjunction with the growth morphology to determine the Ni chemical potential as a function of Ni nanoparticle size as well as the adhesion energy of Ni metal to graphene/Ni(111). The He^+ LEIS experiments showed that Ni grows as 3D nanoparticles on graphene/Ni(111) at 100 K with a particle density of 2.23×10^{16} particles/m^2. At 300 K, Ni vapor deposited onto graphene/Ni(111) instead forms flat-topped islands with an average height of 1.54 ± 0.18 nm in the coverage range 0.2 to 3.0 ML. QMS measurements showed an initial sticking probability for Ni vapor of 94% at 300 K and 96% at 100 K. This is consistent with expectations since the ratio of the desorption rate to the diffusion rate is much lower at 100 K than at 300 K (since the activation barrier for desorption is much larger than that for diffusion). The heat of Ni adsorption at 300 K is initially 336 kJ/mol and rapidly increases to 400 kJ/mol in the first 0.1 ML of Ni deposition (where the Ni particles already reach ~1 nm thick), and further increases to the bulk heat of Ni sublimation (430 kJ/mol) by 2 ML. The heat of adsorption at 100 K begins at 230 kJ/mol, increases much more slowly with coverage than at 300 K, and reaches the bulk heat of Ni sublimation by 3.5 ML. The Ni chemical potential as a function of average Ni particle diameter (from 0.5 to 4 nm) was determined from the 100 K heats of adsorption and was shown to decrease with Ni coverage and diameter. By fitting the measured chemical potential as a function of diameter to a previously reported model, we determined an adhesion energy of 3.60 J/m^2 for Ni particles (in the larger-size limit) on graphene/Ni(111). This adhesion energy is in good agreement with STM and DFT investigations of Ni/graphene/Ni(111) and its value is in between those for Ni/MgO(100) and Ni/CeO_2(111). These chemical potential versus diameter results are best fitted if we assume that these small Ni nanoparticles at 100 K form an HCP phase with a sublimation enthalpy ~25 kJ/mol smaller than that of the normal bulk FCC phase, consistent with those earlier reports for Ni on MgO(100) and CeO_2(111).

6.5 Figures

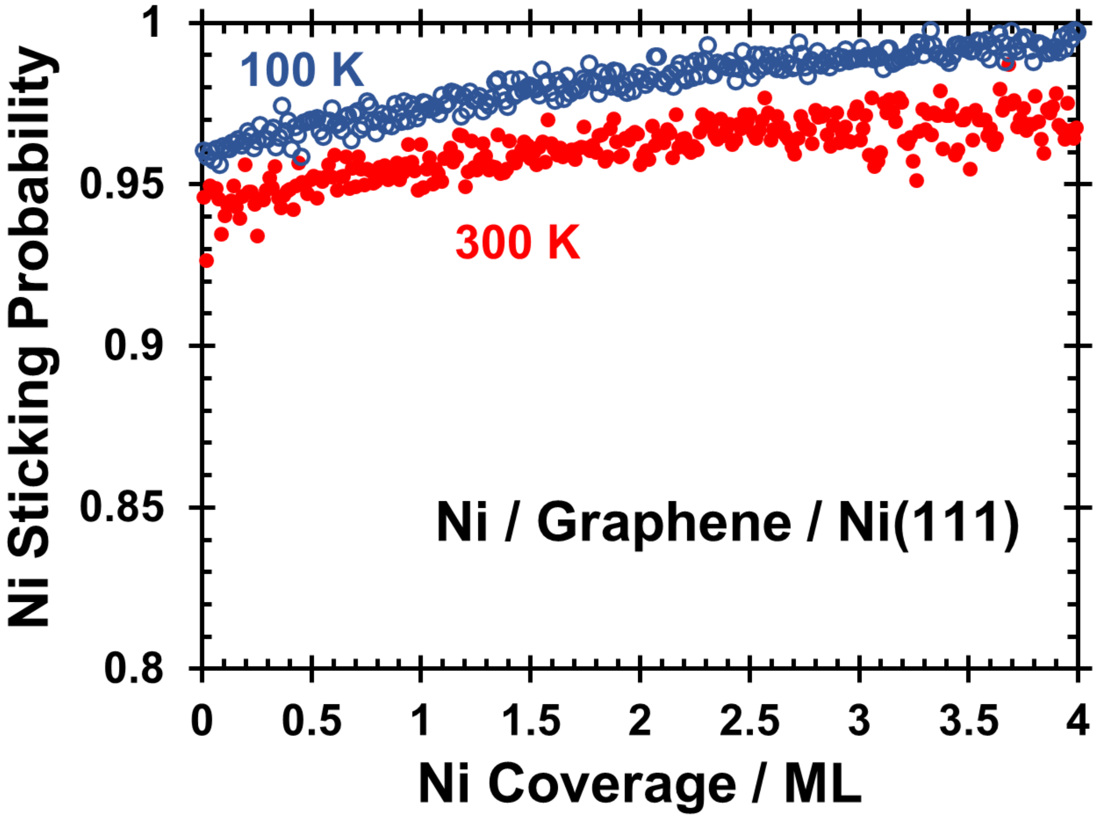

Figure 6.1 Sticking probability of Ni gas atoms onto graphene/Ni(111) as a function of Ni coverage at 300 K (red, filled points) and 100 K (blue, open points). The absolute coverage of 1 ML is defined here as 1.87×10^{19} atoms/m^2.

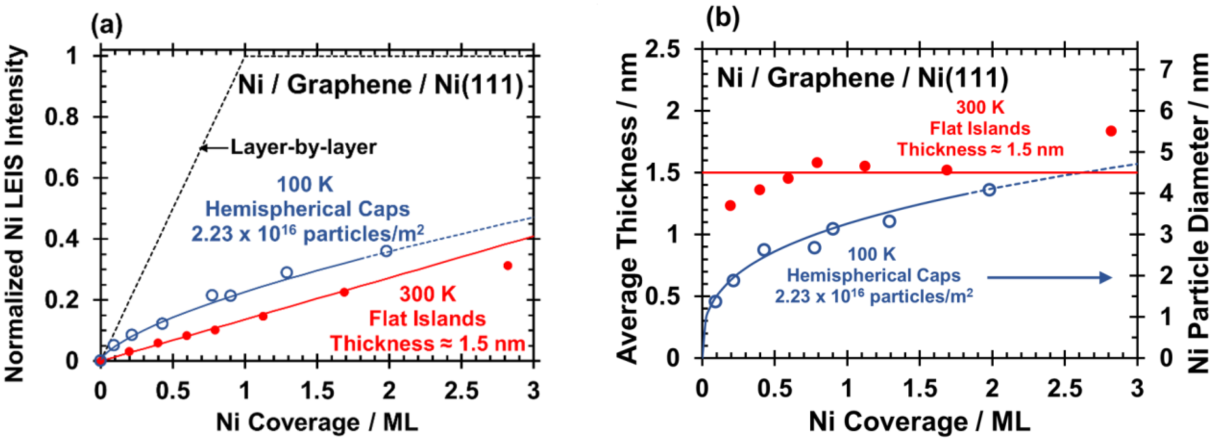

Figure 6.2 (a) Integrated Ni LEIS signal normalized to a thick multilayer Ni film as a function of the Ni coverage following deposition onto graphene/Ni(111) at 300 K (red, filled points) and 100 K (blue, open points). The black dashed line corresponds to the signal that would be observed if Ni grew in a layer-by-layer fashion on this substrate. The colored red line corresponds to a model in which Ni grows as flat islands with a thickness of 1.5 nm. The colored blue line corresponds to a model with Ni growing as 3D hemispherical caps with a particle density of 2.23 × 10^{16} particles/m^2. The dotted line above a normalized Ni LEIS signal of 0.33 is only a guide to the eye since the model should not be applied at those higher coverages. (b) Average Ni particle thickness as a function of coverage, and on the right axis, the average diameter of hemispherical caps that correspond that this thickness. The colored red line shows a constant average thickness of 1.5 nm (for 300 K) and the colored blue line corresponds to the model in which Ni grows as hemispherical caps at 100 K with a particle density of 2.23 × 10^{16} particles/m^2.

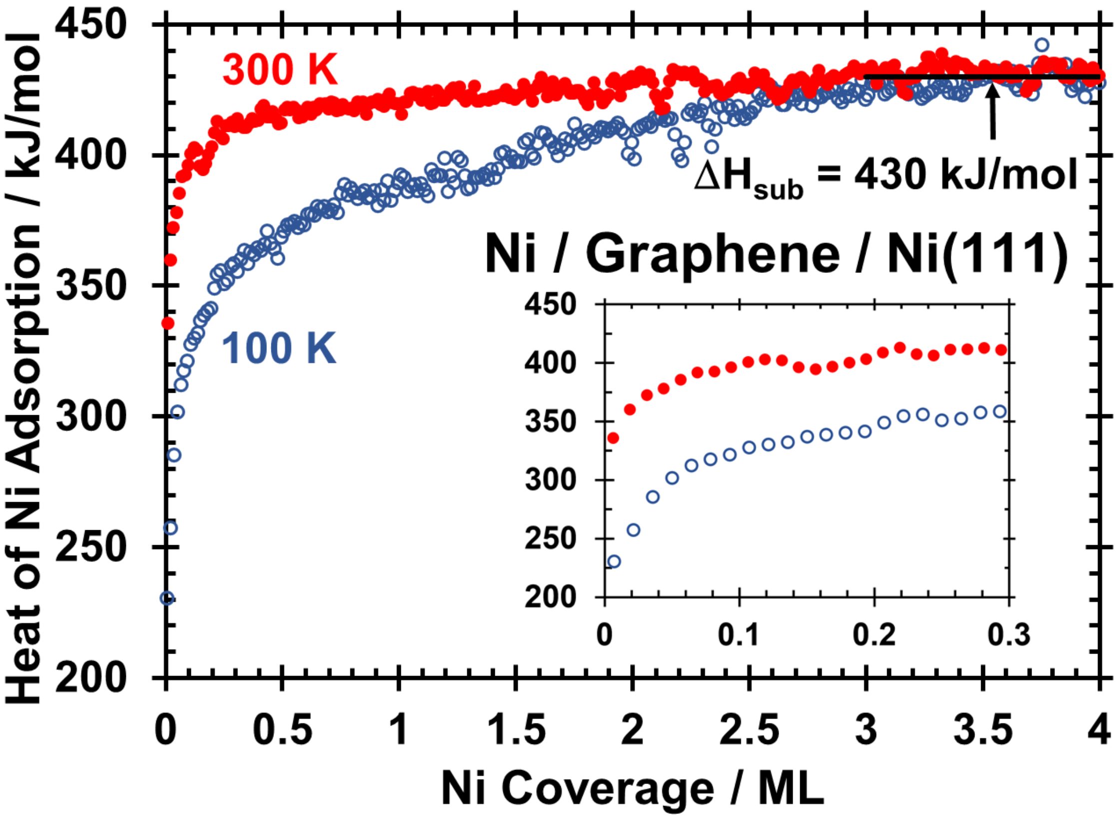

Figure 6.3 Differential heat of adsorption of Ni gas atoms onto graphene/Ni(111) as a function of Ni coverage at 300 K (red, filled points) and 100 K (blue, open points). The inset shows the low coverage regime (<0.3 ML) on an expanded scale.

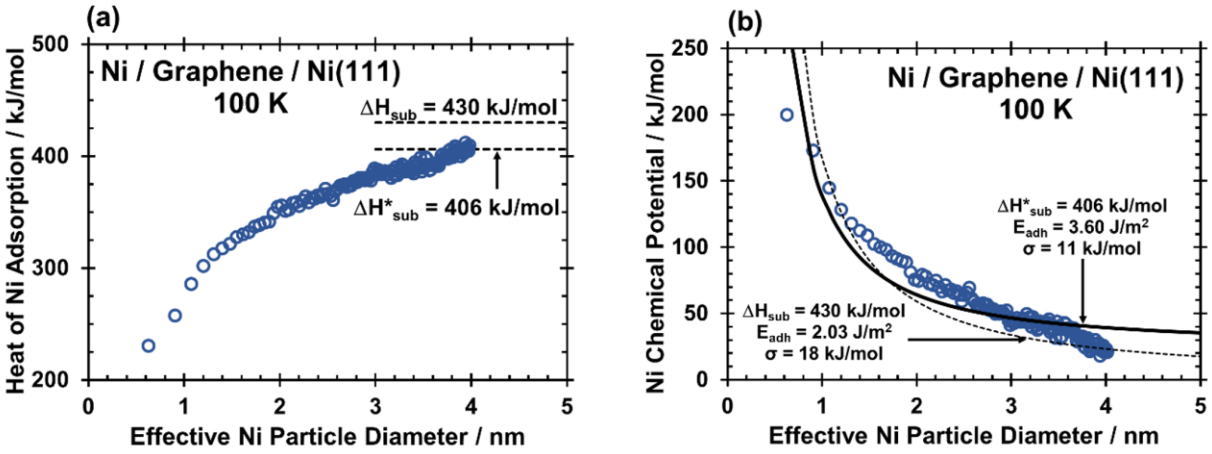

Figure 6.4 (a) Differential heat of adsorption of Ni vapor adsorption onto graphene/Ni(111) at 100 K as a function of the effective Ni particle diameter to which Ni adds during growth. Particles with diameters larger than 4 nm could not be analyzed since the hemispherical cap model assumptions break down above that size. (b) Chemical potential of Ni atoms on graphene/Ni(111) at 100 K as a function of the average Ni particle diameter to which Ni atoms add during growth.

Chapter 7. Adhesion energies of solvent films to Pt (111) and Ni (111) surfaces by adsorption calorimetry

This chapter has been published as:

Rumptz, J. R. & Campbell, C. T. (2019). *ACS Catalysis*, 9 (12), 11819-11825.

Chapter Abstract

Solvent/metal adhesion energies are crucial for understanding solvent effects on adsorption energies, which are, in turn, central to understanding liquid-phase catalysis, electrocatalysis, and other technologies such as adsorption-based separations and chemical sensors. Reactant adsorption energies in different solvents are dominated by differences in their solvent/metal adhesion energies. Here, the adhesion energies of five liquid solvents to clean Pt(111) and Ni(111) surfaces have been estimated using ultrahigh vacuum calorimetric measurements of heats of adsorption versus coverage integrated from zero coverage up to thick (bulk-like) multilayer solid films. The adhesion energies are found to vary from 0.15 to 0.60 J/m^2, increasing in the trend CH_3OH < HCOOH < H_2O < benzene ≈ phenol. This trend indicates that solvents with higher heats of adsorption per unit area in the first adsorbed layer have higher adhesion energies to a given metal surface. The adhesion energies to Ni(111) are generally larger than to Pt(111) (on average by 0.09 J/m^2). This is due to the 24% higher number of metal atoms per unit area on Ni(111) than on Pt(111) and, with oxygen-containing solvents, the greater oxophilicity of Ni compared to that of Pt.

7.1 Introduction

Catalytic and electrocatalytic reactions occurring at solid surfaces in liquid solvents are becoming increasingly important for clean energy, environmental, and chemical technologies.

Detailed understanding of the kinetics of these reactions and the reasons one catalyst may be more active or more selective than another requires knowledge of the energies of the adsorbed reaction intermediates and the transition states for their surface reactions. There are accurate measurements of the energies of many adsorbed catalytic reaction intermediates on clean and well-defined metal surfaces in ultrahigh vacuum or gas phase,[294–299] and there have been a huge number of calculations of these energies using density functional theory.[297–303] In contrast, very little is known about the energies of adsorbed reaction intermediates in the presence of liquid solvents since the methods for studying surfaces in the presence of liquids are much more challenging and less developed than in the gas phase. In addition, the choice of solvent is known to have marked effects on the catalyst's activity and selectivity.[59–63] Understanding such solvent effects surely requires an understanding of how the adsorption energies of the key reaction intermediates (and transition states) depend upon the solvent, yet very little is known about this. We show below that the adhesion energy of the solvent to the solid surface (E_{adh}) is perhaps the dominant factor that determines the differences between adsorption energies in different solvents. Motivated by that observation, we report experimental measurements of adhesion energies of five different solvents to clean Pt(111) and Ni(111) surfaces extracted from our earlier calorimetric measurements of the adsorption energies of the solvent molecules on these clean metal surfaces that extended from zero coverage up to bulk-like multilayer solvent films.

7.2 Effect of Solvent / Solid Adhesion Energy on Adsorption Energies in Solvents

As noted above, there is great motivation to leverage the vast amount we already know about the energies of adsorbates at the gas/solid or vacuum/solid interface to estimate adsorption energies on solid surfaces in the presence of liquid solvents and to predict the effects of different solvents on adsorption energetics. Several studies have already addressed these effects.[53,59,311–320,60,321–324,304–310]

We recently analyzed the differences between adsorption energies in the gas phase and in liquid solvents within a simple pairwise bond additivity model and a standard thermodynamic cycle approach.[64] That approach required that the adsorbate be a flat molecule, which adsorbs parallel to the solid surface. Its accuracy was validated by comparing the heat of adsorption of phenol on Pt(111) measured in liquid water to the heat of gaseous phenol adsorption on Pt(111) measured in ultrahigh vacuum.[64,325,326]

We reproduce that model in Figure 7.1, but present it here in a more general form than we suggested when first presenting it, i.e., by replacing water with the general solvent “S” and the metal surface (Pt(111)) with the general material surface “M”. (We refer to M as a metal below, but the analysis applies to any solid material.) The adsorbing reactant “R” is any flat molecule like phenol. We imagine here a vertical column of the solvent with a cross-sectional area equal to the area required for one adsorbed molecule of R (σ_R). Since the molecule R is flat (one atom thick), edge effects on energies were assumed to be negligible, but we argued that this model should also be applicable to thicker molecules when reasonably flat.[64]

In this bond additivity model, the first two steps, when combined, are just the solvation of R(gas) in liquid S to make solvated R, or R(solv). The energy for these two combined steps (shown as the arrow across the top) is $\Delta U_{solvation,R(gas)}$. Its value is often able to be determined using the reported experimental temperature dependence of Henry’s law constant (or the solubility constant) for R(gas) in S, as we did for phenol in water (giving $\Delta U_{solvation,phenol(gas)} = -47.5$ kJ/mol).[64,71] In the first step, the solvent−solvent bonding in the area of one R molecule must be broken to make two vacuum/solvent interfaces. The energy cost for this is called S−S, for the solvent−solvent bond energy. The value of S−S is by definition twice the surface energy of the liquid solvent at its gas or vacuum interface ($\gamma_{S(liq)}$) multiplied by the surface area occupied by one R molecule, σ_R. One can estimate this energy change using the reported experimental surface free energy of the liquid solvent, since it is generally dominated by the energy cost to break the strong solvent−solvent bonding with only small contributions from entropy. The two solvent surfaces are then bonded to both sides of a gaseous R molecule, which is downhill in energy by twice the solvent−R bond energy over the area of one R, or 2(S−R). The net reaction depicted in the top arrow then has energy

$$\Delta U_{solvation,R(gas)} = (S-S) - 2(S-R) = 2[(\gamma_{S(liq)} \cdot \sigma_R) - (S-R)] \qquad (7.1)$$

One can set this equal to the experimental $\Delta U_{solvation,R(gas)}$ for steps 1 and 2 combined (if known) and solve for S−R to get

$$(S-R) = -\frac{\Delta U_{solvation,R(gas)}}{2} + (\gamma_{S(liq)} \cdot \sigma_R) \qquad (7.2)$$

When applied to phenol in water, this equation gave S−R= 50.1 kJ per mole of phenol surface area.[64]

The next step is to separate the solvent from the metal, which is uphill in energy by S−M, equal by definition to the solvent/metal adhesion energy per unit area times the area required for the adsorbed reactant, $E_{adh,S/M} \cdot \sigma_R$. Next, the solvent column below the R is separated from the R, which has an energy cost of S−R, as given by (7.2). The lower solvent column is next attached to the upper solvent column, which is downhill in energy by the S−S bond energy, i.e., $\Delta U = -S-S = -2(\gamma_{S(liq)} \cdot \sigma_R)$. Finally, the bottom of the solvent column (which is now terminated in molecule R) is attached to the metal surface. This last step is downhill by the molecule−metal surface bond energy, $\Delta U = R-M$, which, in this simple bond additivity model, is assumed to be the same as the adsorption energy in the gas phase, $\Delta U_{ads,R(gas)}$. As shown by the bottom arrow, these last four steps combine to make the net reaction (from R in the solvent and M in the solvent to R adsorbed on M in the solvent) or the solvent-phase adsorption of R. Therefore, the energy for this net solvent-phase adsorption reaction, $\Delta U_{ads,R(solvent)}$, is just the sum of energies for each of these four steps

$$\Delta U_{ads,R(solvent)} = (S - M) + (S - R) - (S - S) - (R - M)$$

$$\Delta U_{ads,R(solvent)} = E_{adh,S/M} \cdot \sigma_R + (S - R) - 2\left(\gamma_{S(liq)} \cdot \sigma_R\right) + \Delta U_{ads,R(gas)} \qquad (7.3)$$

Substituting for S−R from (7.2) into (7.3) above gives

$$\Delta U_{ads,R(solvent)} = E_{adh,S/M} \cdot \sigma_R - \frac{\Delta U_{solvation,R(gas)}}{2} - \left(\gamma_{S(liq)} \cdot \sigma_R\right) + \Delta U_{ads,R(gas)}$$

Or

$$\Delta U_{ads,R(solvent)} = \Delta U_{ads,R(gas)} + E_{adh,S/M} \cdot \sigma_R - \frac{\Delta U_{solvation,R(gas)}}{2} - \left(\gamma_{S(liq)} \cdot \sigma_R\right) \qquad (7.4)$$

Note that the last two terms in this equation are often known from the bulk behavior of the liquid solvent (and its solvation of R), provided the area covered by adsorbed R can be estimated. Thus, (7.4) provides a simple way to estimate the adsorption energy in a solvent from its adsorption energy in vacuum, provided the adhesion energy of the solvent to the solid surface is known. Alternatively, (7.4) provides a potentially useful way to estimate this adhesion energy if any molecule’s adsorption energy has been measured in both vacuum and this solvent.

We emphasize that this is a very simple model. Most importantly, it would have a large error if there were a large amount of charge transfer between the adsorbate and the metal. Thus, it is designed for neutral adsorbates, not adsorbed anions or cations. While this is a severe limitation, the fact is that the computational catalysis community is still struggling with how to accurately include solvent effects in even the simplest adsorption systems. Thus, the simplicity of experimental systems it can treat and its simple elementary-step breakdown of the process in

Figure 7.1 offers important advantages, in that it can provide simple experimental benchmarks for testing computational models for solvent effects.

(7.4) shows that the solvent-phase adsorption energy is markedly less exothermic than the gas phase $\Delta U_{ads,R(gas)}$ due to the adhesion energy of the solvent to the metal and the exothermicity of solvation of the gas. We applied (7.3) and (7.4) to aqueous-phase phenol adsorption on Pt(111) and found that the dominant difference between $\Delta U_{ads, R(solvent)}$ and $\Delta U_{ads,R(gas)}$ was the adhesion energy term, $E_{adh,S/M \cdot \sigma R}$, which is ∼116 kJ per mol phenol for that case.[64] The two terms $-\Delta U_{solvation,R(gas)/2}$ and $-\gamma_{S(liq) \cdot \sigma R}$ were much smaller in magnitude (∼26 kJ per mol phenol) and had opposite signs; so, they nearly canceled. This observation suggests that differences in $E_{adh,S/M}$ between different solvents may often be the largest contribution that determines the differences in energy between the adsorption of the same molecule on the same surface in different solvents. This important effect of the solvent/metal adhesion energy on adsorption energies provides strong motivation for making experimental estimates of solvent/metal adhesion energies for other systems. We report below nine new experimental estimates of solvent/metal adhesion energies, which show that E_{adh} varies strongly with the solvent and is generally larger to Ni(111) than to Pt(111).

When we introduced the concepts in Figure 7.1 and (7.4),[64] we also presented a similar thermodynamic cycle ("Scheme 4" in that paper[64]) that used the adsorption energy of the solvent in the first layer instead of the adhesion energy. That cycle made the assumption that the solvent−solvent bond energy between the first and second layers of the solvent is the same as in the bulk of the solvent. That assumption is only approximately correct. The raw heat versus coverage data cited in Table 7.1 shows that the heat of adsorption in the second layer is generally ∼5−20% larger than in the third and thicker layers. So, using (7.4) and adhesion energies is more accurate than using only first-layer adsorption energies within that paper's Scheme 4.[64] The difference is 12.4 kJ/mol for phenol adsorption on Pt(111) in water.[64] Perhaps, more importantly, using that paper's Scheme 4 requires knowing the exact coverage where the first layer completes and the second layer starts. This is not always possible to accurately determine from the experiments. The use of adhesion energies and (7.4) completely avoids the need to do that.

7.3 Solvent / Metal Adhesion Energies

To our knowledge, there is presently no known way to directly measure the adhesion energy of any liquid solvent to any clean surface. However, we have repeatedly measured solid/solid adhesion energies since 1997 using a method we developed based on calorimetric heats of vapor adsorption onto clean solid surfaces in ultrahigh vacuum (UHV) whose accuracy has been validated.[30,37] This method involves integrating the measured heat of adsorption from zero coverage up to a high coverage where the vapor has grown a thick (bulk-like) solid multilayer. Until our recent report of E_{adh} for water(solid)/Pt(111) interface,[64] we had only used this approach to measure E_{adh} for solid metal films on clean oxide and metal surfaces. We will use that same approach here to estimate the adhesion energies of bulk-like films of five different solvents (water, methanol, formic acid, benzene, and phenol) to clean Pt(111) and Ni(111) surfaces.

We will use the same equation as derived in ref [30] for measuring adhesion energies of solid metal films to clean single-crystal surfaces, only now applying it to the adhesion energy of solvents onto clean Pt(111) or Ni(111) surfaces. Figure 7.2 shows the thermodynamic cycle used to derive the needed equation, adapted from ref [30] to the different species involved here, with S referring to the solvent species. The calorimetric measurement is depicted as the arrow that goes from the top state (n molecules of gaseous S and a clean solid surface of material M with area A in UHV) down to the state at the bottom right (a multilayer slab of condensed liquid solvent S on the solid surface). The enthalpy change for this step is just the sum of the enthalpies of adsorption of all n molecules of S, equal to the negative of the heat of adsorption integrated over the coverage range from 0 to n/A, or $-Q_{adsorption}$.

The same net reaction can be realized by first taking the arrow down to the left to condense the n solvent molecules into a freestanding multilayer slab of pure S liquid, S(liq), and then taking the arrow from the bottom left to right attaching the liquid slab of S to the solid surface. The first step has an enthalpy change equal to negative n times the bulk heat of vaporization of pure S ($-n\cdot\Delta H_{vap,S}$) and two times the surface energy of the pure liquid S times the area ($2A\cdot\gamma_{S(liq)}$). The energy for the second step is, by definition, just equal to the area times the adhesion energy ($-A\cdot E_{adh,S(liq)/M(s)}$). The enthalpy change for the second step is equal to its energy change since there is no significant change in volume. The sum of enthalpy changes for all three steps in the cycle must sum to zero so that

$$-A\cdot E_{adh,S(liq)/M(s)} = +\left(n\cdot\Delta H_{vap,S} - 2A\cdot\gamma_{S(liq)}\right) - Q_{adsorption} \qquad (7.5)$$

This can be rearranged to give

$$E_{adh,S(liq)/M(s)} = [Q_{adsorption} - n\cdot\Delta H_{vap,S}]/A + 2\cdot\gamma_{S(liq)} \qquad (7.6)$$

Since the heats of vaporization and surface energies are known for many liquid solvents at room temperature, the integrated heat of adsorption of S(gas) per unit area ($Q_{adsorption}/A$) provides all that is needed to apply this equation to estimate the solvent/metal adhesion energy.

Unfortunately, $Q_{adsorption}$ can only be measured at lower temperatures, where the solvents grow as solid films rather than liquid films. For that reason, we make the assumption that the first term here, $[Q_{adsorption} - n\cdot\Delta H_{vap,S}]/A$ at room temperature, is approximately equal to the analogous quantity which we can measure at low temperatures when S is a solid: $[Q_{adsorption} -$

$n \cdot \Delta H_{sub,S}$]/A, where $\Delta H_{sub,S}$ is the bulk heat of sublimation of pure S. The assumption that this equals [$Q_{adsorption} - n \cdot \Delta H_{vap,S}$]/A at room temperature is based on our expectation that the zero-Kelvin chemical bond energies dominate these energies at all temperatures. It is equivalent to assuming that the first two layers and multilayers have the same difference in heat capacities at all temperatures. This is similar to the assumption of zero difference in heat capacities made in deriving both the famous Clausius−Clapeyron and van't Hoff equations,[327] but it is less accurate since the heat of fusion is involved here in the multilayers and possibly also in the near-surface layers. Since the heat of fusion is small compared to the heat of sublimation, this is expected to be a small error.

Figure 7.3 shows an example of such a heat of adsorption versus coverage measurement, for the case of methanol adsorption on Ni(111) at 120 K from ref [328]. All such data were measured in ultrahigh vacuum by single-crystal adsorption calorimetry (SCAC). As seen, the heat of adsorption is high until the first layer is saturated, and it drops down to near (but still above) the heat of sublimation of the pure, thick multilayer ($\Delta H_{sub,S}$) in the second layer, but closely approaches this high-coverage asymptotic limit of $\Delta H_{sub,S}$ by the third layer. This decrease is typical of all of the systems analyzed here. The quantity [$Q_{adsorption} - n \cdot \Delta H_{sub,S}$]/A is just the shaded area shown. As was derived above, this quantity added to twice the surface free energy of the solvent yields the adhesion energy between the solvent and the metal surface.

The adhesion energies for thin multilayer films of solvent molecules on Pt(111) and Ni(111) determined from SCAC data like those in Figure 7.3 using (7.6) are summarized in Table 7.1. Also listed there are the experimental surface energies (γ_i) and sublimation energies used in (7.6) and their sources.

Figure 7.4 summarizes the adhesion energies from Table 7.1. As seen, the adhesion energies to Pt(111) increase in the sequence CH_3OH < HCOOH < H_2O < benzene ≈ phenol, and the values to Ni(111) follow the same sequence except that they are generally larger than to Pt(111) (on average by 0.09 J/m^2 or 37%), and phenol is instead lower than benzene. Note that these values reflect the internal energy contributions only. They do not include any entropic contributions.

The larger adhesion energy of the oxygen-containing solvents on Ni(111) in comparison to that on Pt(111) is likely a result of the larger oxophilicity of Ni compared with that of Pt. Previous work by our group has shown that the −OR bond energies to Ni(111) are ∼70 kJ/mol larger than their bond energies to Pt(111),[329] reflecting the well-known greater oxophilicity of Ni. This leads to stronger adhesion of the oxygen-containing solvents (i.e., all except benzene) to Ni(111) than to Pt(111). For benzene, the heats of adsorption versus coverage (per surface metal atom) are almost identical on Ni(111) and Pt(111).[330] However, the number of metal atoms per unit area is 24% larger on Ni(111) than on Pt(111); so, this leads to a stronger adhesion energy per unit area for benzene on Ni(111) than on Pt(111).

The trend in Figure 7.4 of adhesion energy with different solvent molecules is quite similar on both Pt(111) and Ni(111). As one moves to the right in Figure 7.4, the observed increase in E_{adh} is dominated by the increase in the $[Q_{adsorption} - n \cdot \Delta H_{sub,S}]/A$ term in Table 7.1. Close inspection of the heats of adsorption versus coverage reveals that this term is dominated by the heat of adsorption in the first layer of adsorbed molecules that are in direct contact with the metal surface. Thus, one can approximately state that the solvents with higher heats of adsorption per unit area (relative to the multilayer) in the first adsorbed layer have higher adhesion energies. A variety of physical effects contribute to the heat of adsorption per unit area for any given molecularly adsorbed solvent molecule; so, any further discussion of this trend in Figure 7.4 would require an in-depth analysis with the aid of quantum mechanics calculations.

We have recently used a very similar approach to estimate the adhesion energy of water to Pt(111) using the same calorimetric values for $[Q_{adsorption} - n{\cdot}\Delta H_{sub,S}]/A$, as listed in Table 7.1.[64] However, in that case, we estimated E_{adh} of solid water to Pt(111) rather than liquid water so that the term $2{\cdot}\gamma_{S(liq)}$ in (7.6) here was replaced with that for solid water, $2{\cdot}\gamma_{S(solid)}$ (which for solid water is 0.109 J/m^2).[331] This solid water surface energy is 0.036 J/m^2 larger than that for liquid water; so, it gave E_{adh} = 0.32 J/m^2, averaged over the two temperatures of the calorimetry experiments (0.345 and 0.302 J/m^2 at 88 and 120 K, respectively). The liquid E_{adh} value in Table 7.1 (also averaged for these two temperatures) is 0.07 J/m^2 (or 22%) smaller. Since we could not find $\gamma_{S(solid)}$ values from the literature for the solid surfaces of other solvent molecules, we cannot make this comparison for them. However, since the other solvents have liquid surface energies that are ∼40−70% smaller than for water, we expect a smaller absolute difference between the estimated solid versus liquid adhesion energies than this 0.07 J/m^2 difference seen for water. This would not have much of an effect on the trends in E_{adh} plotted in Figure 7.4, which would still hold if using these solid solvent values instead. For the water on Ni(111) system, using the surface energy for ice stated above leads to a calculated adhesion energy of 0.417 J/m^2 at 100 K, which is also 0.075 J/m^2 (or 22%) larger than the liquid value of 0.342 J/m^2 listed in Table 7.1.

As with the examples above for water, in general, the surface energy of the solid will be larger than that of the liquid, as shown in the well-known relationship[332]

$$\gamma_{solid} \geq \gamma_{liquid} + \gamma_{solid/liquid} \tag{7.7}$$

It follows that the adhesion energies reported here will be systematically smaller than the solid's value obtained from using the solid surface energy. Results investigating the surface energy of pure metals suggest a constant ratio of the solid to liquid surface energy with a value of $\gamma_{\text{Solid}}/\gamma_{\text{Liquid}} \approx 1.18$.[332] Using this ratio to estimate the solid surface energies of the solvents in Table 7.1 leads to the conclusion that the 18% increase in the surface energy (from liquid to solid) leads to an average increase of only ∼6% in the calculated adhesion energy due to the dominance of the term $[Q_{\text{adsorption}} - n\cdot\Delta H_{\text{sub,S}}]/A$ in the adhesion energy calculation.

The adhesion energy between two condensed phases or materials is defined as the energy per unit area required to separate them to form two distinct surfaces. For a solvent S and a material M, this is reflected in (7.8)

$$E_{adh} = \gamma_M + \gamma_S - \gamma_{S/M} \tag{7.8}$$

Based on the values reported in Table 7.1 for adhesion energies and solvent surface energies, and using the reported surface energies of pure metals ($\gamma_{\text{Pt(111)}} = 2.49$ J/m^2 and $\gamma_{\text{Ni(111)}} = 2.38$ J/m^2),[245,332] it is straightforward to use this equation to calculate the surface energy of the solvent/metal interface. This interfacial energy often appears in equations relating to the wetting of a material substrate;[333,334] so, its calculation from the above data may be useful to some readers.

7.4 Conclusions

Using cryogenic calorimetric measurements of the heats of adsorption of solvent molecules on clean Pt(111) and Ni(111) surfaces as a function of coverage up to high coverages where the molecules grow thick (bulk-like) solid films, we have extracted the adhesion energies per unit area of five liquid solvents (methanol, formic acid, water, benzene, and phenol) on Pt(111) and Ni(111). The results are summarized in Figure 7.4. To estimate these adhesion energies, we assumed that the measured heat of adsorption in the first few layers is the same amount above the multilayer heat on these cold surfaces (i.e., at ∼100 K) as it would be if measured near room temperature where the solvent is a liquid. This leads to some error, estimated to be small compared to the differences between solvents in Figure 7.4. These adhesion energies can be used in thermodynamic cycles, like the bond additivity model in Figure 7.1, to help clarify solvent effects on adsorption energies and the rates of liquid-phase catalytic and electrocatalytic reactions.

7.5 Figures and Tables

Table 7.1. Adhesion Energies of Solvent Films to Single-Crystal Metal Surfaces[a]

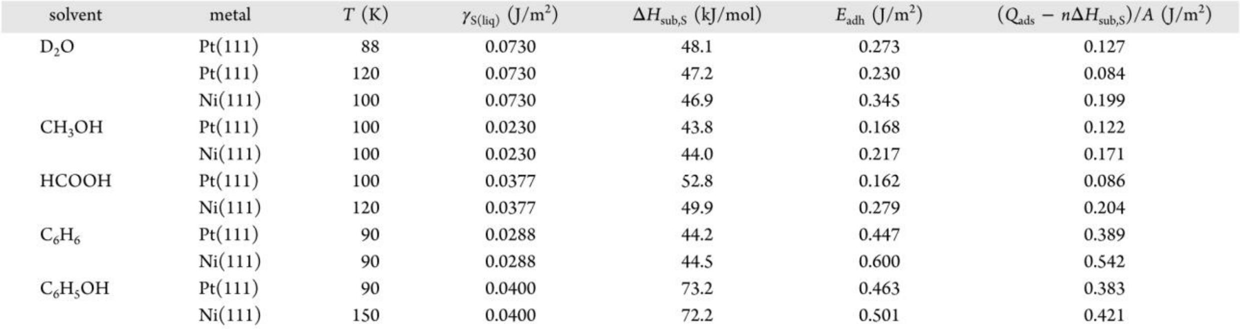

solvent	metal	T (K)	$\gamma_{S(liq)}$ (J/m^2)	$\Delta H_{sub,S}$ (kJ/mol)	E_{adh} (J/m^2)	$(Q_{ads} - n\Delta H_{sub,S})/A$ (J/m^2)
D_2O	Pt(111)	88	0.0730	48.1	0.273	0.127
	Pt(111)	120	0.0730	47.2	0.230	0.084
	Ni(111)	100	0.0730	46.9	0.345	0.199
CH_3OH	Pt(111)	100	0.0230	43.8	0.168	0.122
	Ni(111)	100	0.0230	44.0	0.217	0.171
HCOOH	Pt(111)	100	0.0377	52.8	0.162	0.086
	Ni(111)	120	0.0377	49.9	0.279	0.204
C_6H_6	Pt(111)	90	0.0288	44.2	0.447	0.389
	Ni(111)	90	0.0288	44.5	0.600	0.542
C_6H_5OH	Pt(111)	90	0.0400	73.2	0.463	0.383
	Ni(111)	150	0.0400	72.2	0.501	0.421

[a] Surface energies of pure liquids of molecular species ($\gamma_{S(liq)}$) are from refs [70,335,336]. Their heats of sublimation (ΔH_{sub}) at the measurement temperature are taken to be equal to the high-coverage limits for their heats of adsorption from the SCAC measurements used to get $Q_{adsorption}/A$, i.e., from refs [325,328,330,337–341] as was proven in those papers to be true to within the accuracy of the absolute calibration of the calorimeter heat signal (3%), except for benzene,[330] where the difference was larger. Adhesion energies (E_{adh}) were determined using the above values in (7.6), assuming that $[Q_{adsorption} - n\cdot\Delta H_{vap,S}]/A$ at room temperature equals $(Q_{adsorption} - n\cdot\Delta H_{sub,S})/A$ here.

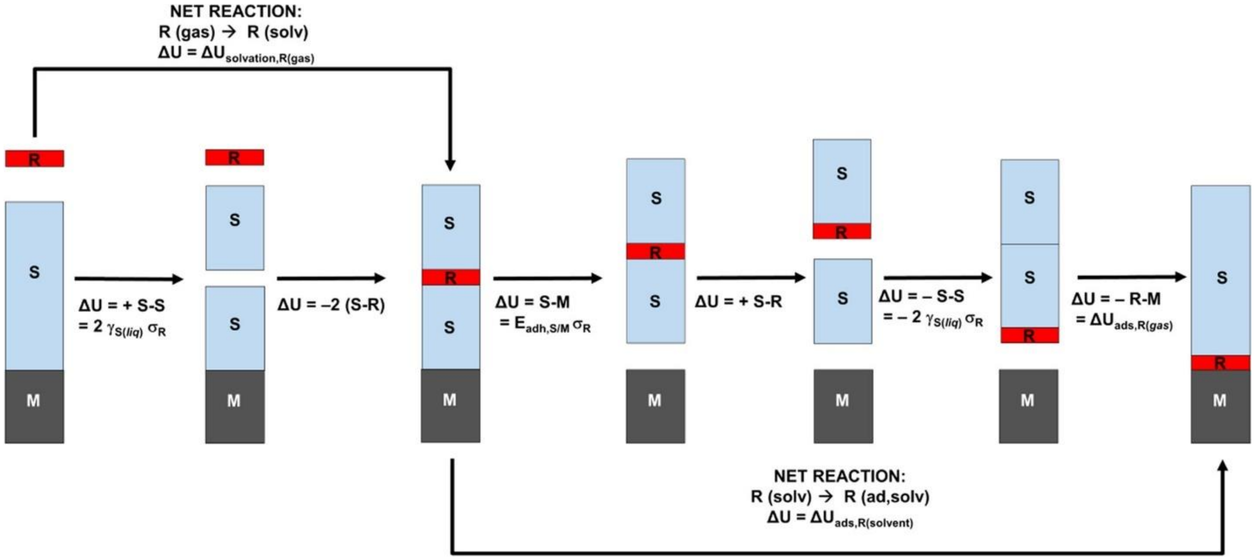

Figure 7.1 Thermodynamic cycle using pairwise bond additivity to relate the energy of adsorption of a flat reactant molecule (R) onto a clean metal surface (M) in the gas phase (−R–M) with that measured in a solvent (S). Here, we show each step's change in internal energy (ΔU) at the temperature of interest. The surface energy ($\gamma_{S(liq)}$) and adhesion energy (E_{adh}) are energies per unit area; so, these are multiplied by the area per adsorbed R molecule (σ_R).

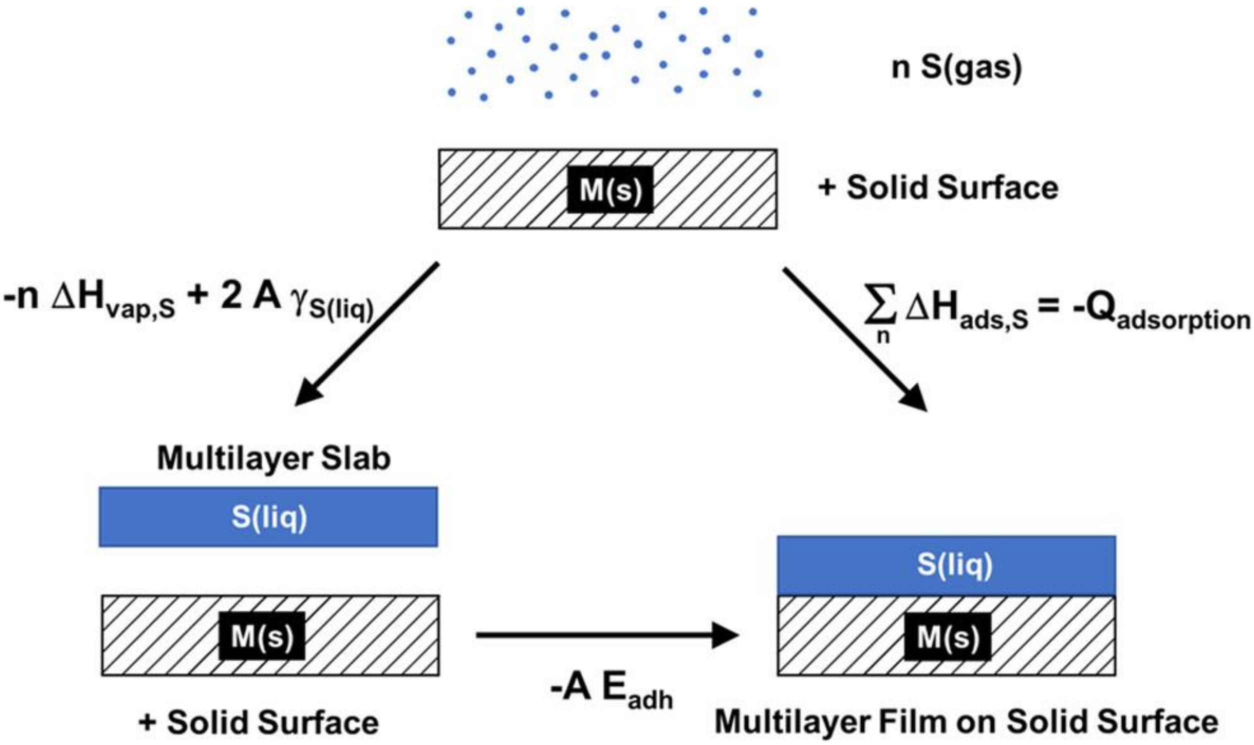

Figure 7.2. Thermodynamic cycle connecting the integrated heat of adsorption of gas-phase solvent molecules (S) to its adhesion energy (E_{adh}) for a thick multilayer film of S(liq) on a surface of some solid material (M) covering some surface area (A).

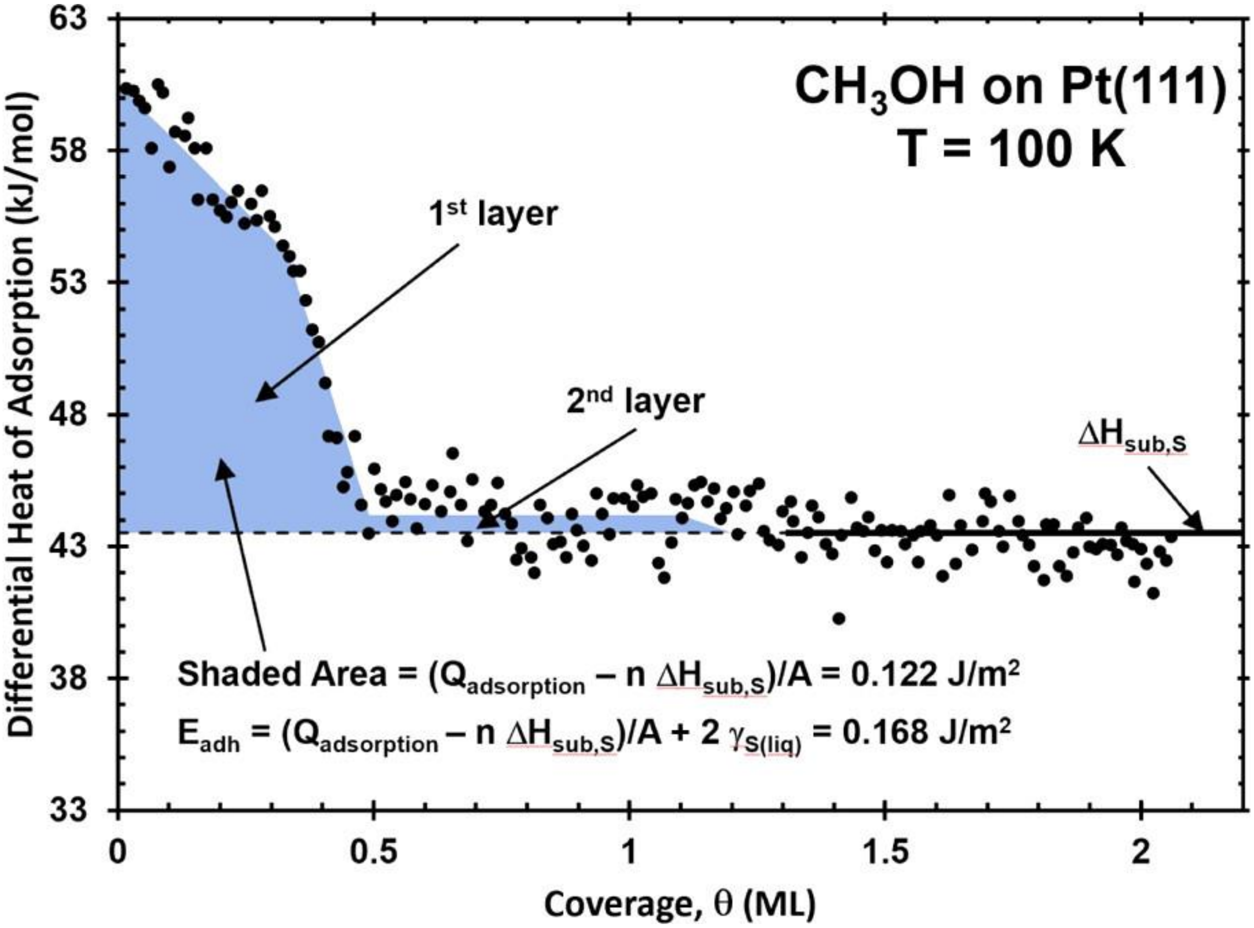

Figure 7.3. Heat of adsorption of methanol gas versus coverage on Pt(111) at 100 K measured by SCAC, from ref [337]. The coverage axis here is in absolute units of “monolayers” or ML, defined as the number of methanol molecules per Pt(111) surface atom where 1 ML corresponds to the surface atom density of Pt(111) (1.51×10^{15} molecules/cm^2). The first layer saturates at a coverage of 1/2 ML. The shaded area is the quantity $[Q_{\mathrm{adsorption}} - n \cdot \Delta H_{\mathrm{sub,S}}]/A$ used to estimate $[Q_{\mathrm{adsorption}} - n \cdot \Delta H_{\mathrm{vap,S}}]/A$ when applying (7.6) to estimate the adhesion energy.

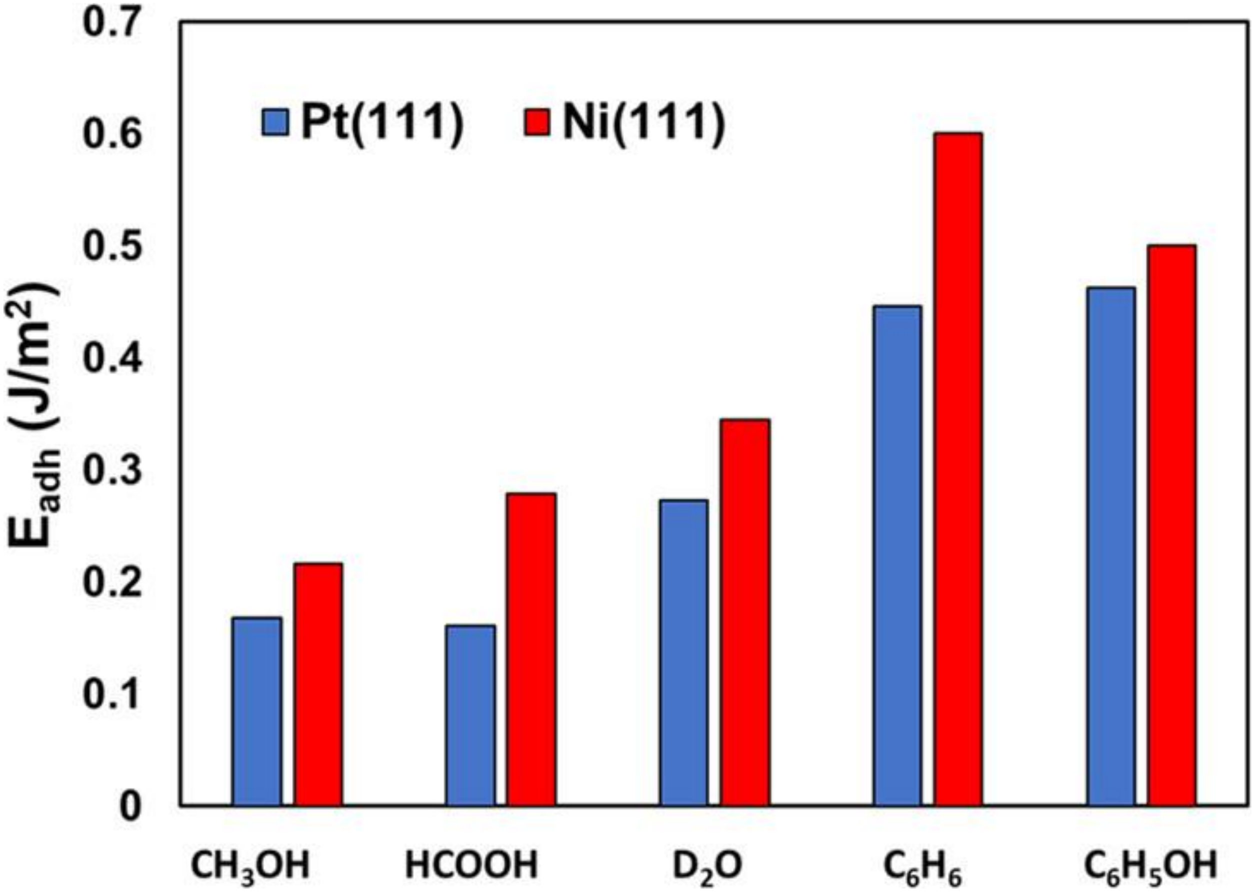

Figure 7.4. Adhesion energies for each liquid solvent on clean Pt(111) and Ni(111) surfaces determined using (7.6) together with low-temperature calorimetric heats of adsorption. See Table 7.1 for temperatures used.

Chapter 8. Adhesion Energies of Liquid Hydrocarbon Solvents onto Pt(111), MgO(100), Graphene, and TiO2(110) from Temperature-Programmed Desorption Energies

This chapter has been published as:

Rumptz, J. R. & Campbell, C. T. (2021). *The Journal of Physical Chemistry C*, 125 (51), 27931-27937.

Chapter Abstract

Knowledge of the adhesion energy between a liquid solvent and a clean solid surface allows for a straightforward estimation of the decrease in the adsorption energy of reactant molecules on that surface due to the presence of that liquid solvent relative to gas-phase adsorption energies. Such estimations in turn can be used to aid the design of liquid-phase catalysts, electrocatalysts, and chemical separations. We report here adhesion energies for 13 liquid-on-solid systems involving alkane and aromatic hydrocarbon films on clean single-crystal surfaces estimated by using temperature-programmed desorption (TPD) measurements of their low-temperature adsorption energies versus coverage up through bulklike multilayer coverages. Because TPD is the most common experimental technique for measuring adsorption energies, the method employed here opens new opportunities for many other estimates of liquid/solid adhesion energies. The adhesion energies of various n-alkanes on MgO(100), graphene (on Pt(111)), and Pt(111) show that the adhesion energy (per unit area) of n-alkanes is nearly independent of chain length. Based on the adhesion energies of hexanes, we show that the adhesion energy changes significantly on different materials, increasing in the order of MgO(100) < graphene < TiO_2(110) ≈ Pt(111).

8.1 Introduction

Heterogeneous catalysis and electrocatalysis in liquid solvents are rapidly growing in importance for chemical, energy, and environmental applications. The presence of the liquid solvent and the choice of solvent often have dramatic effects on activity and/or selectivity.[61–63,310,318,342–345] As with gas-phase catalysis, reaction kinetics in a liquid solvent are determined by the energetics of adsorbed intermediate states in the reaction pathway, and the energies of these states are determined by their adsorption energies in that solvent, which surely change from solvent to solvent. Direct measurements of these adsorption energies in liquid solvents are presently difficult and limited in number, whereas there are many accurate measurements and many calculations of adsorption energies on well-defined surfaces in the gas phase and in vacuum.[295–297,300,303] It would be of great value if one could use these known gas-phase adsorption energetics to estimate adsorption energies in different liquid solvents. Singh and Campbell[64] showed that the liquid solvent's adhesion energy to the solid surface (per unit area of solid surface), E_{adh}, can indeed be used with gas-phase adsorption energies to estimate the adsorption energies of flat molecules (like aromatics) in that solvent by using a simple thermodynamic cycle. Subsequently, they extended that model to charge-neutral adsorbate molecules of arbitrary shape and showed that the adsorption energy in solvent is given by[346]

$$\Delta U_{ads,R(solvent)} = \Delta U_{ads,R(gas)} + \left[E_{adh,S/M} - \frac{\Delta U_{solvation,R(gas)}}{\sigma_{tot}} - \gamma_{S(liq)}\right]\sigma_R \qquad (8.1)$$

(8.1) shows that the adsorption energy of a reactant molecule, R, in a solvent ($\Delta U_{ads,R(solvent)}$) is related to the adsorption energy of that molecule in the gas phase ($\Delta U_{ads,R(gas)}$) modified by the adhesion energy per unit area of the solvent, S, to the metal ($E_{adh,S/M}$), the solvation energy of the molecule ($\Delta U_{solvation,R(gas)}$), the surface energy per unit area of the solvent ($\gamma_{S(liq)}$), and the molecular footprint area (σ_R) and total outer surface area of the reactant molecule

(σ_{tot}), per mole. Note that σ_R refers to the area on the solid surface (per mole of R) where solvent molecules cannot bond to the solid due to the presence of adsorbed R.

When that work was started by Singh and Campbell, there were no values for E_{adh} of solvents to clean metal surfaces, so they developed a method that uses heats of adsorption measured in ultrahigh vacuum (UHV) on clean metal surfaces versus coverage up through multilayer coverage to estimate adhesion energies for liquid solvents.[64] So far, application of that method has been limited to using heats of adsorption from single crystal adsorption calorimetry to determine solvent adhesion energies.[64,347] Because calorimetric measurements of the heat of adsorption are difficult, it is desirable to obtain solvent adhesion energies from more common methods. This present work shows that the necessary heat of solvent adsorption versus coverage data can be obtained from temperature-programmed desorption (TPD) measurements and demonstrates how to apply it to calculate solvent adhesion energies. We also apply it to previously published TPD data and report the adhesion energies of some n-alkanes to MgO(100), C(0001), and Pt(111) as well as the adhesion energies of some cyclic hydrocarbons to $TiO_2(110)$.

8.2 Methods

Temperature-programmed desorption (TPD) is probably the most common experimental technique used to measure adsorption energies on clean solid surfaces. TPD measurements of desorption rate versus temperature can be used with inversion analysis[348] or the Redhead equation[349] to determine desorption energies when adsorption/desorption is reversible. Assuming there is negligible energetic barrier for adsorption (which is a safe assumption when the sticking probability is near unity as it is in the cases analyzed here), the desorption activation energies from these methods are equivalent to the adsorption energies of the reverse process, with a small correction of 1/2RT,[295] which we will ignore here since it cancels out in taking the difference in (8.2) below to get E_{adh}.

TPD data from the literature for n-alkane adsorption on MgO(100), C(0001)/Pt(111), and Pt(111) surfaces were used to determine the adsorption energies of three n-alkanes (n-hexane, n-octane, and n-decane) on each of the above surfaces.[348,350,351] That work utilized a sophisticated inversion-optimization method to determine desorption parameters. Those results are presented in Table 8.1. Using their reported prefactors and peak temperatures, we were able to reproduce their reported adsorption energies within ±0.2 kJ/mol using the Redhead method. They did not extend this inversion analysis into the multilayer regime, so we have estimated a single energy of adsorption for the entire multilayer regime using the peak temperature they reported for the multilayer peak in TPD (at a coverage of ∼2 adsorbed layers) and Redhead analysis. We estimated the prefactor for multilayer desorption based on the prefactor they measured in the first layer and a small entropy-based correction associated with the temperature difference between the multilayer and first-layer TPD peaks, as derived in the Appendix. The multilayer energies estimated in this way are shown in Table 8.1 and Figure 8.1.

Previous work from our group has shown that solvent adhesion energies can be estimated by integrating the differential heat of adsorption from zero coverage up to a coverage where thick, bulklike multilayer films form using[347]

$$E_{adh} = \frac{\left[Q_{adsorption} - n \cdot \Delta H_{vap,S}\right]}{A} + 2\gamma_{S(liq)} \tag{8.2}$$

where E_{adh} is the solvent/solid adhesion energy per unit area, $Q_{adsorption}$ is the integrated heat of adsorption (i.e., the negative of the standard enthalpy of adsorption) of the solvent molecules up through bulklike multilayer coverage for n moles of solvent molecules over an area A, $\Delta H_{vap,S}$ is the standard molar heat of vaporization of the bulk liquid solvent), and $\gamma_{S(liq)}$ is the surface energy per unit area of the bulk solvent. (The "standard" here means at the standard pressure of 1 bar, but since the gases studied here behave ideally up to 1 bar, these enthalpies are all the same as in a vacuum.) The full derivation of this equation based on a simple thermodynamic cycle can be found in other work.[347] In applying this equation, we approximated the surface energy of the liquid solvent using literature values for the surface tension. We have applied (8.2) only to estimate adhesion energies at room temperature,[347] so in principle all values in the equation are at 298 K and 1 bar pressure.

The first part in (8.2), $[Q_{\text{adsorption}} - n\Delta H_{\text{vap,S}}]/A)$, has previously been determined by using heats of adsorption versus coverage measured by single crystal adsorption calorimetry (SCAC).[347] It is obvious, however, that the needed heats of adsorption versus coverage can also be determined by other methods. Here, we use TPD data to obtain these. It is important to note that either method for getting this term for use in (8.2) is limited to use in systems for which the absolute coverage for the adsorbate (molecules/m^2) is well-known at each adsorption energy (or heat) measurement.

It is an unfortunate fact that, at present, most experimental heats of adsorption can only be measured at low temperatures where the adsorbed film grows as a solid rather than a liquid. Thus, we must make the same assumption as we used previously,[347] that the quantity $([Q_{\text{adsorption}} - n\Delta H_{\text{vap,S}}]/A)$at room temperature is approximately equal to the similar quantity $([Q_{\text{adsorption}} - n\Delta H_{\text{sub,S}}]/A)$ at the lower experimental temperature, T, where $\Delta H_{\text{sub,S}}$ is the standard molar heat of sublimation of the bulk solid solvent. This assumes that the molar heat capacities of the solvent molecules in the first adsorbed layer and in the bulk multilayer are the same at all temperatures between T and 298 K (including the contributions from their heats of fusion). Because the heat of fusion is small compared with the heat of vaporization, we expect only a small error from making this assumption. Note that the experimental temperature (T) here is either the sample temperature used in the calorimetry measurement or the peak temperature for desorption seen in the TPD measurement (T_p).

In our previous measurements of E_{adh} using (8.2) and heats of adsorption from calorimetry,[347] we analyzed heats of adsorption versus coverage that converged to a constant multilayer heat value (equal to $\Delta H_{sub,S}$ within data scatter) above a certain coverage. Thus, the quantity ($[Q_{adsorption} - n\Delta H_{sub,S}]/A$) is independent of the choice of final coverage used for getting the integral heat ($Q_{adsorption}$), provided it is above that coverage. By far the largest contribution to $[Q_{adsorption} - n\Delta H_{sub,S}]/A$ came from the first adsorbed molecular layer for all those ten systems measured, since the heat in the second layer was always very close to $\Delta H_{sub,S}$ already, and essentially indistinguishable for the third layer and beyond. In our analysis of TPD data to determine Eadh for n-alkanes below, we neglect this small contribution of the second layer, since it was indistinguishable from the multilayer peak in the TPD results.

8.3 Results and Discussion

Table 8.1 lists the desorption activation energies (ΔE_{des}) and pre-exponential factors (ν) for first-layer and multilayer desorption obtained from published TPD results for n-alkanes on clean MgO(100), one-layer graphene on Pt(111), and clean Pt(111).[348,350,351] The two longest n-alkanes studied (n-octane and n-decane) were found to partially dissociate on Pt(111) and thus could not be studied accurately by using TPD.[351] While these prefactors were found to increase systematically with n-alkane chain length in the range studied in those papers (C1 to C6 or C10), and explained theoretically,[300] the small increase expected for the smaller range of Table 8.1 (a factor of ~30) was not obvious for C(0001) due to experimental error bars (also a factor of ~30).[351]

The multilayer T_p values listed here for alkanes on C(0001) and Pt(111) were obtained from ref [351], while those on MgO(100) were obtained from ref [350].The multilayer prefactors were obtained from the method outlined in the Appendix. The values of ΔE_{des} for the multilayer were computed by using the first-order Redhead equation with these multilayer peak temperatures and prefactors. We note that the ΔE_{des} values for first-layer desorption calculated with the Redhead equation were within ~0.2 kJ/mol of those listed here from the more accurate inversion analysis method, so we assume the errors in ΔE_{des} for multilayer desorption are within 1 kJ/mol.

In using the values from Table 8.1 to estimate adhesion energies on the perfect terraces, we neglect defect sites (populated at low coverage; see below) and assume a steplike decrease in the desorption energy from this first-layer value to this multilayer value at the completion of the first layer. We further assume that the first layer completes at the same nearly closest-packed packing density on graphene and MgO(100) as reported for n-alkanes on Pt(111) based on studies by low-energy electron diffraction (LEED), where that coverage is given by 1/(n + 1) times the Pt(111) surface atom density of 1.51×10^{19} m^{-2}.[352]

The dashed lines in Figure 8.1 show the result of those assumptions in terms of the desorption energy versus coverage for the example case of n-alkanes on graphene(0001). Also shown is the raw inversion analysis result,[351] the solid lines, where stronger binding defect sites were clearly populated at very low coverages, and a constant desorption energy was seen at higher coverages (attributed to adsorbates in 2D islands). Because we are more interested in the adhesion of molecules to pristine (defect-free) terraces, the defect sites are neglected in estimating adhesion energies here. They are therefore calculated from the flat dashed lines shown based on the values in Table 8.1, which will be used for the remainder of this work.

The desorption energies versus coverage, like the dashed lines in Figure 8.1, were used together with (8.2) to calculate the adhesion energies for the systems listed in Table 8.1. These results are summarized in Figure 8.2. As seen, the adhesion energy (per unit area) for n-alkanes shown is almost independent of chain length but increases as MgO(100) < graphene < Pt(111). The independence with chain length is consistent with a model whereby each CH_2 (or CH_3) group in the first layer of adsorbed n-alkanes occupies almost the same area on the surface and has almost the same contribution to the adsorption energy. Consistent with this, it has previously been shown (based on these same TPD data) that the heat of adsorption in the first layer increase with chain length nearly proportional to n for these three surfaces.[350,351]

Figure 8.3 shows the reported desorption activation energies versus coverage for various cyclic hydrocarbons on rutile TiO_2(110), as obtained from inversion analysis of TPD data in ref [353]. These data in Figure 8.3 were used with (8.2) to determine the adhesion energies for these systems. Those adhesion energies are presented in Table 8.2, with some of them (benzene and its methyl substitutions) plotted in Figure 8.4 versus their numbers of carbon atoms.

As seen in Figure 8.4, the adhesion energy is nearly constant for all these methyl-substituted benzenes but increases slightly with methyl addition, by 0.0147 J/m^2 per added methyl group, on average, from the value of 0.139 J/m^2 for simple benzene. We attribute this increase to the fact that the methyl-substituted benzenes have increasingly higher heat of adsorption in the first layer (by ~10 kJ/mol per added methyl), but their packing density at completion of the first layer (0.51 ML for trimethylbenzene) is nearly as high as that of benzene (0.56 ML).

Table 8.2 also presents a comprehensive list of all the liquid solvent adhesion energies on clean single crystal surfaces that have been estimated at 298 K by using (8.2) and the adsorption energies versus coverages measured at lower temperatures in ultrahigh vacuum by TPD (in this present paper) or by SCAC in earlier work.[347] As seen, the value for n-hexane on Pt(111) terraces determined here (0.157 J/m^2) is similar to that previously reported for methanol on Pt(111) (0.168 J/m^2) but considerably smaller than for water on Pt(111) and much smaller than for the aromatic molecules on Pt(111). Interestingly, the adhesion energy for n-hexane on MgO(100) (0.051 J/m^2) is much weaker than that for cyclohexane on TiO_2(110) (0.135 J/m^2), while this value on TiO_2(110) is nearly as large as for n-hexane on Pt(111) (0.157 J/m^2). We attribute this to the well-known reactivity of the coordinatively unsaturated Ti atoms on this TiO_2 surface facet.[353]

While we know of no other values of liquid solvent adhesion energies that have been measured on solid surfaces that were verifiably clean, there are quite a few old measurements that were made on a variety of solids (metals, oxides, and graphite) and on liquid mercury that were not verified to be clean by surface analysis. Those values were obtained by using a combination of the contact angle for the liquid droplet and the pressure-integrated adsorption isotherm, as reviewed by Zisman in 1964.[354] The value there for n-heptane on graphite (0.097 J/m^2) is within 0−2% of the values we report in Table 8.2 for n-octane and n-hexane on clean graphene(0001). Of the solid surfaces reported there, graphite is probably the easiest to keep clean, so this seems reasonable. The values for water, propanol, and benzene on graphite there (0.136, 0.118, and 0.096 J/m^2, respectively) might thus be somewhat reliable. The values there for n-heptane on Cu and Fe (0.069 and 0.093 J/ m^2) are both considerably below our value for n-hexane on Pt(111) in Table 8.2 (0.157 J/m^2), probably due to surface contamination. The value there for n-octane on Hg (0.123 J/ m^2) is much closer to this clean Pt(111) value, but liquid Hg surfaces are easier to keep clean. The value for water on Hg there (0.174 J/m^2) might thus be rather reliable, as also with the values listed there for propanol, acetone, and benzene on liquid Hg. The value there for n-heptane on TiO_2 (0.078 J/m^2) is considerably below our value for cyclohexane on clean TiO_2(110) in Table 8.2 (0.137 J/m^2), again probably due to surface contamination.

8.4 Conclusions

Using published TPD data for desorption (adsorption) energies versus coverage, we have estimated the adhesion energies for 13 different liquid/solid interfaces, including alkanes and aromatic hydrocarbons on clean, single-crystal surfaces of several materials (Pt(111), graphene on Pt(111), MgO(100), and rutile-TiO_2(110)). The results of these TPD- based estimates of adhesion energies are listed in Table 8.2, along with all the liquid adhesion energies determined previously on clean single-crystals surfaces by using heats of adsorption versus coverage measured by single crystal adsorption calorimetry at low temperatures. These solvent adhesion energies can be used along with thermodynamic bond-additivity models such as that recently proposed by Akinola et al.[346] to estimate the effects of liquid solvents on the adsorption energies of catalytic and electrocatalytic reaction intermediates (compared to their values in the gas phase). Estimates of these adsorption energies in liquid solvent allow for the estimation of rates and equilibrium constants important in many chemical technologies that are employed in liquid solvents, including catalysts, electrocatalysts, and adsorption- based separations.

8.5 Appendix. Estimating the Prefactor for Multilayer Desorption

The prefactors for desorption derived by using the inversion analysis of TPD data described in the main text only apply to the first molecular layer's desorption. We estimated the multilayer desorption prefactors based on those monolayer prefactors. Because the prefactor depends weakly on temperature even for the same adsorbate system, and since the multilayer desorbs at a lower temperature than the corresponding monolayer, it was necessary to correct the monolayer prefactors to be suitable for multilayer desorption. We assumed here that this difference in prefactor arises solely from the fact that the multilayer and monolayer desorb at different peak temperatures during TPD, and that there is no other difference in the molecule's entropy in these two molecularly adsorbed forms. The transition state for desorption is the same in both cases: a 2D gas well separated from the surface, so that it feels no interaction with the surface.

The prefactor for monolayer desorption has been shown to be approximately equal to:[355]

$$\nu_{des} = \frac{k_B T}{h} \exp\left[\frac{0.3\, S^0_{gas} + 3.3R - S^0_{gas,1D\, trans}}{R}\right]$$

where S^0_{gas} is the standard-state entropy of the gas molecule at the same temperature T, $S^0_{gas,1Dtrans}$ is the contribution to that entropy of one translation degree of freedom (which is always lost upon adsorption), and R is the gas constant. This equation has proven to fit experimentally measured prefactors very well, with a standard deviation from experiments in log(des υ /s^{-1})of 0.86.[355] The ratio of prefactors for multilayer (multi)/ monolayer (ML) desorption is then

$$\frac{\nu_{des,multi}}{\nu_{des,ML}} = \frac{\frac{k_B T_{p,multi}}{h} \exp\left[\frac{0.3\, S^0_{gas}(T_{p,multi}) + 3.3R - S^0_{gas,1D\, trans}(T_{p,multi})}{R}\right]}{\frac{k_B T_{p,ML}}{h} \exp\left[\frac{0.3\, S^0_{gas}\left(T_{p,ML}\right) + 3.3R - S^0_{gas,1D\, trans}\left(T_{p,ML}\right)}{R}\right]}$$

$$\frac{\nu_{des,multi}}{\nu_{des,ML}} = \frac{T_{p,multi} \exp\left[\frac{0.3\, S^0_{gas}(T_{p,multi}) - S^0_{gas,1D\, trans}(T_{p,multi})}{R}\right]}{T_{p,ML} \exp\left[\frac{0.3\, S^0_{gas}\left(T_{p,ML}\right) - S^0_{gas,1D\, trans}\left(T_{p,ML}\right)}{R}\right]}$$

where $T_{p,multi}$ and $T_{p,ML}$ are the TPD peak temperatures for multilayer and monolayer desorption, respectively.

For a nonlinear molecule, S^0_{gas} varies with temperature approximately as c_1 +3R ln(T/K),[356] where c_1 is a constant and $S^0_{gas,1Dtrans}$ = c_2 + (5/6)R ln(T/K) where c_2 is a constant. This equation for $S^0_{gas,1Dtrans}$ can be easily seen from eq 2 in ref [351]. Substituting these expressions for S^0_{gas} and $S^0_{gas,1Dtrans}$ into the preceding equation for the prefactor ratio gives

$$\frac{\nu_{des,multi}}{\nu_{des,ML}} = \left(\frac{T_{p,multi}}{T_{p,ML}}\right) \exp\left[0.3\left(3\, ln\left(\frac{T_{p,multi}}{T_{p,ML}}\right)\right) - \left(\frac{5}{6}\ ln\left(\frac{T_{p,multi}}{T_{p,ML}}\right)\right)\right]$$

$$\frac{\nu_{des,multi}}{\nu_{des,ML}} = \left(\frac{T_{p,multi}}{T_{p,ML}}\right) \exp\left[\left(\frac{9}{10} - \frac{5}{6}\right) ln\left(\frac{T_{p,multi}}{T_{p,ML}}\right)\right] = \left(\frac{T_{p,multi}}{T_{p,ML}}\right)^{1.067}$$

For the adsorption of cyclic hydrocarbons on $TiO_2(110)$, we used the coverage-dependent desorption energy data from Chen et al. to estimate the adhesion energies.[353] That work utilized the inversion of the Polanyi−Wigner equation with TPD desorption rates to obtain coverage-dependent desorption energies from zero to multilayer coverages. Because they were not able to accurately determine the desorption prefactors experimentally, they instead selected three physically reasonable prefactors based on different assumed mobilities of the adsorbed hydrocarbons. These three prefactors corresponded to a completely immobile adsorbed phase (ν_{max}), a completely mobile adsorbed phase with two degrees of translational freedom and one degree of rotational freedom about the surface normal ($\nu_{2T,1R}$), and an intermediate prefactor with one degree of translational freedom but no rotational modes ($\nu_{1T,0R}$). They found that the intermediate prefactor ($\nu_{1T,0R}$) best matched the results obtained by using DFT and transition state theory (ν_{theory}), and so they used that $\nu_{1T,0R}$ in their analysis at all coverages, including multilayer coverages. We use their coverage-dependent desorption energies based on that same prefactor here for calculating adhesion energies.

8.6 Figures and Tables

Table 8.1. Experimental TPD Results for *n*-alkanes on MgO(100), C(0001)/Pt(111), and Pt(111) at conditions where they form nearly close-packed 2D islands with a nearly coverage-independent desorption energy (from refs [348,350,351])[a]

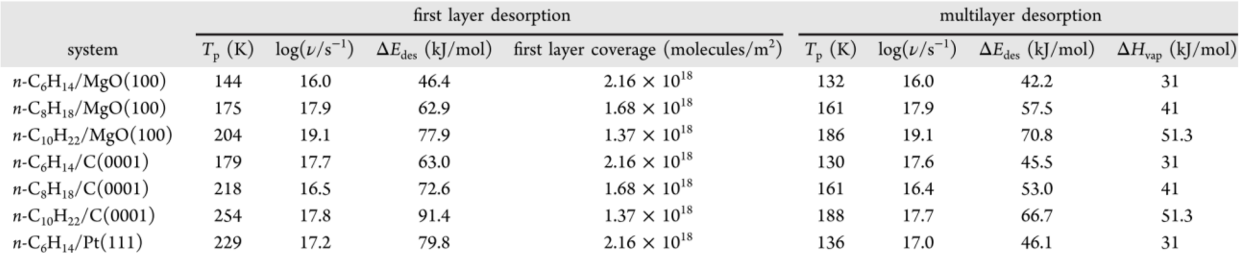

	first layer desorption				multilayer desorption			
system	T_p (K)	$\log(\nu/s^{-1})$	ΔE_{des} (kJ/mol)	first layer coverage (molecules/m^2)	T_p (K)	$\log(\nu/s^{-1})$	ΔE_{des} (kJ/mol)	ΔH_{vap} (kJ/mol)
n-C_6H_{14}/MgO(100)	144	16.0	46.4	2.16×10^{18}	132	16.0	42.2	31
n-C_8H_{18}/MgO(100)	175	17.9	62.9	1.68×10^{18}	161	17.9	57.5	41
n-$C_{10}H_{22}$/MgO(100)	204	19.1	77.9	1.37×10^{18}	186	19.1	70.8	51.3
n-C_6H_{14}/C(0001)	179	17.7	63.0	2.16×10^{18}	130	17.6	45.5	31
n-C_8H_{18}/C(0001)	218	16.5	72.6	1.68×10^{18}	161	16.4	53.0	41
n-$C_{10}H_{22}$/C(0001)	254	17.8	91.4	1.37×10^{18}	188	17.7	66.7	51.3
n-C_6H_{14}/Pt(111)	229	17.2	79.8	2.16×10^{18}	136	17.0	46.1	31

[a] Included are the TPD peak temperatures (T_P), the desorption prefactors (ν), and the activation energy of desorption (ΔE_{des}) determined by inversion analysis of TPD spectra at 50% completion of the first molecular layer and also for bulklike multilayers. Also listed are the standard enthalpies of vaporization (ΔH_{vap}) at 298 K, from ref [357].

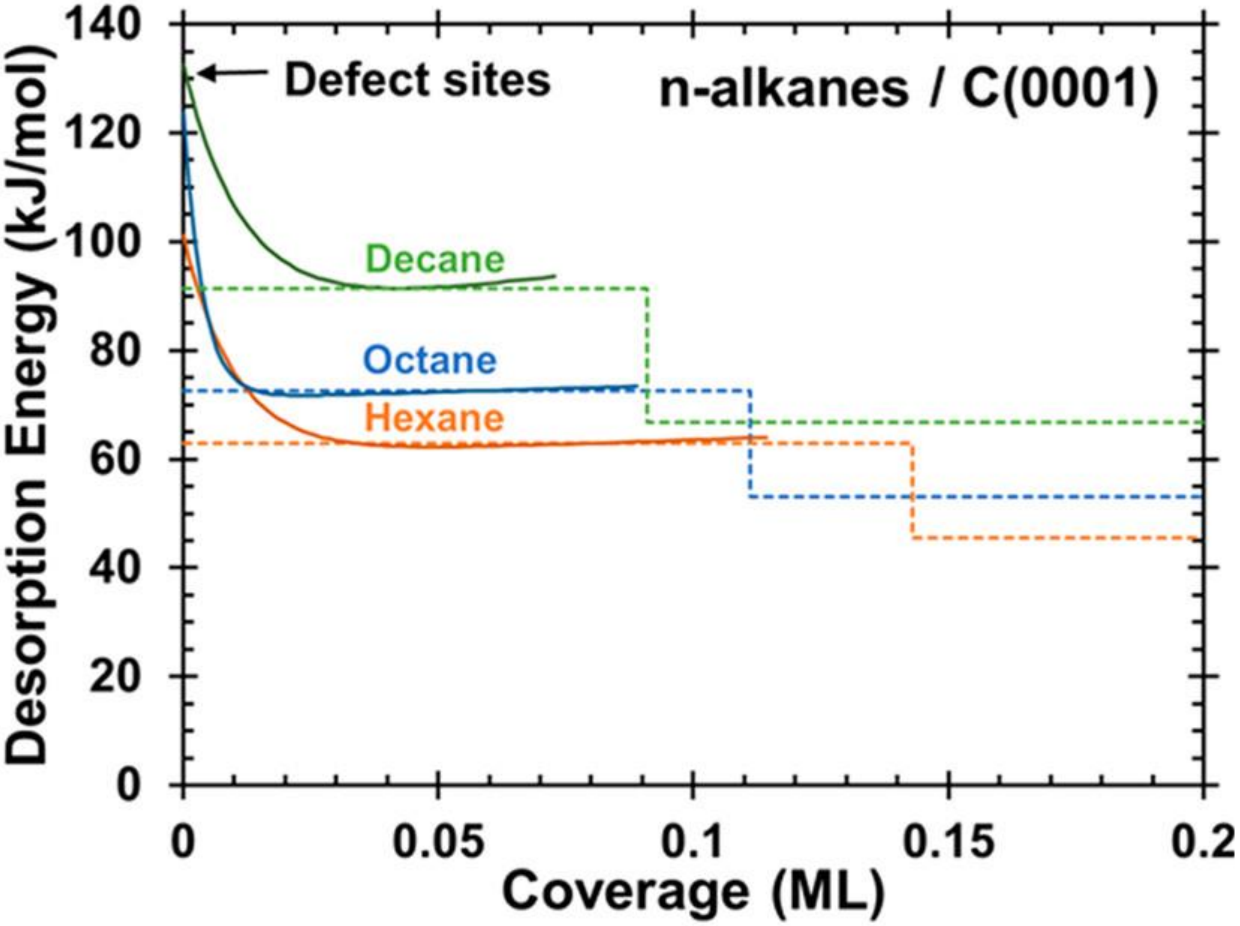

Figure 8.1. Desorption energies for decane (green), octane (blue), and hexane (orange) adsorbed on a single-layer film of graphene (single-layer C(0001)) on Pt(111)). The absolute coverage of 1 ML here is defined as 1 ML = 1.51×10^{19} molecules/m^2, which is equivalent to the atomic density of the underlying Pt(111) surface. The inversion method (solid lines) shows the effect of defects on the energy of desorption. The dashed lines show the defect-free desorption energy, assumed to be coverage-independent in the first layer and equal to the result from the inversion analysis at completion of 50% of the first molecular layer and equal to the multilayer desorption energy from Table 8.1 after completion of the first layer.

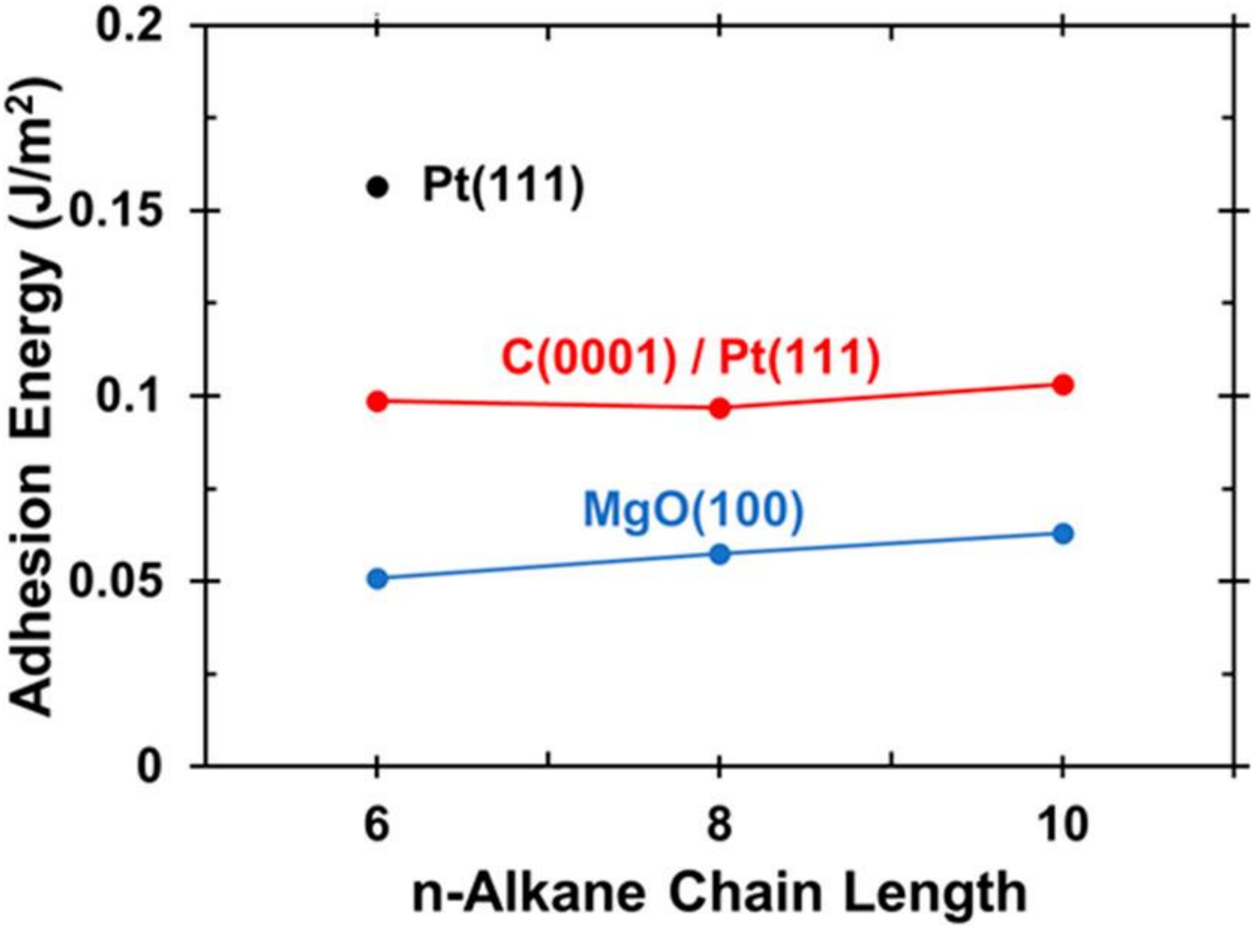

Figure 8.2. Calculated adhesion energies of three n-alkanes (n-hexane, n-octane, and n-decane) to MgO(100) (blue), C(0001)/Pt(111) (red), and Pt(111) (black) using the Redhead method.

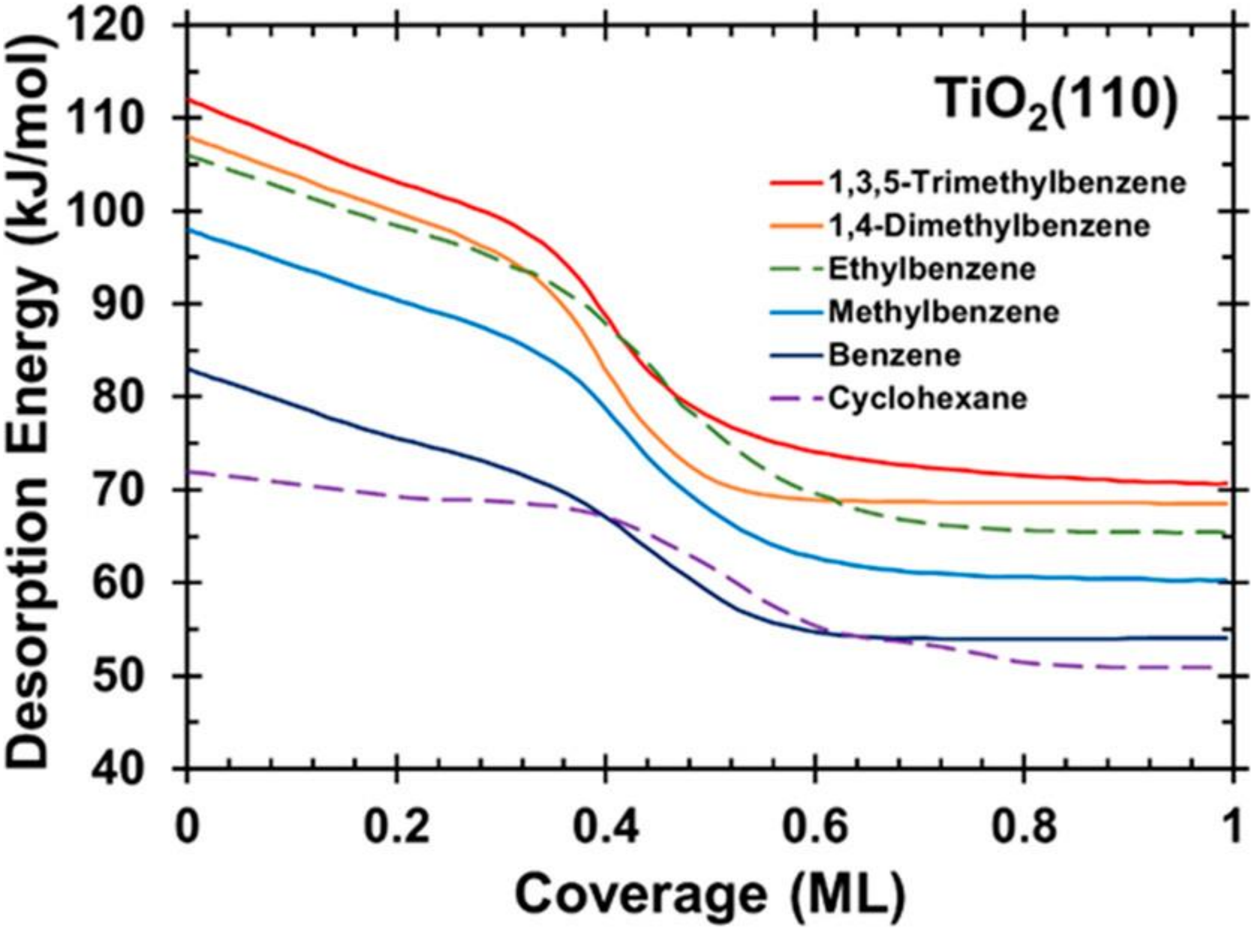

Figure 8.3. Activation energies for desorption versus coverage for various cyclic hydrocarbons on rutile-TiO_2(110), as determined by inversion analysis of TPD data (assuming prefactors corresponding to nonrotating adsorbates, freely moving along the Ti_{5c} rows), from ref [353]. The absolute coverage of 1 ML here is defined as 1 ML = 5.2×10^{18} molecules/m^2, which is the number of 5-fold coordinated Ti sites on the TiO_2(110) surface. The contribution from stronger binding defects in the low coverage regime ($\theta < 0.1$ ML) has been removed by extrapolating the higher coverage desorption energies to the value in the zero-coverage limit for Ti_{5c} terraces reported in Table 8.2 of ref [353].

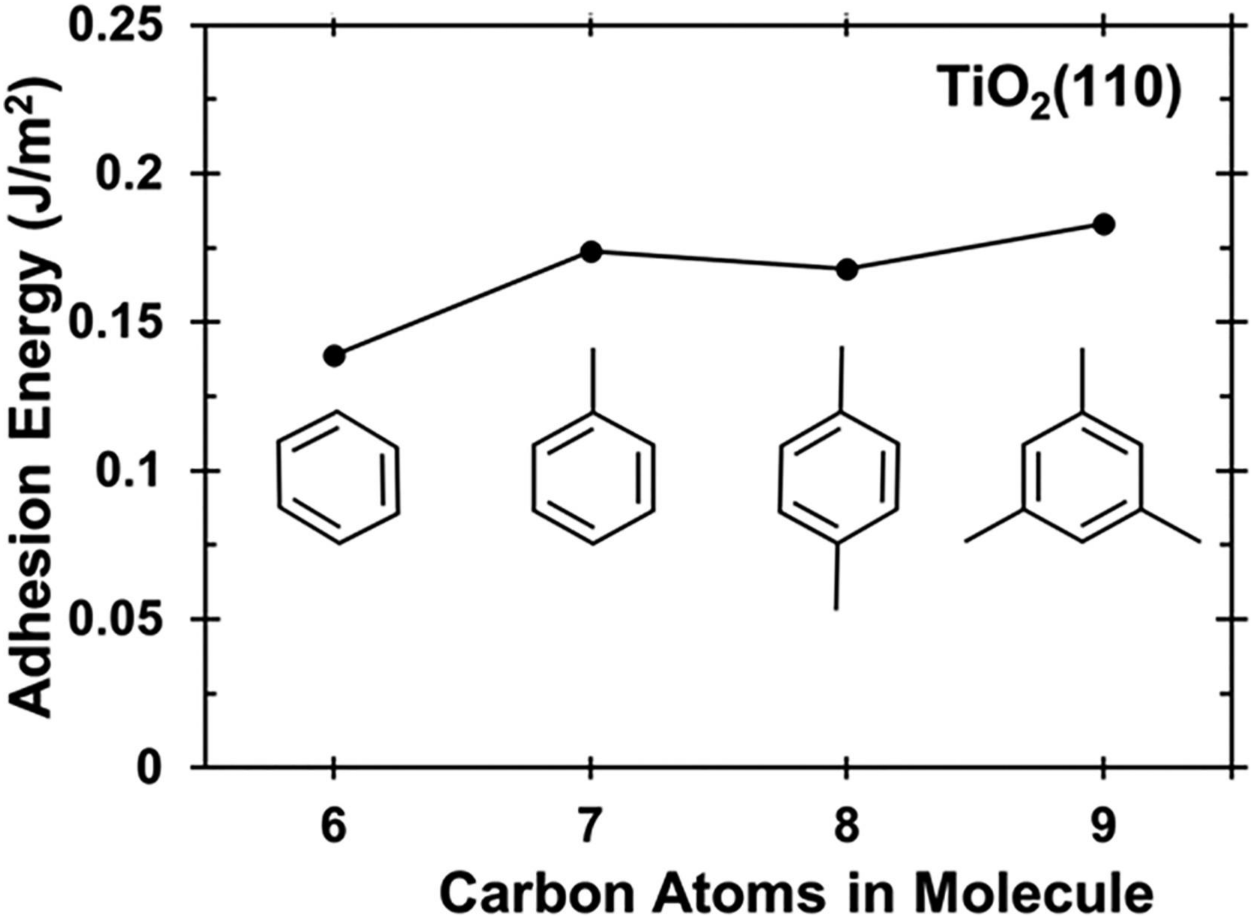

Figure 8.4. Adhesion energies of benzene and alkyl-substituted benzene derivatives onto the rutile-TiO_2(110) surface, per unit TiO_2 surface area, determined by applying (8.2) to the TPD desorption energies versus coverage in Figure 8.3, taken from ref [353].

Table 8.2. Adhesion energies (E_{adh}) of liquid solvent films to single crystal surfaces at 298 K estimated via (8.2), and quantities used in that equation, including the experimental measurement temperature of calorimetry or first-layer Desorption in TPD (T), measured difference between the integrated heat of adsorption and the heat of sublimation per unit area ($[Q_{ads} – n\Delta H_{sub}]/A$), and the surface energy of the liquid solvent at 298 K ($\gamma_{S(liq)}$), taken from the literature ([68,69,347])

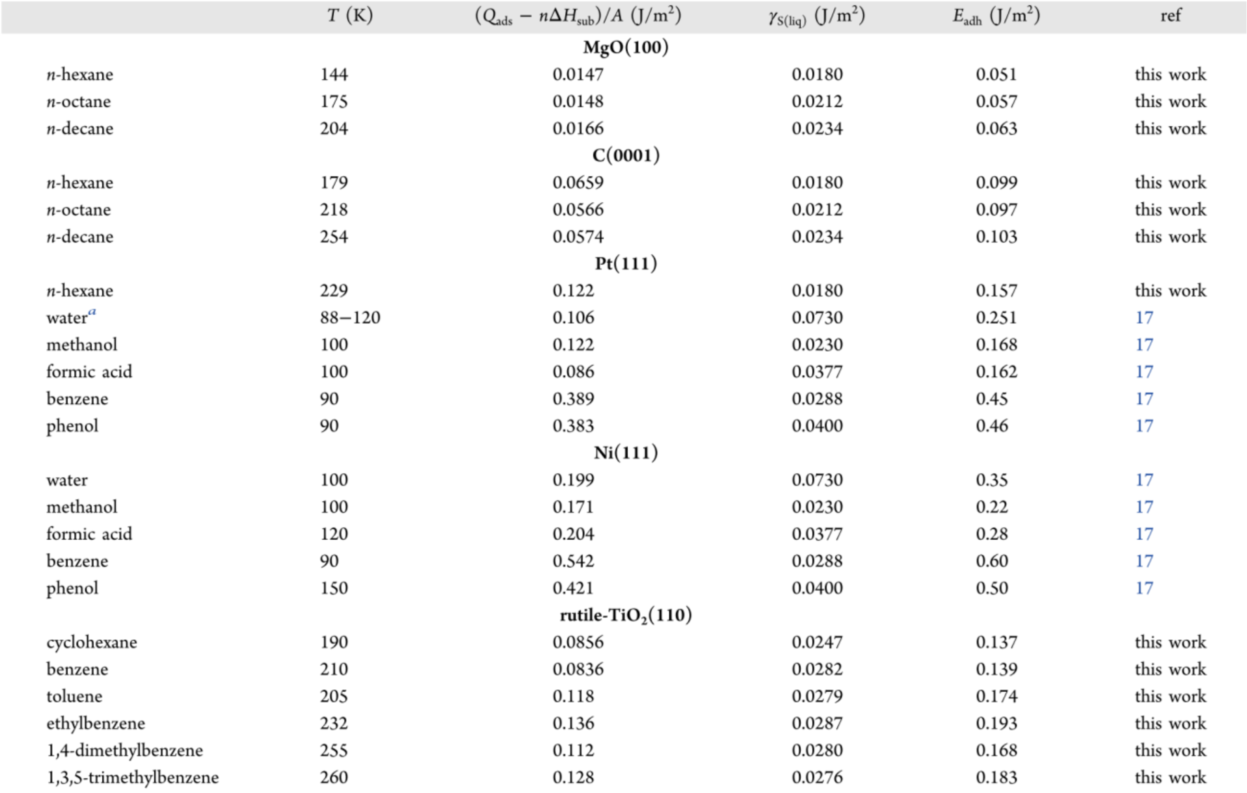

	T (K)	$(Q_{ads} - n\Delta H_{sub})/A$ (J/m^2)	$\gamma_{S(liq)}$ (J/m^2)	E_{adh} (J/m^2)	ref
		MgO(100)			
n-hexane	144	0.0147	0.0180	0.051	this work
n-octane	175	0.0148	0.0212	0.057	this work
n-decane	204	0.0166	0.0234	0.063	this work
		C(0001)			
n-hexane	179	0.0659	0.0180	0.099	this work
n-octane	218	0.0566	0.0212	0.097	this work
n-decane	254	0.0574	0.0234	0.103	this work
		Pt(111)			
n-hexane	229	0.122	0.0180	0.157	this work
water[a]	88−120	0.106	0.0730	0.251	17
methanol	100	0.122	0.0230	0.168	17
formic acid	100	0.086	0.0377	0.162	17
benzene	90	0.389	0.0288	0.45	17
phenol	90	0.383	0.0400	0.46	17
		Ni(111)			
water	100	0.199	0.0730	0.35	17
methanol	100	0.171	0.0230	0.22	17
formic acid	120	0.204	0.0377	0.28	17
benzene	90	0.542	0.0288	0.60	17
phenol	150	0.421	0.0400	0.50	17
		rutile-TiO$_2$(110)			
cyclohexane	190	0.0856	0.0247	0.137	this work
benzene	210	0.0836	0.0282	0.139	this work
toluene	205	0.118	0.0279	0.174	this work
ethylbenzene	232	0.136	0.0287	0.193	this work
1,4-dimethylbenzene	255	0.112	0.0280	0.168	this work
1,3,5-trimethylbenzene	260	0.128	0.0276	0.183	this work

[a] Average of two calorimetry runs at different temperatures (88 and 120 K).

[b] Note that the listed “ref 17” in this table refers to ref [347] in this thesis.

Chapter 9. Conclusions and Future Outlook

The work presented in this dissertation describes progress that has been made in understanding how catalyst performance depends on (1) the structure of the catalyst and (2) the solvent. While these two important factors influencing the catalyst performance are intimately related in real catalysts, they were studied at a fundamental level using very different methods and so this dissertation was roughly broken into two parts to describe them separately.

In chapters 2-6 of this dissertation, the relationship between the catalyst structure and its chemical properties was studied with experimental measurements of metal heats of adsorption onto single-crystal oxide and carbon surfaces. These measurements provide the size and support dependence of the metal chemical potential and important descriptors for this property such as the adhesion energy between the metal and the support. This metal chemical potential in turn can be used to design catalysts with long-term sinter resistance and altered adsorption energies of small molecules.

The effect of the solvent on the adsorption energies of small molecules was studied in Chapters 7 and 8 by analyzing the adsorption energies of solvent molecules onto different single-crystal surfaces. From these adsorption energies, we determined the adhesion energies of many solvents onto many single-crystal surfaces. Work by the Campbell group, including that described in Chapters 7 and 8, suggest that these solvent adhesion energies can be used with a thermodynamic cycle to explain how the adsorption energies of small molecules depend on the solvent of choice. The combination of this thermodynamic cycle with measured solvent adhesion energies provides researchers with a route to tailor the adsorption energies of small molecules in the liquid-phase and intelligently design better catalysts and electrocatalysts.

Chapter 3 discusses a study of the adsorption, physical structure, and charge transfer of nickel nanoparticles on $CeO_2(111)$ using a combination of experimental measurements and DFT calculations. These experiments showed that the extent of reduction of $CeO_{2-x}(111)$ does not significantly affect the particle density, however changing the temperature from 300 K to 100 K on $CeO_{1.95}(111)$ resulted in ~3-fold larger particle densities. The heats of adsorption onto $CeO_{1.95}(111)$ at 300 K showed an initial decrease in the heats of adsorption from 345 kJ/mol to 323 kJ/mol within the first 0.2 ML before a gradual increase to the bulk Ni heat of sublimation. This initial decrease in heats was not observed on reduced $CeO_{1.8}(111)$ or at 100 K on $CeO_{1.95}(111)$ and was thus attributed to the preferential binding of the Ni particles at oxygenated step-edge sites. This finding was corroborated by DFT calculations showing a strong preference for Ni binding to oxygen atoms which are in excess at the step-edges. XPS measurements showed that Ni atoms are oxidized upon adsorption and the extent of electron transfer decreases as the particles grow. This agreed with DFT calculations which confirmed this charge transfer and showed that the charge is localized to the interfacial atoms in the particles and support. These electronic effects significantly change the chemical properties of the Ni nanoparticles on ceria and help explain the catalytic properties of Ni/CeO_2 materials.

In chapter 4 we described the adsorption and adhesion of silver nanoparticles to TiO_2 thin films on Mo(110) investigated with a combination of LEED, SCAC, LEIS, and XPS. A LEED analysis of the TiO_2 films showed these films to be $TiO_2(100)$ with three rotational domains rotated at ~120˚ with respect to the others. Particle density measurements with LEIS showed a ~3-fold higher particle density for $Ag/TiO_2(100)$ at 100 K compared with at 300 K due to the lower diffusion at the lower temperature. At 100 K, an initial heat of adsorption of 141 kJ/mol was measured which is 67 kJ/mol lower than at 300 K. This is likely the result of particle size differences as was shown by comparing the heat of adsorption as a function of the average particle diameter. Using both a thermodynamic cycle as well as fitting the measured Ag chemical potential to a well-studied model, an adhesion energy of 2.5 ± 0.1 J/m^2 was determined for Ag/TiO_2(100) in the large particle size limit.

Chapter 5 of this dissertation investigated the thermodynamics and morphology of silver nanoparticles supported on graphene/Ni(111). He^+ LEIS growth mode experiments showed a low saturation particle density for Ag/graphene compared with Ag/oxides. In addition, the particle densities were ~3-fold higher at 300 K due to a larger diffusion constant at 300 K. The initial sticking probability of Ag/graphene was 75% at 300 K and 85% at 100 K which is consistent with a weak interaction of Ag monomers to the graphene support. The initial heat of adsorption at 300 K was 230 kJ/mol which quickly rose to 270 kJ/mol due to the rapidly growing particle size. At 100 K, the initial heat of adsorption was 223 kJ/mol which dropped to 207 kJ/mol in the next pulse before gradually rising to the bulk Ag heat of sublimation. This initial drop in the heats of adsorption at 100 K is likely due to the small particles binding at defect sites while this effect is washed out at 300 K due to larger particles at low coverages. The chemical potential as a function of average particle diameter showed a fantastic agreement between the two temperatures and shows that the chemical potential equation developed by our group for oxides can extend to carbon-based support materials as well. The adhesion energy for Ag/graphene was determined to be 1.8 ± 0.1 J/m^2 using both a thermodynamic cycle as well as fitting the measured chemical potential to that same equation used by our group for metals on oxide supports.

Chapter 6 describes the results of experiments investigating the adsorption of nickel nanoparticles onto graphene/Ni(111). The heat of Ni adsorption at 300 K is initially 336 kJ/mol and rapidly increases with coverage before reaching the bulk heat of Ni sublimation by 2 ML. At

100 K, the heat of Ni adsorption begins lower at 230 kJ/mol and reaches the heat of sublimation by 3.5 ML. Particle morphology measurements with He^+ LEIS showed that Ni grows as flat-topped FCC islands with a thickness of ~1.5 nm when deposited at 300 K and as hemispherical HCP particles with a particle density of 2.23×10^{16} particles/m^2 when deposited at 100 K. Using the Ni heats of adsorption and LEIS particle density, we determined the Ni chemical potential as a function of average particle diameter and found an adhesion energy of 3.60 J/m^2 for Ni particles on graphene/Ni(111). This adhesion energy is in good agreement with STM and DFT investigations of Ni/graphene/Ni(111) and is double the adhesion energy of Ag/graphene/Ni(111).

In chapters 7 and 8, we described the adhesion energies of solvent films to a variety of single crystal materials. These works showed the possibility of using data from SCAC or TPD to determine the adhesion energies of solvents to well-defined single crystal surfaces. These adhesion energies can in turn be used with a simple bond-additivity model to estimate the change in adsorption energy of molecules in a solvent when compared with in the gas-phase. Using the methods discussed in those chapters, we determined the adhesion energies of 23 solvent / single-crystal surfaces and developed explanations on how the solvent and material surface can influence these adhesion energies. It is our hope that these adhesion energies will be used to help clarify solvent effects on adsorption energies and rate constants for catalysts, electrocatalysts, and adsorption-based separations.

For metals on oxide supports there are now predictive correlations of the adhesion energy with the metal's oxophilicity, however how this adhesion energy correlates with the properties of the oxide is still unclear. While the data for Ag/TiO_2(110) supports a trend of decreasing adhesion energy with increasing the enthalpy of oxide reduction, additional data on the adhesion energies of metals to different oxides must be collected to obtain more quantitative relationships.

The work presented in Chapters 5 and 6 of this dissertation provided some of the first experimental measurements of the adhesion energies of metals onto graphene as a model for carbon-based supports. We expect that the adhesion energies of metals on graphene should follow predictive trends in much the same way as they have for metals on oxides, perhaps using “carbophilicity” rather than an oxophilicity. Additional data of adhesion energies for metals on graphene must be collected for any sort of predictive trends to immerge. Our group has almost finished a project studying the adsorption of palladium onto graphene as of the writing of this thesis which will hopefully shine light onto this open question. Future experiments onto different carbon-based supports including multilayer graphite, diamond, or other forms of modified carbon may also be of interest in unraveling these trends.

Chapters 7 and 8 of this dissertation included new adhesion energies of many solvent films onto many single-crystalline surfaces. While there is some data that supports the fact that these adhesion energies can be used to calculate the adsorption energies of small molecules in those solvents, there is a need for many more careful experiments studying the heats of adsorption of small molecules in solvents to confirm these relationships. If these relationships prove to be quantitative for a large range of molecules, surfaces, and solvents then further study of the adhesion energies from both experimental and theoretical points of view will be incredibly important.

Finally, it is our hope that the performance-based properties of the structure and environment of catalysts discussed in this dissertation are not limited to single-crystalline model catalyst systems. Our primary goal is that the relationships developed by our research group for model systems can be used in practice by other researchers to develop more effective real catalysts. Our work is most impactful if used by others to aid in the rational design of new materials that can have a tangible effect on chemical production, energy usage, and pollution prevention.

Chapter 10. Bibliography

1. J. Hagen. *Industrial catalysis: A practical approach*. *Industrial Catalysis: A Practical Approach* (2015). doi:10.1002/9783527684625
2. J. Hagen, I. Chorkendorff, & J. W. Niemantsverdriet. *Concepts of Modern Catalysis and Kinetics Catalysis from A to Z Principles and Practice of Heterogeneous Catalysis Catalytic Membranes and Membrane Reactors Spectroscopy in Catalysis*. *Simulation* (2006).
3. J. N. Armor. A history of industrial catalysis. *Catal. Today* **163**, 3–9 (2011).
4. C. M. Friend & B. Xu. Heterogeneous catalysis: A central science for a sustainable future. *Accounts of Chemical Research* **50**, 517–521 (2017).
5. R. Schlögl. Heterogeneous catalysis. *Angewandte Chemie - International Edition* **54**, 3465–3520 (2015).
6. J. M. Lents & W. J. Kelly. Cleaning the Air in Los Angeles. *Sci. Am.* **269**, 32–39 (1993).
7. C. T. Campbell. Ultrathin metal films and particles on oxide surfaces: structural, electronic and chemisorptive properties. *Surf. Sci. Rep.* **27**, 1–111 (1997).
8. D. W. Goodman. Model Studies in Catalysis Using Surface Science Probes. *Chem. Rev.* **95**, 523–536 (1995).
9. L. T. Roling, L. Li, & F. Abild-Pedersen. Configurational Energies of Nanoparticles Based on Metal-Metal Coordination. *J. Phys. Chem. C* **121**, 23002–23010 (2017).
10. L. T. Roling & F. Abild-Pedersen. Structure-Sensitive Scaling Relations: Adsorption Energies from Surface Site Stability. *ChemCatChem* **10**, 1643–1650 (2018).
11. R. D. Cortright, J. A. Dumesic, B. C. Gates, & H. Knozinger. Kinetics of heterogeneous catalytic reactions: Analysis of reaction schemes. *Adv. Catal.* **46**, 161–264 (2001).

12. C. T. Campbell, S. C. Parker, & D. E. Starr. The effect of size-dependent nanoparticle energetics on catalyst sintering. *Science* **298**, 811–814 (2002).

13. S. C. Parker & C. T. Campbell. Kinetic model for sintering of supported metal particles with improved size-dependent energetics and applications to Au on TiO2 (110). *Phys. Rev. B - Condens. Matter Mater. Phys.* **75**, (2007).

14. T. W. Hansen, A. T. Delariva, S. R. Challa, & A. K. Datye. Sintering of Catalytic Nanoparticles: Particle Migration or Ostwald Ripening? *Acc. Chem. Res.* **46**, 1720–1730 (2013).

15. Z. Hou, J. Gao, J. Guo, D. Liang, H. Lou, & X. Zheng. Deactivation of Ni catalysts during methane autothermal reforming with CO2 and O2 in a fluidized-bed reactor. *J. Catal.* **250**, 331–341 (2007).

16. N. E. Tsakoumis, M. Rønning, Ø. Borg, E. Rytter, & A. Holmen. Deactivation of cobalt based Fischer–Tropsch catalysts: A review. *Catal. Today* **154**, 162–182 (2010).

17. J. R. C. Parmeter & E. J. Metal CVD for microelectronics applications: an examination of surface chemistry and kinetics. *Crit. Rev. Sol. State Mater. Sci.* **18**, 175 (1993).

18. D. L. S. Marks & J. T. MOCVD routes to thin metal-oxide films for superconducting electronics. *Adv. Mater.* **6**, 719 (1994).

19. D. A. Neaman. *Semiconductor Physics and Devices*. (McGraw Hill, 2012).

20. G. S. May & C. J. Spanos. *Fundamentals of Semiconductor Manufacturing and Process Control*. (John Wiley and Sons, 2006).

21. L. S. Jung, C. T. Campbell, T. M. Chinowsky, M. Mar, & S. S. Yee. Quantitative Interpretation of the Response of Surface Plasmon Resonance Sensors to Adsorbed Films. *Langmuir* **14**, 5636–5648 (1998).

22. A. Dey. Semiconductor metal oxide gas sensors: A review. *Materials Science and Engineering B: Solid-State Materials for Advanced Technology* **229**, 206–217 (2018).

23. G. F. Fine, L. M. Cavanagh, A. Afonja, & R. Binions. Metal oxide semi-conductor gas sensors in environmental monitoring. *Sensors* **10**, 5469–5502 (2010).

24. E. Comini, C. Baratto, G. Faglia, M. Ferroni, A. Vomiero, & G. Sberveglieri. Quasi-one dimensional metal oxide semiconductors: Preparation, characterization and application as chemical sensors. *Progress in Materials Science* **54**, 1–67 (2009).

25. Y. Luo, C. Zhang, B. Zheng, X. Geng, & M. Debliquy. Hydrogen sensors based on noble metal doped metal-oxide semiconductor: A review. *International Journal of Hydrogen Energy* **42**, 20386–20397 (2017).

26. F. Frusteri, S. Freni, L. Spadaro, V. Chiodo, G. Bonura, S. Donato, & S. Cavallaro. H2 production for MC fuel cell by steam reforming of ethanol over MgO supported Pd, Rh, Ni and Co catalysts. *Catal. Commun.* **5**, 611–615 (2004).

27. F. Charreteur, F. Jaouen, S. Ruggeri, & J. P. Dodelet. Fe/N/C non-precious catalysts for PEM fuel cells: Influence of the structural parameters of pristine commercial carbon blacks on their activity for oxygen reduction. *Electrochim. Acta* **53**, 2925–2938 (2008).

28. C. Rice, R. I. Ha, R. I. Masel, P. Waszczuk, A. Wieckowski, & T. Barnard. Direct formic acid fuel cells. *J. Power Sources* **111**, 83–89 (2002).

29. N. M. Markovic & P. N. Ross. Surface science studies of model fuel cell electrocatalysts. *Surf. Sci. Rep.* **45**, 121–229 (2002).

30. J. T. Stuckless, D. E. Starr, D. J. Bald, & C. T. Campbell. Metal adsorption calorimetry and adhesion energies on clean single-crystal surfaces. *J. Chem. Phys.* **107**, 5547–5553 (1997).

31. C. E. Borroni-Bird, N. Al-Sarraf, S. Andersoon, D. A. King, S. Andersson, & D. A. King. Single crystal adsorption microcalorimetry. *Chem. Phys. Lett.* **183**, 516–520 (1991).

32. J. T. Stuckless, D. E. Starr, D. J. Bald, & C. T. Campbell. A New Single-Crystal Adsorption Calorimeter for Determining Metal Adsorption and Adhesion Energies. *Mater. Res. Soc. Proc.* **440**, 103–108 (1997).

33. J. T. Stuckless, N. A. Frei, & C. T. Campbell. A novel single-crystal adsorption calorimeter and additions for determining metal adsorption and adhesion energies. *Rev. Sci. Instrum.* **69**, 2427–2438 (1998).

34. J. R. V Sellers, T. E. James, S. L. Hemmingson, J. A. Farmer, & C. T. Campbell. Adsorption calorimetry during metal vapor deposition on single crystal surfaces: Increased flux, reduced optical radiation, and real-time flux and reflectivity measurements. in *Review of Scientific Instruments* **84**, 123901–123901 (2013).

35. C. T. Campbell & Z. Mao. Chemical Potential of Metal Atoms in Supported Nanoparticles: Dependence upon Particle Size and Support. *ACS Catal.* **7**, 8460-8466. See also erratum: DOI: 10.1021/acscatal (2017).

36. Z. Mao & C. T. Campbell. Predicting a Key Catalyst-Performance Descriptor for Supported Metal Nanoparticles: Metal Chemical Potential. *ACS Catal.* **11**, 8284-8291. See also erratum: DOI: 10.1021/acscatal (2021).

37. S. L. Hemmingson & C. T. Campbell. Trends in Adhesion Energies of Metal Nanoparticles on Oxide Surfaces: Understanding Support Effects in Catalysis and Nanotechnology. *ACS Nano* **11**, 1196–1203 (2017).

38. C. T. Campbell & J. R. V. Sellers. Anchored metal nanoparticles: Effects of support and size on their energy, sintering resistance and reactivity. *Faraday Discussions* **162**, 9–30

(2013).

39. S. D. Senanayake, J. Evans, S. Agnoli, L. Barrio, T. L. Chen, J. Hrbek, & J. A. Rodriguez. Water-gas shift and CO methanation reactions over Ni-CeO2(111) catalysts. in *Topics in Catalysis* **54**, 34–41 (Springer, 2011).

40. W. Q. Xu, Z. Y. Liu, A. C. Johnston-Peck, S. D. Senanayake, G. Zhou, D. Stacchiola, E. A. Stach, & J. A. Rodriguez. Steam reforming of ethanol on Ni/CeO2: Reaction pathway and interaction between Ni and the CeO2support. *ACS Catal.* **3**, 975–984 (2013).

41. Z. Y. Liu, S. Y. Yao, A. Johnston-Peck, W. Q. Xu, J. A. Rodriguez, & S. D. Senanayake. Methanol Steam Reforming over Ni-CeO2 Model and Powder Catalysts: Pathways to High Stability and Selectivity for H2/CO2 Production. *Catal. Today* **311**, 74–80 (2018).

42. Z. Y. Liu, T. Duchon, H. R. Wang, E. W. Peterson, Y. H. Zhou, S. Luo, J. Zhou, V. Matolin, D. J. Stacchiola, J. A. Rodriguez, & S. D. Senanayake. Mechanistic Insights of Ethanol Steam Reforming over Ni-CeOx(111): The Importance of Hydroxyl Groups for Suppressing Coke Formation. *J. Phys. Chem. C* **119**, 18248–18256 (2015).

43. Z. Liu, D. C. Grinter, P. G. Lustemberg, T. D. Nguyen-Phan, Y. Zhou, S. Luo, I. Waluyo, E. J. Crumlin, D. J. Stacchiola, J. Zhou, J. Carrasco, H. F. Busnengo, M. V. Ganduglia-Pirovano, S. D. Senanayake, & J. A. Rodriguez. Dry Reforming of Methane on a Highly-Active Ni-CeO2Catalyst: Effects of Metal-Support Interactions on C−H Bond Breaking. *Angew. Chemie - Int. Ed.* **55**, 7455–7459 (2016).

44. P. G. Lustemberg, P. J. Ramirez, Z. Y. Liu, R. A. Gutierrez, D. G. Grinter, J. Carrasco, S. D. Senanayake, J. A. Rodriguez, & M. V Ganduglia-Pirovano. Room-Temperature Activation of Methane and Dry Re-forming with CO2 on Ni-CeO2(111) Surfaces: Effect of Ce3+ Sites and Metal-Support Interactions on C-H Bond Cleavage. *ACS Catal.* **6**,

8184–8191 (2016).

45. P. G. Lustemberg, R. M. Palomino, R. A. Gutiérrez, D. C. Grinter, M. Vorokhta, Z. Y. Liu, P. J. Ramírez, V. Matolín, M. V. Ganduglia-Pirovano, S. D. Senanayake, J. A. Rodriguez, R. A. Gutierrez, D. C. Grinter, M. Vorokhta, Z. Y. Liu, P. J. Ramirez, V. Matolin, M. V. Ganduglia-Pirovano, *et al.* Direct Conversion of Methane to Methanol on Ni-Ceria Surfaces: Metal-Support Interactions and Water-Enabled Catalytic Conversion by Site Blocking. *J. Am. Chem. Soc.* **140**, 7681–7687 (2018).

46. Z. Mao, W. Zhao, Z. A. Al-Mualem, & C. T. Campbell. Energetics and Structure of Nickel Atoms and Nanoparticles on MgO(100). *J. Phys. Chem. C* **124**, 14685–14695 (2020).

47. Z. Mao, P. G. Lustemberg, J. R. Rumptz, M. V. Ganduglia-Pirovano, & C. T. Campbell. Ni Nanoparticles on CeO2(111): Energetics, Electron Transfer, and Structure by Ni Adsorption Calorimetry, Spectroscopies, and Density Functional Theory. *ACS Catal.* **10**, 5101–5114 (2020).

48. S. F. Chen, J. P. Li, K. Qian, W. P. Xu, Y. Lu, W. X. Huang, & S. H. Yu. Large scale photochemical synthesis of M@TiO2 nanocomposites (M= Ag, Pd, Au, Pt) and their optical properties, CO oxidation performance, and antibacterial effect. *Nano Res.* **3**, 244–255 (2010).

49. G. L. Chiarello, M. H. Aguirre, & E. Selli. Hydrogen production by photocatalytic steam reforming of methanol on noble metal-modified TiO2. *J. Catal.* **273**, 182–190 (2010).

50. I. Paramasivam, J. M. Macak, & P. Schmuki. Photocatalytic activity of TiO2 nanotube layers loaded with Ag and Au nanoparticles. *Electrochem. commun.* **10**, 71–75 (2007).

51. S. Sarina, E. R. Waclawik, & H. Zhu. Photocatalysis on supported gold and silver

nanoparticles under ultraviolet and visible light irradiation. *Green Chem.* **15**, 1814–1833 (2013).

52. D. Tsukamoto, A. Shiro, S. Y., Y. Sugano, S. Ichikawa, S. Tanaka, & T. Hirai. Photocatalytic H2O2 Production from Ethanol/O2 System Using TiO2 Loaded with Au−Ag Bimetallic Alloy Nanoparticles. *ACS Catal.* **2**, 599–603 (2012).

53. N. Singh, M. T. Nguyen, D. C. Cantu, B. L. Mehdi, N. D. Browning, J. L. Fulton, J. Zheng, M. Balasubramanian, O. Y. Gutiérrez, V. A. Glezakou, R. Rousseau, N. Govind, D. M. Camaioni, C. T. Campbell, & J. A. Lercher. Carbon-supported Pt during aqueous phenol hydrogenation with and without applied electrical potential: X-ray absorption and theoretical studies of structure and adsorbates. *J. Catal.* **368**, 8–19 (2018).

54. C. Kim, H. S. Jeon, T. Eom, M. S. Jee, H. Kim, C. M. Friend, B. K. Min, & Y. J. Hwang. Achieving Selective and Efficient Electrocatalytic Activity for CO2 Reduction Using Immobilized Silver Nanoparticles. *J. Am. Chem. Soc.* **137**, 13844–13850 (2015).

55. Y. Song, U. Sanyal, D. Pangotra, J. D. Holladay, D. M. Camaioni, O. Y. Gutiérrez, & J. A. Lercher. Hydrogenation of benzaldehyde via electrocatalysis and thermal catalysis on carbon-supported metals. *J. Catal.* **359**, 68–75 (2018).

56. G. R. Dieckmann & S. H. Langer. Comparisons of Ebonex® and graphite supports for platinum and nickel electrocatalysts. *Electrochim. Acta* **44**, 437–444 (1998).

57. M. L. Toebes, J. A. van Dillen, K. P. De Jong, & Y. P. de Jong. Synthesis of supported palladium catalysts. *J. Mol. Catal. A Chem.* **173**, 75–98 (2001).

58. E. J. Yoo, T. Okata, T. Akita, M. Kohyama, J. Nakamura, & I. Honma. Enhanced electrocatalytic activity of Pt subnanoclusters on graphene nanosheet surface. *Nano Lett.* **9**, 2255–2259 (2009).

59. T. W. Walker, A. K. Chew, H. Li, B. Demir, Z. C. Zhang, G. W. Huber, R. C. Van Lehn, & J. A. Dumesic. Universal kinetic solvent effects in acid-catalyzed reactions of biomass-derived oxygenates. *Energy Environ. Sci.* **11**, 617–628 (2018).

60. M. A. Mellmer, C. Sener, J. M. R. Gallo, J. S. Luterbacher, D. M. Alonso, & J. A. Dumesic. Solvent effects in acid-catalyzed biomass conversion reactions. *Angew. Chemie - Int. Ed.* **53**, 11872–11875 (2014).

61. M. A. Mellmer, C. Sanpitakseree, B. Demir, P. Bai, K. Ma, M. Neurock, & J. A. Dumesic. Solvent-enabled control of reactivity for liquid-phase reactions of biomass-derived compounds. *Nat. Catal.* **1**, 199–207 (2018).

62. L. Qi, R. Alamillo, W. A. Elliott, A. Andersen, D. W. Hoyt, E. D. Walter, K. S. Han, N. M. Washton, R. M. Rioux, J. A. Dumesic, & S. L. Scott. Operando Solid-State NMR Observation of Solvent-Mediated Adsorption-Reaction of Carbohydrates in Zeolites. *ACS Catal.* **7**, 3489–3500 (2017).

63. J. He, M. Liu, K. Huang, T. W. Walker, C. T. Maravelias, J. A. Dumesic, & G. W. Huber. Production of levoglucosenone and 5-hydroxymethylfurfural from cellulose in polar aprotic solvent-water mixtures. *Green Chem.* **19**, 3642–3653 (2017).

64. N. Singh & C. T. Campbell. A Simple Bond-Additivity Model Explains Large Decreases in Heats of Adsorption in Solvents Versus Gas Phase: A Case Study with Phenol on Pt(111) in Water. *ACS Catal.* **9**, 8116–8127 (2019).

65. G. Bramley, M. T. Nguyen, V. A. Glezakou, R. Rousseau, & C. K. Skylaris. Reconciling Work Functions and Adsorption Enthalpies for Implicit Solvent Models: A Pt (111)/Water Interface Case Study. *J. Chem. Theory Comput.* **16**, 2703–2715 (2020).

66. G. A. Bramley, M. T. Nguyen, V. A. Glezakou, R. Rousseau, & C. K. Skylaris.

Understanding Adsorption of Organics on Pt(111) in the Aqueous Phase: Insights from DFT Based Implicit Solvent and Statistical Thermodynamics Models. *J. Chem. Theory Comput.* **18**, 1849–1861 (2022).

67. M. Suyetin, S. Bag, P. Anand, M. Borkowska-Panek, F. Gußmann, M. Brieg, K. Fink, & W. Wenzel. Modelling peptide adsorption energies on gold surfaces with an effective implicit solvent and surface model. *J. Colloid Interface Sci.* **605**, 493–499 (2022).

68. E. W. Lemmon, M. O. McLinden, & D. G. Friend. Thermophysical Properties of Fluid Systems. in *NIST Chemistry WebBook, NIST Standard Reference Database Number 69* (eds. Linstrom, P. J. & Mallard, W. G.) (National Institute of Standards and Technology, 2021).

69. J. J. Jasper. The Surface Tension of Pure Liquid Compounds. *J. Phys. Chem. Ref. Data* **1**, 841–1010 (1972).

70. J. Israelachvili. *Intermolecular and Surface Forces*. *Intermolecular and Surface Forces* (Academic Press, 2011). doi:10.1016/C2009-0-21560-1

71. R. Sander. Henry’s Law Constants “in NIST Chemistry WebBook, NIST Standard Reference Database Number 69, Eds. *PJ Linstrom WG Mallard, Natl. Inst. Stand. Technol. Gaithersbg. MD* **20899**, (2000).

72. C. T. Campbell & T. E. James. Ion scattering spectroscopy intensities for supported nanoparticles: The hemispherical cap model. *Surf. Sci.* **641**, 166–169 (2015).

73. J. A. Farmer, J. H. Baricuatro, & C. T. Campbell. Ag adsorption on reduced CeO2(111) thin films. *J. Phys. Chem. C* **114**, 17166–17172 (2010).

74. M. Grunze, H. Ruppender, & O. Elshazly. Chemical cleaning of metal surfaces in vacuum systems by exposure to reactive gases. *J. Vac. Sci. Technol. A* **6**, 1266 (1988).

75. T. E. James, S. L. Hemmingson, T. Ito, & C. T. Campbell. Energetics of Cu Adsorption and Adhesion onto Reduced CeO2(111) Surfaces by Calorimetry. *J. Phys. Chem. C* **119**, 17209–17217 (2015).

76. Q. Guo, W. S. Oh, & D. W. Goodman. Titanium oxide films grown on Mo(110). *Surf. Sci.* **437**, 49–60 (1999).

77. X. Lai, Q. Guo, B. K. Min, & D. W. Goodman. Synthesis and characterization of titania films on Mo(110). *Surf. Sci.* **487**, 1–8 (2001).

78. J. Lahiri, T. S. Miller, A. J. Ross, L. Adamska, I. I. Oleynik, & M. Batzill. Graphene growth and stability at nickel surfaces. *New J. Phys.* **13**, 025001 (2011).

79. M. Batzill. The surface science of graphene: Metal interfaces, CVD synthesis, nanoribbons, chemical modifications, and defects. *Surface Science Reports* **67**, 83–115 (2012).

80. W. Zhao, S. M. Kozlov, O. Höfert, K. Gotterbarm, M. P. A. Lorenz, F. Viñes, C. Papp, A. Görling, & H. P. Steinrück. Graphene on Ni(111): Coexistence of different surface structures. *J. Phys. Chem. Lett.* **2**, 759–764 (2011).

81. F. Giubileo & A. Di Bartolomeo. The role of contact resistance in graphene field-effect devices. *Progress in Surface Science* **92**, 143–175 (2017).

82. L. C. A. van den Oetelaar, S. N. Mikhailov, & H. H. Brongersma. Mechanism of neutralization in low-energy He+ ion scattering from carbidic and graphitic carbon species on rhenium. *Nucl. Inst. Methods Phys. Res. B* **85**, 420–423 (1994).

83. S. N. Mikhailov, L. C. A. van den Oetelaar, & H. H. Brongersma. Strong matrix effect in low-energy He+ ion scattering from carbon. *Nucl. Inst. Methods Phys. Res. B* **93**, 210–214 (1994).

84. N. B. Luna, F. J. Bonetto, R. A. Vidal, E. C. Goldberg, & J. Ferrón. Low energy ion scattering in He/HOPG system. *J. Mol. Catal. A Chem.* **281**, 237–240 (2008).

85. D. A. King & M. G. Wells. Method for measureing sticking probabilities. *Surf. Sci.* **29**, 454 (1972).

86. D. A. King & M. G. Wells. Molecular beam investigation of adsorption kinetics on bulk metal targets: Nitrogen on tungsten. *Surf. Sci.* **29**, 454–482 (1972).

87. J. Carrasco, L. Barrio, P. Liu, J. A. Rodriguez, & M. V. Ganduglia-Pirovano. Theoretical studies of the adsorption of CO and C on Ni(111) and Ni/CeO2(111): Evidence of a strong metal-support interaction. *J. Phys. Chem. C* **117**, 8241–8250 (2013).

88. S. D. Senanayake, J. A. Rodriguez, & D. Stacchiola. Electronic metal-support interactions and the production of hydrogen through the water-gas shift reaction and ethanol steam reforming: Fundamental studies with well-defined model catalysts. *Top. Catal.* **56**, 1488–1498 (2013).

89. J. Carrasco, D. Lopez-Duran, Z. Y. Liu, T. Duchon, J. Evans, S. D. Senanayake, E. J. Crumlin, V. Matolin, J. A. Rodriguez, M. V. Ganduglia-Pirovano, D. Lõpez-Durán, Z. Y. Liu, T. Duchoň, J. Evans, S. D. Senanayake, E. J. Crumlin, V. Matolín, J. A. Rodríguez, *et al.* In Situ and Theoretical Studies for the Dissociation of Water on an Active Ni/CeO2 Catalyst: Importance of Strong Metal-Support Interactions for the Cleavage of O-H Bonds. *Angew. Chemie-International Ed.* **54**, 3917–3921 (2015).

90. M. V. Ganduglia-Pirovano. The Non-Innocent Role of Cerium Oxide in Heterogeneous Catalysis: A Theoretical Perspective. *Catal. Today* **253**, 20–32 (2015).

91. Z. Y. Liu, T. Duchon, H. R. Wang, D. C. Grinter, I. Waluyo, J. Zhou, Q. Liu, B. Jeong, E. J. Crumlin, V. Matolin, D. J. Stacchiola, J. A. Rodriguez, & S. D. Senanayake. Ambient

Pressure XPS and IRRAS Investigation of Ethanol Steam Reforming on Ni-CeO2(111) Catalysts: an In Situ Study of C-C and O-H Bond Scission. *Phys. Chem. Chem. Phys.* **18**, 16621–16628 (2016).

92. Z. Y. Liu, P. Lustemberg, R. A. Gutierrez, J. J. Carey, R. M. Palomino, M. Vorokhta, D. C. Grinter, P. J. Ramirez, V. Matolin, M. Nolan, M. V Ganduglia-Pirovano, S. D. Senanayake, & J. A. Rodriguez. In Situ Investigation of Methane Dry Reforming on Metal/Ceria(111) Surfaces: Metal-Support Interactions and C-H Bond Activation at Low Temperature. *Angew. Chemie-International Ed.* **56**, 13041–13046 (2017).

93. D. Voychok, C. J. Guild, J. Llorca, R. M. Palomino, I. Waluyo, J. A. Rodriguez, S. L. Suib, & S. D. Senanayake. Structural and Chemical State of Doped and Impregnated Mesoporous Ni/CeO2 Catalysts for the Water-Gas Shift. *Appl. Catal. a-General* **567**, 1–11 (2018).

94. P. G. Lustemberg, L. Feria, & M. V Ganduglia-Pirovano. Single Ni Sites Supported on CeO2 (111) Reveal Cooperative Effects in the Water-Gas Shift Reaction. *J. Phys. Chem. C* **123**, 7749–7757 (2019).

95. M. Akri, S. Zhao, X. Y. Li, K. T. Zang, A. F. Lee, M. A. Isaacs, W. Xi, Y. Gangarajula, J. Luo, Y. J. Ren, Y. T. Cui, L. Li, Y. Su, X. L. Pan, W. Wen, Y. Pan, K. Wilson, B. T. Qiao, *et al.* Atomically Dispersed Nickel as Coke-Resistant Active Sites for Methane Dry Reforming. *Nat. Commun.* **10**, (2019).

96. R. Farrauto, S. Hwang, L. Shore, W. Ruettinger, J. Lampert, T. Giroux, Y. Liu, & O. Ilinich. New material needs for hydrocarbon fuel processing: Generating hydrogen for the PEM fuel cell. *Annu. Rev. Mater. Res.* **33**, 1–27 (2003).

97. C. T. Campbell & C. H. F. Peden. Chemistry - Oxygen vacancies and catalysis on ceria

surfaces. *Science* **309**, 713–714 (2005).

98. E. Rocchini, A. Trovarelli, J. Llorca, G. W. Graham, W. H. Weber, M. Maciejewski, & A. Baiker. Relationships between structural/morphological modifications and oxygen storage-redox behavior of silica-doped ceria. *J. Catal.* **194**, 461–478 (2000).

99. J. A. Farmer & C. T. Campbell. Ceria maintains smaller metal catalyst particles by strong metal-support bonding. *Science* **329**, 933–936 (2010).

100. L. Kundakovic & M. Flytzani-Stephanopoulos. Cu- and Ag-modified cerium oxide catalysts for methane oxidation. *J. Catal.* **179**, 203–221 (1998).

101. J. M. Schwartz & L. D. Schmidt. Microstructures of Pt-Ce and Rh-Ce Particles on Alumina and Silica. *J. Catal.* **138**, 283–293 (1992).

102. C. T. Campbell. The Energetics of Supported Metal Nanoparticles: Relationships to Sintering Rates and Catalytic Activity. *Acc. Chem. Res.* **46**, 1712–1719 (2013).

103. T. E. James, S. L. Hemmingson, & C. T. Campbell. Energy of Supported Metal Catalysts: From Single Atoms to Large Metal Nanoparticles. *ACS Catal.* **5**, 5673–5678 (2015).

104. S. L. Hemmingson, T. E. James, G. M. Feeley, A. M. Tilson, & C. T. Campbell. Adsorption and Adhesion of Au on Reduced CeO2(111) Surfaces at 300 and 100 K. *J. Phys. Chem. C* **120**, 12113–12124 (2016).

105. E. L. Wilson, W. A. Brown, & G. Thornton. RAIRS studies of CO adsorption on Pd/CeO2-x(111)/Pt(111). *Surf. Sci.* **600**, 2555–2561 (2006).

106. G. Kresse & J. Hafner. Ab Initio Molecular-Dynamics for Liquid-Metals. *Phys. Rev. B* **47**, 558–561 (1993).

107. G. Kresse & J. Furthmüller. Efficient Iterative Schemes for Ab Initio Total-Energy Calculations Using a Plane-Wave Basis Set. *Phys. Rev. B* **54**, 11169 (1996).

108. G. Kresse & D. Joubert. From ultrasoft pseudopotentials to the projector augmented-wave method. *Phys. Rev. B* **59**, 1758–1775 (1999).

109. S. L. Dudarev, G. A. Botton, S. Y. Savrasov, C. J. Humphreys, & A. P. Sutton. Electron-energy-loss spectra and the structural stability of nickel oxide: An LSDA+U study. *Phys. Rev. B* **57**, 1505–1509 (1998).

110. J. P. Perdew, K. Burke, & M. Ernzerhof. Generalized Gradient Approximation Made Simple. *Phys. Rev. Lett.* **78**, 1396 (1996).

111. S. Fabris, G. Vicario, G. Balducci, S. de Gironcoli, & S. Baroni. Electronic and atomistic structures of clean and reduced ceria surfaces. *J. Phys. Chem. B* **109**, 22860–22867 (2005).

112. C. W. M. Castleton, J. Kullgren, & K. Hermansson. Tuning LDA+U for Electron Localization and Structure at Oxygen Vacancies in Ceria. *J. Chem. Phys.* **127**, 244704 (2007).

113. D. A. Andersson, S. I. Simak, B. Johansson, I. A. Abrikosov, & N. V Skorodumova. Modeling of CeO2, Ce2O3, and CeO2-x in the LDA plus U formalism. *Phys. Rev. B* **75**, (2007).

114. J. L. F. Da Silva, M. V. Ganduglia-Pirovano, J. Sauer, V. Bayer, & G. Kresse. Hybrid functionals applied to rare-earth oxides: The example of ceria. *Phys. Rev. B* **75**, (2007).

115. D. Du, M. J. Wolf, K. Hermansson, & P. Broqvist. Screened Hybrid Functionals Applied to Ceria: Effect of Fock Exchange. *Phys. Rev. B* **97**, 235203 (2018).

116. C. Loschen, J. Carrasco, K. M. Neyman, & F. Illas. First-principles LDA plus U and GGA plus U study of cerium oxides: Dependence on the effective U parameter. *Phys. Rev. B* **75**, (2007).

117. S. Grimme, J. Antony, S. Ehrlich, & H. Krieg. A Consistent and Accurate Ab Initio Parametrization of Density Functional Dispersion Correction (DFT-D) for the 94 Elements H-Pu. *J. Chem. Phys.* **132**, 154104 (2010).

118. S. Grimme, S. Ehrlich, & L. Goerigk. Effect of the Damping Function in Dispersion Corrected Density Functional Theory. *J. Comput. Chem.* **32**, 1456–1465 (2011).

119. Y. H. Zhou, J. M. Perket, A. B. Crooks, & J. Zhou. Effect of ceria support on the structure of Ni nanoparticles. *J. Phys. Chem. Lett.* **1**, 1447–1453 (2010).

120. J. A. Venables. Atomic processes in crystal growth. *Surf. Sci.* **299–300**, 798–817 (1994).

121. N. J. Castellani, M. M. A. Branda, K. M. Neyman, & F. Illas. Density Functional Theory Study of the Adsorption of Au Atom on Cerium Oxide: Effect of Low-Coordinated Surface Sites. *J. Phys. Chem. C* **113**, 4948–4954 (2009).

122. N. C. Hernández, R. Grau-Crespo, N. H. de Leeuw, J. F. Sanz, N. C. Hernandez, R. Grau-Crespo, N. H. de Leeuw, & J. F. Sanz. Electronic Charge Transfer between Ceria Surfaces and Gold Adatoms: A GGA Plus U Investigation. *Phys. Chem. Chem. Phys.* **11**, 5246–5252 (2009).

123. C. J. Zhang, A. Michaelides, D. A. King, & S. J. Jenkins. Anchoring Sites for Initial Au Nucleation on CeO2{111}: O Vacancy versus Ce Vacancy. *J. Phys. Chem. C* **113**, 6411–6417 (2009).

124. C. Zhang, A. Michaelides, D. A. King, & S. J. Jenkins. Structure of Gold Atoms on Stoichiometric and Defective Ceria Surfaces. *J. Chem. Phys.* **129**, (2008).

125. M. F. Camellone & S. Fabris. Reaction Mechanisms for the CO Oxidation on Au/CeO2 Catalysts: Activity of Substitutional Au3+/Au+ Cations and Deactivation of Supported Au+ Adatoms. *J. Am. Chem. Soc.* **131**, 10473–10483 (2009).

126. P. G. Lustemberg, Y. Pan, B. J. Shaw, D. Grinter, C. Pang, G. Thornton, R. Perez, M. V Ganduglia-Pirovano, & N. Nilius. Diffusion Barriers Block Defect Occupation on Reduced CeO2(111). *Phys. Rev. Lett.* **116**, (2016).

127. Y. Pan, N. Nilius, H. J. Freund, J. Paier, C. Penschke, & J. Sauer. Titration of Ce 3 + Ions in the CeO2(111) Surface by Au Adatoms. *Phys. Rev. Lett.* **111**, (2013).

128. J. A. Rodriguez, X. Wang, P. Liu, W. Wen, J. C. Hanson, J. Hrbek, M. Perez, & J. Evans. Gold nanoparticles on ceria: importance of O vacancies in the activation of gold. *Top. Catal.* **44**, 73–81 (2007).

129. Y. Pan, Y. Cui, C. Stiehler, N. Nilius, & H.-J. J. Freund. Gold adsorption on CeO2 thin films grown on Ru (0001). *J. Phys. Chem. C* **117**, 21879–27447 (2013).

130. J. A. Rodriguez, M. Perez, J. Evans, G. Liu, & J. Hrbek. Reaction of SO2 with Au/CeO2(111): Importance of O vacancies in the activation of gold. *J. Chem. Phys.* **122**, (2005).

131. S. M. Kozlov & K. M. Neyman. O Vacancies on Steps on the CeO2(111) Surface. *Phys. Chem. Chem. Phys.* **16**, 7823–7829 (2014).

132. M. Romeo, K. Bak, J. El-Fallah, F. Lenormand, & L. Hilaire. XPS Study of the Reduction of Cerium Dioxide. *Surf. Interface Anal.* **20**, 508–512 (1993).

133. S. Tanuma, C. J. Powell, & D. R. Penn. Calculations of Electron Inelastic Mean Free Paths for 31 Materials. *Surf. Interface Anal.* **11**, 577–589 (1988).

134. A. P. Grosvenor, M. C. Biesinger, R. S. C. Smart, & N. S. McIntyre. New interpretations of XPS spectra of nickel metal and oxides. *Surf. Sci.* **600**, 1771–1779 (2006).

135. Y. H. Zhou & J. Zhou. Interactions of Ni Nanoparticles with Reducible CeO2(111) Thin Films. *J. Phys. Chem. C* **116**, 9544–9549 (2012).

136. H. J. Monkhorst & J. D. Pack. Special Points for Brillouin-Zone Integrations. *Phys. Rev. B* **13**, 5188–5192 (1976).

137. W. Tang, E. Sanville, & G. Henkelman. A Grid-Based Bader Analysis Algorithm without Lattice Bias. *J. Phys. Condens. Matter* **21**, 84204 (2009).

138. P. Janthon, S. Luo, S. M. Kozlov, F. Viñes, J. Limtrakul, D. G. Truhlar, & F. Illas. Bulk Properties of Transition Metals: A Challenge for the Design of Universal Density Functionals. *J. Chem. Theory Comput.* **10**, 3832–3839 (2014).

139. G.-X. Zhang, A. M. Reilly, A. Tkatchenko, & M. Scheffler. Performance of Various Density-Functional Approximations for Cohesive Properties of 64 Bulk Solids. *New J. Phys.* **20**, 63020 (2018).

140. H. Y. Kim & G. Henkelman. CO oxidation at the interface of Au nanoclusters and the stepped-CeO2 (111) surface by the Mars–van Krevelen mechanism. *J. Phys. Chem. Lett.* **4**, 216–221 (2013).

141. M. V Ganduglia-Pirovano, A. Hofmann, & J. Sauer. Oxygen Vacancies in Transition Metal and Rare Earth Oxides: Current State of Understanding and Remaining Challenges. *Surf. Sci. Rep.* **62**, 219–270 (2007).

142. G. E. Murgida & M. V Ganduglia-Pirovano. Evidence for Subsurface Ordering of Oxygen Vacancies on the Reduced CeO2(111) Surface Using Density-Functional and Statistical Calculations. *Phys. Rev. Lett.* **110**, (2013).

143. Z.-K. Han, Y.-Z. Yang, B. Zhu, M. V. Ganduglia-Pirovano, & Y. Gao. Unraveling the Oxygen Vacancy Structures at the Reduced CeO2(111) Surface. *Phys. Rev. Mater.* **2**, 35802 (2018).

144. J. Paier, C. Penschke, & J. Sauer. Oxygen Defects and Surface Chemistry of Ceria:

Quantum Chemical Studies Compared to Experiment. *Chem. Rev.* **113**, 3949–3985 (2013).

145. R. K. Hailstone, A. G. DiFrancesco, J. G. Leong, T. D. Allston, & K. J. Reed. A Study of Lattice Expansion in CeO2 Nanoparticles by Transmission Electron Microscopy. *J. Phys. Chem. C* **113**, 15155–15159 (2009).

146. C. T. Campbell. Bimetallic Surface Chemistry. *Annu. Rev. Phys. Chem.* **41**, 775–837 (1990).

147. A. J. Medford, A. Vojvodic, J. S. Hummelshoj, J. Voss, F. Abild-Pedersen, F. Studt, T. Bligaard, A. Nilsson, & J. K. Norskov. From the Sabatier principle to a predictive theory of transition-metal heterogeneous catalysis. *J. Catal.* **328**, 36–42 (2015).

148. J. Dean, M. G. Taylor, & G. Mpourmpakis. Unfolding adsorption on metal nanoparticles: Connecting stability with catalysis. *Sci. Adv.* **5**, eaax5101 (2019).

149. S. Kattel, P. J. Ramirez, J. G. Chen, J. A. Rodriguez, & P. Liu. Active sites for CO2 hydrogenation to methanol on Cu/ZnO catalysts. *Science* **355**, 1296-+ (2017).

150. J. A. Rodriguez, D. C. Grinter, Z. Y. Liu, R. M. Palomino, & S. D. Senanayake. Ceria-based model catalysts: fundamental studies on the importance of the metal-ceria interface in CO oxidation, the water-gas shift, CO2 hydrogenation, and methane and alcohol reforming. *Chem. Soc. Rev.* **46**, 1824–1841 (2017).

151. W. Zhang, R. Uppuluri, T. E. Mallouk, & C. T. Campbell. Silver Adsorption on Calcium Niobate (001) Nanosheets: Calorimetric Energies That Explain Sinter-Resistant Support. *J. Am. Chem. Soc.* **142**, 15751–15763 (2020).

152. Y. Dai, P. Lu, Z. Cao, C. T. Campbell, & Y. Xia. The physical chemistry and materials science behind sinter-resistant catalysts. *Chem. Soc. Rev.* (2018). doi:10.1039/c7cs00650k

153. J. Jones, H. F. Xiong, A. T. Delariva, E. J. Peterson, H. Pham, S. R. Challa, G. S. Qi, S. Oh, M. H. Wiebenga, X. I. P. Hernandez, Y. Wang, & A. K. Datye. Thermally stable single-atom platinum-on-ceria catalysts via atom trapping. *Science* **353**, 150–154 (2016).

154. C. T. Campbell & D. E. Starr. Metal adsorption and adhesion energies on MgO(100). *J. Am. Chem. Soc.* **124**, 9212–9218 (2002).

155. U. Diebold. The surface science of titanium dioxide. *Surf. Sci. Rep.* **48**, 53–229 (2003).

156. C. E. Kliewer, S. L. Soled, & G. Kiss. Morphological transformations during Fischer-Tropsch synthesis on a titania-supported cobalt catalyst. *Catal. Today* **323**, 233–256 (2019).

157. M. Valden, X. Lai, & D. W. Goodman. Onset of catalytic activity of gold clusters on titania with the appearance of nonmetallic properties. *Science* **281**, 1647–1650 (1998).

158. I. X. Green, W. Tang, M. Neurock, & J. T. Yates Jr. Insights into Catalytic Oxidation at the Au/TiO2 Dual Perimeter Sites. *Acc. Chem. Res.* **47**, 805–815 (2014).

159. D. A. Panayotov & J. R. Morris. Surface chemistry of Au/TiO2: Thermally and photolytically activated reactions. *Surf. Sci. Rep.* **71**, 77–271 (2016).

160. M. Shekhar, J. Wang, W. S. Lee, W. D. Williams, S. M. Kim, E. A. Stach, J. T. Miller, W. N. Delgass, & F. H. Ribeiro. Size and Support Effects for the Water-Gas Shift Catalysis over Gold Nanoparticles Supported on Model Al2O3 and TiO2. *J. Am. Chem. Soc.* **134**, 4700–4708 (2012).

161. D. Widmann & R. J. Behm. Active Oxygen on a Au/TiO2 Catalyst: Formation, Stability, and CO Oxidation Activity. *Angew. Chemie-International Ed.* **50**, 10241–10245 (2011).

162. J. A. Rodriguez, J. Evans, J. Graciani, J. B. Park, P. Liu, J. Hrbek, & J. F. Sanz. High Water-Gas Shift Activity in TiO2(110) Supported Cu and Au Nanoparticles: Role of the

Oxide and Metal Particle Size. *J. Phys. Chem. C* **113**, 7364–7370 (2009).

163. C. L. Pang, R. Lindsay, & G. Thornton. Chemical reactions on rutile TiO2(110). *Chem. Soc. Rev.* **37**, 2328–2353 (2008).

164. R. E. Tanner, M. R. Castell, & G. A. D. Briggs. High resolution scanning tunnelling microscopy of the rutile TiO2(110) surface. *Surf. Sci.* **412**, 672–681 (1998).

165. C. Pang, R. Lindsay, & G. Thornton. Structure of Clean and Adsorbate-Covered Single-Crystal Rutile TiO2 Surfaces. *Chem. Rev.* **113**, 3887–3948 (2013).

166. A. G. Thomas & K. L. Syres. Adsorption of organic molecules on rutile TiO2 and anatase TiO2 single crystal surfaces. *Chem. Soc. Rev.* **41**, 4207–4217 (2012).

167. S. Wendt, R. Schaub, J. Matthiesen, E. K. Vestergaard, E. Wahlstrom, M. D. Rasmussen, P. Thostrup, L. M. Molina, E. Laegsgaard, I. Stensgaard, B. Hammer, & F. Besenbacher. Oxygen vacancies on TiO2(110) and their interaction with H2O and O-2: A combined high-resolution STM and DFT study. *Surf. Sci.* **598**, 226–245 (2005).

168. R. A. Bennett, P. Stone, N. J. Price, & M. Bowker. Two (1 × 2) reconstructions of TiO2(110): Surface rearrangement and reactivity studied using elevated temperature scanning tunneling microscopy. *Phys. Rev. Lett.* **82**, 3831–3834 (1999).

169. C. Di Valentin, A. Tilocca, A. Selloni, T. J. Beck, A. Klust, M. Batzill, Y. Losovyj, & U. Diebold. Adsorption of water on reconstructed rutile TiO2(011)-(2x1): Ti=O double bonds and surface reactivity. *J. Am. Chem. Soc.* **127**, 9895–9903 (2005).

170. E. Wahlstrom, N. Lopez, R. Schaub, P. Thostrup, A. Ronnau, C. Africh, E. Laegsgaard, J. K. Norskov, & F. Besenbacher. Bonding of gold nanoclusters to oxygen vacancies on rutile TiO2(110). *Phys. Rev. Lett.* **90**, 26101 (2003).

171. H. Iddir, S. Ogut, N. D. Browning, & M. M. Disko. Adsorption and diffusion of Pt and Au

on the stoichiometric and reduced TiO2 rutile (110) surfaces. *Phys. Rev. B* **72**, 81407 (2005).

172. S. Kielbassa, M. Kinne, & R. J. Behm. Thermal stability of Au nanoparticles in O-2 and air on fully oxidized TiO2(110) substrates at elevated pressures. An AFM/XPS study of Au/TiO2 model systems. *J. Phys. Chem. B* **108**, 19184–19190 (2004).
173. U. Diebold, J. Pan, & T. E. Madey. Ultrathin metal film growth on TiO2(110): an overview. *Surf. Sci.* **331**, 845–854 (1995).
174. R. Lazzari, G. Renaud, J. Jupille, & F. Leroy. Self-similarity during growth of the Au/TiO2(110) model catalyst as seen by the scattering of x-rays at grazing-angle incidence. *Phys. Rev. B* **76**, 125412 (2007).
175. L. Zhang, F. Cosandey, R. Persaud, & T. E. Madey. Initial growth and morphology of thin Au films on TiO2(110). *Surf. Sci.* **439**, 73–85 (1999).
176. W. Zhang & C. T. Campbell. Calorimetric metal vapor adsorption energies for characterizing industrial catalyst support materials. *J. Catal.* **392**, 209–216 (2020).
177. C. Hu, Y. Lan, J. Qu, X. Hu, & A. Wang. Ag/AgBr/TiO2 Visible Light Photocatalyst for Destruction of Azodyes and Bacteria. *J. Phys. Chem. B* **110**, 4066–4072 (2006).
178. J. Schneider, M. Matsuoka, M. Takeuchi, J. Zhang, Y. Horiuchi, M. Anpo, & D. W. Bahnemann. Understanding TiO2 photocatalysis: mechanisms and materials. *Chem. Rev.* **114**, 9919–9986 (2014).
179. S. U. M. Khan, M. Al-Shahry, & W. B. Ingler. Efficient photochemical water splitting by a chemically modified n-TiO2. *Science* **297**, 2243–2245 (2002).
180. A. L. Linsebigler, G. Q. Lu, J. T. Yates Jr, & J. T. Yates. Photocatalysis on TiO2 surfaces: principles, mechanisms, and selected results. *Chem. Rev.* **95**, 735–758 (1995).

181. R. Asahi, T. Morikawa, T. Ohwaki, K. Aoki, & Y. Taga. Visible-light photocatalysis in nitrogen-doped titanium oxides. *Science* **293**, 269–271 (2001).

182. F. Zhang, R. Jin, J. Chen, C. Shao, W. Gao, L. Li, & N. Guan. High photocatalytic activity and selectivity for nitrogen in nitrate reduction on Ag/TiO2 catalyst with fine silver clusters. *J. Catal.* **232**, 424–431 (2005).

183. S. X. Liu, Z. P. Qu, X. W. Han, & C. L. Sun. A mechanism for enhanced photocatalytic activity of silver-loaded titanium dioxide. *Catal. Today* **93**, 877–884 (2004).

184. X. Lai, T. P. St. Clair, D. W. Goodman, T. P. St Clair, & D. W. Goodman. Oxygen-induced morphological changes of Ag nanoclusters supported on TiO2(110). *Faraday Discuss.* **114**, 279–284 (1999).

185. Y. Lei, F. Mehmood, S. Lee, J. Greeley, B. Lee, S. Seifert, R. E. Winans, J. W. Elam, R. J. Meyer, P. C. Redfern, D. Teschner, R. Schlogl, M. J. Pellin, L. A. Curtiss, & S. Vajda. Increased Silver Activity for Direct Propylene Epoxidation via Subnanometer Size Effects. *Science* **328**, 224–228 (2010).

186. A. Nagy & G. Mestl. High temperature partial oxidation reactions over silver catalysts. *Appl. Catal. A Gen.* **188**, 337–353 (1999).

187. W. Grünert, A. Brückner, H. Hofmeister, & P. Claus. Structural properties of Ag/TiO2 catalysts for acrolein hydrogenation. *J. Phys. Chem. B* **108**, 5709–5717 (2004).

188. L. Giordano, G. Pacchioni, T. Bredow, & J. F. Sanz. Cu, Ag, and Au atoms adsorbed on TiO2(110): cluster and periodic calculations. *Surf. Sci.* **471**, 21–31 (2001).

189. P. Schlexer, A. R. Puigdollers, & G. Pacchioni. Tuning the charge state of Ag and Au atoms and clusters deposited on oxide surfaces by doping: a DFT study of the adsorption properties of nitrogen- and niobium-doped TiO2 and ZrO2. *Phys. Chem. Chem. Phys.* **17**,

22342–22360 (2015).

190. A. S. Mazheika, V. E. Matulis, & O. A. Ivashkevich. Quantum chemical study of adsorption of Ag2, Ag4 and Ag8 on stoichiometric TiO2(110) surface. *J. Mol. Struct.* **942**, 47–54 (2010).

191. A. S. Mazheika, T. Bredow, V. E. Matulis, & O. A. Ivashkevich. Theoretical study of adsorption of Ag clusters on the anatase TiO2(100) surface. *J. Phys. Chem. C* **115**, 17368–17377 (2011).

192. E. Lira, J. O. Hansen, L. R. Merte, P. T. Sprunger, Z. Li, F. Besenbacher, & S. Wendt. Growth of Ag and Au nanoparticles on reduced and oxidized rutile TiO2(110) surfaces. *Top. Catal.* **56**, 1460–1476 (2013).

193. X. Lai, T. P. St Clair, M. Valden, & D. W. Goodman. Scanning tunneling microscopy studies of metal clusters supported on TiO2(110): Morphology and electronic structure. *Prog. Surf. Sci.* **59**, 25–52 (1998).

194. D. A. Chen, M. C. Bartelt, S. M. Seutter, & K. F. McCarty. Small, uniform, and thermally stable silver particles on TiO2(110)-(1×1). *Surf. Sci.* **464**, L708–L714 (2000).

195. G. Ertl & J. Küppers. *Low Energy Electrons and Surface Chemistry*. (VCH).

196. J. T. Mayer, U. Diebold, T. E. Madey, & E. Garfunkel. Titanium and reduced titania overlayers on titanium dioxide(110). *J. Electron Spectros. Relat. Phenomena* **73**, 1–11 (1994).

197. G. G. Fuentes, E. Elizalde, F. Yubero, & J. M. Sanz. Electron inelastic mean free path for Ti, TiC, TiN and TiO2 as determined by quantitative reflection electronenergy-loss spectroscopy. *Surf. INterface Anal.* **33**, 230–237 (2002).

198. K. Luo, T. P. St. Clair, X. Lai, & D. W. Goodman. Silver Growth on TiO2(110) (1×1) and

(1×2). *J. Phys. Chem. B* **104**, 3050–3057 (2000).

199. W. M. Haynes. *CRC handbook of chemistry and physics*. (CRC Press, 2014).

200. J. H. Larsen, J. T. Ranney, D. E. Starr, J. E. Musgrove, & C. T. Campbell. Adsorption energetics of Ag on MgO(100). *Phys. Rev. B* **63**, 195410 (2001).

201. J. H. Wang, M. L. Liu, & M. C. Lin. Oxygen reduction reactions in the SOFC cathode of Ag/CeO2. *Solid State Ionics* **177**, 939–947 (2006).

202. S. Prada, M. Rosa, L. Giordano, C. Di Valentin, & G. Pacchioni. Density functional theory study of TiO2/Ag interfaces and their role in memristor devices. *Phys. Rev. B* **83**, 245314 (2011).

203. H. Tsunoyama, H. Sakurai, Y. Negishi, & T. Tsukuda. Size-specific catalytic activity of polymer-stabilized gold nanoclusters for aerobic alcohol oxidation in water. *J. Am. Chem. Soc.* **127**, 9374–9375 (2005).

204. M. M. Schubert, S. Hackenberg, A. C. Van Veen, M. Muhler, V. Plzak, & J. J. Behm. CO oxidation over supported gold catalysts -"Inert" and ‘active’ support materials and their role for the oxygen supply during reaction. *J. Catal.* **197**, 113–122 (2001).

205. M. P. Andersson, F. Abild-Pedersen, I. N. Remediakis, T. Bligaard, G. Jones, J. Engbæk, O. Lytken, S. Horch, J. H. Nielsen, J. Sehested, J. R. Rostrup-Nielsen, J. K. Nørskov, & I. Chorkendorff. Structure sensitivity of the methanation reaction: H2-induced CO dissociation on nickel surfaces. *J. Catal.* **255**, 6–19 (2008).

206. P. N. Plessow & C. T. Campbell. Influence of Adhesion on the Chemical Potential of Supported Nanoparticles as Modeled with Spherical Caps. *ACS Catal.* Advance online publication. DOI: 10.1021/acscatal. (2021). doi:10.1021/acscatal.1c04633

207. A. V Nartova, A. V. Bukhtiyarov, R. I. Kvon, E. M. Makarov, I. P. Prosvirin, & V. I.

Bukhtiyarov. Atomic scale structural defects in the graphite layer for model catalysis. *Surf. Sci.* **677**, 90–92 (2018).

208. D. Appy, H. Lei, C. Z. Wang, M. C. Tringides, D. J. Liu, J. W. Evans, & P. A. Thiel. Transition metals on the (0001) surface of graphite: Fundamental aspects of adsorption, diffusion, and morphology. *Progress in Surface Science* **89**, 219–238 (2014).

209. J. Gebhardt, R. J. Koch, W. Zhao, O. Höfert, K. Gotterbarm, S. Mammadov, C. Papp, A. Görling, H. P. Steinrück, & T. Seyller. Growth and electronic structure of boron-doped graphene. *Phys. Rev. B - Condens. Matter Mater. Phys.* **87**, 155437 (2013).

210. R. J. Koch, M. Weser, W. Zhao, F. Viñes, K. Gotterbarm, S. M. Kozlov, O. Höfert, M. Ostler, C. Papp, J. Gebhardt, H. P. Steinrück, A. Görling, & T. Seyller. Growth and electronic structure of nitrogen-doped graphene on Ni(111). *Phys. Rev. B - Condens. Matter Mater. Phys.* **86**, 075401 (2012).

211. X. Bao, M. Muhler, B. Pettinger, R. Schlögl, & G. Ertl. On the nature of the active state of silver during catalytic oxidation of methanol. *Catal. Letters* **22**, 215–225 (1993).

212. Z. Qu, M. Cheng, W. Huang, & X. Bao. Formation of subsurface oxygen species and its high activity toward CO oxidation over silver catalysts. *J. Catal.* **229**, 446–458 (2005).

213. X. Zhang, Z. Qu, X. Li, M. Wen, X. Quan, D. Ma, & J. Wu. Studies of silver species for low-temperature CO oxidation on Ag/SiO2 catalysts. *Sep. Purif. Technol.* **72**, 395–400 (2010).

214. P. J. van den Hoek, E. J. Baerends, & R. A. van Santen. Ethylene epoxidation on Ag(110): the role of subsurface oxygen. *J. Phys. Chem.* **93**, 6469–6475 (1989).

215. J. G. Serafin, A. C. Liu, & S. R. Seyedmonir. Surface science and the silver-catalyzed epoxidation of ethylene: An industrial perspective. *J. Mol. Catal. A Chem.* **131**, 157–168

(1998).

216. M. S. Shivakumar, G. Krishnamurthy, C. R. Ravikumar, & A. S. Bhatt. Decoration of silver nanoparticles on activated graphite substrate and their electrocatalytic activity for methanol oxidation. *J. Sci. Adv. Mater. Devices* **4**, 290–298 (2019).

217. C. Tan, F. Wang, J. Liu, Y. Zhao, J. Wang, L. Zhang, K. C. Park, & M. Endo. An easy route to prepare carbon black-silver hybrid catalysts for electro-catalytic oxidation of hydrazine. *Mater. Lett.* **63**, 969–971 (2009).

218. B. Zahed & H. Hosseini-Monfared. A comparative study of silver-graphene oxide nanocomposites as a recyclable catalyst for the aerobic oxidation of benzyl alcohol: Support effect. *Appl. Surf. Sci.* **328**, 536–547 (2015).

219. P. Christopher, H. Xin, & S. Linic. Visible-light-enhanced catalytic oxidation reactions on plasmonic silver nanostructures. *Nat. Chem.* **3**, 467–472 (2011).

220. S. Gao, Z. Zhang, K. Liu, & B. Dong. Direct evidence of plasmonic enhancement on catalytic reduction of 4-nitrophenol over silver nanoparticles supported on flexible fibrous networks. *Appl. Catal. B Environ.* **188**, 245–252 (2016).

221. H. Zhou, C. Qiu, F. Yu, H. Yang, M. Chen, L. Hu, & L. Sun. Thickness-dependent morphologies and surface-enhanced Raman scattering of Ag deposited on n-layer graphenes. *J. Phys. Chem. C* **115**, 11348–11354 (2011).

222. C. wen Huang, H. Y. Lin, C. H. Huang, R. J. Shiue, W. H. Wang, C. Y. Liu, & H. C. Chui. Layer-dependent morphologies of silver on n-layer graphene. *Nanoscale Res. Lett.* **7**, 1–6 (2012).

223. I. M. Goldby, L. Kuipers, B. Von Issendorff, & R. E. Palmer. Diffusion and aggregation of size-selected silver clusters on a graphite surface. *Appl. Phys. Lett.* **69**, 2819–2821

(1996).

224. G. M. Francis, I. M. Goldby, L. Kuipers, B. Von Issendorff, & R. E. Palmer. Deposition and growth of noble metal clusters on graphite. *J. Chem. Soc. - Dalt. Trans.* 665–671 (1996). doi:10.1039/dt9960000665

225. J. G. Jackson, R. W. Fonesca, & J. A. Holcombe. Detection of surface aggregates of trace amounts of copper and silver on graphite using secondary ion mass spectrometry at elevated temperatures. *J. Anal. At. Spectrom.* **9**, 167–170 (1994).

226. M. H. Schaffner, J. F. Jeanneret, F. Patthey, & W. D. Schneider. An ultrahigh vacuum sputter source for in situ deposition of size-selected clusters: Ag on graphite. *J. Phys. D. Appl. Phys.* **31**, 3177–3184 (1998).

227. E. Ganz, K. Sattler, & J. Clarke. Scanning tunneling microscopy of silver, gold, and aluminum monomers and small clusters on graphite. *J. Vac. Sci. Technol. A Vacuum, Surfaces, Film.* **6**, 419–423 (1988).

228. E. Ganz, K. Sattler, & J. Clarke. Scanning tunneling microscopy of the local atomic structure of two-dimensional gold and silver islands on graphite. *Phys. Rev. Lett.* **60**, 1856–1859 (1988).

229. G. F. Ndlovu, W. D. Roos, Z. M. Wang, J. K. O. Asante, M. G. Mashapa, C. J. Jafta, B. W. Mwakikunga, & K. T. Hillie. Epitaxial deposition of silver ultra-fine nanoclusters on defect-free surfaces of HOPG-derived few-layer graphene in a UHV multi-chamber by in situ STM, ex situ XPS, and ab initio calculations. *Nanoscale Res. Lett.* **7**, 1–8 (2012).

230. G. M. Wang, J. J. BelBruno, S. D. Kenny, & R. Smith. Interaction of silver adatoms and dimers with graphite surfaces. *Surf. Sci.* **541**, 91–100 (2003).

231. R. E. Ambrusi, S. G. García, & M. E. Pronsato. Formation of Ag nanowires on graphite

stepped surfaces. A DFT study. *Appl. Surf. Sci.* **324**, 710–717 (2015).

232. T. Jadoon, K. Carter-Fenk, M. B. A. Siddique, J. M. Herbert, R. Hussain, S. Iqbal, J. Iqbal, & K. Ayub. Silver clusters tune up electronic properties of graphene nanoflakes: A comprehensive theoretical study. *J. Mol. Liq.* **297**, 111902 (2020).

233. I. Shtepliuk & R. Yakimova. Computational Appraisal of Silver Nanocluster Evolution on Epitaxial Graphene: Implications for CO Sensing. *ACS Omega* **6**, 24739–24751 (2021).

234. J. P. Jalkanen, M. Halonen, D. Fernandez-Torre, K. Laasonen, L. Halonen, D. Fernández-Torre, K. Laasonen, & L. Halonen. A computational study of the adsorption of small Ag and Au nanoclusters on graphite. *J. Phys. Chem. A* **111**, 12317–12326 (2007).

235. M. Amft, S. Lebègue, O. Eriksson, & N. V. Skorodumova. Adsorption of Cu, Ag, and Au atoms on graphene including van der Waals interactions. *J. Phys. Condens. Matter* **23**, 395001 (2011).

236. A. Dahal & M. Batzill. Graphene–nickel interfaces: a review. *Nanoscale* **6**, 2548–2562 (2014).

237. J. Wintterlin & M. L. Bocquet. Graphene on metal surfaces. *Surf. Sci.* **603**, 1841–1852 (2009).

238. D. A. King & M. G. Wells. Reaction mechanism in chemisorption kinetics: nitrogen on the {100} plane of tungsten. *Proc. R. Soc. London. A. Math. Phys. Sci.* **339**, 245–269 (1974).

239. D. W. Goodman, R. D. Kelley, T. E. Madey, & J. T. Yates. Kinetics of the hydrogenation of CO over a single crystal nickel catalyst. *J. Catal.* **63**, 226–234 (1980).

240. J. P. Coad & J. C. Rivière. Auger spectroscopy of carbon on nickel. *Surf. Sci.* **25**, 609–624 (1971).

241. S. L. Hemmingson, G. M. Feeley, N. J. Miyake, & C. T. Campbell. Energetics of 2D and 3D Gold Nanoparticles on MgO(100): Influence of Particle Size and Defects on Gold Adsorption and Adhesion Energies. *ACS Catal.* **7**, 2151–2163 (2017).

242. U. Diebold, J. M. Pan, & T. E. Madey. Growth mode of ultrathin copper overlayers on TiO2(110). *Phys. Rev. B* **47**, 3868–3876 (1993).

243. X. Liu, Y. Han, J. W. Evans, A. K. Engstfeld, R. J. Behm, M. C. Tringides, M. Hupalo, H. Q. Lin, L. Huang, K. M. Ho, D. Appy, P. A. Thiel, & C. Z. Wang. Growth morphology and properties of metals on graphene. *Progress in Surface Science* **90**, 397–443 (2015).

244. K. L. Walton, N. S. Jacobson, B. A. Kowalski, J. D. Brockman, & S. K. Loyalka. Sorption isosteres and isotherms of silver on NBG-17 graphite. *J. Nucl. Mater.* **557**, 153264 (2021).

245. L. Vitos, A. V Ruban, H. L. Skriver, & J. Kollar. The Surface Energy of Metals. *Surf. Sci.* **411**, 186–202 (1998).

246. Z. Mao, J. R. Rumptz, & C. T. Campbell. Energetics of Ag Adsorption on and Adhesion to Rutile TiO2(100) Studied by Microcalorimetry. *J. Phys. Chem. C* **125**, 3036–3046 (2021).

247. P. Wynblatt & N. A. Gjostein. Supported metal crystallites. in *Progess in Solid State Chemistry* (eds. McCaldin, J. O. & Somorjai, G. A.) **9**, 21 (Pergamon, 1975).

248. E. M. Dietze & P. N. Plessow. Predicting the Strength of Metal-Support Interaction with Computational Descriptors for Adhesion Energies. *J. Phys. Chem. C* **123**, 20443–20450 (2019).

249. S. Hu & W.-X. Li. Sabatier principle of metal-support interaction for design of ultrastable metal nanocatalysts. *Science* **374**, 1360–1365 (2021).

250. D. R. Rainer & D. W. Goodman. Metal Clusters on Ultrathin Oxide Films: Model

Catalysts for Surface Science Studies. *J. Mol. Catal. A Chem.* **131**, 259 (1998).

251. M. Shao, A. Peles, & K. Shoemaker. Electrocatalysis on platinum nanoparticles: Particle size effect on oxygen reduction reaction activity. *Nano Lett.* **11**, 3714–3719 (2011).

252. X. Liu & L. Dai. Carbon-based metal-free catalysts. *Nature Reviews Materials* **1**, 16064 (2016).

253. X. Duan, J. Xu, Z. Wei, J. Ma, S. Guo, S. Wang, H. Liu, & S. Dou. Metal-Free Carbon Materials for CO2 Electrochemical Reduction. *Advanced Materials* **29**, (2017).

254. I. C. Gerber & P. Serp. A Theory/Experience Description of Support Effects in Carbon-Supported Catalysts. *Chemical Reviews* **120**, 1250–1349 (2020).

255. E. Lam & J. H. T. Luong. Carbon Materials as Catalyst Supports and Catalysts in the Transformation of Biomass to Fuels and Chemicals. *ACS Catal.* **4**, 3393–3410 (2014).

256. J. R. Rumptz, Z. Mao, & C. T. Campbell. Size-Dependent Adsorption and Adhesion Energetics of Ag Nanoparticles on Graphene Films on Ni(111) by Calorimetry. *ACS Catal.* **12**, 2888–2897 (2022).

257. J. Guo, H. Lou, H. Zhao, D. Chai, & X. Zheng. Dry reforming of methane over nickel catalysts supported on magnesium aluminate spinels. *Appl. Catal. A* **273**, 75–82 (2004).

258. J. A. Montoya, E. Romero-Pascual, C. Gimon, P. Del Angel, & A. Monzon. Methane reforming with CO2 over Ni/ZrO2–CeO2 catalysts prepared by sol–gel. *Catal. Today* **63**, 71–85 (2000).

259. S. Li & J. Gong. Strategies for improving the performance and stability of Ni-based catalysts for reforming reactions. *Chem. Soc. Rev.* **43**, 7245–7256 (2014).

260. D. Li, Y. Nakagawa, & K. Tomishige. Methane reforming to synthesis gas over Ni catalysts modified with noble metals. *Appl. Catal. A* **408**, 1–24 (2011).

261. C. Vogt, E. Groeneveld, G. Kamsma, M. Nachtegaal, L. Lu, C. J. Kiely, P. H. Berben, F. Meirer, & B. M. Weckhuysen. Unravelling structure sensitivity in CO2 hydrogenation over nickel. *Nat. Catal.* **1**, 127–134 (2018).

262. C. Vogt, M. Monai, E. B. Sterk, J. Palle, A. E. M. Melcherts, B. Zijlstra, E. Groeneveld, P. H. Berben, J. M. Boereboom, E. J. M. Hensen, F. Meirer, I. A. W. Filot, & B. M. Weckhuysen. Understanding carbon dioxide activation and carbon-carbon coupling over nickel. *Nat. Commun.* **10**, 1–10 (2019).

263. G. S. Ferdowsi, S. A. Seyedsadjadi, & A. Ghaffarinejad. Ni nanoparticle modified graphite electrode for methanol electrocatalytic oxidation in alkaline media. *J. Nanostructure Chem.* **5**, 17–23 (2015).

264. A. B. Soliman, H. S. Abdel-Samad, S. S. Abdel Rehim, M. A. Ahmed, & H. H. Hassan. High performance nano-Ni/Graphite electrode for electro-oxidation in direct alkaline ethanol fuel cells. *J. Power Sources* **325**, 653–663 (2016).

265. B. M. Thamer, M. H. El-Newehy, N. A. M. Barakat, M. A. Abdelkareem, S. S. Al-Deyab, & H. Y. Kim. In-situ synthesis of Ni/N-doped CNFs-supported graphite disk as effective immobilized catalyst for methanol electrooxidation. *Int. J. Hydrogen Energy* **40**, 14845–14856 (2015).

266. Z. Zhuang, S. A. Giles, J. Zheng, G. R. Jenness, S. Caratzoulas, D. G. Vlachos, & Y. Yan. Nickel supported on nitrogen-doped carbon nanotubes as hydrogen oxidation reaction catalyst in alkaline electrolyte. *Nat. Commun.* **7**, (2016).

267. Y. J. Wang, N. Zhao, B. Fang, H. Li, X. T. Bi, & H. Wang. Carbon-Supported Pt-Based Alloy Electrocatalysts for the Oxygen Reduction Reaction in Polymer Electrolyte Membrane Fuel Cells: Particle Size, Shape, and Composition Manipulation and Their

Impact to Activity. *Chemical Reviews* **115**, 3433–3467 (2015).

268. U. Sanyal, Y. Song, N. Singh, J. L. Fulton, J. Herranz, A. Jentys, O. Y. Gutiérrez, & J. A. Lercher. Structure Sensitivity in Hydrogenation Reactions on Pt/C in Aqueous-phase. *ChemCatChem* **11**, 575–582 (2019).

269. N. Singh, U. Sanyal, G. Ruehl, K. A. Stoerzinger, O. Y. Gutiérrez, D. M. Camaioni, J. L. Fulton, J. A. Lercher, & C. T. Campbell. Aqueous phase catalytic and electrocatalytic hydrogenation of phenol and benzaldehyde over platinum group metals. *J. Catal.* **382**, 372–384 (2020).

270. S. Mukerjee. Particle size and structural effects in platinum electrocatalysis. *Journal of Applied Electrochemistry* **20**, 537–548 (1990).

271. S. Mukerjee & J. McBreen. Effect of particle size on the electrocatalysis by carbon-supported Pt electrocatalysts: An in situ XAS investigation. *J. Electroanal. Chem.* **448**, 163–171 (1998).

272. R. E. Ambrusi, V. Orazi, J. M. Marchetti, & M. E. Pronsato. Ni clusters embedded in multivacancy graphene substrates. *J. Phys. Chem. Solids* **138**, 109258 (2020).

273. X. Zhou, W. Chu, W. Sun, Y. Zhou, & Y. Xue. Enhanced interaction of nickel clusters with pyridinic-N (B) doped graphene using DFT simulation. *Comput. Theor. Chem.* **1120**, 8–16 (2017).

274. W. Gao, J. E. Mueller, J. Anton, Q. Jiang, & T. Jacob. Nickel cluster growth on defect sites of graphene: A computational study. *Angew. Chemie - Int. Ed.* **52**, 14237–14241 (2013).

275. C. R. C. Rêgo, P. Tereshchuk, L. N. Oliveira, & J. L. F. Da Silva. Graphene-supported small transition-metal clusters: A density functional theory investigation within van der

Waals corrections. *Phys. Rev. B* **95**, 235422 (2017).

276. M. Sicot, S. Bouvron, O. Zander, U. Rüdiger, Y. S. Dedkov, & M. Fonin. Nucleation and growth of nickel nanoclusters on graphene Moiŕ on Rh(111). *Appl. Phys. Lett.* **96**, 93115 (2010).

277. M. Marz, K. Sagisaka, & D. Fujita. Ni nanocrystals on hopg(0001): A scanning tunnelling microscope study. *Beilstein J. Nanotechnol.* **4**, 406–417 (2013).

278. M. Bäumer, J. Libuda, & H. J. Freund. The temperature dependent growth mode of nickel on the basal plane of graphite. *Surf. Sci.* **327**, 321–329 (1995).

279. M. Manadé, F. Viñes, & F. Illas. Transition metal adatoms on graphene: A systematic density functional study. *Carbon N. Y.* **95**, 525–534 (2015).

280. O. V Yazyev & A. Pasquarello. Metal adatoms on graphene and hexagonal boron nitride: Towards rational design of self-assembly templates. *Phys. Rev. B - Condens. Matter Mater. Phys.* **82**, 045407 (2010).

281. K. H. Ernst, A. Ludviksson, R. Zhang, J. Yoshihara, & C. T. Campbell. Growth model for metal films on oxide surfaces: Cu on ZnO (0001)-O. *Phys. Rev. B* **47**, 13782 (1993).

282. E. Soy, N. P. Guisinger, & M. Trenary. Growth of Pd Nanoclusters on Single-Layer Graphene on Cu(111). *J. Phys. Chem. B* **122**, 572–577 (2018).

283. U. Diebold, J. M. Pan, & T. E. L. B.-M. on T. then (110) Madey. Growth Mode of Ultrathin Copper Overlayers on TiO2(110). *Phys. Rev. B* **47**, 3868–3876 (1993).

284. W. Tian, H. P. Sun, X. Q. Pan, J. H. Yu, M. Yeadon, C. B. Boothroyd, Y. P. Feng, R. A. Lukaszew, & R. Clarke. Hexagonal close-packed Ni nanostructures grown on the (001) surface of MgO. *Appl. Phys. Lett.* **86**, 131915 (2005).

285. J. Higuchi, M. Ohtake, Y. Sato, T. Nishiyama, & M. Futamoto. Preparation and Structural

Characterization of hcp and fcc Ni Epitaxial Thin Films on Ru Underlayers with Different Orientations. *Jpn. J. Appl. Phys.* **50**, 63001 (2011).

286. M. Ohtake, Y. Sato, J. Higuchi, & M. Futamoto. Microstructure of hcp-Ni(1100)/bcc-Cr(211) Bi-layer Film Grown on MgO(110) Substrate. in *Journal of Physics: Conference Series* **266**, (2011).

287. M. Ohtake, Y. Sato, J. Higuchi, T. Tanaka, F. Kirino, & M. Futamoto. Epitaxial growth of metastable hcp-Ni and hcp-NiFe thin films on Au (100) fcc single-crystal underlayers and their structure characterization. *Jpn. J. Appl. Phys.* **50**, 103001 (2011).

288. J. Y. Hwang, A. R. P. Singh, M. Chaudhari, J. Tiley, Y. Zhu, J. Du, & R. Banerjee. Templated growth of hexagonal nickel carbide nanocrystals on vertically aligned carbon nanotubes. *J. Phys. Chem. C* **114**, 10424–10429 (2010).

289. H. Cheng, N. Yang, Q. Lu, Z. Zhang, & H. Zhang. Syntheses and properties of metal nanomaterials with novel crystal phases. *Adv. Mater.* **30**, 1707189 (2018).

290. S. Illy, O. Tillement, F. Machizaud, J. M. Dubois, F. Massicot, Y. Fort, & J. Ghanbaja. First direct evidence of size-dependent structural transition in nanosized nickel particles. *Philos. Mag. A* **79**, 1021–1031 (1999).

291. J. Singh, Tarachand, S. S. Samatham, D. Venkateshwarlu, N. Kaurav, V. Ganesan, & G. S. Okram. Quantum size effect on the heat capacity of nickel nanolattice. *Appl. Phys. Lett.* **111**, 201904 (2017).

292. H. Lin, H. Lin, J. X. Liu, H. Fan, & W. X. Li. Compensation between Surface Energy and hcp/fcc Phase Energy of Late Transition Metals from First-Principles Calculations. *J. Phys. Chem. C* **124**, 11005–11014 (2020).

293. R.-T. Chiang, R.-K. Chiang, & F.-S. Shieu. Emergence of interstitial-atom-free HCP

nickel phase during the thermal decomposition of Ni 3 C nanoparticles. *RSC Adv.* **4**, 19488–19494 (2014).

294. C. T. Campbell. Energies of Adsorbed Catalytic Intermediates on Transition Metal Surfaces: Calorimetric Measurements and Benchmarks for Theory. *Acc. Chem. Res.* **52**, 984–993 (2019).

295. W. A. Brown, R. Kose, & D. A. King. Femtomole adsorption calorimetry on single-crystal surfaces. *Chem. Rev.* **98**, 797–832 (1998).

296. T. L. Silbaugh & C. T. Campbell. Energies of formation reactions measured for adsorbates on late transition metal surfaces. *J. Phys. Chem. C* **120**, 25161–25172 (2016).

297. J. Wellendorff, T. L. Silbaugh, D. Garcia-Pintos, J. K. Nørskov, T. Bligaard, F. Studt, & C. T. Campbell. A benchmark database for adsorption bond energies to transition metal surfaces and comparison to selected DFT functionals. *Surf. Sci.* **640**, 36–44 (2015).

298. P. Dementyev, K. H. Dostert, F. Ivars-Barcelõ, C. P. O'Brien, F. Mirabella, S. Schauermann, X. Li, J. Paier, J. Sauer, & H. J. Freund. Water Interaction with Iron Oxides. *Angew. Chemie - Int. Ed.* **54**, 13942–13946 (2015).

299. M. M. Montemore, M. A. Van Spronsen, R. J. Madix, & C. M. Friend. O2 Activation by Metal Surfaces: Implications for Bonding and Reactivity on Heterogeneous Catalysts. *Chem. Rev.* **118**, 2816–2862 (2018).

300. J. K. Norskov, F. Abild-Pedersen, F. Studt, & T. Bligaard. Density functional theory in surface chemistry and catalysis. *Proc. Natl. Acad. Sci.* **108**, 937–943 (2011).

301. V. G. Ruiz, W. Liu, E. Zojer, M. Scheffler, & A. Tkatchenko. Density-functional theory with screened van der Waals interactions for the modeling of hybrid inorganic-organic systems. *Phys. Rev. Lett.* **108**, (2012).

302. S. Gautier, S. N. Steinmann, C. Michel, P. Fleurat-Lessard, & P. Sautet. Molecular adsorption at Pt(111). How accurate are DFT functionals? *Phys. Chem. Chem. Phys.* **17**, 28921–28930 (2015).

303. M. Mavrikakis. Computational methods: A search engine for catalysts. *Nat. Mater.* **5**, 847–848 (2006).

304. J. O. M. Bockris & K. T. Jeng. In-situ studies of adsorption of organic compounds on platinum electrodes. *J. Electroanal. Chem.* **330**, 541–581 (1992).

305. H. H. Kristoffersen, J.-E. Shea, & H. Metiu. Catechol and HCl Adsorption on TiO2(110) in Vacuum and at the Water–TiO2 Interface. *J. Phys. Chem. Lett.* **6**, 2277–2281 (2015).

306. W. Song, N. Martsinovich, W. M. Heckl, & M. Lackinger. Born-haber cycle for monolayer self-assembly at the liquid-solid interface: Assessing the enthalpic driving force. *J. Am. Chem. Soc.* **135**, 14854–14862 (2013).

307. W. Song, N. Martsinovich, W. M. Heckl, & M. Lackinger. Thermodynamics of halogen bonded monolayer self-assembly at the liquid-solid interface. *Chem. Commun.* **50**, 13465–13468 (2014).

308. W. Song, N. Martsinovich, W. M. Heckl, & M. Lackinger. Thermodynamics of 4,4′-stilbenedicarboxylic acid monolayer self-assembly at the nonanoic acid-graphite interface. *Phys. Chem. Chem. Phys.* **16**, 13239–13247 (2014).

309. Y. Yoon, R. Rousseau, R. S. Weber, D. Mei, & J. A. Lercher. First-principles study of phenol hydrogenation on Pt and Ni catalysts in aqueous phase. *J. Am. Chem. Soc.* **136**, 10287–10298 (2014).

310. N. Singh, M. S. Lee, S. A. Akhade, G. Cheng, D. M. Camaioni, O. Y. Gutiérrez, V. A. Glezakou, R. Rousseau, J. A. Lercher, & C. T. Campbell. Impact of pH on Aqueous-Phase

Phenol Hydrogenation Catalyzed by Carbon-Supported Pt and Rh. *ACS Catal.* **9**, 1120–1128 (2019).

311. C. M. Gray, K. Saravanan, G. Wang, & J. A. Keith. Quantifying solvation energies at solid/liquid interfaces using continuum solvation methods. *Mol. Simul.* **43**, 420–427 (2017).

312. M. M. Montemore, O. Andreussi, & J. W. Medlin. Hydrocarbon adsorption in an aqueous environment: A computational study of alkyls on Cu(111). *J. Chem. Phys.* **145**, (2016).

313. Z. W. She, J. Kibsgaard, C. F. Dickens, I. B. Chorkendorff, J. K. Nørskov, T. F. Jaramillo, Z. W. Seh, J. Kibsgaard, C. F. Dickens, I. B. Chorkendorff, J. K. Norskov, & T. F. Jaramillo. Combining theory and experiment in electrocatalysis: Insights into materials design. *Science* **355**, (2017).

314. F. Calle-Vallejo, R. F. De Morais, F. Illas, D. Loffreda, & P. Sautet. Affordable Estimation of Solvation Contributions to the Adsorption Energies of Oxygenates on Metal Nanoparticles. *J. Phys. Chem. C* **123**, 5578–5582 (2019).

315. L. P. Granda-Marulanda, S. Builes, M. T. M. Koper, F. Calle-Vallejo, L. P. Granda-Marulanda, S. Builes, M. T. M. Koper, & F. Calle-Vallejo. Influence of Van der Waals Interactions on the Solvation Energies of Adsorbates at Pt-Based Electrocatalysts. *Chemphyschem* **DOI: 10.10**, (2019).

316. O. M. Magnussen & A. Groß. Toward an Atomic-Scale Understanding of Electrochemical Interface Structure and Dynamics. *Journal of the American Chemical Society* **141**, 4777–4790 (2019).

317. C. J. Bodenschatz, X. H. Zhang, T. J. Xie, J. Arvay, S. Sarupria, & R. B. Getman. Multiscale Sampling of a Heterogeneous Water/Metal Catalyst Interface using Density

Functional Theory and Force-Field Molecular Dynamics. *J. Vis. Exp.* **2019**, (2019).

318. M. Saleheen & A. Heyden. Liquid-Phase Modeling in Heterogeneous Catalysis. *ACS Catal.* **8**, 2188–2194 (2018).

319. M. Saleheen, M. Zare, M. Faheem, & A. Heyden. Computational Investigation of Aqueous Phase Effects on the Dehydrogenation and Dehydroxylation of Polyols over Pt(111). *J. Phys. Chem. C* **123**, 19052–19065 (2019).

320. X. Zhang, T. E. Sewell, B. Glatz, S. Sarupria, & R. B. Getman. On the water structure at hydrophobic interfaces and the roles of water on transition-metal catalyzed reactions: A short review. *Catal. Today* **285**, 57–64 (2017).

321. X. Zhang, R. S. Defever, S. Sarupria, & R. B. Getman. Free Energies of Catalytic Species Adsorbed to Pt(111) Surfaces under Liquid Solvent Calculated Using Classical and Quantum Approaches. *J. Chem. Inf. Model.* **59**, 2190–2198 (2019).

322. S. Dasetty, P. J. Meza-Morales, R. B. Getman, & S. Sarupria. Simulations of interfacial processes: recent advances in force field development. *Current Opinion in Chemical Engineering* 138–145 (2019). doi:10.1016/j.coche.2019.04.003

323. J. Hussain, H. Jónsson, & E. Skúlason. Calculations of Product Selectivity in Electrochemical CO2 Reduction. *ACS Catal.* **8**, 5240–5249 (2018).

324. J. Hussain, H. Jónsson, & E. Skúlason. Faraday efficiency and mechanism of electrochemical surface reactions: CO2 reduction and H2 formation on Pt(111). *Faraday Discuss.* **195**, 619–636 (2016).

325. S. J. Carey, W. Zhao, Z. Mao, & C. T. Campbell. Energetics of Adsorbed Phenol on Ni (111) and Pt (111) by Calorimetry. *J. Phys. Chem. C* **123**, 7627–7632 (2018).

326. N. Singh, U. Sanyal, J. L. Fulton, O. Y. Gutiérrez, J. A. Lercher, & C. T. Campbell.

Quantifying Adsorption of Organic Molecules on Platinum in Aqueous Phase by Hydrogen Site Blocking and in Situ X-ray Absorption Spectroscopy. *ACS Catal.* **9**, 6869–6881 (2019).

327. P. Atkins & J. de Paula. *Physical Chemistry: Thermodynamics, Structure, and Change*. (Oxford University Press, 2014).

328. W. Zhao, S. J. Carey, S. E. Morgan, & C. T. Campbell. Energetics of adsorbed formate and formic acid on Ni(111) by calorimetry. *J. Catal.* **352**, 300–304 (2017).

329. S. J. Carey, W. Zhao, & C. T. Campbell. Bond energies of adsorbed intermediates to metal surfaces correlate with H-ligand and H-surface bond energies and electronegativities. *Angew. Chemie Int. Ed.* **(in press)**, (2018).

330. S. J. Carey, W. Zhao, & C. T. Campbell. Energetics of adsorbed benzene on Ni(111) and Pt(111) by calorimetry. *Surf. Sci.* **676**, 9–16 (2018).

331. W. M. Ketcham, P. V Hobbs, & V. P. Hobbs. An Experimental Determination of the Surface Energies of Ice. *Philos. Mag.* **19**, 1161–1173 (1969).

332. W. R. Tyson & W. A. Miller. Surface free energies of solid metals: Estimation from liquid surface tension measurements. *Surf. Sci.* **62**, 267–276 (1977).

333. E. Chibowski & R. Perea-Carpio. Problems of contact angle and solid surface free energy determination. *Advances in Colloid and Interface Science* **98**, 245–264 (2002).

334. P. Müller & R. Kern. Equilibrium nano-shape changes induced by epitaxial stress (generalised Wulf-Kaishew theorem). *Surf. Sci.* **457**, 229–253 (2000).

335. R. B. Badachhape, K. Gharpurey, & A. B. Biswas. Density and Surface Tension of Phenol, (Mono-, Di-, and Tri-) chlorophenols, Salol, and (o-and m-)Chloronitrobenzenes. *J. Chem. Eng. Data* **10**, 143–145 (1965).

336. J. F. Padday & D. R. Russell. The measurement of the surface tension of pure liquids and solutions. *J. Colloid Sci.* **1**, 503–511 (1960).

337. E. M. Karp, T. L. Silbaugh, M. C. Crowe, & C. T. Campbell. Energetics of adsorbed methanol and methoxy on Pt(111) by microcalorimetry. *J. Am. Chem. Soc.* **134**, 20388–20395 (2012).

338. W. Zhao, S. J. Carey, Z. Mao, & C. T. Campbell. Adsorbed Hydroxyl and Water on Ni(111): Heats of Formation by Calorimetry. *ACS Catal.* **8**, 1485–1489 (2018).

339. S. J. Carey, W. Zhao, E. Harman, A. K. Baumann, Z. Mao, W. Zhang, & C. T. Campbell. Energetics of Adsorbed Methanol and Methoxy on Ni(111): Comparisons to Pt(111). *ACS Catal.* **8**, 10089–10095 (2018).

340. W. Lew, M. C. Crowe, E. Karp, & C. T. Campbell. Energy of molecularly adsorbed water on clean Pt(111) and Pt(111) with coadsorbed oxygen by calorimetry. *J. Phys. Chem. C* **115**, 9164–9170 (2011).

341. T. L. Silbaugh, E. M. Karp, & C. T. Campbell. Energetics of formic acid conversion to adsorbed formates on Pt(111) by transient calorimetry. *J. Am. Chem. Soc.* **136**, 3964–3971 (2014).

342. B. N. Zope, D. D. Hibbitts, M. Neurock, & R. J. Davis. Reactivity of the gold/water interface during selective oxidation catalysis. *Science* **330**, 74–78 (2010).

343. D. M. Alonso, S. G. Wettstein, & J. A. Dumesic. Gamma-valerolactone, a sustainable platform molecule derived from lignocellulosic biomass. *Green Chem.* **15**, 584–595 (2013).

344. B. S. Akpa, C. D’Agostino, L. F. Gladden, K. Hindle, H. Manyar, J. McGregor, R. Li, M. Neurock, N. Sinha, E. H. Stitt, D. Weber, J. A. Zeitler, & D. W. Rooney. Solvent effects

in the hydrogenation of 2-butanone. *J. Catal.* **289**, 30–41 (2012).

345. H. Wan, A. Vitter, R. V Chaudhari, & B. Subramaniam. Kinetic investigations of unusual solvent effects during Ru/C catalyzed hydrogenation of model oxygenates. *J. Catal.* **309**, 174–184 (2014).

346. J. Akinola, C. T. Campbell, & N. Singh. Effects of Solvents on Adsorption Energies: A General Bond-Additivity Model. *J. Phys. Chem. C* **125**, 24371–24380 (2021).

347. J. R. Rumptz & C. T. Campbell. Adhesion Energies of Solvent Films to Pt(111) and Ni(111) Surfaces by Adsorption Calorimetry. *ACS Catal.* **9**, 11819–11825 (2019).

348. S. L. Tait, Z. Dohnalek, C. T. Campbell, B. D. Kay, Z. Dohnálek, C. T. Campbell, & B. D. Kay. n-alkanes on MgO(100). I. Coverage-dependent desorption kinetics of n-butane. *J. Chem. Phys.* **122**, 164707 (2005).

349. P. A. Redhead. Thermal desorption of gases. *Vacuum* **12**, 203–211 (1962).

350. S. L. Tait, Z. Dohnálek, C. T. Campbell, B. D. Kay, Z. Dohnalek, C. T. Campbell, & B. D. Kay. n-alkanes on MgO(100). II. Chain length dependence of kinetic desorption parameters for small n-alkanes. *J. Chem. Phys.* **122**, 164708 (2005).

351. S. L. Tait, Z. Dohnálek, C. T. Campbell, & B. D. Kay. n-alkanes on Pt(111) and on C(0001)/Pt(111): Chain length dependence of kinetic desorption parameters. *J. Chem. Phys.* **125**, 234308 (2006).

352. A. R. Bishop, G. S. Girolami, & R. G. Nuzzo. Structural Models and Thermal Desorption Energetics for Multilayer Assemblies of the n-Alkanes on Pt(111). *J. Phys. Chem. B* **104**, 754–763 (2000).

353. L. Chen, S. Zhang, R. R. Persaud, R. S. Smith, B. D. Kay, D. Dixon, & Z. Dohnálek. Understanding the Binding of Aromatic Hydrocarbons on Rutile TiO2(110). *J. Phys.*

Chem. C **123**, 16766–16777 (2019).

354. W. A. Zisman. Relation of the Equilibrium Contact Angle to Liquid and Solid Constitution. in *Contact Angle, Wettability, and Adhesion* (ed. Fowkes, F. M.) 1–51 (American Chemical Society, 1964). doi:10.1021/ba-1964-0043.ch001

355. C. T. Campbell & J. R. V. V Sellers. The entropies of adsorbed molecules. *J. Am. Chem. Soc.* **134**, 18109–18115 (2012).

356. D. A. McQuarrie. *Statistical Mechanics*. (University Science Books, 2000).

357. W. E. Acree & J. S. Chikos. Phase Transition Enthalpy Measurements of Organic and Organometallic Compounds. in *NIST Chemistry WebBook, NIST Standard Reference Database Number 69* (eds. Linstrom, P. J. & Mallard, W. G.) (National Institute of Standards and Technology, 2021).

Vita

John Rumptz was born and raised in the California Bay Area. He received a Bachelor of Science degree in Chemical Engineering from the University of Colorado Boulder. While pursuing his undergraduate degree he researched electrochemical CO_2 reduction, solar thermal ammonia synthesis, and inorganic materials thermochemistry using density functional theory and machine learning. His undergraduate research was performed primarily under the guidance of Dr. Christopher Bartel and supervised by Professor Charles Musgrave.

John conducted his PhD research in the University of Washington Department of Chemical Engineering under the supervision of Professor Charles Campbell from the Department of Chemistry. His PhD work focused on the energetics and structure of late transition metal nanoparticles supported on single crystal oxide and carbon materials as well as how the adhesion energies of solvents affect the stability of adsorbed molecules. During his time at the University of Washington, John helped mentor four undergraduate students and was a teaching assistant for undergraduate-level process design and thermodynamics and graduate-level transport phenomena in the Department of Chemical Engineering and for graduate-level statistical mechanics in the Department of Chemistry.